The evolution of the Patagonian Ice Sheet from 35 ka to the Present Day (PATICE)

Abstract

We present PATICE, a GIS database of Patagonian glacial geomorphology and recalibrated chronostratigraphic data. PATICE includes 58,823 landforms and 1,669 geochronological ages, and extends from 38°S to 55°S in southern South America. We use these data to generate new empirical reconstructions of the Patagonian Ice Sheet (PIS) and subsequent ice masses and ice-dammed palaeolakes at 35 ka, 30 ka, 25 ka, 20 ka, 15 ka, 13 ka (synchronous with the Antarctic Cold Reversal), 10 ka, 5 ka, 0.2 ka and 2011 AD. At 35 ka, the PIS covered of 492.6 $x10^3$ km^2, had a sea level equivalent of ~1,496 mm, was 350 km wide and 2090 km long, and was grounded on the Pacific continental shelf edge. Outlet glacier lobes remained topographically confined and the largest generated the suites of subglacial streamlined bedforms characteristic of ice streams. The PIS reached its maximum extent by 33 – 28 ka from 38°S to 48°S, and earlier, around 47 ka from 48°S southwards. Net retreat from maximum positions began by 25 ka, with ice-marginal stabilisation then at 21 – 18 ka, which was then followed by rapid irreversible deglaciation. By 15 ka, the PIS had separated into disparate ice masses, draining into large ice-dammed lakes along the eastern margin, which strongly influenced rates of recession. Glacial readvances or stabilisations occurred at least at 14 – 13 ka, 11 ka, 6 – 5 ka, 2 – 1 ka, and 0.5 – 0.2 ka. We suggest that 20th century glacial recession (% a^{-1}) is occurring faster than at any time documented during the Holocene.


A
35 ka Ice Sheet
Glaciers
High confidence
Medium confidence
Low confidence
Allipen
Villarrica
Calafquen
Huechulafquen
Ranco
Puyehue
Nahuel Huapi
Llanquihue
Ancud
Epuyen
Cholila
Corcovado
Quimei
Palena
Pico
Cisnes
Fortana
Coyt
Coyhaique
Balmaceda
GCBA
CP
MSL
Sangra
San Martin / O'Higgins
Viedma
Argentino
Baguales
Coyle/TDP
del Toro
BV/RG/UE
Skyring
Otway
Magellan
Bahia Inutil
Fagnano
Beagle
Kilometers
0 62.5125 250 375 500
B
LGM flowline
LGM Ice divide
Col spillway
35 ka Ice Sheet
Glacial lake 35 ka
PATICE

The evolution of the Patagonian Ice Sheet from 35 ka to the Present Day (PATICE)

Bethan J. Davies[1]*, Christopher M. Darvill[2], Harold Lovell[3], Jacob M. Bendle[1], Julian A. Dowdeswell[4], Derek Fabel[5], Juan-Luis García[6], Alessa Geiger[6], Neil F. Glasser[7], Delia M. Gheorghiu[5], Stephan Harrison[8], Andrew S. Hein[9], Michael R. Kaplan[10], Julian R.V. Martin[1], Monika Mendelova[9], Adrian Palmer[1], Mauri Pelto[11], Ángel Rodés[5], Esteban A. Sagredo[6,12], Rachel Smedley[13], John L. Smellie[14], Varyl R. Thorndycraft[1].

*Corresponding author: Bethan.davies@rhul.ac.uk

[1]Centre for Quaternary Research, Department of Geography, Royal Holloway University of London, Egham Hill, Egham, Surrey, TW20 0EX, UK

[2]Department of Geography, The University of Manchester, Oxford Road, Manchester M13 9PL, UK

[3]School of the Environment, Geography and Geosciences, University of Portsmouth, Buckingham Building, Lion Terrace, Portsmouth PO1 3HE, UK

[4]Scott Polar Research Institute, University of Cambridge, Cambridge CB2 1ER, UK

[5]Scottish Universities Environmental Research Centre (SUERC), Rankine Avenue, East Kilbride G75 0QF, UK

[6]Instituto de Geografía, Facultad de Historia, Geografía y Ciencia Política, Pontificia Universidad Católica de Chile, Avenida Vicuña Mackenna 4860, Macul, Santiago 782-0436, Chile

[7]Faculty of Earth and Life Sciences, Prifysgol Aberystwyth University, Campws Penglais / Penglais Campus, Aberystwyth, Ceredigion, SY23 3DB, UK

[8]College of Life and Environmental Sciences, University of Exeter, Cornwall Campus, Penryn, TR10 9EZ, UK

[9]School of GeoSciences, University of Edinburgh, Drummond Street, Edinburgh EH8 9XP, UK

[10]Lamont-Doherty Earth Observatory of Columbia University, Palisades, NY, 10964, USA

[11]Nichols College, 121 Centre Road, PO Box 5000, Dudley MA 01571, USA

[12]Millenium Nuclei Palaeoclimate

[13]School of Geography and Planning, University of Liverpool, Liverpool L69 7ZT, UK

[14]School of Geography, Geology and the Environment, University of Leicester, University Road, Leicester LE1 7RH, UK

Key words:

Patagonia, ice sheet, geochronology, Quaternary, glaciation, geomorphology

Abbreviations

GIS	Geographical Information System
LGM	Last Glacial Maximum
LLGM	Local Last Glacial Maximum
PIS	Patagonian Ice Sheet
ACR	Antarctic Cold Reversal
Lago GCBA	Lago General Carrera/Buenos Aires
Lago CP	Lago Cochrane/Pueyrredón
UE/BV	Última Esperanza /Bella Vista—Río Gallegos Lobe
SWW	Southern Westerly Winds
m asl	metres above sea level
ka	thousands of years ago
cal. ka BP	calibrated thousands of years ago
Gt	Gigatonnes
DEM	Digital Elevation Model
MIS	Marine Isotope Stage
SLE	Sea Level Equivalent
ACC	Antarctic Circumpolar Current
SAM	Southern Annular Mode
MSL	Monte San Lorenzo
OSL	Optically stimulated luminescence
SD	Standard deviation
μ	Mean

Abstract

We present PATICE, a GIS database of Patagonian glacial geomorphology and recalibrated chronostratigraphic data. PATICE includes 58,823 landforms and 1,669 geochronological ages, and extends from 38°S to 55°S in southern South America. We use these data to generate new empirical reconstructions of the Patagonian Ice Sheet (PIS) and subsequent ice masses and ice-dammed palaeolakes at 35 ka, 30 ka, 25 ka, 20 ka, 15 ka, 13 ka (synchronous with the Antarctic Cold Reversal), 10 ka, 5 ka, 0.2 ka and 2011 AD. At 35 ka, the PIS covered of 492.6 x10^3 km^2, had a sea level equivalent of ~1,496 mm, was 350 km wide and 2090 km long, and was grounded on the Pacific continental shelf edge. Outlet glacier lobes remained topographically confined and the largest generated the suites of subglacial streamlined bedforms characteristic of ice streams. The PIS reached its maximum extent by 33 – 28 ka from 38°S to 48°S, and earlier, around 47 ka from 48°S southwards. Net retreat from maximum positions began by 25 ka, with ice-marginal stabilisation then at 21 – 18 ka, which was then followed by rapid irreversible deglaciation. By 15 ka, the PIS had separated into disparate ice masses, draining into large ice-dammed lakes along the eastern margin, which strongly influenced rates of recession. Glacial readvances or stabilisations occurred at least at 14 – 13 ka, 11 ka, 6 – 5 ka, 2 – 1 ka, and 0.5 – 0.2 ka. We suggest that 20th century glacial recession (% a^{-1}) is occurring faster than at any time documented during the Holocene.

1 Introduction

Glacier recession is accelerating in Patagonia (Aniya, 1999; Davies and Glasser, 2012; Meier et al., 2018; Braun et al., 2019), causing sea level rise (Gardner et al., 2013; Malz et al., 2018), enlarging glacial lakes and increasing flood risk (Loriaux and Casassa, 2013; Wilson et al., 2018), and affecting water availability and hydropower opportunities (Huss and Hock, 2018; Milner et al., 2017). The Southern Andes region had a mass loss of 1,208 Gt from 1961 to 2016, and is the largest contributor to global sea level rise outside of Greenland and Alaska (Zemp et al., 2019). This mass loss from global glaciers provides a global contribution of 0.92 ± 0.39 mm a^{-1} to global sea-level rise (totalling 27 ± 22 mm from 1961 – 2016), accounting for 25 – 30% of total observed sea level rise; this is equivalent to mass loss from the Greenland Ice Sheet and exceeds loss from Antarctica (Zemp et al., 2019). In order to understand how future climate change will influence the world's glaciers, and how this will affect societies, it is imperative to model future climate, glacier response and hydrology. Detailed analyses of past glacier-climate interactions can be used to constrain and test numerical models and to untangle externally driven changes versus internally forced changes (e.g. climate compared with calving, ice divide change and topography).

During past glacial periods, the Patagonian Ice Sheet (PIS) was centred on the central chain of the Andes, stretched from ~38°S to 55°S, consisted of terrestrial lobes that retreated into large palaeolakes on the east,

89 and is inferred to have reached the continental shelf on the west coast. The past behaviour of the PIS during
90 different climate states and during rapid climatic transitions could shed insights into the ways in which the
91 region is sensitive to changes and could respond to future climate change. Reconstruction of the evolution of
92 the former PIS provides a unique insight into past terrestrial cryospheric and climatic change in the southern
93 mid-latitudes, a particularly data-sparse area of the globe, and forms an important proxy for changes in
94 circum-hemispheric atmospheric and oceanic systems during global deglaciation (Harrison and Glasser,
95 2011; Kilian and Lamy, 2012). Improved understanding of the ice-ocean-atmosphere dynamics across the
96 large latitudinal expanse of Patagonia also has the potential to yield insights into the past north/south
97 contraction and expansion of the Southern Westerly Winds (SWW) during key palaeoclimatic transitions
98 (Kohfeld et al., 2013; Sime et al., 2013). The SWW are one of the most important climatic controls of the
99 Patagonian Andes and are responsible for driving major changes in ocean currents, resulting in cryospheric
100 change in West Antarctica (Rignot et al., 2019). However, large uncertainties in the long-term dynamics of
101 the SWW make it challenging to contextualise recent change in this atmospheric circulation system.

102 Data-calibrated numerical models provide insights into ice sheet and glacier response to periods of rapid
103 climate change (e.g. Briggs et al., 2014; Ely et al., 2019; Golledge et al., 2014; Patton et al., 2017; Stokes et
104 al., 2015; Tarasov et al., 2012) . Well-constrained numerical models are used to test hypotheses regarding
105 ice-sheet behaviour under different climatic regimes (e.g. Golledge et al., 2012, 2014; Hulton et al., 2002;
106 Patton et al., 2016, 2017; Stokes and Tarasov, 2010), allowing insights into likely future glacier behaviour.
107 They also yield insights into the mechanisms and climatic controls forcing palaeo ice sheets (e.g. Hubbard et
108 al., 2005), and assist in assessments of the vulnerability of ice masses to future climatic change. Data-
109 calibrated numerical model simulations are reliant on high quality empirical data of glacier fluctuations with
110 well-understood and quantified uncertainties. Improved, open source, ice sheet models such as PISM
111 (Winkelmann et al., 2011), BISICLES (Martin et al., 2013) and GLIMMER (Rutt et al., 2009) now make it
112 possible to simulate PIS evolution from the Last Glacial Maximum (LGM) to present. However, such models
113 clearly require a robust geological framework (including accurate inferences of the direction of ice flow,
114 timing of ice-free conditions, ice-marginal locations, extent and thickness, with an evaluation of uncertainty,
115 at different times), against which they can be calibrated (cf. Ely et al., 2019; Hughes et al., 2016).

116 There is a large volume of ages and geomorphology constraining past ice sheet extent and dynamics across
117 Patagonia. The first quantified reconstructions of the evolution of the PIS with chronological constraints
118 relied on radiocarbon dating (Mercer, 1968; Mercer, 1970; Porter, 1981). Chronologies of pre-LGM ice
119 extent used $^{40}Ar/^{39}Ar$ (and K-Ar) dating of interbedded moraines and volcanic sequences (e.g. Singer et al.,
120 2004a, b; Clague et al. 2020). Glacier recession over the last few centuries has been mapped using
121 lichenometry (Winchester and Harrison, 2000; Garibotti and Villalba, 2017), dendrochronology (e.g.

Winchester et al., 2014), and historical documents dating from the exploration era (e.g. Casassa et al., 1997). Note that since there is debate about whether the "Little Ice Age" is a global event, in this article we use the term "Late Holocene" for the most recent glacier expansion, dating from 0.5 – 0.2 ka BP. More recently, the application of innovative forms of cosmogenic nuclide exposure-age dating (Ackert et al., 2008; Douglass et al., 2006; García et al., 2012; Hein et al., 2011; Kaplan et al., 2005, 2011; Cogez et al., 2018), cosmogenic nuclide depth profiles (Darvill et al., 2015b; Hein et al., 2009), optically stimulated luminescence dating (Blomdin et al., 2012; Smedley et al., 2016; Garcia et al., 2019), tephrochronology (Kilian et al., 2003; Stern, 2008; Stern et al., 2016; Weller et al., 2015) and varve-age dating (Bendle et al., 2017a, 2019) has resulted in new insights into the timing and dynamics of both ice-sheet behaviour and palaeolake development.

However, age calculation techniques differ between studies, at times using different erosion corrections (often untested), outlier-removal strategies, marine reservoir effects for radiocarbon dating, and different calibration curves. Further, the calibration of radiocarbon dating (Hogg et al., 2013; Ortlieb et al., 2011; Stuiver et al., 2009) and cosmogenic nuclide dating (Borchers et al., 2016; Kaplan et al., 2011; Lal, 1991; Stone, 2000) has improved over time, making inter-study comparisons difficult given the varying times at which data were gathered and published. Moreover, research has long highlighted the importance of ice-dammed proglacial palaeolake development in eastern Patagonia during deglaciation (e.g., Bell, 2009; Bendle et al., 2017b; Caldenius, 1932; García et al., 2014; Thorndycraft et al, 2019a; Turner et al., 2005), but these have not been included in previous ice sheet reconstructions.

While geomorphological data has been compiled previously (Glasser et al., 2008), a geomorphological and chronological database of palaeolake development throughout southern South America has not been attempted. To date, no attempt has been made to gather these numerous geochronological ages and geomorphological data from across Patagonia into a single database, recalibrate ages using the latest protocols, and assess their reliability. Although LGM ice extent has previously been reconstructed (e.g. Caldenius, 1932, Coronato and Rabassa, 2011), no attempt has been made to calculate ice volume from empirical data, assess confidence in ice-marginal positions, or reconstruct the entire ice sheet and its changing palaeolakes through time. This is required as a first step to improving data-calibrated numerical modelling of the PIS.

Here, we present an original, pan-ice sheet, empirical reconstruction (PATICE) of the PIS (38°S to 56°S) from 35 ka to 2011 AD (0 ka) in 5000 year increments, with additional reconstructions at periods of significant ice-margin stabilisation (13 ka, coeval with the ACR, and during the Late Holocene, 0.2 ka). We do not include pre-35 ka glacial fluctuations of the PIS due to a lack of data across the study area, but note that there is evidence of extensive ice prior to 35 ka in southern Patagonia (cf. Garcia et al., 2018; Darvill et al., 2015). We use volume-area scaling to provide a new estimate of ice volume for each time slice. Our reconstruction

155 compiles existing geomorphological and chronological data, which have been robustly standardised,
156 together with an assessment of the reliability of each age. Our new PATICE database includes 58,823
157 landforms, 1,669 geochronological ages that constrain ice-free conditions (all recalibrated according to the
158 latest protocols), and spans the breadth of the published literature from 38°S to 56°S centred around the
159 Andes in southernmost South America. It is the first large-scale synthesis to integrate both the terrestrial and
160 offshore geomorphology and chronology. We generate an assessment of confidence (low, medium and high)
161 for each reconstructed ice margin, based on multiple lines of geomorphological and chronological evidence.
162 We interrogate and reveal spatial and temporal variability in ice-mass change over the last 35,000 years,
163 made manifest in terrain and landform evolution. In doing so, we present a novel reconstruction from
164 maximum glaciation, to the present small glaciers, ice caps and ice fields, incorporating palaeolake evolution
165 and drainage. In our synthesis (Section 6), we compare our new empirical LGM and post-LGM
166 reconstructions directly with published empirical reconstructions (Caldenius, 1932; Clapperton 1993;
167 Coronato and Rabassa, 2011) and modelled reconstructions (e.g. Hubbard et al., 2005; Hulton et al., 2002).
168 Our reconstruction yields important insights into rates of change for the PIS during deglaciation, emphasises
169 where ice margins are well constrained or poorly constrained and highlights priorities for future work, and
170 presents a framework that can be used to tune and test future ice-sheet models.

171

172

173 In this paper, Section 2 outlines and describes the study area (geology, topography, present-day climate and
174 proxy records of palaeoclimate). Section 3 summarises the geomorphological and chronological methods
175 used, with more information provided in the Supplementary Methods. Section 4 presents a new analysis of
176 the four key glacial landsystems in Patagonia: upland land-terminating glacier, lowland land-terminating
177 glacier, glaciolacustrine and glaciomarine. Section 5 presents the new PATICE reconstruction for the six
178 sectors of the study area: the Chilean Lake District (38°S – 42°S), Isla de Chiloe and Archipiélago de los
179 Chonos and the adjacent mainland (42°S – 46°S), the Northern Patagonian Icefield (46°S to 48°S), the
180 Southern Patagonian Icefield (48°S– 52°S), Gran Campo Nevado (52°S – 53°S), and Cordillera Darwin (53°S –
181 56°S). Section 6 synthesises these data, examines the timing and characteristics of the key advances, and
182 highlights latitudinal variations in glaciation. We compare our empirical reconstruction to published
183 numerically modelled reconstructions. We also highlight rates of ice and palaeolake area and volume
184 change, and identify key research questions and gaps in knowledge.

185

2 Study area

2.1 Geological setting

Topography and geology are key influencers of Quaternary and recent glaciation. Patagonia is located at the junction of four key continental plates; the Nazca, Antarctic, South American and Scotia plates (Figure 1). North of the Chile Triple Junction, the Nazca Plate is subducting beneath the South American plate in a north-easterly direction at 66 mm/yr (Rosenau et al., 2006). South of the Triple Junction, the Antarctic Plate has been subducted at a rate of about 20 mm/yr. Patagonia is bounded to the north by the Gastre Fault System, a major dextral shear zone and geological boundary with perhaps 500 km of lateral displacement. The Gastre Fault System is a fundamental crustal structure, regarded as an intraplate boundary that divides thick cratonic crust to the north from thinner continental crust beneath southern Patagonia, and it marks the northern limit of the Mesozoic-Cenozoic Patagonian Batholith, an important part of one of the largest Cordilleran batholiths on Earth (Rapela and Pankhurst, 1992).

The western edge of Patagonia contains outcrops of low-grade metasedimentary rocks and glaucophane-bearing metabasites (Figure 1). Together, they form a metamorphic complex interpreted as a Late Palaeozoic accretionary prism that was subsequently intruded by the Patagonian batholith (Hervé et al., 2003). The batholith forms a prominent north—south-trending zone about 100 km wide that is dominated by evolved I-type granitoids (mainly tonalities, granodiorites and granites) and associated widespread coeval volcanism, with an age range of Jurassic to Neogene (c. 180 – 15 Ma; Hervé et al., 2007; Rapela et al., 2005). Pliocene and younger products of the magmatic arc are represented by calc-alkaline volcanism that occupies a linear zone on the same axis as the batholith. About 60 volcanic centres are recognised, including 40 of Holocene age. In southern Chile and Tierra del Fuego, back-arc basin strata called the Rocas Verdes were created during Late Jurassic extension (Dalziel et al., 1974; Fildani and Hessler, 2005), together with voluminous bimodal, mainly felsic volcanism that forms a large igneous province (Chon Aike Province). In the north of the study region, these volcanoes provide a local nucleus for glacierisation (Braun et al., 2019; Reindthaler et al., 2019).

Finally, extensive outcrops of Eocene and Plio-Pleistocene alkaline back-arc flood basalts are also present in the east and have been related to the passage of windows in the oceanic slab subducted under the Andean arc (Forsyth and Prior, 1992). This past volcanism has aided the dating of Cenozoic glaciation (Singer et al., 2004a).

Figure 1. Geology of the study region, after Schenk et al. (1997). Plate boundaries from Bird (2003). Gastre Fault and Cenozoic fold-and-thrust belt from Rosenau et al. (2006). Inset shows wider arrangement of plate boundaries.

2.2 Topography

The Andes stretch for 7,000 km along the west coast of South America, and form a major barrier to the prevailing Southern Westerly Winds (Ackert et al., 2008). Patagonia incorporates part of this mountain range and extends from about 38°S to the southern tip of the continent at 56°S. Mountain summits reach 4,000 m high, decreasing to 1,500 – 2,000 m in the south of the study region (Figure 2).

East of the Andes, Argentine Patagonia and Tierra del Fuego feature low-lying (100 – 200 m asl) steppe-like plains extending for hundreds of kilometres to the Atlantic Ocean (Garreaud et al., 2013). The wide continental shelf mostly less than 150 m deep on the eastern Atlantic margin extends hundreds of kilometres offshore (Ponce et al., 2011) (Figure 2, Figure 3). Iceberg ploughmarks are present on the sea floor as far north as 45°S, but these are mainly derived from the full-glacial Antarctic Ice Sheet (López-Martínez et al., 2011). Over-deepened basins east of the Andes are occupied by large proglacial lakes.

The continental shelf on the western, Pacific, margin of Patagonia is located close (tens of kilometres) to the present-day coast. The western Patagonian coastline comprises many channels, islands and fjords, carved out by repeated Cenozoic glaciations. The western coastline receives freshwater from direct precipitation, surface runoff, groundwater and major rivers draining the Patagonian icefields, such as the Baker, Pascua and Bravo rivers. The fjords typically have an estuarine circulation, with rivers discharging at their upstream end to build sedimentary deltas. These fjords have irregular and sometimes over-deepened seafloor topography and sills relating to their excavation by glaciers during full-glacial periods (Syvitski et al., 1987). They are infilled by tens of metres of Holocene fine-grained, laminated sediments (DaSilva et al., 1997; Dowdeswell et al., 2016b, 2016c; Bertrand et al., 2017).

2.3 Glaciers and Icefields

Today, the Patagonian Andes support four main icefields: the Northern Patagonian Icefield at 46.4°S to 47.5°S, the Southern Patagonian Icefield at 48.3°S to 52°S, the Gran Campo Nevado at 52.8°S, and the Cordillera Darwin icefield at 54.5°S. The region also hosts numerous small icefields and mountain glaciers, often centred on volcanoes, and the lowest Southern Hemisphere latitude at which glaciers reach the sea today are found in the Chilean fjords at 47°S in the Northern Patagonian Icefield (Dowdeswell and Vásquez, 2013).

In total, present-day icefields and glaciers comprise around 617 glaciers amounting to a total area of 22,718 km^2 in 2011 (Davies and Glasser, 2012) (Figure 2). This equates to a total volume of 5,955 ± 1,191 km^3 (5,458 ± 1,092 Gt) of ice or 15.1 ± 3.0 mm of sea level equivalent (Carrivick et al., 2016). The region has a specific annual mass change of -1.18 ± 0.38 m w.e. a^{-1}, or -34 ± 11 Gt a^{-1} (2006 to 2016) (Zemp et al., 2019).

During glacial maxima, the icefields coalesced to form a single large ice mass extending westwards to the continental shelf edge and eastwards into steppe-like plains (Caldenius, 1932; Clapperton and Clapperton, 1993; Coronato and Rabassa, 2011; Glasser and Jansson, 2008; Glasser et al., 2011b; Glasser et al., 2008; Hein et al., 2010; McCulloch et al., 2000; Mercer, 1968, 1976). During ice recession, a series of large proglacial lakes formed along the eastern ice margin, dammed between the ice sheet and higher ground or moraines (Bourgois et al., 2016; Caldenius, 1932; Glasser et al., 2016b; García et al., 2014; Lovell et al., 2012; Martinod et al., 2016; McCulloch and Bentley, 1998; Sagredo et al., 2011; Thorndycraft et al, 2019a; Turner et al., 2005). On the eastern side of the Andes, terminal moraines from these maxima often form the present-day continental watershed divide, following lake drainage events causing Atlantic to Pacific drainage reversals and underfit valleys in the sectors 42 – 49°S and 51 – 53°S (Thorndycraft et al, 2019a). Some of these palaeolakes, such as Pico (Caldenius, 1932) and Cisnes (Garcia et al., 2019) drained completely, while others dropped to their current level, dammed by sills at their outflows.

Figure 2. Study area, the Patagonian Icefields, and key placenames mentioned in text. Mapped glaciers are shown (from Davies and Glasser, 2012, part of the Randolph Glacier Inventory) overlain on a GEBCO GDEM. Bathymetry shows location of the continental shelf. Inset shows location of Patagonia within South America. Location of marine cores mentioned in the text are shown. The Chilean Lake District, Isla de Chiloé, Archipiélago de los Chonos, Northern Patagonian Icefield, Southern Patagonian Icefield, Gran Campo Nevado and Cordillera Darwin are highlighted.

2.4 Present-day climate and oceanography

The modern climate of southern South America has been thoroughly reviewed by Aravena and Luckman (2009) and Garreaud et al. (2013, 2009). South of 40°S, the climate regime is temperate owing to its location between the Sub-Tropical and Sub-Antarctic Fronts (Kohfeld et al., 2013) and the strong influence of the circumpolar Southern Westerly Winds (SWW) (Figure 3). The SWW bring precipitation to Patagonia from the Pacific Ocean. Western Patagonia has annual mean precipitation in the region of 5,000 to 10,000 mm per year (Garreaud et al., 2013; Lenaerts et al., 2014) (Figure 3B). Rainfall decreases rapidly eastwards, resulting in a significant rain shadow east of the Andes (Aravena and Luckman, 2009). Eastern Patagonia tends to have a continental climate dominated by the SWW, with highly evaporative conditions at the surface (Garreaud et al., 2013). Increases in the strength of the SWW will result in a decreased amplitude of the local temperature

annual cycle (Garreaud et al., 2013). These climatic gradients lead to strong westwards and southwards variations in the vegetation communities in Patagonia (Montade et al., 2019), and have likely played a role in controlling past glaciation.

In the southernmost parts of Patagonia this precipitation is evenly distributed throughout the year, but to the north, around Puerto Montt (Figure 2), it falls mostly during the austral winter (Aravena and Luckman, 2009; Rodbell et al., 2009). West of the Andes, seasons with stronger SWW augment precipitation, but east of the Andes, increases in the SWW decrease local precipitation. Thus, SWW strength and precipitation are generally anti-correlated between the west and east sides of the Andes. This includes a possible weakening of the orographic effect; studies have also recently highlighted that for southern Patagonia, when the SWW are relatively weak, easterly-derived moisture can be important on the Atlantic side of the continent (e.g., Mayr et al., 2007; Quade and Kaplan, 2017). For example, high lake levels east of the Andes (e.g. at around 10 ka at Lago Cardiel), may be associated with reduced glacier extent. Such periods, with increased easterly moisture delivery, may include the warmer periods of the Holocene, perhaps due to intensity or displacement of the westerlies far to the south.

Over decadal timescales, large-scale climate cycles such as the El Niño Southern Oscillation (ENSO) influence Patagonian climate variability, largely through atmospheric teleconnections that modulate westerly airflow and thus regional heat and moisture distribution (Aravena and Luckman, 2009; Garreaud et al., 2009). Between 45°S and 55°S, strongly positive El Niño years result in approximately 15% less precipitation as a result of a decreased strength in the SWW (Schneider and Gies, 2004).

Other large-scale climatic oscillations include the Southern Annular Mode (SAM; also known as the Antarctic Oscillation). During SAM positive phases, there is a poleward expansion of the band of stronger westerlies, affecting the Antarctic periphery, while the winds weaken between ~40 – 50°S (Moreno et al., 2018). In Patagonia, cold and wet conditions are associated with negative SAM modes; conversely, warm and dry conditions are associated with positive SAM modes (Quade and Kaplan, 2017; Moreno et al., 2018). Quade and Kaplan (2017) suggested that dominantly positive or negative SAM-like conditions can persist for centuries, influencing ecologic and glacier systems. The most recent cold/wet negative SAM interval was contemporaneous with the European “Little Ice Age” (Moreno et al., 2018), which suggests that interhemispheric correlation of centennial-scale events over the last millennium was apparently mediated through changes in the position and intensity of the SWW (*ibid.*).

Wind stress from the SWW (Figure 3D) drives the Antarctic Circumpolar Current (ACC) through the deep-water Drake Passage, the channel between Patagonia and Antarctica, exerting control on physical, chemical, and biological exchanges between the Pacific and Atlantic Oceans (Toggweiler, 2009) (Figure 2), and

dominating ocean surface circulation around Patagonia. The ACC brings cold, Subantarctic water to the Pacific coast (Kaiser et al., 2007). Around 43°S, this splits into the southward-flowing Cape Horn Current and the equator-ward flowing Peru-Chile Current (Figure 2). Low-salinity Chilean Fjord water, fed by freshwater input from glaciers, flows northward within 150 – 200 km of the coast (Kaiser et al., 2007). Sea surface temperatures at 47°S are 10°C, decreasing to 7°C at 55°S (*ibid.*), meaning that the fjords of Patagonia are a relatively mild environment with abundant freshwater delivered by glaciers and icefields (Dowdeswell et al., 2016a).

Figure 3. A. Mean annual air temperature (°C) (1970 – 2000) at 30 Arc Seconds resolution, from the WorldClim2 dataset (Fick and Hijmans, 2017). B. Mean annual precipitation (mm) (1970 – 2000) at 30 Arc Seconds resolution, from the WorldClim2 dataset. C. Mean annual air windspeed (m s^{-1}) (1970 – 2000) at 30 Arc Seconds resolution, from the WorldClim2 dataset. Location of the northerly limit of the mean present-day SWW and Subtropical Front after Kohlfeld et al. (2013). D. Approximate distribution of the SWW and oceanic polar fronts that control Patagonia's climate. The westerlies bring rain and snowfall to the west coast of Patagonia. The Subtropical Front (STF) sits at the northern limit of the westerly wind belt.

2.5 Proxy records of Patagonian palaeoclimate

2.5.1 The Last Glacial Maximum

Variations in the position and strength of the SWW were a key control on palaeoclimate in Patagonia through glacial-interglacial cycles. During glacial cycles, a reduction in the strength of the ACC through the Drake Passage (Figure 3D) has been linked to a northward shift in the SWW (Lamy et al., 2015). This was associated with a decrease in strength of the SWW over their present core zone in the northern Drake Passage during colder intervals (Lamy et al., 2010, 2015). At the same time, stronger SWW extended northwards, bringing enhanced precipitation to the PIS. While the relationship between wind strength, precipitation and temperature is well understood, the relative importance of this for glacier mass balance is poorly constrained empirically.

Continuous palaeoclimate records reaching back to the full glacial period are not common in Patagonia. Kilian and Lamy (2012) provide a review of the existing records, which are summarised briefly here to contextualise the glacial fluctuations analysed in this study. In the northerly parts of the study area, Heusser et al. (1999) record progressive cooling during Marine Isotope Stage (MIS) 3 from 47 ^{14}C ka BP on Isla Grande de Chiloé, where Subantarctic Evergreen Forest was replaced with parkland. In the lowlands of the Chilean Lake District (41°S), palynological records suggest colder conditions between 24.0 and 23.4 cal. ka BP, with a slight warming from 23.4 to 22.6 cal. ka BP (Moreno et al., 2015). Cooler conditions and a depression in the regional treeline returned from 22.6 to 21.8 cal. ka BP. Warming conditions then occurred until 19.3 cal. ka

BP, resulting in a rising treeline and an increase in arboreal abundance (Moreno et al., 2015). Abrupt cooling with hyperhumid conditions occurred from 19.3 to 17.8 cal. ka BP, with a decrease in arboreal pollen. Moreno et al. (2015) interpret this to reflect a stronger influence of the SWW at this time, with extreme glacial conditions. The last glacial termination in the Chilean Lake District began at ~17.7 cal. ka BP, with a relatively rapid warming pulse and establishment of *Northofagus,* with drier and warmer conditions.

Further south, palynological records from marine core MD07-3088 at 46°S (Figure 2) indicate lower precipitation than the present-day prior to 18 cal. ka BP (Montade et al., 2019), and cooler mean winter temperatures (*ca* 3°C). However, low pollen counts due to reduced vegetation during the glacial period mean that these interpretations must be treated cautiously.

Marine sediment core MD07-3128 (53°S, off the Pacific entrance of the Strait of Magellan; Figure 2) dates back to 60 ka (Caniupán et al., 2011). The core indicates that sea surface temperatures were ~8°C lower during full glacial periods, with millennial-scale fluctuations (Kilian and Lamy, 2012). This strong cooling suggests a substantial northward expansion of polar water masses and the Southern Ocean fronts, with the Sub-Antarctic front likely close to this site. The coldest sea surface temperatures were recorded at ~19 ka, which has been related to an increase in cold melt water from the PIS. This core also shows pronounced pulses of iceberg-rafted debris between 30 and 18 ka BP, associated with fluctuations of the nearby ice sheet.

Laguna Potrok Aike in the Province of Santa Cruz, Southern Patagonia (51° 57’47”S, 70°22’46”W; Figure 2), provides a unique continuous palaeoclimate record through the last glacial cycle (Recasens et al., 2012). Palynological records from this maar lake suggest cooler and drier conditions during glacial periods. The Lateglacial and Holocene record is characterised by warming and wetter conditions, with increased primary production.

2.5.2 The Late Glacial period

The late glacial palaeoclimate of Patagonia (*ca* 15 to 11.5 ka) has been reconstructed using numerous proxy records, mostly located east of the ice fields (Kilian and Lamy, 2012). Several studies have compiled such records to infer broad changes in atmospheric circulation (Björck et al., 2012; Fletcher and Moreno, 2012; Iglesias et al., 2016; Kilian and Lamy, 2012; Lamy et al., 2010; Mancini et al., 2005; Montade et al., 2019; Moreno et al., 2015). In general, deglaciation began after 18 ka (Bendle et al., 2017a, 2019), during a period of warmer conditions (Kilian and Lamy, 2012).

In the northern part of the study area, the Chilean Lake District (41°S; Figure 2), pollen records reflect long term cool and wet conditions between 16 and 11 cal. ka BP, with enhanced variability in the late glacial

(Moreno, 2004; Moreno and Videla, 2016). Particular cold periods have been identified during the Antarctic Cold Reversal (ACR), Younger Dryas, and Huelmo–Mascardi Cold Reversal (a cool episode between 11,400 and 10,200 ^{14}C yr BP, or 13.2 to 11.8 cal. ka BP) (Hajdas et al., 2003; Massaferro et al., 2014; Moreno and Videla, 2016). A marine core (MD07-3088; Figure 2) taken off the Taitao Peninsula at 46°S records the development of North Patagonian Rainforest following the last deglaciation, with expansion of Magellanic Moorland, associated with cooler temperatures and increased precipitation, during the ACR (Montade et al., 2013, 2019). This agrees with proxy oceanic data, which record cooling in the South Atlantic and all regions south of 40°S (Pedro et al., 2016). Increases in the strength of the SWW are suggested by elevated dust deposition in Tierra del Fuego during the ACR (Vanneste et al., 2015), associated with a glacial readvance.

South of the Chilean Lake District at 44°S, the isotopic and pollen records from Lago Nos Niños and Laguna La Pava indicate low but variable moisture levels over the same time (Iglesias et al., 2016), suggesting a cold climate characterised by increased precipitation with major wet periods between 13.4 and 11.8 cal. ka BP (Villa-Martínez et al., 2012). South of the Southern Patagonian Icefield from Laguna Potrol Aike (51°S; Figure 2), palynological records and transfer functions are interpreted to indicate a relatively dry late glacial period (Schäbitz et al., 2013), with precipitation increasing into the Holocene (Tonello et al., 2009). Weaker westerlies in the early Holocene may have allowed increased precipitation east of the Andes, with increased easterly derived moisture. Late-Glacial temperatures were broadly warm, but with a colder period coeval with the ACR in Fuego-Patagonia (53°S) (Mansilla et al., 2016), as at sites to the north. In Torres del Paine (50°S), glacial readvance occurred during a cold episode from 14.8 to 12.6 ka (Moreno et al., 2009, García et al. 2012), with warming occurring after 11.5 ka.

Due to a strong relationship between westerly airflow and precipitation in southern South America (Garreaud, 2007), precipitation proxies have been used to infer the timing and nature of past latitudinal shifts and expansion and contraction of the SWW belt. As with temperature and precipitation reconstructions, there are discrepancies between studies (see e.g. Kilian and Lamy, 2012), but some broad patterns emerge between proxies and sites. During the late glacial, SWW strength was generally low, but increased during the ACR and Younger Dryas, perhaps as the core of the SWW also migrated northwards (Fletcher and Moreno, 2012; Mayr et al., 2013; Montade et al., 2019; Moreno and Videla, 2016; Oehlerich et al., 2015; Vanneste et al., 2015). A lake sediment record from Lago Pichilaguna (51°S) in the Chilean Lake District indicates strong westerlies during the ACR, favourable for glacier growth, followed by anomalously low intensity during the Early Holocene (Moreno et al., 2018).

412 *2.5.3 The Holocene*

413 Multiple proxy records from the Chilean Lake District (41°S) to southern Patagonia (52°S) indicate that the
414 Holocene began with an extended warm and dry period (Caniupán et al., 2011; Iglesias et al., 2016; Mansilla
415 et al., 2016; Moreno et al., 2018; Moreno and Videla, 2016; Siani et al., 2010; Villa-Martínez et al., 2012).
416 Although, as mentioned above, the east side of the continent may have experienced slightly higher
417 precipitation during this time due to weakening of the westerlies (e.g., Quade and Kaplan, 2017). The mid-
418 Holocene was characterised on both sides of the Andes at several sites from 41°S to 47°S by cooler and
419 wetter periods with reduced fire activity (Iglesias et al., 2016; Moreno, 2004; Moreno and Videla, 2016; Villa-
420 Martínez et al., 2012). In contrast to farther north, southern Patagonian (52°S) pollen, charcoal and lake level
421 records provide evidence for a dry period at some point in the mid-Holocene (Kilian and Lamy, 2012;
422 Schäbitz et al., 2013; Mansilla et al., 2016), although this is not replicated everywhere (Tonello et al., 2009).
423 The late Holocene was generally characterised by centennial switches between cold-wet and warm-dry
424 conditions from 41°S to 52°S (Álvarez et al., 2015; Elbert et al., 2013; Haberzettl et al., 2009; Moreno and
425 Videla, 2016; Schäbitz et al., 2013; Tonello et al., 2009; Moreno et al., 2018).

426 The strength of the SWW generally decreased into the early Holocene before increasing during the middle
427 Holocene, coinciding with the onset of Holocene neoglaciations (Porter, 2000; Moreno et al., 2018). An
428 increase in wind strength in central Patagonia (45°S) supports the hypothesis that the wind belt broadened
429 during the early and mid-Holocene (Van Daele et al., 2016). In the late Holocene, wind intensity reduced
430 towards conditions similar to present (Lamy et al., 2010; Oehlerich et al., 2015). Sites to the west of the
431 Andes suggest an anti-phasing between the winds' core and northern margin during the Holocene, with a
432 stronger core and weaker northern margin during the early Holocene and the opposite occurring in the late-
433 Holocene (Lamy et al., 2010). During the Holocene, nine positive SAM events occurred at a centennial scale
434 since 5.8 ka, that alternate with cold and wet intervals, favourable for glacier growth (Moreno et al., 2018).

435

436 # 3 Methods: PATICE database and ice-sheet reconstruction

437 ## *3.1 Geomorphological mapping*

438 Our overall methodology is shown in Figure 4. The geomorphological data in this reconstruction provide
439 detailed information on former ice sheet margins, ice-dammed palaeolake evolution, and ice-flow direction.
440 Mapping of moraines underpins the empirical reconstruction, providing information on the shape and
441 position of the ice margin, and the pattern of retreat (cf. Ely et al., 2019). In Patagonia, the pioneering work
442 of Caldenius (1932), Mercer (1965, 1968, 1970, 1976), Denton et al. (1999), Andersen et al. (1999),
443 McCulloch and Bentley (1998) and McCulloch et al. (2005b) laid the foundations for subsequent compilation
444 and mapping of glacial geomorphology by Glasser and Jansson (2008). Our compilation builds on the Glasser

and Jansson (2008) "Glacial Map of South America" with updates from around the former PIS (e.g., Ackert et al., 2008; Bendle et al., 2017b; Coronato et al., 2009; Darvill et al., 2014, 2015a; De Muro et al., 2018; García 2012, García et al., 2014; Izagirre et al., 2018; Lovell et al., 2011, 2012; Waldmann et al., 2010, Davies et al., 2018; Thorndycraft et al., 2019b) and original mapping by the authors of this study of key landforms in data-sparse regions.

At the scale of the PIS, glacial landforms were mapped from remotely sensed images, particularly satellite imagery (for details on overall methods, see: Boulton and Clark, 1990; Chandler et al., 2018; Clark, 1997; Clark et al., 2012, 2018; Glasser and Jansson, 2008; Jansson and Glasser, 2005). The most commonly used sensors in previous mapping efforts in Patagonia are Landsat 8 OLI and Landsat 7 ETM+ scenes (30 m resolution, 15 m when pan-sharpened), and ASTER (15 m spatial resolution) satellite images, as well as the higher resolution Digital Globe images now widely available in Google Earth Pro and ESRI ArcGIS. Satellite images are commonly overlaid on a Digital Elevation Model (DEM) to provide topographic context, the most commonly used elevation models being the Shuttle Radar Topography Mission (SRTM) DEM, ASTER GDEM (30 m spatial resolution), and the GEBCO 2019 DEM for bathymetric data (The General Bathymetric Chart of the Oceans; GEBCO Compilation Group, 2019). Aerial photographs, where available, have also proven to be useful for more detailed mapping of smaller areas of complex terrain (García et al., 2014; Darvill et al., 2014, 2017).

Our compiled geomorphological record includes moraines, trimlines, glacial lineations (bedrock and sedimentary), meltwater palaeochannels, outwash plains, shorelines, deltas, and cirques. Our compiled maps also display related landforms and topographic features such as rivers, lakes and volcanoes. The detailed criteria used to identify these different landforms on the basis of their morphology, colour, structure and texture are listed by Glasser and Jansson (2008; their Table 1), Martin et al. (2019; their Table 1) and Bendle et al. (2017b; their Table 2).

Compared to the terrestrial record, relatively little has been published on the glacier-influenced marine geomorphology in the fjords around the Patagonian icefields (Araya-Vergara, 2008; Boyd et al., 2008; Dowdeswell et al., 2016c; Dowdeswell and Vásquez, 2013; Fernández et al., 2017; Lastras and Dowdeswell, 2016). In addition to the multibeam echo-sounder data on seafloor morphology described and interpreted in these papers (horizontal resolution usually a few tens of metres), we used the GEBCO 2019 15 Second Arc Grid (GEBCO Compilation Group, 2019) to investigate the geomorphology of the continental shelf edge around Patagonia. The resolution of the GEBCO 2019 DEM is too coarse to map many types of submarine glacial landforms, but allows mapping of major glacial troughs and the possible suggestion of some moraines. Published bathymetric mapping is included in our compilation (Dowdeswell et al., 2016a, b, c).

Our PATICE compilation also includes an updated version of the 2011 AD inventory of 617 glaciers mapped by Davies and Glasser (2012). The inventory now includes a further 393 small mountain glaciers on plateaux and mesetas around the modern icefields, mapped using satellite imagery from 2011 AD. Shapefiles of present-day glacier extent and mapped glacial landforms are provided in the Supplementary Information to facilitate further research.

3.2 Chronology

3.2.1 Compilation of ages

Fluctuations of Patagonian outlet glaciers have been dated using multiple techniques, listed in Tables 1 and 2. Each of the techniques is applied within a specific set of circumstances that directly challenge comparison, even when corrected to calendar years. For instance, radiocarbon methods can date the onset of ice-free conditions, but represent minimum deglacial ages for the associated ice limits. In contrast, cosmogenic nuclide exposure dating of boulders on a moraine crest provides a more direct age for landform deposition (and onset of glacial retreat), but invariably may still represent a minimum age given post-depositional processes can then act to reduce the cosmogenic nuclide concentrations. OSL dating of outwash plains has been used to constrain when the ice limit was positioned on the moraine (Smedley et al., 2016). Each of the methods used, and the corrections and calibrations we apply, is discussed in detail in the Supplementary Methods.

Compiling published ages from the literature (census date August 2019) gives us greater confidence in reconstructing glacial chronology than considering different studies in isolation. Here, we use a compilation of ages that provides insights into the lateral and vertical extents of the PIS and the later ice fields the PIS disintegrates into(Tables 1 and 2). Our compilation builds on earlier efforts to produce databases of ages (Coronato and Rabassa, 2011; Hall et al., 2017; Martínez et al., 2011; Mendelova et al., 2017; Rabassa et al., 2011). These databases were cross-checked, and additional published literature was scoured for data pertaining to the geographical position of ages, which were further cross-checked in ArcGIS using the maps and datasets provided. In some instances, errors were found in original papers and where possible these were rectified via communication with the original authors. In a few rare cases, errors in ages or geographical location meant that published ages were excluded from the dataset. Compiled ages are recalibrated according to the methodology set out in the Supplementary Methods, and use the Kaplan et al. (2011) production rate. Throughout this study, ages are given as before 1950 AD, except for lichenometry and dendrochronology ages, which are given in calendar years AD. Ages are presented with the age formats shown in Table 1.

All final ages were mapped in ArcGIS as ESRI point shapefiles (*.shp), projected to UTM Zone 18S (datum: WGS 84). Each individual age contains attribute information including the publication reference, location (latitude, longitude, description), altitude (m asl), site name, dating method, comments regarding sample characteristics, material dated, stratigraphic context, our own assessment of age reliability and any other applicable information (see Supplementary Methods and Figure 4). Each age in our compilation has a unique ID (Table 1) that can be cross-referenced between the Supplementary Information (Excel datasets and GIS shapefiles). This PATICE database uses datasets from 148 peer-reviewed publications spanning some 50 years (Table 1; Table 2). See 'Data Availability' for more information.

Table 1. Unique IDs for the different categories of ages within the PATICE database; see Table 2 for more information and Supplementary Information for the full database.

Type of age and format used in text and on figures	**Age format**	**Unique ID in database**	**Number of ages**	**Number of publications**
Ar/Ar	ka	>1	16	3
Cosmogenic nuclide exposure age (^{10}Be, ^{26}Al)	ka	>101	581	36
Calibrated Radiocarbon	cal. ka BP	>1000	903	77
Uncalibrated Radiocarbon	^{14}C ka BP			
Cosmogenic depth profiles	ka	>2000	2	1
Tephrochronology	ka	>3000	31	10
Dendrochronology	years AD	>4000	21	5
Lichenometry	years AD	>4500	29	2
Historical sources	years AD	>5000	9	4
Varve age	ka	>6000	3	1
Cosmogenic nuclide exposure age (^{3}He)	ka	>7001	13	1
Cosmogenic nuclide exposure age (^{36}Cl)	ka	>8001	11	2
Optically stimulated luminescence (OSL)	ka	>9001	50	6
Total			*1,669*	*148*

Table 2. Publications included in the PATICE compilation, with number and type of ages produced. See Supplementary Information for the full database. Some ages appear in more than one publication. Ages are listed only once, with the reference being the original publication where they were first published. Only ages relevant to reconstructing the glacial history of Patagonia are included.

Publication	**Number of Ages**	**Publication**	**Number of Ages**
Ar/K		**Radiocarbon**	
Singer et al. (2004a)	6	Ashworth et al. (1991)	1
Singer et al. (2004b)	1	Bennett et al. (2000)	4
Wenzens (2006)	9	Bentley (1997)	14
		Boyd et al. (2008)	4

^{10}Be exposure ages	
Ackert et al. (2008)	9
Boex et al. (2013)	18
Bourgois et al. (2016)	20
Davies et al. (2018)	8
Douglass et al. (2005)	19
Douglass et al. (2006)	40
Evenson et al. (2009)	4
Fogwill and Kubik (2005)	4
García et al. (2012)	27
García et al. (2018)	64
García et al. (2019)	4
Glasser et al. (2006a)	3
Glasser et al. (2011b)	10
Glasser et al. (2012)	15
Harrison et al. (2008)	3
Hein et al. (2009)	23
Hein et al. (2010)	13
Hein et al. (2011)	13
Hein et al. (2017)	25
Kaplan et al. (2004)	12
Kaplan et al. (2005)	18
Kaplan et al. (2007)	23
Kaplan et al. (2008)	14
Kaplan et al. (2016)	69
McCulloch et al. (2005b)	10
Menounos et al. (2013)	9
Moreno et al. (2009)	15
Nimick et al. (2016)	11
Reynhout et al. (2019)	30
Sagredo et al. (2018)	24
Sagredo et al. (2011)	4
Sagredo et al. (2016)	3
Strelin et al. (2014)	15
Thorndycraft et al. (2019a)	6
Turner et al. (2005)	2
^{36}Cl exposure ages	
Ackert et al. (2008)	9
Douglass et al. (2005)	2
^{3}He exposure ages	
Kaplan et al. (2004)	13
Cosmogenic depth profile	
Darvill et al. (2015b)	2
Optically stimulated luminescence	
García et al. (2019)	8
Glasser et al. (2016b)	17
Harrison et al. (2008)	3
Harrison et al. (2012)	6
Nimick et al. (2016)	3
Smedley et al. (2016)	13

Breuer et al. (2013)	1
Clapperton et al. (1995)	26
Coronato et al. (2009)	5
Denton et al. (1999)	278
de Porras et al. (2012)	1
de Porras et al. (2014)	1
Fernandez et al. (2012)	1
García (2012)	2
García et al. (2019)	6
Gordillo et al. (1992)	1
Glasser et al. (2002)	10
Haberle and Bennett (2004)	2
Hall et al. (2013)	13
Hall et al. (2019)	83
Henriquez et al. (2017)	2
Heusser (1989)	2
Heusser (1998)	7
Heusser (1999)	1
Heusser (2003)	1
Heusser et al. (1989)	1
Heusser et al. (1995)	2
Denton et al. (1999); Heusser et al. (1999)	174
Horta et al. (2019)	4
Iglesias et al. (2016)	1
Kaplan et al. (2004)	3
Kilian et al. (2003)	3
Kilian et al. (2007a)	2
Kilian et al. (2007b)	4
Kilian et al. (2013b)	1
Kuylenstierna et al. (1996)	6
Lowell et al. (1995)	1
Lumley and Switsur (1993)	1
Marden and Clapperton (1995)	6
McCulloch and Bentley (1998)	3
McCulloch and Davies (2001)	1
McCulloch et al. (2005a; 2005b)	24
Mercer (1965)	3
Mercer (1968)	1
Mercer (1976)	8
Mercer and Ager (1983)	2
Montade et al. (2013)	1
Moreno (1998) and Denton et al. (1999)	2
Moreno et al. (1999)	9
Moreno et al. (2009)	12
Moreno et al. (2015)	28
Nimick et al. (2016)	1
Porter (1981)	5
Porter (1990)	4
Porter et al. (1984)	1
Porter et al. (1992)	3
Rabassa and Clapperton (1990)	1
Rabassa et al. (1998)	1
Rabassa et al. (2000)	3
Roig et al. (1996)	3
Sagredo et al. (2011)	13

		Stern (1990), in Marden and Clapperton (1995)	1
Tephrochronology		Stern (1992)	4
Biester et al. (2003)	1	Strelin et al. (2011)	6
Breuer et al. (2013)	2	Strelin et al. (2014)	42
Kilian et al. (2013b)	2	Turner et al. (2005)	14
Kilian et al. (2003)	3	Uribe (1982), in Clapperton (1995) and McCulloch et al. (2005a; 2005b)	2
McCulloch et al. (2005a)	1	Van Daele et al. (2016)	1
Stern (1992)	3	Villa-Martínez et al. (2012)	2
Stern et al. (2016)	10	Villagran (1988)	2
Stern et al. (2015)	2	Waldmann et al. (2010)	2
Van Daele et al. (2016)	1	Weller et al. (2015)	4
Weller et al. (2015)	4	Weller et al. (2017)	1
		Wenzens (1999)	12
Dendrochronology		Wenzens (2005)	15
Koch and Kilian (2005)	3		
Masiokas et al. (2009b)	10		
Winchester et al. (2014)	5	**Historical documents**	
Winchester et al. (2001)	1	Casassa et al. (1997)	3
Winchester and Harrison (2000)	2	Rivera et al. (2012b)	2
		Araneda et al. (2007)	3
Lichenometry		Garibotti and Villalba (2017)	1
Garibotti and Villalba (2009)	11		
Garibotti and Villalba (2017)	18	**Varve years**	
		Bendle et al. (2017a)	3

3.2.2 Consistency and quality control of published ages

We assign all ages in the PATICE database a quality control rating to aid interpretation over the scale of an entire ice sheet and to enable the identification of poorly resolved ages (Figure 4). This approach is pragmatic given the resolution of isochrones produced (5 kyr), the size of the area analysed, and the scale and quantity of ages compiled. This rating scheme should not be taken to indicate that the ages or associated studies are perceived to be of low, medium or high quality themselves, and we strongly urge readers to consult original studies when using our compilation to investigate a particular area or higher-resolution time-step. Principally, the quality index reflects the availability of data needed to recalculate ages from the original publication, whether samples are outliers or are part of a group that replicates the same age, and whether they are *in situ* with well constrained geomorphic or stratigraphic context.

Following the approach used by recent studies that encourage model-data comparisons (e.g. Hughes et al., 2016; Small et al., 2017; Ely et al., 2019), ages are assigned a quality index rating of 1, 2 or 3, based on the criteria in Table 3. Decisions are made by the lead and co-authors at the time of writing. These ages are symbolised with green, amber or red circles respectively in the figures in this article.

1. All criteria are met and the age is considered reliable (green);
2. Most of the criteria are met and the age is probably reliable (amber);

3. No criteria met or the age is an outlier; the age is considered unreliable (red).

Key criteria for assessing reliability of all samples include a clearly defined geomorphic context and recording of the geographical and geological context, as well as the degree to which standard protocols are followed for given dating methods (Table 3). The "All samples" criteria are considered first, and then dating method-specific criteria are applied. The number of ages in each category is shown in Table 4.

The evolution and development of dating protocols over time means that ages published a longer time ago may now be deemed less reliable. Some older radiocarbon ages are rated as (2) because $\delta^{13}C$ was not measured or provided, for example. Where ages are rated as (3), there is an explanation in the attribute table of the ESRI Shapefile.

For our reconstruction, the ratings of cosmogenic nuclide ages are most critical as only highly (1) rated ^{10}Be ages are used to generate mean landform ages. Of particular importance, we emphasize that our goal is to define ice margin positions; hence, our quality control rating should consider our rationalization for rating. As an example, a single ^{14}C age may provide precise and unparalleled information on the timing of an event, but within the stratigraphy it may tell little about where the ice margin was at that moment; in comparison, cosmogenic date directly ice margin positions, which is our main desired output. Where ^{14}C studies are arguably most abundant, such as in the Chilean Lake District, the change to our main reconstructions and findings are insignificant with different ratings on individual ages, e.g., a 1 or 2. While some may decide that individual datasets warrant higher ratings, such decisions would not affect the overall 5kyr reconstructions that we present to the community, and so would not affect our conclusions.

Table 3. Criteria for assessing the reliability of published ages once compiled in the PATICE database.

Dating technique	**Indicators of reliability**
All samples	Sample appears *in situ*; Age uncertainty specified; Geomorphic context defined; Geographical and geological context provided; sample can be accurately located; Considered reliable by original authors. Outliers identified by original authors score 3.
Cosmogenic nuclide dating (^{10}Be, ^{26}Al, ^{3}He, ^{36}Cl): surface exposure age dating	Multiple (≥ideally 3) samples from the same landform or site. Ages are internally consistent; spread in ages similar to measurement uncertainty. Uncertainties overlapping with others from same landform/site. Data provided to recalibrate ages using latest published calibration models (cf. Lowe and Walker, 2015).
Cosmogenic nuclide dating: depth profiles	Ideally, modelled profile age compared to separate surface cobble ages. Several samples in profile (≥ideally 5), including at least one sample >1.5 m deep. Profile ages internally consistent and clustered. Geomorphological situation is accounted for: (1) terraces stabilised shortly after moraine deposition;

	(2) nuclide inheritance is low; (3) post-depositional shielding is minimal; (4) terrace sediment not mixed post-depositionally
Radiocarbon dating (^{14}C)	Known and uncontaminated sample material. Material dated is clear. Organic content >5% LOI. Bulk samples (including gyttja, organic silt, carbonate clasts etc.) considered lower quality than samples from individual plants and macrofossils. Uncalibrated age provided with full errors to enable recalibration with modern calibration curves. Multiple or stratigraphically consistent ages if in a core. Appropriate δ13 values: -25‰ to -32‰ for terrestrial plants; -15‰ for marine plants; -0‰ for marine carbonates (Lowe and Walker, 2015). Within calibration range of SHCal13 / Marine13 dataset (Hogg et al., 2013; Reimer et al., 2013). For marine radiocarbon ages, ΔR is well understood. Not from aquatic taxa (freshwater plants), since algae and aquatic mosses build carbon from dissolved inorganic carbon, and reflect the ^{14}C:^{12}C ratios of the water from which they grew. These aquatic taxa are vulnerable to the hard water effect, dissolved carbonate from surrounding rocks, the residence time of the bog or lake, and other factors. As a result, the ^{14}C activity of the dissolved inorganic carbon is ^{14}C depleted, resulting in artificial ageing with wide variation (Hatté and Jull, 2013).
Optically stimulated luminescence (OSL)	Any potential for partial bleaching has been addressed using small aliquot/single grain measurements. The proglacial outwash sampled can be directly linked with the corresponding moraine Multiple or stratigraphically consistent ages. Dose rate information and equivalent described in source. Ages determined for K-feldspar address the potential impacts of anomalous fading. Age is not determined using an experimental analysis protocol.
Tephrochronology	Tephra age is consistent and in stratigraphic order with other tephra layers and independent ^{14}C dating within the core. Tephra is geochemically analysed and compared with other tephras. Tephra layer is independently dated.
Dendrochronology	Ecesis time is calculated and provided Growth rate is calculated and provided Sample context is clear Age of tree is calculated clearly.
Historical documents	Textural source is identified and errors and uncertainties are discussed. Ice margin is clearly located in textural /historical source.
Varve records	Process model of varve formation is provided. Multiple varve counts are carried out by independent analysts. Varve count uncertainty is expressed. The 'floating' varve chronology is anchored in absolute time (e.g. using tephrochronology or radiocarbon dating).

564

565

566 *Table 4. Number of ages assigned to each category in the PATICE database. Ages marked "unassigned" either*
567 *predate 35 ka but are included because older ages help to constrain the LGM ice limit, or could not be*
568 *recalibrated.*

Dating Method	Green (1)	Amber (2)	Red (3)	Unassigned	Total Ages
^{10}Be exposure age	446	94	28	13	582
^{36}Cl exposure age			11		11
^{3}He exposure age	6	1	5	1	13
Tephra	28	3			31
Ar/Ar				16	16
OSL	37	3	10		50
Radiocarbon	312	461	129	1	903
Depth profile	2				2
Dendrochronology	15	6			21
Lichenometry	29				29
Historical documents	9				9
Varve age	3				3
Total Number	*887*	*568*	*183*	*31*	*1,669*

569

570 *3.2.3 Calculation of landform mean ages*

571 Where multiple ^{10}Be cosmogenic nuclide exposure ages (≥2) exist for a particular moraine or landform, we
572 have generated mean (μ) ages, which we present with one standard deviation (SD), based on high quality
573 (green) ages only (see section 3.2.2), and using external uncertainties. The presentation of mean ages with
574 standard deviations follows guidelines from Ludbrook (2008) and Curran-Everett and Benos (2004) for
575 presentation of statistical data. They argue that the standard deviation is a single value that quantifies
576 scatter, and should not follow a plus and minus symbol. Therefore, in this paper, mean ages of landforms are
577 presented as, for example, 5.2 ka (SD 0.5). This makes them clearly distinguishable from individual ages with
578 a measured uncertainty, which are shown as, for example, 5.2 ± 0.5 ka.

579 Outliers without overlapping uncertainties at 2 sigma are excluded from this calculation. This approach
580 reduces and simplifies the data, and facilitates inter-regional comparison and identification of key ice
581 margins in different parts of Patagonia. It also allows an evaluation of the spread of the ages on each
582 landform, without being biased by measurement uncertainty. This is because the laboratory measured
583 uncertainty in ^{10}Be ages may not be representative of the uncertainty in the age, which can be greatly
584 influenced by geological factors. Presenting the spread of ^{10}Be ages on a particular landform instead provides
585 a more robust estimate of the uncertainty in the age of a landform. Landform mean ^{10}Be ages (μ) with
586 standard deviations (SD) are represented with pink crosses on figures in this study.

587 Varve years provide a direct age for a moraine with a measured uncertainty (shown as ±). Bracketing tephra,
588 radiocarbon or OSL ages inside and outside the ice margin are used as a check for the mean moraine age but

589 are not included in the landform mean age calculation. If the bracketing ages were to suggest that the mean
590 landform age was incorrect, this would be highlighted, but we have not found this to the case. For more
591 information, see Supplementary Methods.

592

593 *Figure 4. Workflow model, showing the different stages in the methodology for our new empirical*
594 *reconstruction. See also Figure 5.*

595

596 ## *3.3 Palaeo-glaciological reconstruction*

597 ### *3.3.1 Ice extent in isochrones*

598 Following the methodology used in several recent reviews of Antarctic, Laurentide and pan-European
599 glaciation (Bentley et al., 2014; Hillenbrand et al., 2014; Hodgson et al., 2014; Hughes et al., 2016; Larter et
600 al., 2014; Ó Cofaigh et al., 2014; Margold et al., 2018), at well dated ice-marginal positions we generated
601 short, isolated isochrones of ice-sheet extent at 5 kyr intervals from analysis of published ages and
602 geomorphology. These isochrones are therefore drawn along well-dated moraine positions. Reconstructions
603 at a resolution finer than 5 kyr time-slices were not possible due to the scarcity of dating in many regions of
604 Patagonia. The density of published ages varies spatially and temporally, and multiple techniques have been
605 applied in different settings. Published ages tend to occur in clusters around the more accessible parts of the
606 palaeo ice-margin. In addition, some data reduction is necessary to make the most useful palaeo ice-sheet
607 reconstructions. However, in some places (e.g. eastern Northern Patagonian Icefield, Torres del Paine), there
608 is enough dating resolution to separate out time-slices at 15, 13 and 10 ka, which allows us to generate a
609 specific ice advance coeval with the ACR. Another additional time-slice through the Late Holocene uses
610 published data (Davies and Glasser, 2012; Glasser et al., 2011a; Meier et al., 2018) and new geomorphic
611 mapping to constrain ice extent at 0.5 – 0.2 ka.

612 In drawing the isochrones, context was used to assess whether ages related directly to an ice margin (e.g.,
613 ^{10}Be ages on a moraine), or whether they denoted a minimum age for ice-free conditions (e.g., ^{14}C ages from
614 a peat bog inside a moraine), or maximum ages for ice advance. Tephras are taken to denote ice-free
615 conditions and provide a chronological tie point across multiple sites. They are particularly important for
616 dating palaeolake evolution (e.g., Bendle et al., 2017a; McCulloch et al., 2005a; Thorndycraft et al, 2019a).
617 All of these data (ages, isochrones, moraines) are available in the Supplementary Information as ESRI
618 Shapefiles.

619

3.3.2 Interpolation of isochrones

New and published glacial geomorphological mapping were used to reconstruct ice-sheet limits (Figure 4, Figure 5). We interpolated between isochrones using these geomorphological and topographical data to produce the maps of past ice-sheet extent. Reconstructions of ice limits were conducted 'blind': relying on geomorphological, chronological and topographical data, but without comparison to established LGM reconstructions.

We assume that prominent moraines indicate a period when the ice margin stabilised and, therefore, in the absence of dating control, that moraines adjacent to dated ice limits or a similar distance from the ice divide have a similar age. Where no moraines were visible from previously published mapping or from new analysis of satellite imagery, ice limits in immediately adjacent valleys with the same orientation were assumed to have reached a similar position and elevation. Reconstructing former ice limits from the geomorphological record was also complicated by the presence of high ground (flat-topped mesetas) beyond the present ice fields. For example, the pattern of latero-terminal moraines for major outlet lobes of the eastern ice sheet suggests they separated and flowed around mesetas. However, determining where ice lobes became topographically confined between mesetas is hard to assess reliably, as broad, high plateaus could have sustained independent ice fields, contributing to the outlet lobes. In such instances, we relied on landform evidence: some mesetas show little geomorphic evidence of glaciation and are dominated by fluvial geomorphology, with steeply incised valleys. They typically have lateral moraines on their sides, suggesting ice was confined to the valley. These are considered not to have been glaciated at any time in our reconstruction. We do note that areas with cold-based glaciation would have left little geomorphic impact, and could be erroneously excluded from the reconstruction. Mesetas closer to the ice divide possess alpine glacial geomorphology (Araos et al., 2018; Glasser and Jansson, 2008; Glasser et al., 2008). The presence of abandoned cirques, truncated spurs, parabolic valleys and arêtes suggests that even if they are not glacierised today, these areas at least supported valley glaciation during past glacial cycles. In the absence of sufficient geomorphic or chronological data, we assume that if mesetas are glacierised today, they contributed ice to outlet lobes during glaciation. More work is required to ascertain the lateral margins of the major outlet ice lobes at different times during the last glaciation.

An additional challenge is inferring an ice margin's position in places where there is limited or no published chronological data. For example, where there is no clear LGM limit for a particular ice lobe, we keep the ice in the same position from 35 – 20 ka, or until dating controls are available. For many lobes, the 15 ka and ACR ice extents are indistinguishable, and so are held constant between these two time-slices. For the 5 ka ice extent, where geomorphological or chronological data are unavailable, we hold the ice margin position at the Late Holocene (0.2 ka) ice extent (therefore a minimum estimate). Likewise, the updated 0.2 ka ice

extent is still largely derived from Davies and Glasser (2012), which is also considered a minimum estimate because where no other data (geomorphic or otherwise) are available, the ice margin is mapped using the earliest available satellite imagery (1970s or 1980s). In areas with limited or no dating of mapped ice limits, the ice limits are mapped using geomorphological data and relative chronology (where the outermost landforms are assumed to be oldest).

Our approach contains assumptions in areas where the geomorphology of ice limits is unclear or where there has been limited or no dating of landforms. In these places, we essentially construct a relative chronology, with the caveat that this is an imperfect approach, and has been shown to be problematic in parts of Patagonia (e.g. Darvill et al., 2015b). Nonetheless, we highlight such locations (which have a *low confidence* ice margin; see below) as ideal targets for testing in future dating campaigns.

3.3.3 Uncertainty estimate of ice-sheet extent

Empirical ice-sheet reconstructions should have clearly quantified ice-margin uncertainties, indicating where there are data (e.g., mapped moraines) or interpretations (e.g. interpolated ice margin positions where moraines are absent) (Stokes et al., 2015). These data can then be used in data-calibrated model ensembles and provide targets for further work. In our reconstruction, each ice limit is assigned a level of confidence (e.g., see Figure 5):

- *High confidence* ice limits have both well-defined moraines and a well-constrained chronology.
- *Medium confidence* ice limits are defined by geomorphology or topography and lie close to published ages (e.g., Figure 5). For example, if outlet lobes immediately to the north or south have a well-defined chronology, we can make a reasonable estimate of the ice extent if there is well defined glacial geomorphology.
- *Low confidence* limits have no well-defined geomorphology, and no nearby published ages. These ice limits are interpretations, interpolated from mapped moraines where possible. In such areas, we view the reconstructed ice limits as a first tentative hypothesis that requires testing using field surveys or numerical modelling.

Unlike the Hughes et al. (2016) reconstructions of the Eurasian Ice Sheet, we do not provide minimum, maximum and 'best estimate' extents for each time-slice, as our resolution is lower, and the density of dated material is sparser. Our ice-sheet extents at each time interval are simply a best estimate.

682

683 *Figure 5. Demonstration of the stages in ice sheet reconstruction around the eastern margin of the Southern*
684 *Patagonian Icefield (49 – 51°S) at 35 ka. See also Figure 4 for an overview of the methods. A. Development of*
685 *isochrones at moraine limits where there are sufficient high quality ages and geomorphology. Current ice*
686 *catchments are shown in black with white outline. Cosmogenic and Ar/Ar ages older than MIS 3 are not*
687 *shown. B. The ice margin location is calculated by interpolating between isochrones. Note the* high
688 confidence *in ice extent areas with both ages and geomorphology relevant to the time slice,* medium
689 confidence *where there is clear geomorphology but a lack of ages (but there may be published ages nearby);*
690 *and* low confidence *where there is an absence of ages or geomorphology. Interlobate areas tend to be*
691 *particularly difficult to constrain, typically resulting in* low confidence *margins. C. Development of palaeo ice-*
692 *flow lines and ice divides using mapped geomorphology and topography.*

693

694 *3.3.4 Palaeo ice-flow and ice divides*

695 We use the orientation of streamlined glacial lineations (including roche moutonnées, whalebacks, drumlins
696 and flutes), topography, bathymetric troughs, fjords and moraines (lateral and terminal) to determine palaeo
697 ice-flow direction (Clark, 1993; Figure 5C). However, in comparison to the much larger Laurentide and
698 Eurasian ice sheets during the last glacial cycle, glacial lineations in Patagonia are largely focused in
699 topographically constrained outlet glacier corridors and demonstrate a consistent ice-flow direction with
700 little evidence of significant changes in drainage patterns. We did not identify the complex cross-cutting
701 flow-sets that are indicative of changes in palaeo ice-flow patterns (cf. Stokes et al., 2015). This suggests that
702 the main corridors for ice flow remained relatively unchanged, and topographically constrained, through
703 time. Palaeo ice-flow is used to identify the location of the ice divides. Interpreted ice divides are provided
704 for indicative use only and have low confidence in the absence of ice-sheet elevation data. We suggest that
705 the ice divides are located along the Andes, orthogonal to ice flow.

706

707 *3.3.5 Glacier area and volume calculations*

708 The total area of each reconstructed time-slice was calculated in ArcGIS 10.3. To give a first-order estimate
709 of total ice-sheet volume, the areas of each individual closed GIS polygon at each time-slice was converted to
710 volume using the relationship in equation (1):

711 (1)

712 $$\log V = 1.23(\log A - 1)$$

713 where V = volume in km^3, and A = area in km^2, following Hughes et al. (2016). This relationship between ice-
714 sheet area and volume is derived from a logarithmic relationship of the area and volume of the world's
715 largest present-ice sheets and ice caps (e.g. Bahr et al., 2014b; Paterson, 1994). This relationship is based on

observations of present-day ice masses and so may underestimate ice volume during colder periods of time, when ice masses likely had steeper surface gradients due to the greater stiffness of colder ice, although this is likely to present less of an issue in temperate regions like Patagonia. Alternatively, where ice sheets rest on soft beds and are thinning and retreating with many fast-flowing outlet ice streams, this equation may tend to over-estimate volume (Hughes et al., 2016). The estimate of ice volume therefore likely becomes increasingly erroneous as deglaciation progressed, and the ice sheet thinned. We use this equation on the PIS from 30 to 20 ka.

We use different volume-area scaling relationships as the PIS breaks down into smaller ice masses (ice fields, ice caps and glaciers) from 15 ka onwards. Throughout our reconstruction, each ice mass (an enclosed GIS polygon) is given an attribute of ice sheet, ice field, mountain ice cap or glacier following standard protocols (Rau et al., 2005; Raup and Khalsa, 2010; Raup et al., 2007). Appropriate volume-area scaling laws were then applied (Bahr, 2014; Bahr et al., 2014a, b). For glaciers and dome-shaped mountain ice caps, ice volume (km^3) is therefore calculated using equation (2):

(2)

$$V = kA^{\gamma}$$

where *k* and *γ* are constants: $k = 0.033\ km^{3-2\gamma}$; $\gamma = 1.36$ for glaciers and icefields, and 1.22 for dome-shaped mountain ice caps. For the present-day ice volume, we use an already published calculation that uses a more sophisticated method (Carrivick et al., 2016).

For ice sheets, ice fields, glaciers and mountain ice caps, conversion of ice volume in km^3 to gigatonnes (Gt) assumes an ice density of ice of 0.9167 Gt/km^3. To convert ice volume to sea level equivalent, we use a global surface ocean area of 361.8 Mkm^2 and a sea water density of 1028 kg m^3. This gives an ice:water density ratio of 0.892 and assumes that sea water replaces ice grounded below sea level (cf. Hughes et al., 2016). However, in our reconstruction we note that ice grounded below sea level is fairly minimal due to the shallow Pacific continental shelf and the extensive sea level lowering at the LGM (Guilderson et al., 2000). Therefore, our calculated sea level equivalent is likely over-estimated where ice is grounded below sea level. Regretfully, in the absence of a three-dimensional ice surface and well-reconstructed relative sea levels across the study area, this uncertainty is challenging to quantify without a numerical model that can account for isostatic adjustment.

3.3.6 Palaeolakes

We map the extent of ice-dammed palaeolakes at each timeslice. The extent of the palaeolakes is constrained by published geomorphology and chronology (Bell, 2009; Bendle et al., 2017b; Caldenius, 1932; García et al., 2014; García et al., 2019; Glasser et al., 2016b; Hein et al., 2010; Horta et al., 2019; Martin et al., 2019; Martinod et al., 2016; Thorndycraft et al, 2019a; Turner et al., 2005). The ASTER GDEM dataset was used to interpolate lake levels between mapped shorelines or other datapoints. Differential isostasy is not taken into account in these reconstructions, apart from around the Northern Patagonian Icefield (Thorndycraft et al, (2019a). In other cases, glacial lakes are reconstructed following analysis of the DEM where our reconstruction indicates that current drainage routes are blocked. For each lake, we identify a drainage col spillway and drainage pathway. In this way, we are able to reconstruct drainage pathway reversals for the Patagonian palaeolakes. For comparison purposes, we also provide the areas of those palaeolakes that remain today as proglacial lakes following recession of the glaciers. Palaeolake area is calculated in Esri ArcGIS. In the absence of detailed palaeolake bathymetry, it is difficult to robustly calculate glacial lake volume where current lakes remain in the over-deepening, and so we present only the change in glacial lake area.

3.4 Relative sea level record

We use the relative sea level datapoints in Table 5 throughout our reconstruction figures, where we alter the GEBCO (GEBCO Compilation Group, 2019; www.gebco.net/) marine bathymetry dataset to reflect relative sea level (Table 5). We use published data from the Argentinian Atlantic coast (Guilderson et al., 2000; Peltier and Drummond, 2002; Schellmann and Radtke, 2010; Isla, 2013). There is a dearth of data for the Pacific margin during the LGM, late glacial and Holocene, and sea level change in the northern part of the study area may be overestimated in our reconstruction. Sediments on the Argentine continental shelf in southern Patagonia suggest a local relative sea level lowering of 150 m at the LGM (Guilderson et al., 2000) (Figure 6). During glacial maxima, the fall in eustatic sea level and increased isostatic depression in western South America relative to the broad Argentinian shelf in the east (Peltier and Drummond, 2002) would have contributed to the formation of ice-dammed lakes east of the PIS.

Following the global LGM, the Argentinian record from shells on the continental shelf indicates that there was a rapid increase in relative sea level between 20 and 15 ka (-150 to -120 m), with further rises in relative sea level following the ACR (Guilderson et al., 2000) (Figure 6). By 10 ka, geological data indicate that local relative sea level here was -45 m. Globally, three periods of rapid sea level rise are recognised; from 19.5 – 18.8 ka (10 m rise), one commonly termed Melt Water Pulse 1A (14.8 to 13.0 ka; 20 m rise) and one termed

Meltwater Pulse 1B (11.5 to 11.1 ka; 16 m rise) (Harrison et al., 2019). These data imply rising regional sea levels throughout the Late Glacial and early Holocene.

The mid-Holocene sea level high-stand in southern Patagonia was reached at ~7.4 cal. ka BP (Schellmann and Radtke, 2010; Porter et al., 1984), with sea levels reaching +2 to +3 m above modern sea level. There were also significant falls of 1 and 1-2 m at ~6.6 cal. ka BP and ~2.3 cal. ka BP respectively. The general trend in relative sea level fall since the mid-Holocene transgression was predominantly driven by glacio-isostasy (Schellmann and Radtke, 2010).

Further north, at San Matías Gulf (41°S, 62°W; Argentinian continental shelf), *in situ* pieces of wood from 70 m below sea level yielded radiocarbon ages of 11.3 ± 0.15 cal. ka BP (Isla, 2013). The mid-Holocene highstand of +6 m was reached at 6 ka BP. Sea level fell to near present by 2.6 cal. ka BP.

Table 5. Regional relative sea levels used in the PATICE reconstruction.

Time-slice	Regional relative sea level	Reference
35 ka	-150 m asl	Guilderson et al., 2000
30 ka	-150 m asl	Guilderson et al., 2000
25 ka	-150 m asl	Guilderson et al., 2000
20 ka	-150 m asl	Guilderson et al., 2000
15 ka	-120 m asl	Guilderson et al., 2000
13 ka	-120 m asl	Guilderson et al., 2000
10 ka	-45 m asl	Guilderson et al., 2000
5 ka	+1 m	Schellmann and Radtke, 2010
0.2 ka	0 m asl	
0 ka	0 m asl	

Figure 6. Relative sea level curve for the Argentine Shelf from the ICE-4G viscoelastic model and geological data (Guilderson et al., 2000). Grey bars highlight timing of meltwater pulses 1A and 1B.

4 Glacial landsystems of Patagonia

Today, Patagonia contains outlet glaciers terminating in the full range of environments possible for temperate glaciation (land-terminating, lake-terminating and tidewater-terminating; Glasser et al., 2009). This was also the case during the Pleistocene (Coronato and Rabassa, 2011; Glasser et al., 2005; Martínez et al., 2011; Rabassa, 2008; Rabassa et al., 2011), and glacial landforms included in PATICE are listed in Table 6.

Table 6. Summary of landforms mapped in this study

Landform	Number
Shorelines	2,507
River terraces	8
Perched deltas	269
Alluvial fan and contemporary deltas	61
Lineations (lines)	3,926
Lineations (polygons)	1,390
Bedrock lineations	9,603
Moraines	25,009
Sandur	594
Empty cirques	4,309
Rivers	1,225
Lakes	3,359
Glaciers	1,010
Volcanoes	31
Peaks over 3000 m	7
Bathymetric trough edge	40
Palaeochannels	4,536
Trimlines	939
Total	58,823

In general, there are four distinct temperate glacial sediment-landform assemblages across the Patagonian Andes:

i. An upland glacier landsystem, with an assemblage of cirques, lateral and terminal moraines, some mountain glaciers and snow patches, flutes, and lakes within the overdeepened basins (Aroas et al., 2018; Martin et al. 2019);

ii. In the lowlands, a land-terminating glacial landsystem, with an assemblage of nested lateral-frontal moraine arcs, outwash plains, meltwater channels, sedimentary glacial lineations (including drumlins) and inset hummocky terrain (e.g. Bendle et al., 2017b; Coronato et al., 2009; Darvill et al., 2014; Ercolano et al., 2004; Lovell et al., 2012; Martin et al., 2019; Ponce et al., 2013);

iii. A lowlands glaciolacustrine landsystem, with landforms such as deltas and shorelines, and localised ice-contact glaciofluvial features (e.g. Bell, 2008; Bell, 2009; Bendle et al., 2017b; Davies et al., 2018; García et al., 2014; Thorndycraft et al, 2019a; Turner et al., 2005);

iv. An offshore glaciomarine landsystem with fjords, offshore moraine ridges, streamlined sedimentary lineations, turbidity-current channels, raised fluvial deltas and slope failures (Dowdeswell and Vásquez, 2013; Dowdeswell et al., 2016c).

818

819 ### *4.1 Upland glacier landsystem*

820 The upland mountains of Patagonia beyond the present-day icefields bear evidence of an upland, Alpine-
821 style of glaciation. This landsystem comprises amphitheatre-shaped cirques, some still occupied by glaciers
822 (Glasser et al., 2008; García, 2012; Araos et al., 2018; Martin et al., 2019). Some cirques host remnant
823 moraine-dammed lakes, eroded lateral moraines, closely-spaced frontal moraines and lineations interpreted
824 as flutes (*ibid.*). The fresh lateral and terminal moraines associated with these cirques have allowed the
825 reconstruction of mountain glaciers during the most recent advance at 0.5 - 0.2 ka (Glasser et al., 2011;
826 Davies and Glasser, 2012; Meier et al., 2018).

827 In the Chilean Lake District, Alpine-style glaciation occurred, with discrete piedmont glaciers constrained by
828 mountains and deep lake basins (García, 2012). The landform assemblage here includes cirques, well-
829 developed lateral and end-moraine sets, ice-contact kame terraces, moraine-dammed lakes, meltwater
830 channels and spillways, and outwash plains. These landforms were associated with an active, temperate
831 glacial regime, with erosive, wet-based ice (García, 2012).

832

833 ### *4.2 Lowland land-terminating glacial landsystem*

834 The broad valleys distributed along the eastern margin of North and Southern Patagonian Icefields, and east
835 and west of the Andes in the Chilean Lake District, comprise over-deepened glacial troughs, often occupied
836 by lakes, indicating the action of effluent ice sheet outlet lobes and smaller glaciers flowing away from the
837 Andean divide (Araos et al., 2018). This large-scale sediment-landform assemblage typically comprises
838 multiple moraine sets, for example those in the areas formerly occupied by the large eastern outlet glaciers
839 (Glasser and Jansson, 2005). The terminal moraines are generally complex features with multiple ridges and
840 crests (Figure 7). Throughout Patagonia there are also many smaller moraines close to the contemporary ice
841 margins, which represent mid and late Holocene and Twentieth Century glacier recession (Glasser et al.,
842 2005). Late Holocene erosional trimlines are vegetation free, are typically developed close to the snouts of
843 many contemporary glaciers, and can merge down-glacier with lateral and terminal moraines. They mark a
844 recent time in the last two centuries when ice was thicker, followed by glacier recession (Glasser et al.,
845 2011a; Davies and Glasser, 2012; Meier et al., 2018). Large tracts of ice-scoured and sometimes streamlined
846 bedrock are present along major ice discharge routes to the east of the contemporary icefields, as well as in
847 and around the fjord areas of Patagonia (Glasser and Ghiglione, 2009; Glasser and Harrison, 2005; Glasser et
848 al., 2009).

849 Glacial outwash plains (sandur) and meltwater channels are widespread in Patagonia, especially east of the
850 Andes where they are associated with the large terminal moraine complexes (Cogez et al., 2018; Bendle et
851 al., 2017b; Hein et al., 2009, 2011; Smedley et al., 2016) (Figure 7). Sub-parallel lateral and marginal
852 meltwater channels are also common features along the lateral margins of former outlet glaciers (Benn and
853 Clapperton, 2000; Lovell et al., 2012).

854 Glacial lineations have previously been interpreted as being associated with large, fast-flowing outlet glaciers
855 are present throughout Patagonia (Bendle et al., 2017b; Glasser and Jansson, 2005). Lineations are
856 predominantly found at lower elevations (e.g., Clapperton, 1989; Ponce et al., 2013, 2018) and in discrete
857 topographically controlled corridors (Bendle et al., 2017b; Glasser and Jansson, 2005). They range from
858 streamlined bedrock to elongate sedimentary drumlins in the lowlands (Clapperton, 1989; Ponce et al.,
859 2013, 2018). They are larger in scale than the smaller flutes restricted to upland cirques (cf. Martin et al.,
860 2019).

861

862 *Figure 7. Key landforms associated with the lowland land-terminating glacial landsystem. A: Latero-frontal*
863 *moraines at the eastern margin of Lago GCBA. B: outwash fan. Centre: Geomorphological map showing key*
864 *land-terminating landforms, such as outwash plains, moraines and meltwater channels. C: Detail of*
865 *meltwater channels. D: Detail of moraines and meltwater channels. Location of photographs is shown on the*
866 *central map.*

867

868 ### *4.3 Glaciolacustrine landsystem*

869 This sediment-landform assemblage is dominated by large flat-topped sediment bodies, interpreted as
870 deltas, or perhaps subaqueous fans modified by subsequent falling lake levels (Figure 8), all deposited into
871 former ice-dammed lakes. These were common along the shores of the lakes located east of the
872 contemporary icefields (Bell, 2008, 2009; Bendle et al., 2017b; Davies et al., 2018; De Muro et al., 2018;
873 Glasser et al., 2016b; Hein et al., 2010; Thorndycraft et al, 2019a; Turner et al., 2005). Marine terraces,
874 documenting former sea level high stands following the LGM, have also been mapped in southern Patagonia
875 especially (e.g. Bentley and McCulloch, 2005; De Muro et al., 2017, 2018; Feruglio, 1933; Porter et al., 1984).

876 At Lago GCBA and Lago CP, the glaciolacustrine delta fans have a classic Gilbert form with a braided delta top
877 and a steeply inclined delta front. Adjacent to the fans are concave beach embayments that formed parallel
878 with the deltas as they prograded into the lake. The delta sediments consist predominantly of matrix- and
879 clast-supported gravels (Bell, 2009; Figure 8B). Underflows forming turbidity currents are also likely to be
880 relatively common, given the lack of a density difference between river and lake water, as compared with
881 meltwater entering the marine system and rising to form buoyant plumes of suspended sediment (Syvitski,
882 1989). The palaeolake assemblage also includes subaqueous morainal banks (Figure 8C, D; Bendle et al.,

2017b; Davies et al., 2018; García et al., 2014, 2015; Hein et al., 2010) and palaeo shorelines etched into the hillsides (typically cut into glacial sediments; Figure 8E, F). Shorelines typically have a sloping beachward face and can be tens to hundreds of metres wide. In Torres del Paine, García et al. (2014) and Solari et al. (2012) described substantial glaciolacustrine terraces that flank the valley sides, with consistent elevations over several kilometres. These terraces occur as both continuous and discontinuous fragments that are cut into bedrock and lake sediments. Over 10s of kilometres shorelines are warped upwards towards the Andean Cordillera reflecting glacioisostasy (Thorndycraft et al, 2019a; Turner et al., 2005).

Associated with these glaciolacustrine geomorphological features are extensive deposits of glaciolacustrine rhythmically (and sometimes annually) bedded silts and clays (Caldenius, 1932; Bendle et al., 2017a). These sequences are associated in places with bedded gravel deposits (García et al., 2014, 2015). Tephra horizons may be interbedded within annually-laminated (varved) glaciolacustrine units, and provide the potential for time-anchored, high resolution chronologies for ice-margin recession and palaeolake evolution (Bendle et al., 2017a; Thorndycraft et al, 2019a).

Figure 8. Glaciolacustrine landsystem around Lago Cochrane and Lago Esmeralda, east of the Northern Patagonian Icefield. A: Raised glaciofluvial delta terraces above Logo Cochrane. B: Perched delta and modern delta, Lago General Carrera. C: Morainal bank, Esmeralda Moraines (see Davies et al. 2018). D: Photograph illustrating the Esmeralda morainal bank. E, F: Palaeolake shorelines around Lago Juncal. G: Geomorphological map highlighting glaciolacustrine landforms around Lago Cochrane. For more information see Davies et al. 2018; Thorndycraft et al, 2019a; Martin et al. 2019. See also Figure 21.

4.4 Glaciomarine landsystem

The 15 arc-second GEBCO dataset (GEBCO, 2019) permits a relatively low-resolution visualisation of the wider Patagonian continental shelf. The western, Pacific continental shelf is characterised by 12 relatively deep cross-shelf troughs up to 300 km long between 42° and 55°S (Figure 9A). Troughs are not apparent on the corresponding Atlantic continental shelf, which is typically <100 m deep, gradually deepening to 200 m on the outer shelf before the sharp break in slope at the continental shelf edge. The Pacific coast troughs emanate from the narrow, deep, inter-island fjords that characterise the western Patagonian coastline (Figure 9A). The inner fjords between the islands reach depths of more than 1000 m below sea level and are 3 to 10 km wide. Beyond the coastline, on the continental shelf, the troughs shallow and broaden, reaching depths of ~200 m below sea level and widths of 11 to 38 km). The fjords and troughs often follow a dendritic pattern, with several fjords converging in a single trough on the middle and outer continental shelf edge. Although mapping at a regional scale is sparse, the 27,000 km^2 of fjord floors for which relatively high-resolution multibeam echo-sounder data are available contain a landsystem assemblage that has been interpreted to represent a climatically mild, meltwater-dominated fjord setting (Dowdeswell and Vásquez,

2013). Such meltwater-dominated systems are characterised by relatively rapid delivery of fine-grained sorted sediments from meltwater plumes emanating from tidewater-glacier termini and glacifluvial systems where ice does not reach the sea (Dowdeswell and Vasquez, 2013).

Where fjord floors have been mapped in detail using multibeam echo-sounders, transverse moraine ridges, glaciofluvial and fluvial deltas and turbidity-current channels have commonly been identified (Dowdeswell and Vasquez, 2013) (Figure 9B-D). The moraine ridges are relatively large and are interpreted to represent still-stands of tidewater glaciers during deglacial retreat through the fjord systems of western Patagonia (e.g. Dowdeswell and Vasquez, 2013; Lastras and Dowdeswell, 2016); the broad ridges often protrude through and are draped by Holocene basin-fill (e.g. DaSilva et al., 1997; Boyd et al., 2008). Several moraine ridges are located at the mouths of fjords, which represent likely pinning-points where water deepens by tens to hundreds of metres immediately beyond the ridges (Dowdeswell et al., 2016c). Streamlined subglacial landforms are rarely observed, probably because relatively high rates of Holocene sedimentation after regional deglaciation have buried any subglacially produced landforms under several tens of metres of fine-grained sediment derived from fluvial and glaciofluvial rivers that reach the sea and built prominent deltas (Boyd et al., 2008; DaSilva et al., 1997; Dowdeswell and Vásquez, 2013; Fernández et al., 2012).

Well-developed turbidity-current channels have been mapped in several fjords, appearing to emanate from relatively steep delta fronts (Dowdeswell and Vasquez, 2013). Turbidity-current activity probably continues today, an inference supported by the observation that such channels remain unburied by Holocene sedimentation. The irregular seafloor depressions produced by the ploughing action of iceberg keels, so typical of most glacier-influenced continental shelves (e.g. Lopez-Martinez et al., 2011), are almost absent from the floors of Patagonian fjords despite the presence of calving tidewater-glacier termini. This is probably because heavily crevassed tidewater glaciers, such as Jorge Montt, Tempano and Pio XI (Warren and Aniya, 1999), produce only small icebergs of irregular shape and with shallow keels, similar to many Northern Hemisphere tidewater glacier settings (e.g. Dowdeswell and Forsberg, 1992). These small icebergs rarely ground in the deep fjords of Patagonia and are therefore unable to plough the seafloor.

The fjordlands of Chilean Patagonia represent the mildest climatic and oceanographic end-member of a continuum of glacier-influenced marine settings where ice reaches the sea today (Dowdeswell and Vasquez, 2013); an environment somewhat similar to south-east Alaska in the Northern Hemisphere where glaciers accumulate in mountain ranges and typically have a large altitudinal range and high mass throughput (Cai et al., 1997; Powell and Molnia, 1989). Fjords and associated trough systems similar to these have been observed on the continental shelf around South Georgia (Graham et al., 2008), the Antarctic Peninsula continental shelf (Ó Cofaigh et al., 2014), and in West Antarctica (Ó Cofaigh et al., 2005). They are interpreted to have been formed by palaeo-ice streams during periods of Quaternary glacial maxima. The

951 cross-shelf troughs on the Patagonian continental shelf appear to show over-deepening by glacial erosion in
952 the inner shelf, with depths decreasing seaward, in a similar way to those observed on other continental
953 shelves (Batchelor and Dowdeswell, 2014). On the basis of their morphology, cross-shelf alignment,
954 connection to present-day fjords and characteristically deep fjord bathymetry, we interpret the probable
955 origin of these troughs as a product of enhanced glacial erosion during periods of past glacial maxima. Cross-
956 shelf trough systems in other locations have been associated with trough-mouth fans (Ó Cofaigh et al.,
957 2003), but the resolution of the GEBCO 2019 dataset does not allow the identification or otherwise of fans
958 on the western Chilean outer-shelf and upper-slope of what is a very active continental margin where rapid
959 sediment transfer down-slope by mass-wasting may in any case limit fan growth.

960

961 *Figure 9. Examples of marine glacial geomorphology around Patagonia. A: Cross-shelf troughs on the*
962 *Patagonian continental shelf. Yellow stars indicate location of panels B-D. B: Terminal moraine ridge,*
963 *transverse ridges and streamlined lineations associated with Tempano Glacier, Southern Patagonian Icefield.*
964 *C: Swath bathymetry of the 100 m high recessional moraine in Europa Fjord. D: Glaciofluvial delta in*
965 *Bernardo Fjord, with a braided river. Bernardo Glacier is just to the southeast of the image. Adapted from*
966 *Dowdeswell et al. (2016c).*

967

968 # 5 PATICE Reconstruction (35 – 0 ka)

969 This section provides brief summaries of the geomorphological and chronological data that underpin our ice
970 sheet reconstruction, followed by the results of our 5 ka reconstructions from 35 ka to present. For
971 simplicity, we have sub-divided the former PIS into six key sectors spanning the full latitudinal range of the
972 study area from 38°S to 56°S (Figure 10). From north to south, we refer to these as: Chilean Lake District
973 (38°– 42°S), Isla de Chiloé and Archipielago de los Chonos and the adjacent mainland (42° – 46°S), Northern
974 Patagonian Icefield sector (46° – 48°S), Southern Patagonian Icefield sector (48° – 52°S), Gran Campo Nevado
975 sector (52° – 53°S) and Cordillera Darwin sector (53° – 56°S).

976

977 *Figure 10. Location of six key sectors of the former Patagonian Ice Sheet and distribution of selected*
978 *landforms and all published ages used in this study.*

979

980 ## *5.1 The Chilean Lake District (38 – 42°S)*

981 ### *5.1.1 Present-day characteristics*

982 The Chilean Lake District owes its name to numerous glacially derived lakes in the "Valle Central", located
983 between Cordillera de la Costa to the west and the Andes to the east (Moreno et al., 1999) (Figure 11). The

984 region has a highly maritime climate, with a pronounced west-east precipitation gradient. Precipitation
985 reaches 3 m a^{-1} near the coast (Aravena and Luckman, 2009), but data are limited at higher altitudes (Paul
986 and Mölg, 2014). Seno Reloncaví, a seaway, forms the southernmost boundary of the Chilean Lake District
987 (Figure 2; Figure 11). Mountains and volcanoes reach 1,800 - 2,500 m asl (lower than the peaks in the
988 Patagonian icefields), except for the more substantial extinct stratovolcano Mount Tronador (3,500 m asl),
989 and isolated peaks are capped by small snowfields (Figure 11). Glaciers on these mountains are
990 topographically controlled, with steep slopes allowing only limited accumulation and small glaciers (Paul and
991 Mölg, 2014). Where plateaux allow greater accumulation, icefields are able to form; e.g. in Mount Tronador.

992 The great majority of these mountain glaciers are presently shrinking (Bown and Rivera, 2007; Braun et al.,
993 2019; Davies and Glasser, 2012; Rivera et al., 2005), driven by decreasing precipitation and upper
994 atmosphere warming. The active volcanic centres frequently cover the glaciers with ash layers, which may
995 insulate the glaciers and reduce ablation (Adhikary et al., 2002; Rivera et al., 2005), although geothermal
996 heating may also enhance basal melt (Rivera et al., 2006). These northerly glaciers tend to be higher, steeper
997 and smaller than the more southerly glaciers and icefields, and may therefore have relatively rapid response
998 times and steep mass balance gradients (Davies and Glasser, 2012).

999

1000 *Figure 11. Location of glaciers and published geomorphology and chronological data (MIS 3 to present)*
1001 *constraining ice mass extent in the Chilean Lake District (38°S – 42°S) (data from Andersen et al., 1999;*
1002 *Bentley, 1997; Davies and Glasser, 2012; Denton et al., 1999; Glasser and Jansson, 2008; Heusser et al., 1999;*
1003 *Mercer, 1976; Moreno et al., 1999; Porter, 1981). Isochrones are labelled with blue numbers.*

1004

1005 *5.1.2 Evidence for glaciation*

1006 Deposits of the last glaciation (the "Llanquihue Glaciation" of Heusser, 1974) have allowed reconstruction of
1007 numerous smaller and four larger piedmont lobes in the western Chilean Lake District (Denton et al., 1999;
1008 Lowell et al., 1995; Mercer, 1972; Moreno et al., 2015; Porter, 1981), which excavated deep depressions that
1009 are today infilled with lakes (Figure 11). These lakes are surrounded by extensive inset moraines (Bentley,
1010 1996). At their maximum extents, the icefields were confined to the valleys, and expanded laterally onto the
1011 plain. The moraine belts feature ridges (10 – 20 m relief), hummocky terrain, outwash plains outside the
1012 moraine limits and prominent kame terraces inside the moraines alongside Lago Llanquihue and northern
1013 Seno Reloncaví (Andersen et al., 1999; Denton et al., 1999; Moreno et al., 2015). Other landforms include
1014 ice-contact slopes (30-80 m high), and ice-marginal meltwater channels with spillways at the head of the ice-
1015 contact slopes. Geomorphological mapping of moraines north of Lago Puyehue indicates that the glaciers in

1016 the northern Lake District also formed smaller piedmont lobes on the plain west of the Andes at the LGM
1017 (Andersen et al., 1999; Denton et al., 1999; Glasser and Jansson, 2008; Glasser et al., 2008).

1018 Moraines around Lago Llanquihue and Seno de Reloncaví are largely composed of stratified glaciofluvial
1019 deposits, over-thrusted on their proximal flanks by clay-rich diamictons (Bentley, 1996). Water-saturated,
1020 fine, impermeable sediments in the lake basins may have facilitated glacier advance even with negligible ice-
1021 surface slope by encouraging sedimentary deformation at the ice-bed interface (Bentley, 1996, 1997;
1022 Heirman et al., 2011).

1023 Seismic stratigraphy obtained from Lago Puyehue has revealed a complex sedimentary infill, comprising
1024 morainic, ice-contact or outwash deposits, glaciolacustrine sediments, with sediments deposited by
1025 underflows from sediment-laden meltwater streams, reflecting the deglacial evolution of the lake basin
1026 (Charlet et al., 2008; Heirman et al., 2011).

1027 Morphostratigraphic analysis suggests that there are three age groups of moraines relating to these
1028 piedmont ice lobes. The youngest two groups have well-preserved morphology, separated by morphologic
1029 breaks and weathering differences. The outermost moraines are more weathered and have subdued
1030 expression, and are presumed to be older (Andersen et al., 1999; Denton et al., 1999). These moraines are
1031 thoroughly dated with radiocarbon, and we include 452 of these ages in our database (Andersen et al., 1999;
1032 Denton et al., 1999; Moreno et al., 2015). Other ages are excluded as they are not as relevant to our
1033 reconstruction. Many of these radiocarbon ages are given a reliability rating (see Section 3.3) of 2 rather
1034 than 3 as they date bulk material, have $\delta^{13}C$ values outside of the ideal range, or have an unclear
1035 stratigraphic or geomorphic context.

1036 As the chronology here is based on stratigraphy, dating of organics interbedded with till deposits and
1037 outwash, it is challenging in places to relate this directly to specific ice margins or moraine sets. The
1038 stratigraphy here indicates that the Andean piedmont glaciers achieved glacial maxima numerous times
1039 during MIS 4, 3 and 2 (Moreno et al., 2015). This stratigraphic framework is reviewed thoroughly by Moreno
1040 et al. (2015) and readers are referred to that publication for more details. The key evidence for the timing of
1041 glaciation at Lago Llanquihue is now summarised below.

1042 At “Site 3” (Puerto Octay) (Figure 12), at the top of an ice-contact slope that rises above Bahía Octay of the
1043 lake, an outwash slope rests on organic-rich pyroclastic deposits. The outwash slope would have been
1044 formed by a glacier positioned at the upper crest of the ice-contact slope (Denton et al., 1999). Radiocarbon
1045 dating of organic samples from underneath these outwash sediments yielded a mean age of 33.6 ± 0.2 cal.
1046 ka BP (Moreno et al., 2015; Denton et al., 1999).

1047 At "Site 4" (Bahía Frutillar Bajo; Figure 12), flow till rests on a land-surface developed on a pyroclastic flow,
1048 near the top of an ice-contact slope (Denton et al., 1999; Moreno et al., 2015). Radiocarbon ages on wood
1049 and organics below the flow till yield a mean age of 30.8 ±1.0 cal. ka BP, indicating that the glacial advance
1050 that deposited the flow till post-dated this time (*ibid*.).

1051 The Llanquihue moraine belt around Lago Llanquihue is further dated by maximum-limiting radiocarbon ages
1052 from organic clasts reworked into outwash that grades from the moraine ridges (Sites 8, 9, 10, 11; Figure 12).
1053 These organic clasts yielded mean ages of ranging from 26.2 to 29.3 cal. ka BP (Denton et al., 1999; Moreno
1054 et al., 2015). Minimum-limiting ages are derived from lakeside ice-contact slopes, with organic-rich fills at
1055 Canal de la Puntilla (Site 1) and Canal de Chanchán (Site 12) dating from 24.2 to 24.8 cal. ka BP. Site 13
1056 provides another minimum-limiting age of 23.79 ± 0.31 cal. ka BP.

1057 The youngest advance of the Llanquihue ice lobe into its lake reached the innermost ice-contact slope of the
1058 Llanquihue moraine belt, where it deposited a large kame terrace, which rests conformably on organic
1059 deposits. At Site 18, these uppermost organic samples yielded a mean age of 18.03 ± 0.81 cal. ka BP (Moreno
1060 et al., 2015). At Puerto Varas (Sites 19, 20, 16, 17), intact peat is overlain by kame terrace sediments, and
1061 yields mean radiocarbon ages of 17.70 to 18.10 cal. ka BP (Denton et al., 1999; Moreno et al., 2015).

1062 Further south, the Seno de Reloncaví lobe is dated at "Site 5", where wood and fibrous peat from the upper
1063 surface of an organic bed is overlain by outwash that is, in turn, overlain by the Llanquihue moraines. The
1064 meltwater that deposited this outwash emanated from an ice lobe that reached an ice-contact slope above
1065 Seno Reloncaví (Moreno et al., 2015), and which then advanced over the outwash. The organic material
1066 underneath the outwash yielded mean radiocarbon ages of 26.89 ± 0.17 cal. ka BP (Denton et al., 1999).

1067 At "Site 7" (Puerto Montt, Seno Reloncaví; Figure 12), a road-cutting section in the Llanquihue Drift shows
1068 glacial sediments resting on pyroclastic flow deposits. Organic material on the pyroclastic flow land-surface
1069 is preserved underneath the glacial diamicton (Moreno et al., 2015). The stratified, gravelly diamicton is
1070 interpreted as gravel-rich sediment-flow deposits from a nearby ice margin, and it is capped by a layer of
1071 lodgement till (Denton et al., 1999). Radiocarbon ages from wood from the preserved organic material
1072 provide a mean age of 26.0 ± 0.7 cal. ka BP, indicating that ice advance predated this time.

1073

1074 *Figure 12. Map showing numbered key palynological and stratigraphic sites (large filled yellow circles) named*
1075 *in the text in the Chilean Lake District. After Moreno et al., 2015.*

1076

1077 Glacier recession early in the Last Glacial-Interglacial Transition is documented further north, where Volcán
1078 Villarrica has generated several large explosive eruptions (Moreno et al., 2015). One eruption early in the Late

Glacial led to the emplacement of the Cucido pyroclastic flow and resulting Licán ignimbrite, with the latter being found up to 40 km away from the volcano, covering an area more than 1000 km^2 in size. The Villarrica and Calafquén outlet lobes (Figure 11) here form well-defined arcuate moraine systems and extensive outwash plains west of their lake basins (*ibid*). The Licán ignimbrite mantles these LGM moraines and also extends as tongues into the Andean valleys. The distribution of the Licán ignimbrite shows that the Villarrica and Calafquen outlet lobes had receded deep into the Andes by the time of the eruption, which has a mean age of 16.8 ± 0.1 cal. ka BP (Moreno et al., 2015; Figure 11). This indicates extensive deglaciation of the northern Chilean Lake District prior to 16.8 ± 0.1 cal. ka BP.

East of the Andes, moraines indicated a more restricted ice extent (Glasser and Jansson, 2008; Tatur et al., 2002). Three morainic arcs with ridge crests up to 100 m high enclose the eastern end of Lago Nahuel Huapi, with the inner moraines purportedly marking the end of the Last Glaciation (Tatur et al., 2002). An ice-dammed lake (Palaeolake Elpalafquen and later Palaeolake Nahuel Huapi; del Valle et al., 2000) in this valley is evidenced by post-glacial lacustrine beaches that eroded the inner slopes of the terminal moraines, with strandlines and fluvioglacial plains located up to 100 m above recent lake level.

5.1.3 Ice-sheet reconstruction

Most chronological constraints are focused on radiocarbon dating of the moraines around Lago Puyehue, Lago Llanquihue and Seno de Relconcaví (Figure 11) (Andersen et al., 1999; Bentley, 1997; Denton et al., 1999; Heusser et al., 1999; Lowell et al., 1995; Moreno et al., 1999). In the northern Lake District, a lack of dating control makes determining ice-extent problematic; ice extents at 35, 30, 25 and 20 ka are therefore assumed to be coeval (Figure 13). Denton et al. (1999) and Moreno et al. (2015) argued that radiocarbon ages from the piedmont lobes of the southern Lake District show recurrent expansions of the glaciers to the piedmont lobe moraines at 33.6, 30.8, 26.9, and 26.0 cal. ka BP (Figure 11). They provide a clear stratigraphic record for ice expansion; however, as the chronology is related to stratigraphy rather than directly dating the moraines, the different ice extents at each time are difficult to map. The Seno de Reloncaví outlet lobe is well constrained at the LLGM, with maximal extent at the outer moraines at 35 – 30 ka (Denton et al., 1999), and recession to the current shoreline of the embayment by 20 ka (Porter, 1981).

The youngest advance into the Llanquihue moraine belt occurred at 17.7 – 18.1 cal. ka BP (Moreno et al., 2015). By 16.8 cal. ka BP, ice had retreated from the over-deepenings to the higher ground (Moreno et al. 2015), forming an icefield over the mountains that today sustains only small glaciers. This reconstruction agrees with Bertrand et al. (2008), based on their extrapolated age model from radiocarbon dates from a core from Lago Puyehue. Bentley (1997) demonstrated that the lake was ice-free by 14.1 ± 0.8 cal. ka BP,

1111 although the lake could have been ice-free before this date. By 10 ka, we assume further recession, with
1112 most mountain ice caps disappearing by 5 ka; however, these Holocene reconstructions have a *low*
1113 *confidence.* More data are sorely needed at the highest elevations of the northern Lake District on post-
1114 glacial changes.

1115

1116 *Figure 13. Reconstruction of glaciers and outlet lobes of the Chilean Lake District. Relative sea level data from*
1117 *Guilderson et al. (2000), symbolised using GEBCO topographic and bathymetric data. Shading is illustrative*
1118 *only and does not represent ice thickness. Inferred ice-flow lines (yellow) are shown for 35 ka in this and*
1119 *subsequent reconstruction figures.*

1120

1121 Palaeolake Elpalafquen encompassed both Lago Nahuel Huapo and Lago Mascardi (del Valle et al., 2000). As
1122 the present-day Lago Nahuel Huapi (altitude 770 m) drains towards the Atlantic, this lake was likely dammed
1123 by moraines. Around 13 ka BP, Palaeolake Elpalafquen became several smaller lakes, including Palaeolake
1124 Nahuel Huapi. In order to encompass both Lago Nahuel Huapo and Lago Mascardi, we reconstruct Palaeolake
1125 Elpalafquen at 15 ka at 850 m asl, covering ~470 km^2. Drainage from Lago Mascardi to the south and west
1126 must remain dammed by ice at this time. At 13 ka we reconstruct a smaller ice mass that allows drainage of
1127 Palaeolake Elpalafquen and the formation of Lago Mascardi and Lago Nahuel Huapi at 770 m asl. We give both
1128 the 15 ka and 13 ka ice margins here a *low confidence* and highlight this as an area for further work (Figure
1129 13).

1130

1131 ## *5.2 Isla de Chiloé and Archipiélago de los Chonos and adjacent mainland (42°S – 46°S)*

1132 ### *5.2.1 Present day characteristics*

1133 The Isla de Chiloé-Archipiélago de los Chonos sector comprises the mainland Chiloé region, and the two
1134 large archipelagos to the west of the Andes (Figure 14). The Andes are over 2000 m asl in this sector and
1135 host occasional ice caps, e.g. Cerro Barros Arana (43.9°S) and Macizo Nevado (García, 2012). Water
1136 maximum depth between Isla de Chiloé and the mainland to the east is greater than 400 m.

1137 Isla de Chiloé is located at the northern margin of the SWW belt and the ACC, with a steep thermal
1138 latitudinal gradient between the ACC and the northward Humbolt Current (Lamy et al., 2004). Isla de Chiloé
1139 is separated from the mainland by the Golfo de Ancud and Golfo de Corcovado (Figure 14).

1140

1141 *Figure 14. Location of glaciers and lakes, and chronological and geomorphological evidence for glaciation*
1142 *(MIS 3 to present) in Isla de Chiloé and Archipiélago de los Chonos sector (42°S – 46°S) (Andersen et al., 1999;*
1143 *Caldenius, 1932; Davies and Glasser, 2012; Denton et al., 1999; Douglass et al., 2006; Dowdeswell et al.,*

2016c; García et al., 2019; García, 2012; Glasser and Jansson, 2008; Glasser et al., 2016b; Haberle and Bennett, 2004; Heusser et al., 1999; Lastras and Dowdeswell, 2016; Lowell et al., 1995; Stern et al., 2015; Moreno et al., 2015; Van Daele et al., 2016; Weller et al., 2015). See Figure 15 for more detail in the Río Cisnes valley. Pink crosses indicate uncertainty weighted mean ages for boulder exposure ages. Isochrones are labelled in blue writing.

5.2.2 Evidence for glaciation

The western coastal margin of Isla de Chiloé is the southernmost terrestrial area of the western side of Patagonia that remained ice free at the LGM. The island is characterised by deep, wide glacial valleys (Glasser et al., 2008). Moraine evidence in this area consists of extensive south – north oriented belts extending for more than 50 km (Figure 14), contrasting in form with the piedmont lobes of the Chilean Lake District to the north (García, 2012). The moraine belts record westward advances of the Golfo de Ancud and the Golfo de Corcovado lobes from the Andes (Denton et al., 1999). The glacial landscape comprises different generations of landforms, such as sharp-crested moraines, hummocky moraines with irregular, low-relief topography, outwash plains, and meltwater channels and spillways (García, 2012; Anderson et al., 1999). In the eastern foothills of Cordillera de La Costa, streamlined bedrock is evident. In the eastern parts of Isla de Chiloé, till flutings trending NWW are apparent. The region is covered with subglacial tills, with clasts of Andean origin. Radiocarbon ages (Denton et al., 1999; García, 2012; Heusser et al., 1999) allow us to place the ice margin on eastern Isla de Chiloé from 35 – 25 ka. It remains unknown when the ice buttressed against Cordillera de la Costa and built the westernmost Llanquihue moraines and associated principal outwash plains (García, 2012). Moreno et al. (2015) and Denton et al. (1999) also show an advance here at 18 ka. South of Dalcahue on Isla de Grande Chiloé (Figure 14), the 17.8 cal. ka BP advance may have been the most extensive.

At “Site 6” (Teguaco; Isla de Chiloé; Figure 12), organic material from a gyttja layer is overlain by glaciolacustrine silt and clay (Denton et al., 1999; Moreno et al., 2015). These sediments were deposited in a palaeolake dammed by the Golfo de Corcovado outlet lobe when it advanced onto the eastern flank of Isla Grande de Chiloé (*ibid*.). The organics yield a mean radiocarbon age of 26.8 ± 0.2 cal. ka BP for flooding by the ice-dammed lake (Denton et al., 1999).

On Archipiélago de los Chonos, Bennett et al. (2000) and Haberle and Bennett (2004) obtained bulk basal radiocarbon ages from a series of small lakes across the archipelago (Figure 14). These data suggest that the islands were ice-covered during the LLGM, but that they were ice-free as early as 19.4 ± 0.9 cal. ka BP.

On the eastern side of the Andes, the Epuyen Valley lobe contains some of the earliest records of glaciolacustrine varve analysis (Caldenius, 1932). Here and in the neighbouring Cholila Lobe, a series of flat-topped deltas and rhythmically laminated silts and clays inside terminal moraines evidence a post-LGM

glacial lake. Lago Epuyen drains into Lago Puelo and out to the Pacific Ocean through Río Puelo; during deglaciation, this drainage route was blocked, causing the formation of the ice-dammed lake. Caldenius (1932) suggested that this ice-dammed palaeolake was extant between the terminal moraine crests and the eastern end of the current Lago Epuyen, meaning that this lake occupied the eastern half of Epuyen valley. Currently chronology for this is lacking, but Caldenius (1932) estimated that the lake was extant for about 200 years. The surface elevation of the lake is also uncertain. Caldenius (1932) also described a glaciolacustrine terrace with a width of 200 m, cut to a height of 550 m. Contour analysis suggests that the col for drainage eastwards to the Atlantic lies at 660 m asl, and the palaeochannel for this spillway is clearly visible on satellite imagery. A height of 660 m asl corresponds with deltas mapped in our study from high-resolution satellite imagery. We reconstruct a 660 m asl glacial lake at 20 ka, as the 15 ka ice sheet is presumably too far receded to block the drainage pathway at 15 ka (although this requires further testing).

Caldenius (1932) also reconstructed a palaeolake in the adjacent Cholila Lobe. Again, this is evidenced by a series of flat-topped terraces within the terminal moraines, and abandoned palaeochannels demarking the outflow from the palaeolake to the current Atlantic drainage. The col through the terminal moraines lies at 700 m asl, which fits with the height of flat-topped deltas mapped by the authors in this valley.

In the Río Pico valley, four sets of moraines were mapped by Beraza and Vilas (1989) and Lapido (2000), all of which have normal polarity magnetisation and are therefore younger than the Brunhes Palaeomagnetic Chron (i.e. younger than 0.78 Ma) (Rabassa et al., 2011). The innermost 'Las Mulas' drift has previously been attributed to the LGM; however, a sediment core from a small intermorainic lake, Laguna La Pava, 12 km to the east of this, within the Trenenhau Drift moraines, yielded a basal radiocarbon age of 15 ± 0.5 cal. ka BP (Iglesias et al., 2016) (Figure 14; Figure 15), suggesting that the LGM limit was actually further east. We place the ice limit at 30 ka at the Cherque Drift, with low confidence; this is in keeping with the ice extent reached in the valleys south of here with better chronological controls.

Several moraine belts in the Cisnes valley denote ice extent, with the outermost (CIS I and CIS II) denoting full glacial conditions (García et al., 2019; Figure 15). Basal radiocarbon ages from a core from Lake Shaman within the inner CIS II moraine belt suggest the CIS II moraines were free of ice by 18.9 ± 0.3 cal. ka BP (minimum age; Figure 14; Figure 15). Ice-free conditions at this time are also indicated by the presence of the Ho tephra within the core, dated to 17.4 ka (Stern et al., 2015). There are several sets of moraines inset from these (de Porras et al., 2012). Rapid recession following the LGM is suggested by the presence of the Melimoyu tephra (19.7 ka) at Las Barrancas (Stern et al., 2015), 16.5 km southwest of Lake Shaman (Figure 15). The inner CIS III to V moraines represent still stands during ice retreat. Boulders on the CIS IV moraine dated by ^{10}Be surface exposure dating (mean age 20.1, SD 0.9 ka) indicate that the ice had receded to the

central part of the valley by 20 ka (García et al., 2019) (Figure 15). This suggests a recession of some 35 km in the Río Cisnes valley between the LGM and 20 ka.

The PIS in this region dammed several lakes during deglaciation, when present-day drainage to the Pacific Ocean was obstructed (García et al., 2019). In the Cisnes valley, shorelines and fluvial terraces denote the palaeolake extent. There are two distinct shorelines at 950-920 m, and 860-850 m. The 920 m lake has a distinct col that leads to drainage towards the Atlantic Ocean. The 920 m lake was extant by 20 ka in front of the CIS IV moraine and likely later also, when the ice margin had receded to the central part of the valley (Figure 15) (García et al., 2019).

Further down the valley, a peat core from Mallín El Embudo (Figure 15A) with basal radiocarbon ages of 12.9 ± 0.1 cal. ka BP (de Porras et al., 2014) allows the 15 ka isochrone to be inferred, showing recession of the ice lobe to the west at this time (Figure 15).

Further south, Palaoelake Nirehuao formed in front of the Lago Coyt outlet lobe, with an initial highstand of 740 m, draining towards the Atlantic. The timing of this highstand is unclear, and it could be earlier or later than 20 ka. Following further deglaciation, the Palaeolake Cisnes and Palaoelake Nirehuao united in both the Coyt and Cisnes valleys, likely by 15 ka, to form Palaeolake Cisnes-Nirehuao (Figure 15) at 660 m asl and draining towards the Pacific (García et al., 2019). García et al. (2019) suggested that this united lake could have formed during the ACR, but this awaits confirmation. Radiocarbon ages suggest that this united lake drained below 200 m asl by 12.1 to 12.4 cal. ka BP, and indicates that the ice masses had begun to fragment at this time.

Evidence of a proglacial lake at 20 ka in front of the Coyhaique outlet lobe (Palaeolake Frío) is present in the form of glacier-contact deposits and varves (Van Daele et al., 2016). This lake outlet flowed to the east, with a likely altitude of 660 m asl and drainage most likely could have flowed south, around the ice margin, and into Palaeolake Balmaceda (Figure 15).

A series of moraines east of Coyhaique, with elevations of up to 867 m asl, mark the easternmost extent of the Coyhaique outlet lobe (Miranda et al., 2013). Bedforms are predominantly ice-scoured bedrock there, overlain by glaciolacustrine sediments from Palaeolake Balmaceda, which produced shorelines of up to 610 m asl in the Río Huemules valley. The col today is located at 585 m asl, indicating that lowering through moraine incision may have occurred (Figure 15). This palaeolake was likely extant at 20 ka, in agreement with radiocarbon ages presented by Miranda et al. (2013) (unfortunately, insufficient data is available to allow inclusion of these ages in our database), and numerous Ho tephra ages (Weller et al., 2015). The lake is likely to have disappeared by 15 ka with the fragmentation of the ice masses and the opening of the drainage route to the Pacific (Figure 15). The spillway that would drain this lake sits at 585 m asl.

In the western mainland, in Aysén Fjord at 45° 22'S, two major submarine ridges have been mapped across the fjord; the Cuervo Ridge and the Colorada Ridge (Lastras and Dowdeswell, 2016). These ridges are located 25 and 54 km beyond the fjord-head delta at Puerto Aysén respectively (Figure 14). These undated ridges constrain the extent of a tidewater glacier in this fjord, likely originating from the mid to late Holocene.

Figure 15. A: Detail of published ages and geomorphology in Río Cisnes valley (after García et al., 2019). B, C: Reconstructed glacial lakes (orange) of the Isla de Chiloé and Archipiélago de los Chonos sector at 20 ka and 15 ka respectively. Extent of Panel A is shown in Panel B. Shading of the ice sheet is illustrative only and is not related to ice thickness. Col spillways are shown as yellow stars with red labels.

5.2.3 Ice-sheet reconstruction

The central part of Isla de Chiloé preserves the most extensive glacial advance at this latitude, with a double ice-contact slope in Cordillera de la Costa locations (García, 2012). The outermost moraines are more than 100 km from the Andean catchments, with ice infilling and crossing the Golfo de Corcovado basin. The Golfo de Corcovado lobe did not reach the Pacific Ocean, and no cirques or other glacial landforms are observed on Cordillera de La Costa, indicating that the west coast of northern Isla de Chiloé remained ice-free at the LGM (Denton et al., 1999; García, 2012) (Figure 16). Further south, the western margin of the PIS extended offshore, and is poorly constrained.

In the northern part of the sector, the eastern outlet lobes are poorly dated, but their LGM positions are well marked with moraines, leading to *medium confidence* in the LGM ice extent, if not the exact timing (Figure 16). Although ice extent is well constrained in the Cisnes valley, other lobes lack chronological control for post-LGM recession. Separation of the ice masses by 20 ka is indicated by the lower cols becoming occupied by the palaeolakes, and the drainage of palaeolake Balmaceda and Frío. The palaeolakes drained by 10 ka (García et al., 2019), suggesting a smaller ice mass confined to the higher ground, but we have *low confidence* in ice extent at 15, 10 and 5 ka (Figure 16).

Further south and east of the Andes, ice lobes immediately to the north of the Northern Patagonian Icefield, such as the Balmaceda, Paso Coyhaique and Lago Coyt outlet lobes, have mapped moraines (Glasser and Jansson, 2008) but are poorly constrained chronologically (Figure 14). As is the case further south, it is likely that the outermost moraines of these systems represent an earlier Pleistocene maximum, rather than the LLGM. We tentatively assume that the LLGM (no distinction made from 35 – 20 ka due to limitations in published ages) is located at the eastern-most of the inner moraines. However, in the absence of quantitative data, confidence in the precise location of the ice limits at each time-slice is low. These ice lobes

1274 are therefore identified as a key target for future research. There is very little published data available
1275 constraining the Holocene dynamics of these glaciers.

1276 The Paso Coyhaique outlet lobe has no chronological control associated with the outermost moraines, but a
1277 series of cores from small lake basins around 20 km east of the town of Coyhaique yielded the Ho tephra
1278 (17.4 ka) and basal radiocarbon ages of 17.8 ± 0.5 to 17.9 ± 0.3 cal. ka BP (Weller et al., 2015) (Figure 14). A
1279 sediment core from Lago Castor suggests that the area was ice-free by 28 cal. ka BP, but radiocarbon dating
1280 was inconclusive (Van Daele et al., 2016), and the area being ice free this early is unlikely given the extensive
1281 ice cover demonstrated in nearby ice lobes.

1282 The fjord between Isla de Chiloé and the mainland is ice free at 20 ka (Figure 16) due to radiocarbon ages
1283 from the coast of Isla de Chiloé indicating ice-free conditions at 16.3 ± 0.8 cal. ka BP (Haberle and Bennett,
1284 2004). However, moraines further south on the Taitao Peninsula suggest that ice persisted, perhaps in the
1285 central or higher parts of the island, at this time. We suggest that the deep fjord between the island and the
1286 mainland precipitated calving and the separation of the ice masses. However, our reconstruction here has
1287 low confidence. We suggest that the northern Isla de Chiloé is ice-free by our 15 ka timeslice.

1288 Limited data constraining mid-Holocene ice dynamics is available for this region. The Late Holocene 0.2 ka
1289 advance is constrained by lichenometry and historical photographs from Torrecillas Glacier at 42.7°S, which
1290 indicate that a series of nested, fresh-looking moraines date from 1735 AD to 1906 AD (Garibotti and
1291 Villalba, 2009).

1292

1293 *Figure 16. Ice sheet reconstruction for Isla de Chiloé and Archipiélago de los Chonos, showing palaeolake*
1294 *development (orange) at 20 and 15 ka. Relative Sea Level data from Guilderson et al. (2000), symbolised*
1295 *using GEBCO topographic and bathymetric data. For more detail see Figure 15. Shading is illustrative only*
1296 *and does not represent ice thickness.*

1297

1298 ## *5.3 The Northern Patagonian Icefield (46°S – 48°S)*

1299 ### *5.3.1 Present-day characteristics*

1300 The Northern Patagonian Icefield stretches for 120 km along the spine of the Andes, from 46°30”S to
1301 47°30”S (Figure 17). It is 70 km wide at its widest, has a mean altitude of 1,340 m asl, and covers 3,976 km^2
1302 (Davies and Glasser, 2012). It contains 1,235 km^3 of ice, with a sea level equivalent of 3.1 mm (Carrivick et
1303 al., 2016). It is the largest icefield at this temperate latitude in the Southern Hemisphere. The central high
1304 plateau, located on the Andes mountain range, is drained by large outlet glaciers mainly orientated west and
1305 east. At present, of the 44 outlet glaciers directly draining the Northern Patagonian Icefield, 26 terminate in
1306 lakes, 1 terminates in a tidal lagoon (Glaciar San Rafael) and the rest terminate on land (Glasser et al., 2016a)

(Figure 17). Ice thicknesses reach 1 km for Glaciar San Rafael and Colonia (Gourlet et al., 2016); these bedrock troughs drive fast ice flow to the ice margin. Bed elevation for Glaciar San Rafael reaches sea level.

Between 1987 and 2015 the NPI has undergone substantial changes, including area decreased from 4133 km^2 to 3887 km^2, while debris-covered ice area increased from 246 km^2 to 311 km^2. The area occupied by proglacial and ice-proximal lakes increased from 112 km^2 to 198 km^2. Between 1987 and 2015, the terminal environment of many of the outlet glaciers of the NPI changed from land-terminating to lake-calving, enhancing calving and ablation. The increase in debris cover also increases ablation. The ELA has risen 100 m from 1979 to 2003 (Glasser et al 2016a).

Figure 17. The Northern Patagonian Icefield and the present-day large lakes dammed against high ground in Argentina. Lago GCBA and Lago CP both drain into Río Baker, which flows westwards into the Pacific Ocean. Key moraines and places named in the text are shown.

Today, the outlet glaciers of the Northern Patagonian Icefield are receding, with the highest rates of recession in small, land-terminating glaciers (Aniya and Enomoto, 1986; Davies and Glasser, 2012; Meier et al., 2018). Overall, annual rates of recession are increasing, with the highest rates of annual area loss observed between 2001 and 2011. Northern Patagonian Icefield glaciers are also thinning (Braun et al., 2019; Jaber et al., 2016), with the highest rates observed at Glaciers Steffen and HPN2 between 2000 and 2014 AD. Glaciar San Rafael is a major outlet glacier on the northwestern side of the Northern Patagonian Icefield and currently drains about 20% of the area of the icefield (Rivera et al., 2007). The glacier terminates in the tidal Laguna San Rafael at 46° 40'S, 73° 55'W, and is the only contemporary tidewater outlet glacier of the Northern Patagonian Icefield and the lowest latitude tidewater glacier on Earth (Warren et al., 1995).

Monte San Lorenzo (MSL) (47°35'S, 72°18'W) is situated on the eastern flank of the Andean range, located *ca* 70 km east of the southern point of the Northern Patagonian Icefield, on the border between Chile and Argentina (Figure 17). At 3,706 m asl it is the third highest peak in the Patagonian Andes (Masiokas et al., 2009b). Up to 102 ice bodies have been mapped on MSL, covering an area of 139.34 km^2 (Falaschi et al., 2013). Alongside Sierra de Sangra to the south (see Section 5.4), these represent the most significant ice masses east of the main Patagonian Icefields, and they may have formed independent ice domes that coalesced with ice coming from the main ice sheet during the LGM (Davies et al., 2018).

5.3.2 Evidence for glaciation

The eastern Northern Patagonian Icefield sector has been a strong focus for research, with perhaps the best-constrained PIS outlet lobes during the LGM and Holocene. During glaciations, the Northern Patagonian Icefield was drained to the east by two large outlet lobes: the Lago General Carrera/Buenos Aires (Lago GCBA) lobe, and the Lago Cochrane/Pueyrredón (Lago CP) lobe (Figure 17). The outlet glaciers of the Northern Patagonian Icefield overwhelmed topography and extended far into the foothills. The lobes were separated by flat-topped volcanic mesetas that reach elevations of more than 2,000 m (Caldenius, 1932; Wenzens, 2003). As the land rises farther east of the Andean mountain range, the outlet glacier lobes had a reverse-bed gradient near the terminus positions (Kaplan et al., 2009; Thorndycraft et al. 2019b); hence englacial and subglacial flow were effectively uphill (Barr and Lovell, 2014).

The Lago GCBA outlet lobe is separated from the Lago CP outlet lobe at their maximum extents by Meseta del Lago Buenos Aires (Figure 17; Figure 18), which reaches heights of up to 2300 m asl. This meseta, which covers around 6000 km^2, is one of the largest basaltic plateaus within the Neogene Patagonian plateau lava province (Wolff et al., 2013). This volcanic plateau lacks geomorphic evidence of glaciation and likely remained largely unglaciated during the last glaciation, save for the Meseta Cuadrada Palaeo Ice Cap on the highest ground (Figure 17), which covered 78 km^2 (Wolff et al., 2013). In the Lago CP valley, mid-Pleistocene glaciers imprinted lateral moraines on the sides of Meseta del Lago Buenos Aires (Figure 18). The best evidence for Mid-Pleistocene and pre-LGM glaciation in Lago GCBA is derived from the lateral moraines; terminal moraines here are heavily eroded by outwash and meltwater systems, which were funnelled along the Moreno scarp and down the Deseado River. During the last glacial cycle, the Local LGM ice extent was reached at *ca* 35 to 30 ka, well inside the Pleistocene maximum extent (Hein et al., 2009, 2010; Cogez et al., 2018). The LGM terminal moraines for Lago GCBA lie at 500 to 600 m asl.

Closer to the ice divide, a small mountain range east of the Northern Patagonian Icefield (Reserva Nacional Lago Jeinemeni), with summits up to 2,000 m asl, divided the major Lago GCBA and Lago CP outlet lobes at the LGM, with substantial and well dated ice limits to the north and south of these mountains. These mountains bear small valley glaciers with numerous down-valley moraines today (Glasser and Jansson, 2008) (Figure 17; Figure 18). An ice divide was likely centred across the icefield, with ice flowing north to contribute to Lago GCBA outlet lobe and south to Lago CP outlet lobe during the LGM.

Figure 18. Published geomorphology and ages (ka) of Northern Patagonian Icefield outlet lobes from 46°-48°S (data from Araneda et al., 2007; Bendle et al., 2017a; Bendle et al., 2017b; Boex et al., 2013; Bourgois et al., 2016; Davies and Glasser, 2012; Davies et al., 2018; Douglass et al., 2005, 2006; Fernandez et al., 2012; Glasser and Jansson, 2008; Glasser et al., 2006a, 2012, 2016b; Harrison et al., 2008, 2012; Hein et al., 2009, 2010, 2011, 2017; Kaplan et al., 2004, 2005; Lumley and Switsur, 1993; Martin et al., 2019; Mercer, 1976;

Nimick et al., 2016; Sagredo et al., 2016, 2018; Singer et al., 2004a; Smedley et al., 2016; Stern et al., 2016; Thorndycraft et al, 2019a; Turner et al., 2005; Villa-Martínez et al., 2012; Wenzens, 2005; Winchester et al., 2014). Red inset boxes A, B and C show location of Figure 19, Figure 21 and the central Río Baker valley, and Figure 23 respectively. Altitude and bathymetry as in Figure 17.

East of the Northern Patagonian Icefield, major outlet glaciers advanced along reverse-bed slopes (Kaplan et al., 2009), resulting in the formation of large ice-contact proglacial lakes during periods of glacier recession (Bell, 2008, 2009; Bendle et al., 2017a; Bourgois et al., 2016; Glasser et al., 2016b; Hein et al., 2010; Heusser, 2003; Martinod et al., 2016; Turner et al., 2005; Tweed, 2011). The geomorphic evidence of these ice-dammed palaeolakes is substantial, comprising shorelines, terraces, raised deltas and glaciolacustrine sediments. The extent, palaeolake surface elevation and depth of ice-dammed palaeolakes was controlled by the location of ice dams relative to drainage cols and moraines, which became degraded and failed over time (Glasser et al., 2016b; Thorndycraft et al, 2019a). The spatial extent, elevation and timing of the palaeolake levels can therefore assist in identifying the location of outlet glacier ice fronts at particular times. A potential complication specific to palaeolake evidence is that, due to the large size of the former lakes, differential isostasy has resulted in gently dipping shorelines (Bourgois et al. 2016; Martinod et al. 2016; Thorndycraft et al. 2019; Turner et al. 2005), which differ from drainage col heights. For the same reasons, deltas of equivalent height at the far eastern and western ends are of different age. However, trends in shoreline uplift are now reasonably well quantified (Bourgois et al. 2016; Martinod et al. 2016; Thorndycraft et al. 2019) and most of the dated deltas cluster in the centre of former lakes (Glasser et al. 2016), where differential isostasy is less likely to cause scatter in the ages.

There are few geomorphological or chronological data available to the west of the NPI other than at the more accessible San Rafael and San Quintin ice lobes, largely due to the challenges in conducting fieldwork. Dense forest also makes remotely sensed geomorphological mapping challenging.

Below, we present the evidence for glaciation at each time-slice for the Northern Patagonian Icefield region. The evolution of palaeolakes in this region has been thoroughly reviewed by Thorndycraft et al. (2019) and here we follow their lake evolution model. This model argues that following post-LGM recession from the terminal moraines east of Lago GCBA and Lago CP, large ice-dammed lakes developed and drained eastwards towards the Atlantic Ocean. Ice in the Baker Valley and to the north of the Northern Patagonian Icefield initially impeded the westwards drainage of meltwater to the Pacific Ocean; however, pathways opened up through the course of deglaciation in response to outlet glacier recession.

5.3.3 Ice sheet reconstruction

5.3.3.1 35 to 25 ka

Of the numerous moraines that fringe the eastern margin of Lago GCBA, the Fenix III to V moraines represent the LGM (Douglass et al., 2006) (Figure 18; Figure 19). Excluding outliers, Fenix V has a mean age of 28.0 (SD 1.8) ka (Kaplan et al., 2004), Fenix IV of 28.8 (SD 2.1) ka, Fenix III of 23.3 (SD 2.1) ka, and Fenix II of 22.9 (SD 1.4) ka (Douglass et al., 2006). Due to the abundance of ages, we can have *high confidence* in the location of the ice margin at 35 to 25 ka.

Lacustrine sediments between the moraines indicate that ice-dammed lakes infilled the gaps between moraines during glacier recession, and OSL ages of these sands support the ice extent reaching the Fenix moraines at ~30 ka (Smedley et al., 2016). Lateral moraines with a single exposure age (32.3 ± 10.2 ka) west of Chile Chico at 1,116 m asl provide data on ice-thickness at the LGM (Bourgois et al., 2016). Given that Lago GCBA is > 400 m deep (Murdie et al., 1998), this outlet lobe would have been 1500 – 1700 m thick at the LGM (Bourgois et al., 2016). At the eastern end of Lago GCBA, cosmogenic nuclide ages from Fenix II and III moraines (Douglass et al., 2006; Kaplan et al., 2004) indicate that the ice margin had receded ~4.5 km by 20 ka (Figure 18).

During the LGM, the Jeinemeni icefield contributed ice to the Lago GCBA outlet lobe (Figure 20). A larger valley glacier is also expected to have flowed east from this icefield. However, overall ice contribution to the Lago GCBA along valleys to the east was likely limited, due to the preservation of stratigraphically older latero-terminal moraines in the Lago GCBA valley. The development of these ice masses and their configuration through time is illustrated in Figure 20.

There is a nested series of moraines at the distal end of the Lago CP valley, recording ice extent there (Figure 17). The oldest and outermost moraines (Hatcher Limit and Canadon de Caracoles limit) yield mid-Pleistocene ages (Hein et al., 2009). The innermost moraines of this sequence, the Rio Blanco Moraines, yield progressively younger cosmogenic nuclide exposure ages. The outer Rio Blanco moraines have a mean age 0f 29.9 ka (SD 3.0). Boulders on the innermost Rio Blanco moraines yield mean ages of 24.7 ka (SD 0.4) to 21.0 ka (SD 1.0), with a youngest age of 19.3 ± 1.8 ka (Hein et al., 2010). This suggeststhat the outer Rio Blanco moraines represent the local LGM limit, and that ice remained here until deglaciation began after 20 to 19 ka.

Figure 19. Published ages and geomorphology, and named moraine sequences, for Lago General Carrera-Buenos Aires (Lago GCBA) (Bendle et al., 2017a; Bourgois et al., 2016; Douglass et al., 2006; Glasser et al., 2016b; Hein et al., 2010; Kaplan et al., 2004; Kaplan et al., 2005; Singer et al., 2004a; Smedley et al., 2016). Overlain on Landsat 7 ETM+ image "p231r092_7f20010320_z19_ps742.tif" (acquired 20th March 2001).

Landform evidence in the Chacabuco Valley provides a means to empirically test numerical simulations of ice thickness east of the current Northern Patagonian Icefield (Hubbard et al., 2005; Hulton et al., 1994). Moraines, periglacial/glacial trimlines, and glacially scoured bedrock on the valley flanks can be used to constrain vertical ice limits of the former PIS. Such landforms can also be readily dated using cosmogenic nuclide dating techniques. Boex et al. (2013) represents the only research to date aimed at reconstructing the upper limits of the LGM PIS. This work used valley side evidence related to the Lago CP Lobe to reconstruct changes in ice sheet thickness. The study used a 60 km west – east transect along the Chacabuco Valley, from Cerro Tamango (1,722 m) in the west, through Cerro Oportus (2,076 m) to Sierra Colorado (1,537 m) in the east. The research demonstrated that at the LGM (mean age for the Sierra Colorado lower limit being 12.8 ka, SD 1.9), the PIS in this area reached a maximum elevation of 1,100 m asl at Sierra Colorado, some 120 km from the ice-sheet centre. The summit of Cerro Oportus at over 2,000 m elevation was ice covered at this time, a similar altitude to that reached by the Lago GCBA outlet glacier at this longitude (Boex et al., 2013). The floor of the Lago CP valley here is ~150 m asl, suggesting that the ice mass was ~1,000 m thick at the LGM near Sierra Colorado.

At the LGM, outlet glaciers to the southeast of MSL converged in the Río Belgrano valley, extending *ca* 70 km from the main massif (Figure 17; Figure 20). The hypothesised LGM ice extent in this location is marked by the outermost terminal moraines (cf. Wenzens, 2003, 2005; Caldenius, 1932). However, dating control is poor, and we are unable to distinguish ice-marginal fluctuations there between 35 – 20 ka. We therefore consider the LGM ice margin to be uncertain.

Figure 20. Reconstruction of Northern Patagonian Icefield outlet lobes. Isochrones used in each time-slice reconstruction are shown in red. Development of ice-dammed palaeolakes is illustrated. Yellow stars indicate drainage cols for ice-dammed lakes. Relative sea level data from Guilderson et al. (2000), symbolised using GEBCO topographic and bathymetric data. Shading is illustrative only and does not represent ice thickness.

5.3.3.2 20 ka

After removing outliers, the mean ages of ^{10}Be samples from the Fenix I and II moraines in the northern-most, more lateral parts, of the terminal moraine system have a mean age of 18.9 ka (SD 1.8). The nearby Menucos moraines have mean ^{10}Be ages of 17.6 ka (SD 0.1) and 17.3 ka (SD 1.0) (Figure 19; Douglass et al., 2006). These cosmogenic ages are complemented by a 994 ± 36 yr varve record from the Río Fenix Chico valley in eastern Lago GCBA (46.58°S, 71.07°W), which is anchored to the calendar-year timescale by the Ho tephra found *in situ* within the lake deposits, and related to the ages of the moraines through morphostratigraphy and Bayesian age modelling (Bendle et al., 2017a). Using a combination of varve

counting, tephrochronology and ^{10}Be data yields a start age for the Fenix I moraines of 18.8 ± 6.2 cal. ka BP, and an end age of 18.1 ± 0.2 cal. ka BP. We note that the varve ages represent minimum ages due to the likely short delay in the onset of varve accumulation after retreat from moraines; the immediate ice-proximal area is too high-energy for the formation of varves (see Bendle et al., 2017a).

The onset of significant glacial recession in the Lago GCBA ice lobe and the early formation of an ice-dammed lake therefore occurred at 18.0 ± 0.1 cal. ka BP, likely in response to a southward migration of the SWW (Bendle et al., 2019). By 18.1 ± 0.2 ka, a palaeolake had formed between the LGM moraines and the receding ice mass in Lago GCBA (Figure 20) (Bendle et al., 2017a; Thorndycraft et al, 2019a; Turner et al., 2005). Recession accelerated from 17.8 ± 0.1 cal. ka BP due to a lagged response in the Southern Hemisphere to the gradual ocean-atmosphere warming (Bendle et al., 2019). By 17.4 ± 0.1 cal. ka BP, the Lago GCBA lobe had receded into a deepening proglacial palaeolake, encouraging calving losses and more rapid ice recession, evidenced by an increase in ice rafted debris in the varve record (Bendle et al., 2017a). The "Deseado" palaeolake reached a maximum height of 400 m asl and drained to the Atlantic Ocean via Río Deseado (Figure 22; Thorndycraft et al, 2019a). Palaeolake Deseado expanded due to ice-mass retreat for several thousand years, depositing varves in eastern Lago GCBA between ~18 and 17 ka (Bendle et al., 2017a). Likewise, an ice-dammed lake (at the "Caracoles Level") had formed by this time in front of the receding Lago CP ice lobe, which also drained to the Atlantic through the Caracoles Col (500 m asl) (Hein et al., 2010; Thorndycraft et al, 2019a; Turner et al., 2005).

The Menucos moraine to the northeast of Lago GCBA has a slightly younger ^{10}Be mean age of 17.3 (SD 1.0) ka when outliers are excluded (Figure 18; Figure 19) (Douglass et al., 2006; Kaplan et al., 2004; recalculated in Kaplan et al., 2011 also). Bayesian age modelling of ^{10}Be and varve ages provides an age for the Menucos moraine of 17.7 ± 0.1 cal. ka BP and a subsequent (and probably short-lived) ice-margin at the Santa Maria fan ~4 km further west (17.3 ± 0.1 cal. ka BP). Combining these ages with distances of glacier retreat indicate that rates of local ice-margin recession began slowly (<11 m a^{-1} from the Fenix I to Menucos moraine), but accelerated (>15 m a^{-1}) after 17.32 ± 0.1 cal. ka BP. The persistent formation of varves until 16.9 ± 0.1 cal. ka BP suggests that ice remained in eastern Lago GCBA until at least this time (Bendle et al., 2017a).

The stratigraphically youngest Rio Blanco moraines (3rd limit) at the distal end of the Lago CP lobe are the innermost moraines of this sequence, and yield a mean age of 21.0 ka (SD 1.0) (Hein et al. 2010). A small Palaeolake CP at this time drained through a 500 m asl col towards the Atlantic (Hein et al., 2010; Thorndycraft et al, 2019a). The Lago CP ice lobe flowed around Sierra Colorado, forming lateral moraines on this upland region at ~1,000 m asl (Boex et al. 2013).

Dating evidence presented in Boex et al. (2013) reveals two phases of PIS retreat in the Lago CP valley; an initial rapid ice lobe recession lobe at ~20.0 ka followed by a phase of rapid surface lowering between 16.0 and 14.7 ka. Their evidence indicates that the former PIS remained close to its LGM extent until at least 19.0 ka here. However, rapid ice sheet thinning from 18.1 ka saw ice at or near its present dimension by 15.5 ka (Boex et al., 2013). Radiocarbon and tephra ages from small lakes (Lago Augusta [440 m asl; -47.087°S, -72.402°W] and Lago Edita [570 m asl; -47.12°S, -72.420°W]) on the high ground between the Chacabuco and Cochrane valleys (Cerro Oportus; Figure 21) indicates that this area was ice-free as early as 19.2 cal. ka BP (Villa-Martinez et al. 2012; Henriquez et al., 2017; Stern et al., 2016), suggesting rapid thinning after 20 ka.

Further east, mean ^{10}Be exposure ages of 17.9 ka (SD 0.5) from elevations of 1,895 m asl on Cerro Oportus constrain the thinning of the ice mass during deglaciation and the separation of ice in the Cochrane and Chacabuco valleys. These data indicate that the ice-sheet surface here reached above this elevation at the LGM. With a surface elevation of 1900 m asl and a lake depth of 400 m at this point in Lago CP (Murdie et al., 1998), there was a minimum LGM ice thickness of 2,186 m at that longitude (72°11'W) in Lago CP.

5.3.3.3 15 ka and 13 ka

Ice margins in this sector had retreated substantially up-valley by 15 ka, with the terminus of Soler Glacier situated at the col where Lago GCBA drains into Lago Bertrand (see Figure 17) at 15.6 ± 1.0 to 14.4 ± 0.6 ka (Davies et al., 2018). At that point, Palaeolake Deseado was still dammed by ice in the Baker Valley at 400 m asl (Thorndycraft et al, 2019a). By 15.3-15.0 ka, according to radiocarbon dating of organic sedimentation at Lago Augusta (Villa-Martínez et al., 2012), the ice-dammed lake in Lago CP had fallen to 420 – 440 m asl (the "Sub-Caracoles level"), potentially due to the opening up of a new drainage pathway towards the Pacific through the Barrancos Valley (Thorndycraft et al, 2019a).

In the Cochrane valley, the 'Esmeralda Moraines' and 'Salto Moraines' were deposited by glaciers flowing north from Monte San Lorenzo and the Barrancos Valley (Figure 21) (Davies et al., 2018), as indicated by trimlines and inset sequences of moraines in the valleys (e.g., the 'Moraine Mounds' of Glasser et al. (2012)). The Esmeralda Moraines yielded cosmogenic nuclide ages of 13.4 ka (SD 0.2) (Figure 21), when the Monte San Lorenzo outlet glaciers calved into the 350 m Palaeolake Chelenko, which was unified in the Lago GCBA and Lago CP Valleys (Davies et al., 2018; Thorndycraft et al, 2019a). A series of moraines in the Tranquilo Valley (Monte San Lorenzo) document a smaller advance of Glaciar Tranquilo during the ACR (Sagredo et al., 2016; 2018). Excluding outliers, the moraines yield mean ^{10}Be ages of 13.8 ka (SD 0.5) (RT1); 13.3 ka (SD 0.5) (RT2); 13.7 ka (SD 0.3) (RT4); and 12.1 ka (SD 0.5) (RT5) (Figure 21) (Sagredo et al., 2016; 2018). These moraines, which are high above the level of any palaeolake, together with ACR-aged moraines from NPI-outlet glacier, Glaciar Colonia (mean 13.6 ka, SD 0.7; Nimick et al. 2016), suggest glacier stabilisation during

1536 the ACR (Figure 22). Ice receded following the ACR as evidenced by the recession of Glaciar Calluqueo to the
1537 "Moraine Mounds" by 12.8 ka (SD 0.4) (Glasser et al., 2012).

1538 The unified Palaeolake Chelenko was extant between ~14.2 and 12.6 ka, with ice still blocking the Baker
1539 valley at the Colonia confluence (Thorndycraft et al, 2019a). The lake drained through the Río Bayo col at 350
1540 m asl (Glasser et al., 2016b), north of the Northern Patagonian Icefield towards the Pacific (Figure 22).
1541 Glacier recession from the Baker Valley led to drainage of Palaeolake Chelenko between 12.6 to 11.7 ka
1542 (ages from Bayesian age modelling) through the lower Baker (Thorndycraft et al, 2019a). The fall in lake level
1543 resulted in separate moraine dammed lakes in the Valle Grande, General Carrera and Cochrane basins, as
1544 previously submerged moraines became exposed. Boulder bars immediately downstream of the
1545 contemporary Lago CP outflow and the Colonia confluence suggest at least two glacial lake outburst floods
1546 drained through the lower Baker valley prior to a flood from Lago GCBA. This event was caused by drainage
1547 of ~100 km^3 of lake water from Lago GCBA (Thorndycraft et al, 2019a), resulting in a catastrophic flood of
1548 ~110,000 m^3s^{-1} and creating megaflood-type landforms along the Baker valley (Benito and Thorndycraft,
1549 2020).

1550 Raised deltas in the Tranquilo Valley indicate that a palaeolake was also extant at this time at 520 m asl
1551 ("Palaeolake Tranquilo") to the north of Monte San Lorenzo (Martin et al., 2019). The lake drained over the
1552 Brown Moraines and into Lago Brown (Figure 21; Figure 22), until further recession of Calluqueo Glacier
1553 allowed a new outflow into the Salto Valley to form. This resulted in the palaeolake level dropping to 425 m
1554 asl and a drainage reversal; however, the timing of this currently remains uncertain. Catastrophic drainage is
1555 possible, with boulder bars typical of floods mapped further down Río Salto (Martin et al., 2019).

1556

1557 *Figure 21. Central Baker Valley with published ages and geomorphology (Boex et al., 2013; Davies et al.,*
1558 *2018; Glasser et al., 2012; Henríquez et al., 2017; Martin et al., 2019; Sagredo et al., 2016, 2018; Stern et al.,*
1559 *2016; Thorndycraft et al, 2019a; Turner et al., 2005).*

1560

1561

1562 *Figure 22. Glacier and palaeolake evolution through the ACR on the eastern Northern Patagonian Icefield.*
1563 *Ice-sheet shading is illustrative only and does not indicate ice thickness. Data from Davies et al. (2018),*
1564 *Thorndycraft et al. (2019a) and Martin et al. (2019).*

1565

1566 5.3.3.4 10 ka

1567 As glaciers continued to recede during the Holocene, the influence of topography became more important
1568 as ice masses 'unzipped' around higher ground. By 10 ka, the Northern Patagonian Icefield had evolved into

a series of separate icefields (Figure 20; Figure 22). Some of these disappear by either 5 ka or the LIA, while others, such as Monte San Lorenzo, remain as small mountain icecaps and glaciers today. Dating of boulders on a valley-side lateral moraine at around 1,115 m asl showed that Nef Glacier was over 600 m thicker than today at 11.4 ka (Glasser et al., 2012). Similarly, Leones, Soler Glacier and Colonia glaciers were all larger than present at that time, but remained restricted compared with their ACR extents (Glasser et al., 2012; Nimick et al., 2016). Large moraines bounding Lago Plomo and Lago Negro yield mean ^{10}Be ages of 11.2 ka (SD 0.1) and 11.4 ka (SD 0.5) respectively (Glasser et al., 2012) (Figure 23), suggesting ice-marginal stabilisation at this time, possibly due to palaeolake drainage and changing calving conditions. By 10 ka, all palaeolakes had likely assumed their current extent (Thorndycraft et al, 2019a) (Figure 22).

One substantial moraine limit (Fachinal moraines; Figure 23) to the north of the Reserve Nacional Lago Jeinemeni icefield is dated by ^{10}Be and ^{36}Cl cosmogenic nuclide exposure-age dating (Douglass et al., 2005). The two sets of moraines superimposed on a delta surface 100 m above the current lake level yielded recalculated ages ranging from 20.3 ± 4.8 to 9.4 ± 2.9 ka on individual boulders for the Outer Fachinal moraines, with a wide scatter, but perhaps indicating a Late Glacial ice position around 14-13 ka. The Inner Fachinal moraines yield generally younger ^{10}Be ages of 11.0 ± 2.4 to 5.8 ± 1.9 ka. We do not calculate a mean age for these moraines due to the wide scatter. Possible deltas at ~400 m asl suggest that the Deseado Level ice-dammed lake may have penetrated deeply into the valley, which suggests that the earlier moraines formed before the formation of the lake, indicating a more retreated glacial position further up-valley. However, the geomorphological context and, specifically, the relationship between these moraines and Palaeolake Deseado is unclear, and combined with the wide scatter, we therefore assign them a lower reliability rating.

The Fachinal moraines represent the only dated ice limits for that icefield, but we assume that the large moraines in the lower valleys surrounding the mountain range are all of a contemporary age. These valley glaciers reached a lower elevation limit of 850 m asl in the south, 615 m asl to the west, 850 m asl to the east, and 350 m asl to the north. Douglass et al. (2005) suggest that the Reserva Nacional Lago Jeinemeni icefield that existed at this time had a palaeo-ELA of 1,120 ± 65 m, ~300m lower than the present-day ELA, which may agree with a Late Glacial interpretation of the moraines.

Figure 23. Geomorphological map showing Jeinemeni Reserve and the Fachinal Moraines, and the moraines around Lago Plomo and Lago Bertrand. Published ages and geomorphology from Glasser et al. (2006, 2008, 2012), Douglass et al. (2005), Bourgois et al. (2016), Davies et al. (2018) and Thorndycraft et al. (2019).

On the west of the Northern Patagonian Icefield, a major advance of Glacier San Rafael is marked by a large arcuate moraine system, the Tempanos Moraine, which dams Laguna San Rafael (Harrison et al., 2012; Heusser, 2003; Lawrence and Lawrence, 1959). The Tempanos I, II and III moraines (Heusser, 2003) average 20 – 30 m in height, and mark the position of Glaciar San Rafael when it advanced westwards beyond the Andean mountain front to form a large piedmont lobe (Glasser et al., 2006b) (Figure 18). OSL dating of sediments incorporated in the Tempanos moraine system indicate that Glaciar San Rafael experienced multiple advances between 9.3 to 9.7 ka, 7.7 ka, and again at 5.7 ka (Harrison et al., 2012).

Morphostratigraphically comparable moraine suites exist at the mouths of the Gualas and San Quintin valleys to the north and south of the Laguna San Rafael respectively. The Gualas basin has remained ice free for at least the last 11.3 ± 3.0 ka (Fernandez et al., 2012), although this age represents an extrapolation of the sediment accumulation rate to the base of the core and is therefore considered less reliable than other ages in our compilation. However, if correct, this age suggests that the terminal moraines around Golfo Elephantes are older than their counterparts at Laguna San Rafael. The authors argue that the age of these moraines lies somewhere between the beginning of sedimentation in the Gualas Basin and the end of the local LGM after approximately 12.6 ka (Turner et al., 2005). This supports the view put forward by other authors (Harrison et al., 2012; Warren, 1993) that past glacier fluctuations along the western edge of the Northern Patagonian Icefield were likely asynchronous, with glaciers oscillating at different times.

Bertrand et al. (2012) argue that Glaciar Gualas was close to its present-day position between 5.4 and 4.1 cal. ka BP, with a readvance to the shore of Golfo Elephantes between 4.0 and 0.75 cal. ka BP. Comparison with independent proxy records of precipitation and sea surface temperature suggests that Glaciar Gualas responded most strongly to precipitation, rather than temperature, change since the mid-Holocene (Bertrand et al., 2012). However, the asynchrony of past glacier fluctuations suggests that calving likely played an important role in past glacier dynamics, possibly overwhelming the climate signal on occasion.

5.3.3.5 5 ka

Across the region, where limits at 5 ka are unknown, we place them broadly at the outer limits of the morphostratigraphically fresh Late Holocene moraines. The reconstructed 5 ka ice extent (Figure 20) is therefore likely to be a minimum. Mid-Holocene (Neoglacial) advances in this region of Patagonia began after 6.8 cal. ka BP, coincident with a strong cooling episode at this time and a tendency to negative SAM-like conditions (Moreno et al., 2018). Neoglacial glacier advances in the San Rafael, Colonia and Leones valleys first occurred around 5.7 ± 0.6 ka to 4.7 ± 0.2 ka (Harrison et al., 2012; Nimick et al., 2016). Around Lago Colonia, trees dated by dendrochronology and radiocarbon dating indicate recession behind this limit

followed by a smaller Late Holocene readvance. At Leones Glacier, the 135 m high terminal moraine damming Lago Leones was dated using a combination of OSL on sands deposited within the moraine and ^{10}Be surface exposure ages on large boulder on its distal side. These data showed that the glacier receded from the eastern edge of the lake by about 2.5 ka BP (Harrison et al., 2008).

The glaciers of Monte San Lorenzo are surrounded by mid-Holocene moraines (Sagredo et al., 2018) (Figure 21). The mid-Holocene (radiocarbon dated to 5.2 ± 0.7 cal. ka BP) limit of Río Lacteo glacier lies *ca* 5 km down valley of the current calving front (Mercer, 1968; Garibotti and Villalba, 2017). To the north of MSL in the Río Tranquilo valley, ^{10}Be cosmogenic nuclide dating gives latero-terminal moraines a mean ^{10}Be age of 5.7 ka (SD 0.1) (Sagredo et al., 2016; 2018). Radiocarbon ages from organic sediments within a moraine complex west of Sierra de Sangra (east of the main Andes) yield a basal age of 4.9 ± 0.8 cal. ka BP (Mercer, 1968; Wenzens, 2005) (Figure 21).

Smaller moraines inset up-valley from the larger moraines on the delta north of the Jeinemeni Icefield (Figure 23) are assumed to be 5 ka in age, although it is possible they relate to the LIA. Further dating control is required here. These moraines suggest that by 5 ka, the Jeinemeni Icefield had fragmented into numerous small valley glaciers. Limits on available chronologies and limited detailed mapping means that we have low confidence in the Reserva Nacional Lago Jeinemeni icefield reconstruction and this is highlighted as a key region for future research, especially distinguishing between the 5 ka and 0.2 ka ice limits.

A thrust moraine near the snout of Soler Glacier preserves woody fragments and *in situ* tree remains with radiocarbon ages of 0.5 to 3.1 cal. ka BP (Glasser et al., 2002). This advance precedes the most recent Late Holocene advance (0.2 ka) by several hundred years, and suggests that prior to this time, Soler Glacier was less extensive than present.

5.3.3.6 Late Holocene (0.5 – 0.2 ka)

In many places, the most recent Late Holocene moraines, typically large and well-defined moraines surrounding ice-scoured bedrock around the edges of the valley glaciers (Davies and Glasser, 2012; Glasser and Jansson, 2008; Glasser et al., 2008, 2011a), reach similar extents to the ice limit at 5 ka (Sagredo et al., 2016; 2018). These moraines are constrained to the last 500 to 200 years by dendrochronology and historical documents on the fresh-looking moraines surrounding these glaciers (Harrison et al., 2007; Nimick et al., 2016; Winchester and Harrison, 2000; Winchester et al., 2001, 2014). Late Holocene moraines of Monte San Lorenzo are additionally constrained by lichenometry (Garibotti and Villalba, 2017). Morphological similarities between these moraines allows extrapolation of the 0.2 ka ice margin across the Northern Patagonian Icefield (Davies and Glasser, 2012; Glasser et al., 2011a). This period of time was associated with

a persistent cold/wet negative SAM interval, which produced conditions favourable for glacier growth (Moreno et al., 2018).

5.4 The Southern Patagonian Icefield (48° – 52°S)

5.4.1 Present-day characteristics

The Southern Patagonian Icefield (Figure 24) is the largest of the present-day Patagonian ice masses at 13,219 km^2 (as of 2011) and reaches elevations of up to 3,400 m (Davies and Glasser, 2012). Ice thicknesses reach 1.5 km for Glaciar San Occidental, and bed elevation is below sea level for 15 – 20 km inland of the ice margin for Jorge Montt and O'Higgins (Gourlet et al., 2016).

The outlet glaciers of the Southern Patagonian Icefield are temperate and are among the fastest-flowing glaciers in the world, reaching velocities of up to 10.3 km/yr (Mouginot and Rignot, 2015). This fast ice flow is caused by the high mass balance gradient (with high accumulation and high ablation; Schaefer et al., 2015) and high basal sliding associated with the temperate climate and high precipitation of the Andes (cf. Aravena and Luckman, 2009; Garreaud et al., 2009). Seasonal velocity variations are also observed in a number of these glaciers (Mouginot and Rignot, 2015). These can be attributed to seasonal ocean thermal forcing modulating ice melt at the calving margin, combined with seasonal variations in subglacial meltwater discharge (Mouginot and Rignot, 2015).

Most of the Southern Patagonian Icefield outlet glaciers are receding (Davies and Glasser, 2012), with some notable exceptions. For example, Glacier Perito Moreno, which drains eastwards into Lago Argentino (Figure 24), is in steady-state equilibrium with climate, and experiences periodic fluctuations due to its unique geometry (Stuefer et al., 2007; Davies and Glasser, 2012). In contrast, HPS-12 has receded 13 km from 1985 to 2017. Overall, between 2000 and 2016, the Southern Patagonian Icefield had a mass loss rate of -11.84 ± 3.3 Gt a^{-1} (Malz et al., 2018). This equates to a specific glacier mass balance of -0.941 ± 0.19 m w.e. a^{-1} for the whole icefield.

Figure 24. A. Glaciers, lakes and rivers of the Southern Patagonian Icefield (48°-52°S), and published chronology (ka) and geomorphology (Ackert et al., 2008; Ashworth et al., 1991; Casassa et al., 1997; Davies and Glasser, 2012; Dowdeswell et al., 2016a; Fogwill and Kubik, 2005; García et al., 2012, 2018; Glasser and Jansson, 2008; Glasser et al., 2011b; Horta et al., 2019; Kaplan et al., 2016; Lastras and Dowdeswell, 2016; Marden and Clapperton, 1995; Masiokas et al., 2008; Mercer, 1965, 1968, 1976; Moreno et al., 2009; Sagredo et al., 2011; Strelin et al., 2014; Wenzens, 1999, 2005, 2006). Mean ^{10}Be ages of moraines are shown in pink crosses. See also Figure 5. B. Scale Map. Red boxes C and D show location of Figure 26. Box E shows location of Figure 28. Isochrones are shown in blue lines with blue labels.

5.4.2 Evidence for glaciation

Similar to the Northern Patagonian Icefield, geomorphological and geochronological evidence for past glaciation for the Southern Patagonian Icefield is concentrated east of the icefield. There are few data points constraining ice extent and patterns of recession for the western margin of the ice sheet in this region, except for limited radiocarbon ages from the isolated Puerto Eden (Ashworth et al., 1991). We assume that, at glacier maxima, the ice extended westwards to the continental shelf edge. This is a situation similar to most northern hemisphere marine-terminating Quaternary ice sheets (e.g. Hughes et al., 2016) and is linked to the rapid increase in iceberg calving as water-depth increases beyond the continental shelf edge, which prohibits further growth. The eastern margin of the Southern Patagonian Icefield consisted of four main ice lobes, which are constrained chrono-stratigraphically by radiocarbon and cosmogenic ages. From north to south these are the O'Higgins/San Martin lobe (Glasser et al., 2011b; Wenzens, 2005), Lago Viedma and Lago Argentino lobes (Ackert et al., 2008; Kaplan et al., 2016; Strelin et al., 2011, 2014; Wenzens, 1999), and, south of Cordon de los Baguales, the Torres del Paine/Río Coyle and del Toro lobes (García et al., 2012, 2018; Moreno et al., 2009) (Figure 24). The Bella Vista/Ultima Esperanza lobe is discussed in the Gran Campo Nevado section. During ice sheet recession, ice-dammed lakes formed in the over-deepenings currently occupied by the present-day lakes (García et al., 2014; Glasser et al., 2011b; Horta et al., 2019; Ponce et al., 2018; Sagredo et al., 2011; Strelin et al., 2011) (Figure 24).

The O'Higgins/San Martín Lobe has five major moraine systems (Glasser et al., 2011b). The LGM position of the O'Higgins/San Martin Lobe is placed at M3 at 34.9 ka (SD 3.1) (Glasser et al., 2011b). The outer M4 moraine contains scattered ages, making this ice limit difficult to date, with ages ranging from 28.0 to 59.3 ka. However, the recent publication of older MIS 3 and early MIS 4 ^{10}Be ages from the Torres del Paine area (Garcia et al., 2018) suggests that this oldest age may be realistic for the M4 moraine. Further work is required to clarify LGM ice extent for this lobe. To the south, the Viedma Lobe contains a complex landsystem of glaciotectonic moraines, glacial lineations and crevasse-squeeze ridges located between the glacier maximum moraines and the present-day lake shoreline; Ponce et al. (2018) suggested that such features reflect palaeosurge activity within the lobe at, or following, the LGM.

The Lago Argentino Lobe is clearly delimited by a number of moraine sequences. Little published work is available for the terminal moraines beyond the eastern margin of the lake. However, extensive work on the Puerto Bandera moraines constrains Late Glacial recession from these outer moraines (Ackert et al., 2008; Strelin and Malagnino, 2000; Strelin et al., 2011). Holocene ice dynamics of the Lago Argentino lobe are well dated on the Herminita Peninsula, around Lago Pearson and around Lago Frías (Kaplan et al., 2016; Strelin et al., 2014).

1731 The Torres del Paine/Río Coyle Lobe is denoted by a series of moraines: the outermost RV 1 moraines, which
1732 wrap around Sierra Contreras as a series of lateral moraines, the RV II moraines inside of these, and finally
1733 the TDP I to IV moraines around Laguna Azul, Lago Sarmiento de Gamboa and Lago del Toro. The RV
1734 Moraines (Caldenius, 1932; García et al., 2014, 2018) include multiple concentric moraine ridges deposited
1735 over some 15 km, and continue around into the del Toro outlet lobe.

1736 Just north of Lago Argentino, Holocene glacier dynamics resulted in a sequence of progressively less-
1737 extensive advances of Glaciar Torre (49.3°S) since the LGM (Reynhout et al., 2019). Glaciar Torre is a smaller,
1738 alpine-style glacier, which may be expected to respond sensitively to climatic changes. These moraines have
1739 mean ^{10}Be exposure ages of 16.7 ka (SD 0.6), 13.3 ka (SD 0.3), 9.7 ka (SD 0.3), 6.9 ka (SD 0.1), 6.2 ka (SD 0.2),
1740 and 530 years (SD 40). The ages suggest a readvance during the ACR, Mid-Holocene and Late Holocene, with
1741 the 0.2 ka advance being only slightly smaller than the Mid-Holocene advance. These Late Holocene
1742 moraines were previously dated with dendrochronology to the most recent Late Holocene advance, yielding
1743 ages of 1640 AD to 1829 AD (Masiokas et al., 2009a). The ^{10}Be chronology proposed by Reynhout et al.
1744 (2019) revises the ages of these moraines from last 200 years to mid-Holocene and suggest that previous
1745 studies have under-estimated the age of moraines in this area.

1746 In the west, tidewater glacier extent during the late Holocene is constrained by moraines mapped in Iceberg
1747 Fjord (48° 43.5'S) around 3 km from the current terminus of Tempano Glacier (Dowdeswell et al., 2016c;
1748 Lastras and Dowdeswell, 2016). Associated with these moraines is also a series of sub-parallel ridges
1749 orientated in the direction of past ice-flow, together with areas of smoother sea floor. The outermost ridge
1750 is *ca* 100 m high and is asymmetrical, with a steeper ice-distal face. The largest moraine is interpreted as
1751 dating from the Late Holocene (last two centuries) (Dowdeswell et al., 2016c) (Figure 24). Cross-fjord
1752 moraines are also noted about 40 km from the terminus of Europa Glacier, where the fjord joins the deeper
1753 Wide Fjord, probably representing a still-stand at a pinning point during regional deglaciation after the LGM
1754 (Figure 9). Three other sedimentary ridges are spaced out in the inner fjord between 15 and 25 km from the
1755 modern ice front, but remain undated.

1756

1757 *5.4.3 Ice sheet reconstruction*

1758 Figure 25 shows our ice sheet reconstruction for the Southern Patagonian Icefield section. García et al.
1759 (2018) record a series of progressively less extensive glacier positions pre-dating the global LGM in Torres del
1760 Paine in the southern parts of the study region, with a LLGM of 47.0 ka recorded at the central part (Río de
1761 las Vizcachas) of the Torres del Paine/Río Coyle Lobe. The RV II Lateral moraine, in the north of the study
1762 region (Figure 28), has a mean ^{10}Be age of 35.1 ka (SD 1.2). We assign the ice margin at 35 ka here with *high*

confidence. Although we recognise maximum extents earlier than 35 ka, the evidence suggests significant recession (~12 km) by 35 to 30 ka.

At 35 and 30 ka the margin also extended to the moraines at the eastern extents of the glacial over-deepenings currently occupied by Lago Viedma and Lago Argentino to the north. Glasser et al. (2011b) argued that the M3 moraine (dated to 34.9 ± 3.1 ka) in the O'Higgins/San Martin valley is most likely to represent the local LGM (Figure 26A). Palaeolake Tar likely formed by this time (Horta et al., 2019). However, prior to 35 ka, the ice extent in this valley may have been greater, though the timing is difficult to ascertain. We use this to guide the *medium confidence* LLGM positions of the Viedma and Argentino Lobes, which have less chronological control but are delineated by (in some places detailed) geomorphological mapping (Wenzens, 1999; Strelin et al., 2011; Ponce et al., 2013, 2018; García et al., 2014). We assume that ice extended westwards to the continental shelf edge at these time-slices.

Figure 25. Reconstruction of the Southern Patagonian Icefield at 5 ka time-slices. Ice dammed lakes are highlighted in orange. Relative sea level data from Guilderson et al. (2000), symbolised using GEBCO topographic and bathymetric data. Shading is illustrative only and does not represent ice thickness.

By 25 ka, the O'Higgins/San Martín Lobe had receded 6 km to the M2 moraine (Figure 26A), and begun to flow around, rather than over, the 1,400 m high landmass at the eastern end of Lago O'Higgins/San Martín. During deglaciation, we assume that the high orographic precipitation would sustain larger glaciers to the west than those ice lobes extending east of the ice divide, but the reconstruction of the western margin should be considered highly speculative. We reconstruct a small Palaeolake Tehuelche at 250 m asl here (cf. Solari et al. 2012), although the col location is uncertain. Palaeolake Tar has formed in front of the O'Higgins/San Martin Lobe (Horta et al., 2019). At 20 ka, the extent of many outlet lobes is uncertain. The Torres del Paine/Río Coyle Lobe is well dated at the TDP I moraines around Lago del Toro to 21.3 ka (SD 1.7) (García et al., 2018). This indicates that in general, the ice lobes had pulled back from the LLGM moraines east of the Southern Patagonian Icefield but continued to occupy their over-deepenings. Palaeolake Tehuelche remains at 250 m asl and occupies a larger extent (cf. Solari et al. 2012). We speculatively place the western ice margin along the present-day coastline of Chile at this time.

1794

1795 *Figure 26. Detailed maps of: (A) the Lago O'Higgins/ Lago San Martin/Lago Tar region. Data from Cassassa et*
1796 *al., 1997; Masiokas et al., 2009; Reynhout et al., 2019; Glasser et al., 2011, Wenzens 2005; 2006; Horta et al.,*
1797 *2019. (B) Herminita Peninsula. Numerous sources for published ages and geomorphology (Glasser and*
1798 *Jansson, 2008; Kaplan et al., 2016; Mercer, 1965; Strelin et al., 2014). Pink crosses are mean exposure ages*
1799 *for the landforms. Altitude and symbology as in Figure 24. Lakes are shown in blue.*

1800

1801 At 15 ka, substantial recession has occurred east of the Southern Patagonian Icefield, damming lakes within
1802 the over-deepenings. We place the O'Higgins/San Martín Lobe margin at the M1 moraines (mean ^{10}Be age
1803 14.7 ka, SD 0.5; cf. Glasser et al., 2011b), a recession of some 23 km from the M2 moraines (Figure 26A). In
1804 Lago Argentino, the 13 ka ice extent is well defined by the Puerto Bandera moraines (Figure 5; Figure 27)
1805 (Strelin et al., 2011). These moraines have been comprehensively dated by cosmogenic nuclide (^{10}Be and
1806 ^{36}Cl) and radiocarbon dating (Ackert et al., 2008; Kaplan et al., 2011), indicating a readvance and ice-marginal
1807 stabilisation during the ACR. Minimum-limiting ^{14}C ages on bogs between the Puerto Bandera moraine crests
1808 yield ages older than 12.5 cal. ka BP (Strelin et al., 2011). Given the ^{14}C chronology, this site was used as the
1809 basis for the production rate calibration used in this study (Kaplan et al., 2011). The Puerto Bandera
1810 moraines indicate an ice extent mid-way up Lago Argentino (Figure 27), damming a proglacial lake of a
1811 similar size to the present-day Lago Argentino at this time. Shorelines at elevations of 200 m asl (Glasser and
1812 Jansson, 2008) suggest the lake was slightly higher than today (165 m asl), and likely continued to drain
1813 eastwards to the Atlantic.

1814

1815 *Figure 27. Detail of ages and chronology for the Puerto Bandera Moraines, Lago Argentino, Southern*
1816 *Patagonian Icefield. Data from Mercer (1965), Wenzens (1999), Ackert et al. (2008), Glasser et al. (2008),*
1817 *Strelin et al. (2014), Kaplan et al. (2016). Pink crosses are mean exposure ages for the landforms. Altitude and*
1818 *symbology as in Figure 24. Lakes are shown in blue.*

1819

1820

1821 In the Torres del Paine region (Río Coyle / Torres del Paine Lobe; Figure 28A), the mean ^{10}Be age of the TDP
1822 II-IV moraines around Lago Azul and Lago Sarmiento de Gamboa indicate ice-margin stabilisation at 14.4 ka
1823 (SD 0.7), with extensive moraines extending southwards bearing similar stratigraphic positions again
1824 suggesting ice margin stabilisation during the ACR (García et al., 2012). This is supported by lateral moraines
1825 north of Lago Nordenskjöld with mean ages of 14.9 ka (SD 1.1) and 15.0 ka (SD 1.1) (Fogwill and Kubik, 2005;
1826 Moreno et al., 2009) (Figure 28). An extensive Palaeolake Tehuelche (Solari et al., 2012) had formed by 15 ka
1827 with lake levels at 125–155 m asl, draining southwards towards the Río Gallegos valley (Figure 28C), and

1828 then eastwards towards the Atlantic through Río Gallegos (Sagredo et al., 2011; García et al., 2014, 2015).
1829 This extended ice-dammed palaeolake was confluent with Palaeolake Puerto Consuelo to the south (García
1830 et al., 2014; Solari et al., 2012) and thus we hereafter refer to the combined Palaeolake Tehuelche-Puerto
1831 Consuelo at the 15 ka time-slice. Our reconstruction differs slightly to the reconstruction by Sagredo et al.
1832 (2011) and García et al. (2014), in that we maintain the larger conjoined proglacial lake draining eastwards at
1833 15 ka (Figure 28C), due to other constraints on the ice margin, without compromising the basal radiocarbon
1834 ages, which are above the 125 m lake level.

1835

1836 *Figure 28. A. Geological data pertaining to glaciation of the Torres del Paine region (Ackert et al., 2008;*
1837 *Fogwill and Kubik, 2005; García et al., 2014; García et al., 2012; Glasser and Jansson, 2008; Kaplan et al.,*
1838 *2016; Kaplan et al., 2007; Moreno et al., 2009; Sagredo et al., 2011; Strelin et al., 2014). B. Palaeolake*
1839 *Tehuelche (250 m altitude; cf. Solari et al., 2012) and Paleolake Puerto Consuelo at 20 ka. C. Palaeolake*
1840 *Tehuelche-Puerto Consuelo is formed by 15 ka, here at 125 m elevation (traced by contour analysis). This*
1841 *reconstructed lake represents the combined extent of both Palaeolake Tehuelche in the Torres del Paine area*
1842 *and Palaeolake Puerto Consuelo in the Río Prat area. D. Palaeolake Tehuelche-Puerto Consuelo and ice-sheet*
1843 *extent at 13 ka (during the ACR). Symbology, bathymetry and altitude as in Figure 24. Ice-sheet shading is*
1844 *illustrative only and does not represent ice thickness. E. Map extent*

1845

1846

1847 To the west of the Southern Patagonian Icefield, we hypothesise that an independent ice cap may have been
1848 supported on Isla Wellington at this time, with moraines dated by radiocarbon dating to 13.4 ± 0.4 cal. ka BP
1849 at Puerto Eden suggesting glaciers flowing east from Isla Wellington towards the Southern Patagonian
1850 Icefield (Ashworth et al., 1991).

1851 By 10 ka, the ice sheet was near to its present-day configuration in most areas. We assign a *low confidence*
1852 to ice-margin uncertainty due to the lack of published ages. One location where there are dates at this time
1853 is at the Lago Argentino lobe, where there are several radiocarbon ages at Lago Pearson, on the Herminita
1854 Peninsula (Figure 5; Figure 26B) and at the head of Lago Frias. These ^{14}C ages indicate that recession took
1855 place between 13 and 10 ka, after the ACR, and significantly reduced ice extent through the earliest
1856 Holocene; ice extent at 10 ka was likely limited to the upper valleys (Kaplan et al., 2016; Strelin et al., 2011,
1857 2014; Wenzens, 1999). Elsewhere, a lack of clear moraines at this time means we have *medium confidence* in
1858 this ice margin. It is likely that enlarged ice-dammed lakes persisted at the O'Higgins/San Martín Lobe and
1859 Viedma Lobe at this time-slice, but palaeolakes Argentino and Teheulche-Puerto Consuelo had drained
1860 (García et al., 2014). We suggest a separation of the Southern Patagonian Icefield from the Northern
1861 Patagonian Icefield had occurred between 12.6 and 11.7 ka (Thorndycraft et al, 2019a), based on the lake
1862 drainage through Río Baker south of the Northern Patagonian Icefield by this time (see Northern Patagonian

Icefield section), but note that there are few data constraining glacier recession in this region and especially on the timing of this separation.

There are no data available to constrain Southern Patagonian Icefield extent to the west of the Andes at 10 ka. We assume glacier advances in the fjords given that lobes to the east continue to extend at least partway into their over-deepenings.

Our ice sheet reconstruction is relatively unchanged from 5 ka to the LIA, with little evidence of ice extent beyond the 0.5 - 0.2 ka limits. Where there is evidence, such as at the head of Lago Argentino, it suggests that the 5 ka margin was slightly larger than the ice extent during the 0.2 ka maximum (Kaplan et al., 2016; Strelin et al., 2014) (Figure 5).

The series of inset moraines around Laguna Torres record a mid-Holocene stabilisation of Glacier Torres (mean ^{10}Be ages of 6.9 ka (SD 0.1), 6.2 ka (SD 0.2), and 4.5 ka (SD 0.1)) (Reynhout et al., 2019) (Figure 26A). These moraines (M4 and M4b) are close to the younger Late Holocene moraines, dated to 0.53 ka (SD 0.04) by ^{10}Be exposure ages.

Around the head of Lago Argentino, mid Holocene and late Holocene moraines are well dated by ^{10}Be exposure and ^{14}C ages on ice-marginal landforms mainly in three valleys (Strelin et al. 2014; Kaplan et al., 2016) (Figure 26B); these moraines suggest an ice margin stabilised here repeatedly during the interval from ~6 to 1 and 0.6 to 0.3 ka (Kaplan et al., 2016; Strelin et al., 2014). The ^{10}Be and ^{14}C chronologies in at least three different sectors of the Lago Argentino (Figure 26B) basin show mid-Holocene limits were more extensive than the limits of the most recent Holocene advance at ~0.6 to 0.2 ka. As the ages here are mainly derived from ^{10}Be dating on a number of different moraines, as well as supporting ^{14}C data, we do not calculate mean moraine ages here. In the absence of other data, we use these inferences from this site to predict ice-sheet extent at 5 ka at moraines down-valley of the most recent Late Holocene limits in adjacent valleys (and therefore assign a *medium confidence* classification).

The Late Holocene extent of Glaciar O'Higgins is well constrained with maps based on aerial photographs dating from 1896 AD (Casassa et al., 1997). The extent of Lago Viedma over the last 200 years is well-constrained by dendrochronological dating of moraines (Masiokas et al., 2009b). At the northern section of the Southern Patagonian Icefield, historical photographs date extent and subsequent recession of Glaciar Jorge Montt over the last few hundred years (Rivera et al., 2012a; 2012b).

5.5 Gran Campo Nevado (52° – 53°S)

5.5.1 Present day characteristics

Gran Campo Nevado is an ice cap covering 237 km^2 on the Península Muñoz Gamero, 200 km south of the Southern Patagonian Icefield (Davies and Glasser, 2012) (Figure 29A). It has steep outlet glaciers that are currently receding quickly (Schneider et al., 2007), and due to the ice cap's small size and fast response time the glaciers are possibly responding faster to climate change than those of the Southern Patagonian Icefield or Northern Patagonian Icefield (Möller et al., 2007). The mountain range here reaches only 1,000 – 1,700 m high, with the glaciers being sustained by the high volumes of precipitation and cooler mean annual air temperatures (Möller and Schneider, 2008). The glaciers terminate in tidal fjords or in proglacial lakes, with a few land-terminating glaciers.

5.5.2 Evidence for glaciation

The glacial geomorphology suggests that, at maxima, Gran Campo Nevado ice coalesced with the Southern Patagonian and Cordillera Darwin Icefields to form the southern extent of the PIS (Clapperton, 1993). Multiple ice lobes extended eastwards, including the Última Esperanza /Bella Vista—Río Gallegos Lobe (henceforth UE/BV Lobe), Skyring and Otway lobes (Figure 29). The Magellan and Bahía Inutíl lobes are covered in the Cordillera Darwin section.

A series of moraines in the region east of the UE/BV Lobe document extensive Early and Middle Pleistocene glaciations, with interacting glacial, fluvial, volcanic and aeolian systems (Ercolano et al., 2016). The most recent glacial maximum east of the Andes resulted in the formation of a landsystem comprising sedimentary drumlins, moraines and marginal meltwater channels (Benn and Clapperton, 2000; Clapperton et al., 1995; Darvill et al., 2017; Ercolano et al., 2016; Ercolano et al., 2004; Glasser and Jansson, 2008; Lovell et al., 2011; Meglioli, 1992; Sagredo et al., 2011) (Figure 29). Ice-dammed lakes formed in glacial over-deepenings to the east of the ice sheet during recession, as drainage to the Pacific was blocked by the remaining ice mass (Kilian et al., 2007b, 2013a; Lovell et al., 2012; Sagredo et al., 2011; Stern, 2011). Glaciolacustrine terraces at 25 – 30 m around the eastern shores of Seno Otway are well constrained to around 14 cal. ka BP (Kilian et al., 2013b).

Retreat is constrained by minimum radiocarbon ages from marine and terrestrial sediment cores east of the ice sheet, mostly from the modern Seno Skyring (Breuer et al., 2013; Kilian et al., 2003, 2007a, 2013b, 2013c). Some of these sediment cores also contain well-dated tephra horizons from the Burney (MB1 and MB2) and Reclus (R1) eruptions (Breuer et al., 2013; Kilian et al., 2003, 2013b). In addition, sediment cores to the west of Gran Campo Nevado at Bahía Beaufort constrain recession through the western fjords (Kilian et

al., 2007a). Ice is assumed to have reached the continental margin in the west at the LGM, but the timing remains ambiguous.

Figure 29. Map showing published ages and geomorphology associated with Gran Campo Nevado (52° - 53°S) (data from Breuer et al., 2013; Clapperton et al., 1995; Darvill et al., 2015b; Darvill et al., 2017; Evenson et al., 2009; Fernandez et al., 2017; Kaplan et al., 2007; Kaplan et al., 2008; Kilian et al., 2003, 2007a, 2013b, 2013c; Koch and Kilian, 2005; McCulloch et al., 2005a; McCulloch et al., 2005b; Porter et al., 1992; Stern, 1992) and location of glaciers and lakes of Gran Campo Nevado.

5.5.3 Ice sheet reconstruction

Our reconstruction for the Gran Campo Nevado area is shown in Figure 30. At 35 and 30 ka, we place the ice margin towards the outer limits of the glacial over-deepenings. We are confident with the glacial geomorphology based on in-depth published mapping (Darvill et al., 2014; Lovell et al., 2011). The outermost limit of the UE/BV Lobe is well dated by ^{10}Be exposure ages on the Rio Turbio RT latero-terminal moraines (García et al., 2018), with a mean age of 47.1 ka (SD 1.8). Inboard of this, the Aracuco AR Moraine has a mean ^{10}Be age of 32.4 ka (SD 1.2). In Sierra Dorotea to the north, the Aracuco AR Moraine has a mean ^{10}Be age of 33.0 ka (SD 2.8). We therefore place the 35 and 30 ka ice limits with *high confidence* at these moraines.

We give the margins of the Skyring and Otway lobes *Medium confidence* at 35 ka, as the well-constrained Magellan and UE/BV lobes determine the ice-lobe configuration here (Darvill et al., 2017; Kaplan et al., 2007, 2008; McCulloch et al., 2005b), but there are few independent limiting ages for these outlets.

By 25 ka, ice receded into the over-deepenings. Palaeolake Blanca, defined by raised shorelines around the present-day Laguna Blanca, was dammed in front of Skyring Lobe, initially draining northwards through a col at 190 m (Darvill et al., 2017; Lovell et al., 2012). Subsequently the lake drained through a col 188 m asl as the Skyring and Otway lobes receded, resulting in a drainage switch to the east and into the Strait of Magellan (Figure 30). However, the timing of lake level fall is poorly constrained, as is the location of the ice margin; it is likely that the ice margin retreated back beyond the lower 188 m asl col by 20 ka, given that outwash sediments show drainage passed in front of the well-constrained Magellan lobe (Darvill et al., 2017; Kaplan et al., 2007; Kaplan et al., 2008; Lovell et al., 2012; McCulloch et al., 2005b).

By 20 ka, the UE/BV Lobe had receded to prominent moraines and located east of Lago Balmaceda (Figure 29), constrained by a small number of minimum radiocarbon ages (Sagredo et al., 2011). Palaeolake Puerto Consuelo started to form in front of this ice margin, draining east through a col at 155 m (Sagredo et al., 2011). Palaeolake Blanca likely drained through the 188 m asl col by 20 ka, and may even have drained

completely (Lovell et al., 2012). There are also minimum tephra and radiocarbon ages in Seno Skyring and Seno Otway, indicating that ice filled these basins at this time (Kilian et al., 2007b). However, it is unclear at what point the Skyring and Otway lobes retreated and began forming their respective palaeolakes.

Palaeolake Puerto Consuelo in front of the UE/BV lobe merged with Palaeolake Teheulche to the north to form Palaeolake Tehuelche-Puerto Conseulo by 15 ka. The combined palaeolake initially drained east through a col at 155 m asl (Sagredo et al. 2011) (Figure 28), but later drained completely, either southward into Palaeolake Skyring and/or westward into the Pacific between the shrinking independent ice masses. Eventually, Palaeolake Puerto Consuelo became the modern marine fjord, but it is unclear whether the lake level had dropped to sea level by 15 ka (Sagredo et al. 2011). The Skyring and Otway lobes had retreated from the Seno Skyring and Seno Otway over-deepenings (Figure 29; Figure 30), forming new palaeolakes (Palaeolake Skyring and Palaeolake Otway), constrained by shorelines at 15 m asl and the positions of the respective ice margins (Clapperton et al., 1995; Kilian et al., 2013b; Lovell et al., 2011, 2012).

The development and growth of these palaeolakes suggests that substantial retreat of ice had occurred, supported by ages from glacial landforms around the UE/BV lobe and minimum radiocarbon ages and tephra horizons in sediment cores from the modern Seno Skyring and Seno Otway (Breuer et al., 2013; Kilian et al., 2003, 2007b, 2013b, 2013c; Sagredo et al., 2011). However, differing reconstructions for this time lead us to assign low confidence ice margins, particularly as the precise extent of ice is unclear. It is likely that the Gran Campo Nevado, Cordillera Darwin and Southern Patagonian Icefield ice masses had begun to separate around 15 ka, leaving an independent ice cap over Gran Campo Nevado. However, ice must have been much larger than at present to dam the Straits of Magellan and create the palaeolakes. The glaciolacustrine shorelines indicate that the lakes were extensive.

There are few geomorphological or chronological constraints for the Gran Campo Nevado ice mass at 10 ka or 5 ka, with a few scattered ages suggesting rapid recession but yielding inconclusive results. Palaeolake Tehuelche-Puerto Consuelo had likely drained by 10.3 ka (Sagredo et al. 2011; Stern, 2011). We ascribe stepwise retreat of ice between 15 ka and present day in a pattern based on limits further north, and which agrees with similar reconstructions, but give these limits low confidence. The 0.2 ka maximum limit is dated using dendrochronology on some moraines, and relatively clear geomorphology (moraines, trimlines) assumed to be related to the Late Holocene advance has been mapped around the present icefield (Davies and Glasser, 2012; Koch and Kilian, 2005). It is not possible to determine whether ice at 10 ka or 5 ka was more or less extensive than at 0.2 ka or present day.

Figure 30. Palaeo ice sheet reconstruction for the Gran Campo Nevado region. Yellow stars show location of col spillways for ice-dammed lakes (shown in pink). Relative sea level data from Guilderson et al. (2000),

symbolised using GEBCO topographic and bathymetric data. Ice-sheet shading is illustrative only and does not represent ice thickness.

5.6 Cordillera Darwin (53° – 56°S)

5.6.1 Present day characteristics

The 2,300 km^2 Cordillera Darwin Icefield, at the southern tip of the Andean Mountain range, is the third largest ice mass in present-day South America (Bown et al., 2014) (Figure 31). The icefield receives relatively uniform precipitation throughout the year (up to 5,000 mm a^{-1}) due to its position in the core of the modern SWW system (Garreaud et al., 2013). Mountain peaks in Cordillera Darwin exceed 2,000 m asl, and the icefield is drained by a mixture of tidewater glaciers calving into fjords and land-terminating glaciers, some of which are now retreating with expanding proglacial lakes (Holmlund and Fuenzalida, 1995) (Izagirre et al., 2018). Meier et al. (2018) identified area change of Patagonia glaciers from 1870 – 2016 with a ~16% area loss of Cordillera Darwin Icefield, with more than half of the loss occurring since 1985. They also noted that Cordillera Darwin Icefield glaciers were retreating fastest between 1986 and 2005; afterwards the rate of retreat has decreased. The retreat has been largest on tidewater glaciers such as Marinelli Glacier and Ventisquero Grande Glacier.

Figure 31. Location of published ages, geomorphology, glaciers and lakes in Cordillera Darwin, southernmost Patagonia (53° - 56°S) (Boyd et al., 2008; Breuer et al., 2013; Clapperton et al., 1995; Coronato et al., 2009; Darvill et al., 2015b; Darvill et al., 2017; Davies and Glasser, 2012; Evenson et al., 2009; Glasser and Jansson, 2008; Gordillo et al., 1992; Hall et al., 2013, 2019; Heusser, 1989, 1998; Izagirre et al., 2018; Kaplan et al., 2007; Kaplan et al., 2008; Kilian et al., 2013b; Kilian et al., 2007a; Kilian et al., 2003; Kuylenstierna et al., 1996; McCulloch and Bentley, 1998; McCulloch et al., 2005a; McCulloch et al., 2005b; Menounos et al., 2013; Porter, 1990; Porter et al., 1992; Rabassa et al., 2000; Roig et al., 1996; Stern, 1992).

5.6.2 Evidence for glaciation

Here, we focus on the Magellan, Bahía Inutíl–San Sebastián, Fagnano and Beagle Channel lobes, sourced from the Cordillera Darwin area. During the most recent glacial maximum, an enlarged icefield coalesced with the Gran Campo Nevado Icefield ice to the north, forming the southernmost extent of the PIS (Clapperton, 1993). Multiple ice lobes extended from the former ice sheet across Isla Grande de Tierra del Fuego, leaving well-preserved glacial geomorphology (Bentley et al., 2005; Bujalesky et al., 2001; Clapperton et al., 1995; Coronato et al., 2009; Darvill et al., 2014; Fernández et al., 2017; Glasser and Jansson, 2008; Izagirre et al., 2018; Kuylenstierna et al., 1996; Lozano et al., 2018; Strelin et al., 2008) that has been investigated in numerous studies (e.g. Coronato et al., 2004; McCulloch et al., 2005a, 2005b; Meglioli, 1992; Rabassa, 2008; Rabassa et al., 2000).

2025 The prominent Magellan and Bahía Inútil–San Sebastián ice lobes advanced north and then eastward along
2026 the present-day Strait of Magellan, dissected by Isla Dawson. In the southern Central Strait of Magellan and in
2027 Bahia Inútil (Figure 31), multibeam data show glacial lineations, and iceberg ploughmarks in the channel floor
2028 (Fernández et al., 2017). Seismic facies show high angle or sinuous reflectors, interpreted as ice proximal or
2029 subglacial sediments, and parallel reflectors with no internal complex geometries, interpreted as pelagic or
2030 distal glaciomarine sediments (*ibid*.). These data indicate that grounded ice occupied Seno Almirantazgo,
2031 Whiteside Channel and Bahía Inútil during the last glacial cycle. Evidence for a glacial readvance during the
2032 ACR is equivocal here.

2033 The Fagnano and Beagle Channel lobes also extended to the east and southeast, and ice is assumed to have
2034 reached the continental margin to the south and west, although the extent and timing remain ambiguous.
2035 During retreat, residual ice masses in the Cordillera Darwin range blocked drainage into the Pacific, creating
2036 large proglacial lakes that occupied the present-day Strait of Magellan and Bahía Inútil (McCulloch et al.,
2037 2005a; Porter et al., 1992). Lower relative sea levels at this time expanded the Argentinian continental shelf,
2038 damming the lakes to the east (Peltier and Drummond, 2002). The timing of Quaternary ice activity in the
2039 region has been described using a range of dating techniques (for recent summaries, see Darvill et al., 2017;
2040 Hall et al., 2017).

2041 Evidence for former palaeolake high-stands includes a widespread terrace (18 – 25 m asl) on the Atlantic sector
2042 of the Straits of Magellan (De Muro et al., 2017, 2018). This terrace documents a transition from glacio-fluvial-
2043 lacustrine conditions to littoral-marine environments. Three lower terraces (at 6 – 11 m asl, 3 – 5 m asl, and 1
2044 – 2 m asl respectively) consist of sedimentary sequences of coastal marine origin, documenting sea level fall
2045 during the Holocene (De Muro et al., 2018).

2046 Extensive radiocarbon ages from Fiordo Marinelli and Fiordo Brooks (Figure 32) provide evidence for ice
2047 dynamics following the onset of deglaciation (Hall et al., 2013, 2019). These ages show that after the LLGM,
2048 ice remained extensive near LGM positions until after 18.4 cal. ka BP (Kaplan et al., 2011; Darvill et al., 2017).
2049 Glacier ice then rapidly receded to Bahía Ainsworth and the mouth of Fiordo Brooks by 17.1 cal. ka BP (Hall et
2050 al., 2019). This indicates substantial deglaciation from 18.4 – 17.1 cal. ka BP during Heinrich Stadial 1 (Hall et
2051 al., 2013, 2019). By 15.8 cal. ka BP, the terminus of the glacier in Fiordo Marinelli was 3 km beyond Narrows
2052 Moraine (Figure 32). Holocene glacier dynamics are then well constrained here with a series of radiocarbon
2053 ages from the valley sides (Hall et al., 2019; Figure 32).

2054

2055 *Figure 32. Detail of radiocarbon ages and geomorphology from Fiordo Marinelli and Fiordo Brookes, northern*
2056 *Cordillera Darwin Icefield. Data from Boyd et al. (2008), Hall et al. (2013, 2019), Izagirre et al. (2018).*
2057 *Symbology as in Figure 31. Background image is ESRI Basemap World Imagery.*

5.6.3 Ice sheet reconstruction

Our reconstruction for the Cordillera Darwin area is shown in Figure 33. We are confident in the lateral margins of the Bahía Inútil–San Sebastián Lobe at 35 to 30 ka given clearly-defined moraine limits (Darvill et al., 2014) and recent cosmogenic dating of outwash gravels on the northern margin (Darvill et al., 2015b), but the full extent of ice off-present-shore remains unclear (Coronato et al., 2004; Rabassa, 2008). We are also relatively confident that, stratigraphically, the Magellan Lobe extended beyond Peninsula Juan Mazia (based on previous dating and reconstructions; see Darvill et al., 2017). However, we note that these recent studies are at significant odds with previous work suggesting that outer glacial limits were deposited prior to the last glacial cycle (Bujalesky et al., 2001; Coronato et al., 2004; Evenson et al., 2009; Kaplan et al., 2007; Rabassa, 2008). Cosmogenic ^{10}Be, ^{26}Al and ^{36}Cl nuclide exposure dating of erratic boulders from pre-LGM moraines of the Magellan and Bahía Inútil–San Sebastián lobes has yielded ages substantially younger than expected (Evenson et al., 2009; Kaplan et al., 2007). The effect is most apparent for drifts on the southern margin of the Bahía Inútil–San Sebastián lobe, where the broad range in ages (although most <50 ka) has been attributed to post-depositional exhumation and intense erosion of the boulders (Darvill et al., 2015a; Evenson et al., 2009; García et al., 2018; Kaplan et al., 2007). ^{26}Al /^{10}Be depth profiles through outwash sediments linked to the northern margin of the Bahía Inútil–San Sebastián lobe show that this ice lobe was extensive at ~30.1 ka and possibly also earlier, at ~45.6 ka (Darvill et al., 2015b).

For the Magellan Lobe, ^{10}Be and ^{26}Al exposure ages from erratic boulders at Primera Angostura show that ice was also still extensive at around this time (27.7 ka (SD 1.0) and 25.1 ka (SD 0.9); Kaplan et al., 2008), consistent with more recent exposure dating showing ice was extensive as early as ~60–70 ka (Peltier et al., 2016) (Figure 29). Given the emerging pattern of expansive pre-MIS 2 ice from here and further north in Patagonia (as well as elsewhere in the southern mid-latitudes; Darvill et al., 2016), we opt for extensive limits at 35 ka and 30 ka in this study. The extent and timing of the Fagnano and Beagle lobes, as well as the southern and western ice sheet margins bordering the Pacific coast remain uncertain for 35–10 ka.

At 25 ka, we place limits between those at 30 ka and 20 ka. ^{10}Be exposure ages on the outer lateral moraines show that the Magellan Lobe was likely back at Península Juan Mazía by ~27.4–29.9 ka, suggesting significant retreat occurred shortly after 30 ka (Kaplan et al., 2008; McCulloch et al., 2005b). Exposure ages with a mean age of 25.1 ka (SD 0.9) from the recessional moraines of the Magellan Lobe constrain ice extent at 25 ka (Kaplan et al., 2007). However, we also note that there is geomorphological evidence of readvance at this time and cannot be sure that the 25 ka limits were not less extensive than we portray here.

The extent of the Fagnano and Beagle lobes at 25 ka is unclear but we assume they remained relatively extensive, in a similar manner to the larger ice lobes to the north (Bujalesky et al., 1997; Coronato et al., 2009).

Seismic and sedimentary data from the Fagnano basin suggest post-LGM retreat of ice was punctuated by numerous still-stands or re-advances into a lake level higher than the present Lago Fagnano (Waldmann et al., 2010). Final retreat of the Fagnano Lobe into the Cordillera Darwin range allowed drainage into the Almirantazgo Fjord and Strait of Magellan and lowering of the lake level to present (Waldmann et al., 2010). It is assumed that a palaeolake must have formed in front of the retreating Magellan Lobe, blocked by the Primera Angostura moraine limit (Clapperton et al., 1995; McCulloch et al., 2005b), although the time at which it formed, and its extent are uncertain. Similar palaeo-lakes may not yet have formed in front of the other ice lobes given that drainage was still possible towards the Atlantic and the Bahía Inútil–San Sebastián Lobe had not yet retreated into its over-deepening (Porter et al., 1992).

Ice extent is relatively well-constrained at 20 ka. The major ice lobes skirted their respective over-deepened basins (Darvill et al., 2017) and geomorphological evidence suggests that the Magellan and Bahía Inútil–San Sebastián ice lobes might have re-advanced to these positions (Benn and Clapperton, 2000; Bentley et al., 2005; Clapperton et al., 1995; Darvill et al., 2017; McCulloch et al., 2005b). These lobes may have displayed surge-like behaviour, with an assemblage of thrust moraines and highly elongate streamlined glacial lineations suggesting rapid ice flow, combined with an asymmetry in lobate marginal positions (Darvill et al., 2017; Lovell et al., 2012). ^{10}Be exposure ages demonstrate that the Magellan Lobe reached this limit by ~18.3 – 23.2 ka (Kaplan et al., 2008; McCulloch et al., 2005b) and cosmogenic exposure ages from prominent trains of erratic boulders on the southern side of the Bahía Inútil–San Sebastián lobe generally cluster around 17.6 – 24.9 ka (Darvill et al., 2015a, 2015b; Evenson et al., 2009; Kaplan et al., 2007, 2008; McCulloch et al., 2005b). The extent of the Magallen Lobe at 20 ka is thus constrained by ^{10}Be exposure ages on moraines near the margin of the current fjord on Peninsula Juan Mazía, with mean moraine ages of 19.6 ka (SD 0.1) and 19.9 ka (SD 1.9) (Kaplan et al., 2008). As in the north, an ice margin stabilisation at ~19 ka is apparent, followed by rapid deglaciation after that time. We reconstruct a small Palaeolake Magellan in front of the Magellan Lobe at 20 ka, with a drainage col at 10 m above present-day sea level.

Several lines of evidence now suggest rapid retreat of ice occurred well before 15 ka around Cordillera Darwin (Hall et al., 2017, 2019). In early studies, numerous minimum radiocarbon ages suggest that ice retreat had begun by at least 14–15 ka, if not well before (Anderson and Archer, 1999; Clapperton et al., 1995; McCulloch and Bentley, 1998; McCulloch et al., 2005b; Porter et al., 1992). Radiocarbon ages as old as 16.8 ka from peat bogs close to the centre of Cordillera Darwin imply large-scale, rapid retreat of the Magellan and Bahía Inútil—San Sebastián lobes from LGM positions, perhaps to within a few kilometres of present ice extent (Hall et al., 2013). These ages are supported by minimum radiocarbon ages of up to ~15.7 cal. ka BP in marine sediment cores from Fiordo Almirantazgo, offshore of Bahía Ainsworth (Bertrand et al., 2017; Boyd et al., 2008), as well as marine geological evidence (Fernandez et al., 2017). Such rapid recession may have been driven or

exacerbated by broad, decoupled termini calving into a large combined Palaeolake Magellan–Bahía Inútil (Boyd et al., 2008; Darvill et al., 2017; Porter et al., 1992). The lake could have existed for hundreds or even thousands of years between 20 ka and 15 ka, and the presence of the well-dated Reclús tephra within lake sediments on the northern shore of Bahía Inútil implies that drainage may not have been before ~14.3 ka (McCulloch et al., 2005b). However, this would have required key drainage routes within Cordillera Darwin to have remained blocked despite extensive deglaciation (Hall et al., 2013, 2017; Mansilla et al., 2016), and is at odds with marine conditions in Seno Almirantazgo, radiocarbon dated to ~15.5 cal. ka BP (Boyd et al., 2008; Fernández et al., 2017). The precise timing and extent of the deglacial Palaeolake Magellan–Bahía Inútil requires further examination and we do not include the lake in our 20 ka or 15 ka time-slices. However, a large glacial lake existed at some point between 20 and 15 ka, and we indicate this on our reconstruction (Figure 33). Lastly, further south, along the eastern Beagle Channel, ^{10}Be exposure ages with a mean of 13.5 ka (SD 1.3) and 14.3 ka (SD 0.2) indicate cirque glaciation during the ACR interval (Menounos et al., 2013).

Radiocarbon ages from Fiordo Marinelli indicate that ice from the Cordillera Darwin Icefield was 3 km outboard of Narrows Moraine (Figure 32) at 15.7 cal. ka BP (Hall et al. 2019). There is no evidence of a strong advance during the ACR at this location; ice here terminated inside of this site at 13 ka, most likely at Narrows Moraine. Ice extent during the Early Holocene was similar to, or smaller than present.

Figure 33. Reconstruction of ice in Cordillera Darwin. Ice-dammed palaeolakes are shown in pink. Relative sea level data from Guilderson et al. (2000), symbolised using GEBCO topographic and bathymetric data. Shading is illustrative only and does not represent ice thickness.

The precise extent of Cordillera Darwin ice at 10 ka and 5 ka is well constrained in Fiordo Marinelli, which suggests that ice was near to the present-day configuration (Bertrand et al., 2017; Fernandez et al., 2011; Hall et al. 2013, 2019). Basal peat from Isla Dawson suggests that Palaeolake Magellan-Bahía Inútil had drained west into the Pacific by ~11.8 cal. ka BP (McCulloch et al., 2005b), as ice dams breached during retreat. Sea-level rise during this time would also have formed an island and fjord system similar to present. Many outlet glaciers of the Cordillera Darwin Icefield would have calved and retreated into fjords. Minimum radiocarbon ages from Bahia Ainsworth show that Ensenada Pigafetta was likely ice-free by ~8.0 cal. ka BP (Boyd et al., 2008), demonstrating the reduced nature of the icefield. Marine sediments also suggest a possible readvance of outlet glaciers at 7.3 – 5.7 cal. ka BP, but not to extents greater than at 10 ka (Boyd et al., 2008). Hence we can be confident that glaciers were restricted, and not dissimilar to most recent Late Holocene (0.5 – 0.2 ka) positions just beyond present day extents.

New data from Fiordo Marinelli indicates that during the Holocene there were several periods when ice extent was less than that of 1984 AD. A readvance into the fjord was dated to 6.5 – 5.6 cal. ka BP, with ice reaching nearly to Narrows Moraine. Ice extent from 5.4 – 4.7 cal. ka BP was similar to present, or smaller. There was a late Holocene expansion at 3.8 cal. ka BP (Hall et al., 2019). Another glacier expansion is dated to 2.4 – 1.7 cal. ka BP.

We are relatively confident about ice extent during the Late Holocene given clear geomorphology related to this time period (Davies and Glasser, 2012). Prominent moraines, some of which were captured in historical records (e.g. de Agostini, 1956; de Gasperi, 1922; Izagirre et al., 2018), demonstrate that glaciers were more extensive than present in the last two centuries (Fernandez et al., 2011; Izagirre et al., 2018). Dendrochronology suggests Glaciar Marinelli, a large outlet to the north of the Cordillera Darwin range, advanced to leave a prominent moraine during the last two millennia (Hall et al., 2019) and 0.5 – 0.2 ka (Porter and Santana, 2003), supported by data from marine cores (Boyd et al., 2008). Other geomorphologically and stratigraphically similar moraines around the present icefield are assumed to be correlatives, and formed during the last millennium.

6 Synthesis

6.1 Patagonian Ice Sheet reconstruction at the LGM (PATICE)

Our new PATICE reconstruction demonstrates, for the first time, Patagonian Ice Sheet changes from 35 ka to the present day (Figure 34). The original empirical reconstruction is provided with a level of confidence for each time slice (*high, medium* and *low confidence*) and we include the extent and height of ice-dammed lakes. Our reconstruction of maximum ice extent provides a systematic revision of LLGM ice sheet extent that—like previously published reconstructions—still has similarities with the work of early researchers (e.g. Caldenius, 1932; Mercer, 1968, 1976; Coronato and Rabassa, 2011; Harrison and Glasser, 2011) (Figure 35). Changes are particularly prominent for several of the eastern outlet lobes, following recent chronostratigraphic work in these areas. Detailed geomorphological data, and the topographic control of glacier ice-flow patterns, allow us to reconstruct icefield separation and the dynamics of ice through time. Our compilation highlights areas where further work is needed and allows a detailed assessment of regional trends in ice-sheet response to climatic forcing and the role of palaeolakes in recession dynamics.

Figure 34. Patagonian Ice Sheet reconstruction at 5 ka time-slices from 35 ka to present day, with additional time-slices through periods of ice advance during the ACR (13 ka) and Late Holocene (0.2 ka). Ice-dammed lakes are highlighted in orange. Yellow stars indicate location of drainage cols. Sea level reconstruction is

from geological data in Guilderson et al. (2000), symbolised using the GEBCO marine bathymetry dataset. Ice-sheet shading is illustrative only and does not represent ice thickness.

The Patagonian Ice Sheet covered 492.6 × 10^3 km^2 at 35 ka. We derive an estimate of ice volume of 548.1 × 10^3 Gt (597.5 × 10^3 km^3) at 30 ka, which equates to a sea level equivalent of ~1.5 m. The ice sheet was 350 km wide and 2090 km long and was most probably grounded on the Pacific continental shelf edge. Our new 35 ka reconstruction indicates an ice sheet that is larger than previous reconstructions. Coronato and Rabassa (2011) estimated an ice-covered area of 431.0 × 10^3 km^2 in our study region. Excluding outlying ice masses, our 35 ka reconstruction covers 491.9 × 10^3 km^2, indicating that the new reconstruction is 60,960 km^2, or 12%, larger than previous attempts. The differences are greatest in southern Patagonia, where recent research indicates more extensive ice lobes than were previously documented.

Early reconstructions using numerical ice-sheet modelling predict a slightly smaller reconstruction. Hulton et al. (2002) applied a numerical model to South America for the LGM period. In their modelled reconstruction, disparate ice masses along the Andes joined up to form a continuous mass of ice from 38°S to the southern tip of South America. Fast-flowing ice zones were constrained at their margins by active calving. The modelled change in ice volume from the LGM to present-day was ~500 × 10^3 km^3 of ice, equivalent to a sea-level change of ~1.2 m (Hulton et al., 2002). Hubbard et al. (2005) used a time-dependent model to investigate the PIS between 45° and 48°S during the LGM. These modelling experiments suggested that to reach the LGM moraines bounding Lago GCBA, a lowering of the ELA by ~900 m is required. These modelled experiments suggested that the PIS was highly dynamic, with mean ice thicknesses of 1130 m drained by large ice streams to the western margin and fast-flowing outlet lobes to the east. This model, forced with the Antarctic ice core record of past climate, also recognised a stabilisation during the Antarctic Cold Reversal and rapid collapse after that time, shrinking to near its present-day margins by 11 ka.

We use our geomorphological database (including bathymetric troughs, over-deepened lakes and basins, glacial lineations in both rock [roche moutonnées, whalebacks] and sediment [large streamlined drumlins, smaller flutes in upland regions], fjords, trimlines, parabolic valleys and orientation), topographic data, and the pattern of recession revealed by moraines to determine palaeo ice-flow lines (Figure 35). The LLGM PIS was drained by fast flowing outlet lobes that flowed orthogonally from a north-south ice divide extending the length of the Patagonian Andean mountain chain (although this has low confidence in the absence of ice thickness data). We assume that the ice divide remained more or less over the highest points of the Andes, given the topographically confined nature of the outlet lobes. Subsidiary ice divides were likely above the topographic lows between the present-day Northern and Southern Patagonian ice fields. Ice masses centred on mountains located to the east of the main ice divide, such as Monte San Lorenzo and San Sangra, were

2221 likely confluent with the main outlet lobes, but retained some radial flow, and likely remained as ice
2222 dispersal centres throughout the LLGM. The large fjords and bathymetric troughs located west of the main
2223 present-day icefields suggest the presence of large, well-established outlet lobes with a dendritic flow
2224 pattern, characteristic of fast-flowing glaciers and ice streams. Outlet lobes to the east remained
2225 topographically confined and followed terrestrial valleys and bathymetric troughs on the continental shelf.
2226 Growth on the Pacific margin was likely limited by deepening water beyond the continental shelf edge,
2227 which increased mass loss through enhanced iceberg calving. Outlet lobes on the western side of the Andes
2228 were likely larger than those on the east, as they are today, reflecting an orographic precipitation gradient.
2229 This is apparent in our LLGM reconstructions, in which ice extended further to the west than the present-day
2230 icefields compared with the east (Figure 35).

2231 In the Chilean Lake District, LLGM outlet lobes were relatively small when measured along the reconstructed
2232 flowlines, with maximum lengths (ice divide to terminus) of *ca* 76 km (Lago Ranco), 92 km (Lago Llanquihue),
2233 and 110 km (Seno de Reloncaví) (Figure 35). Ice lobes were larger further south around the present-day
2234 Northern Patagonian Icefield, reaching lengths of up to 180 km (Lago GCBA), and 186 km (Lago CP), and with
2235 widths of 40 – 50 km. Outlet lobes of the Southern Patagonian Icefield attained lengths of ~130 km (Lago
2236 Viedma and Lago Argentino). The most substantial lobes were formed in the far south around Tierra del
2237 Fuego, with the Magellan Lobe reaching 230 km, and the Bahía Inútil Lobe reaching 300 km in length (40 km
2238 in width) (Figure 35). The topographically influenced, highly convergent flow and attenuated bedforms
2239 mapped around some larger outlet lobes in the south (Clapperton, 1989; Darvill et al., 2017; Ercolano et al.,
2240 2004; Lovell et al., 2012; Ponce et al., 2013, 2018) satisfy the criteria for being considered ice streams
2241 (Stokes and Clark, 1999). Further work is required to investigate the potential for the diagnostic offshore
2242 trough-mouth fans along the Pacific margin, in order to establish whether marine-terminating ice streams
2243 were present on the eastern side of the PIS, which is likely.

2244 Ice-dammed lakes featured prominently along the eastern ice sheet margin during ice sheet recession
2245 (Figure 34), due to higher ground east of the ice sheet and glacial over-deepening, exacerbated by isostatic
2246 depression and eustatic sea level fall during glacial maxima (Barr and Lovell, 2014; Kaplan et al., 2009;
2247 Thorndycraft et al., 2019b). These large, deep lakes likely strongly influenced calving, outlet glacier mass
2248 balance and rates of recession (Porter et al., 1992), and should be included in numerical modelling efforts.
2249 Ice-cliff instability would likely have encouraged rapid calving (Pattyn et al., 2017; Pollard et al., 2015),
2250 especially as glaciers retreated and thinned in over-deepened lake basins, and as lake levels changed
2251 dynamically as new spillways opened during recession. Incorporating hydrological and glaciological models,
2252 which can account for changing lake levels and calving dynamics, remains a research priority.

2253

Figure 35. A. Comparison of our 35 ka LGM reconstruction with that of Coronato and Rabassa (2011). Sea level reconstruction (-150 m at the LGM on the Argentine Shelf) is from geological data in Guilderson et al. (2000), symbolised using the GEBCO marine bathymetry dataset. Outlet lobe abbreviations: BV/RG/UE = Bella Vista/Río Gallegos/Ultima Esperanza; Corcovado = Golfo de Corcovado; Ancud = Golfo de Ancud; GCBA = Lago General Carrera/Buenos Aires; CP = Lago Cochrane/Pueyrredón; MSL = Monte San Lorenzo. B. Reconstruction of ice flow pathways and ice divide for the 35 ka ice sheet. Flowlines are reconstructed using mapped geomorphology (glacial lineations, moraines, bathymetric troughs, topography, etc) and the pattern of recession. Ice divide has low confidence and is assumed to lie over the Andean mountain chain.

Our reconstruction lacks detail on the western side of the Patagonian Andes between 46°S and 53°S. While there have been numerous studies on glacier limits to the east of the current North and Southern Patagonian Icefields, very few moraines have been dated on the wetter western flanks of the Icefields (Mercer, 1970). This is partly a function of the relative absence of Late Quaternary moraines as many western outlet glaciers of the current icefields and expanded PIS calved into deep fjords during the Pleistocene and much of the Holocene (Glasser et al., 2008; Harrison et al., 2012). In addition, post-glacial sea level rise has covered much of the geomorphological evidence of past glacier fluctuations. Dating of pre-near-recent neoglacial moraines and glacier fluctuations to the west of the icefields is also difficult. No cosmogenic dates have thus far been successfully obtained from the wet and heavily vegetated western side, and this restricts analysis of ice sheet and glacier fluctuations to OSL, radiocarbon dating and analysis of offshore sedimentary records. As a result of these issues, few attempts have been made to date Late Quaternary glacier behaviour there, and we suggest that this represents a significant gap in our understanding of the dynamics and evolution of Patagonian ice masses and palaeoclimate forcing (cf. Harrison et al., 2012).

6.2 Characteristics of key advances

Analysis of the ^{10}Be ages of moraines and other published ages across our large latitudinal transect allows some interpretation of the key timings of glacial advances within the time frame of this study. Focusing on moraine mean ages allows concentration on timings of ice-margin stabilisation; other ages may be distributed between moraines, or not related directly to a period of ice-margin stabilisation. However, ^{10}Be moraine ages are not evenly distributed; rather, they are clearly focused along particular latitudes, with accessible outlet lobes forming the foci for regional assessment. Analysis of the moraine mean ages across the study region indicates clusters of ages at 40 – 27 ka, a stabilisation with moraine formation at 18 – 19 ka,

2289 a clear cluster coincident with the ACR (15 – 13 ka), evidence of a small stabilisation of outlet glaciers at ~11
2290 ka, and clusters of ages coincident with Holocene advances at 5 – 6 ka, 1 – 2 ka and at 0.5 – 0.2 ka (Figure
2291 36A, B, C).

2292

2293 *6.2.1 Local Last Glacial Maximum: 40 – 30 ka*

2294 The LLGM in Patagonia is well dated by radiocarbon dating (especially in the Chilean Lake District) and
2295 cosmogenic nuclide dating (Figure 36). Nested terminal moraines consistently yield Early and Middle
2296 Pleistocene ages for the outermost moraine belts across Patagonia, with inset moraines yielding Late
2297 Pleistocene ages ranging from ~47 to 19 ka. The spread of ages across the Late Pleistocene terminal
2298 moraines indicates that at least some the outlet lobes achieved their last glacial cycle maximum positions
2299 during MIS 3 (60 to 25 ka; Siddall et al., 2008), with minor recession and stabilisation at inset moraines
2300 through the global LGM (23 to 19 ka; Hughes et al., 2013), and rapid deglaciation after ~18 to 19 ka (Figure
2301 36B, D).

2302 In the Chilean Lake District (38°S to 42°S), radiocarbon ages show recurrent expansions of the piedmont
2303 glaciers to the moraines at 33.6, 30.8, 26.9, and 26.0 cal. ka BP (Moreno et al., 2015). There is little dating
2304 control available in the eastern part of the Andes at this latitude. Moving south, the Río Cisnes Lobe (44.6°S)
2305 shows substantial recession from the LGM moraines by 20.1 ka (SD 0.9).

2306 At 46°S, the Lago GCBA Lobe has the best-dated limits (Figure 35), where a range of older Middle Pleistocene
2307 ages at the outer moraines (Moreno I, II and III moraines) delimit the maximum possible extent (Hein et al.,
2308 2017; Kaplan et al., 2005). Here, the Fenix V Moraines yield a mean age of 28.0 ka (SD 1.8) (Douglass et al.,
2309 2006). The ice margin remained in this area, forming the nearby Fenix IV moraines at 28.8 ka (SD 2.1), and
2310 the Fenix III moraines at 23.3 ka (SD 2.1) (Douglass et al., 2006). The Fenix II and Fenix I moraines yield mean
2311 ages of 22.9 ka (SD 1.4) and 20.9 ka (SD 1.5) respectively (Figure 36D).

2312 Further south (47°S), the LGM limit of the Lago CP outlet lobe of the Northern Patagonian Icefield is similarly
2313 well dated, again with outer Middle Pleistocene moraines at the Hatcher moraines limiting the maximum
2314 possible LGM extent (Hein et al., 2009). The Río Blanco Moraines yielded mean exposure ages of 29.9 ka (SD
2315 3.0) and 27.0 ka (SD 0.5) (Hein et al., 2009, 2010; Smedley et al., 2016). The innermost Río Blanco moraines
2316 yield a mean age of 21.0 ka (SD 1.0).

2317 The Southern Patagonian Icefield moraines are dated at the San Martin/O'Higgins Lobe, where again older
2318 Middle Pleistocene moraines indicate a relatively restricted LLGM ice extent when compared with older
2319 glaciations (Glasser et al., 2011b). Here (49°S), the M4 Moraine yields a mean ^{10}Be age of 32.9 ka (SD 4.9).

The Torres del Paine/Rio Coyle Lobe (51°S) is well dated at the Rio de las Vizcachas (RV I) terminal moraine (García et al., 2018), with a mean age of 47.0 ka (SD 0.6). The RV I lateral moraine yields a mean age of 39.2 ka (SD 3.3), and the RV II moraine has a mean age of 35.1 ka (SD 1.2). The TDP I moraine has a mean age of 21.3 ka (SD 1.7) (García et al., 2018), synchronous with the global LGM in MIS 2, with recession of circa 50 km between the LLGM at 47.0 ka and 20 ka.

The UE/BV Lobe, at the southern margin of the Southern Patagonian Icefield, is constrained by the Rio Turbio Moraine Complex (51.5°S), with mean ages of 47.1 ka (SD 1.8) (Garcia et al., 2018). The Dos Laguna Moraine Complex is dated to 36.3 ka (SD 0.7), and the AR moraine to 33.0 ka (SD 2.8) and 32.4 ka (SD 1.2) (Garcia et al., 2018; Sagredo et al., 2011). Together with the older ages associated with the San Martin and Rio Coyle lobes, this could suggest that the Southern Patagonian Icefield reached its maximum earlier than the Chilean Lake District, Isla de Chiloe area and the Northern Patagonian Icefield (cf. Figure 36D).

In Tierra del Fuego (52°S), the Magellan Lobe reached its maximum extent at a minimum age of 25.1 ka (SD 0.9) (Kaplan et al., 2008), although older moraines exist beyond that site, suggesting that the LLGM may have been earlier (Peltier et al., 2016). The Bahía Inútil-San Sebastián Lobe (53°S) has a series of cosmogenic exposure and depth profile ages (Figure 31), which suggest that the LLGM here was at 30 ka or even 45 ka (Darvill et al., 2015b; Kaplan et al., 2007).

Overall, these data indicate that the PIS reached its local maximum extent well before the global LGM of 19 – 23 ka (Clark et al., 2009; Hughes et al., 2013) and global sea-level lowstand of 29 – 19 ka (Harrison et al., 2019). This PIS instead reached its maximum extent during the last glacial cycle most likely between 47 and 30 ka across most of Patagonia (Figure 36D). We therefore use our 35 ka time-slice as our local LGM reconstruction. Outlet glaciers may have remained near that extent through the global LGM, although some are known to have receded markedly (Darvill et al., 2015b; García et al., 2018). These data suggest that the PIS reached its local LGM position earlier than the Antarctic Peninsula Ice Sheet, which reached its LLGM at 18 ka BP (Davies et al., 2012). However, further work is needed to constrain LLGM extent and timing beyond the few lobes that have a well-developed chronology. For example, there is limited work constraining the LGM timing in the eastern Chilean Lake District, southern Isla de Chiloé and Archipiélago de los Chonos, the area west of the PIS and for large parts of Cordillera Darwin.

The reason for this early LLGM is poorly understood in Patagonia (Darvill et al. 2015; García et al., 2018). However, it reproduces early local glacial maxima observed across the Pacific in New Zealand at ~44 ka, 41 ka, 35 ka, 27 ka and 20 ka (Kelly et al., 2014; Doughty et al., 2015; Strand et al. 2019). It is apparent that unlike the Northern Hemisphere ice sheets, that are linked by Milankovitch forcing to summer insolation at 65°N, the behaviour of the southern mid-latitude glaciers was not tied to summer insolation intensity

(Doughty et al., 2015). In New Zealand at least, Doughty et al. (2015) inferred that the larger glacier extents between 41.2 ka and 18.29 ka were aligned with Southern Ocean surface temperatures and with low atmospheric carbon dioxide. This hypothesis needs to be evaluated more comprehensively for Patagonia, building on García et al. (2018).

Figure 36. A. Latitudinal transect of mean ^{10}Be ages (reliability of 1) and standard deviations (SD) for moraines in Patagonia (using external uncertainties). Grey bars indicate timing of significant advances, during the Local LGM (LLGM), ACR (Pedro et al., 2016), Mid-Holocene and Late Holocene. The global LGM (gLGM) is marked (Hughes et al., 2013). B: Frequency histogram of ^{10}B ages for moraines in Patagonia, 40 ka to present day. C. Gaussian probability density function ("camel plot") of all ^{10}Be ages with an age reliability of 1 or 2 from moraines in Patagonia. D. Box and whisker plot for ^{10}Be ages on terminal moraines of outlet lobes across the study site.

6.2.2 Onset of deglaciation: 18 – 19 ka

In the Chilean Lake District, the youngest advance into the Llanquihue moraine belt occurred at 17.7 – 18.1 cal. ka BP (Moreno et al., 2015). In Lago GCBA, the Fenix II (north) and Menucos moraines yield mean ages of 18.9 ka (SD 1.8) and 17.3 ka (SD 1.0) respectively (Douglass et al., 2006). Here, the FCMC17 varve record also constrains the age of the Fenix I moraines, with a Bayesian modelled start age of 18.8 ± 0.6 cal. ka BP, and an end age of 18.1 ± 0.2 cal. ka BP (Bendle et al., 2017a). Bayesian modelled varve ages provide an age for the Menucos moraine of 17.10 ± 0.1 ka BP. Other outlet lobes showing a stabilisation at that time include the Lago CP Lobe (Rio Blanco 3rd limit; 21.0 ka (SD 1.0); Hein et al., 2010), the TDP I moraines of the Torres del Paine/Río Coyle Lobe (21.3 ka (SD 1.7); García et al., 2018), Magellan Lobe (19.9 ka (SD 1.9); and 19.6 ka (SD 0.1); Kaplan et al., 2008), and the Bahía Inútil Lobe (19.4 ka (SD 0.9); Kaplan et al., 2008). In Cordillera Darwin, extensive ice recession and deglaciation had occurred by 17.2 cal. ka BP. In all these cases, rapid regional deglaciation appeared to begin after 18 – 19 ka, perhaps initiating earlier further north and with ice persisting later further south.

6.2.3 Antarctic Cold Reversal (ACR): 14.6 to 12.8 ka

The ACR (14.6–12.8 ka; Blunier et al., 1997; Cuffey et al., 2016; Pedro et al., 2016, 2018; Steig et al., 1998) is captured in our 13 ka time-slice (Figure 34). There is widespread evidence in Patagonia south of ~46°S that glaciers advanced and stabilised at that time, forming prominent moraines inset from the LGM moraines (Figure 36A, B). In general, where outlet glaciers advanced during the late glacial period, it seems to have been during the ACR rather than during the Northern Hemisphere Younger Dryas (12.9–11.7 ka; Pedro et al., 2016). In several studies that date moraines to both intervals, the ACR limits are more extensive, and lateral moraines are distinctly higher, than limits during the Younger Dryas chronozone (Strelin et al., 2011, 2014;

Kaplan et al., 2011; Sagredo et al., 2018; Davies et al., 2018). While glaciers had receded substantially since the LGM, ice remained sufficiently expansive to continue blocking palaeolake drainage to the Pacific Ocean, resulting in the formation of some of the largest ice-dammed lakes at this time (Figure 36).

In the Chilean Lake District, ice was well within the Andean mountains by the ACR (Moreno et al. 2015). Palaeoenvironmental evidence, such as pollen, indicates a cooling period that began during the ACR and ended during the Younger Dryas chronozone here (Hajdas et al., 2003; Massaferro et al., 2009; Moreno et al., 2001), including to the east of the Andes (Ariztegui et al., 1997). There is no evidence of an ACR advance on Isla de Chiloé or Archipiélago de los Chonos. These sites need further investigation to test the case for an ACR advance here, especially as an advance of tropical glaciers in Peru has been observed at that time (Jomelii et al., 2014), and because oceanic cooling reaching as far north as 40°S (Pedro et al., 2016).

Outlet glaciers extending from the northern part of the Northern Patagonian Icefield underwent asynchronous advances (or relative magnitude of events) during the ACR, with calving dynamics modulating outlet glacier mass balance for those terminating in water (Davies et al., 2018). The Lago GCBA and CP lobes had disintegrated as lobes by the time of the ACR (Boex et al., 2013; Thorndycraft et al, 2019a), but moraines indicating Northern Patagonian Icefield outlet glacier stabilisation during the ACR are common in this region (Davies et al., 2018; Nimick et al., 2016; Thorndycraft et al, 2019a). Just to the east of the Northern Patagonian Icefield, in the San Lorenzo massif, Sagredo et al. (2018) observed ACR moraines from ~13.8 to 13.3 ka. To the west of the Northern Patagonian Icefield, a cold event identified in offshore cores corresponds to the ACR (Montade et al., 2019; Siani et al., 2010).

The Lago Argentino Lobe and outlet glaciers in the Torres Del Paine region advanced from the Southern Patagonian Icefield during the ACR (Fogwill and Kubik, 2005; García et al., 2012; Kaplan et al., 2011; Moreno et al., 2009; Strelin et al., 2011). Dating of the Puerto Bandera moraines at the edge of Lago Argentino provided a maximum limiting age of 13.0 ± 0.1 cal. ka BP, indicating a readvance of 25 km during the ACR (Strelin et al., 2011). This was followed by rapid recession by ~12.5 cal. ka BP to near present-day positions, save for the stabilisation of Glaciar Upsala, around 12.2 ka, at the Herminita moraines (Strelin et al., 2011).

In the Torres Del Paine area of the southern Southern Patagonian Icefield, the Torres del Paine/Rio Coyle outlet glaciers advanced during the ACR at *ca* 14.9 ka (SD 1.1) to 13.7 ka (SD 0.1) (Fogwill and Kubik, 2005; García et al., 2012; Moreno et al., 2009). The maximum extent was reached at ~14.4 ka, forming the TDP II-IV moraines over 45 km from the present-day icefield and within close proximity of the MIS 2 TDP I limits (García et al., 2012). Following the ACR, there was major glacier recession (García et al., 2012), with some reports of subsequent advances of early Holocene age (Marden and Clapperton, 1995; McCulloch et al., 2000) but with limited age precision. A similar pattern is indicated by analysis of ^{14}C ages from peat and

sediment cores from the fjord channel system located to the NE of the present-day Grand Campo Nevado ice cap suggests that the deglaciating Skyring Lobe retreated slowly, and possibly stabilised during the ACR (Kilian et al., 2007a).

The extent of ACR glacier re-advances in the Cordillera Darwin region has been the subject of some debate. McCulloch et al. (2005b) and Sugden et al. (2005) proposed an ACR re-advance from Cordillera Darwin that extended northwards into the Strait of Magellan, reaching Isla Dawson and damming a large proglacial lake. However, Hall et al. (2013) recorded deglaciation ages of ~16.8 ka at a location over 100 km to the south of the previously proposed ACR limits, suggesting there is no evidence for an extensive ACR advance in the Cordillera Darwin. Recently, Hall et al. (2019) argued that Cordillera Darwin glaciers were restricted in ice extent during the ACR. Moraines dating clearly to an ACR readvance are also lacking in the Strait of Magellan (Fernández et al., 2017). ACR glacier advances in the Cordillera Darwin region were also identified by Menounos et al. (2013), who dated advances (~2 km from the backwall) of alpine glaciers in relatively small cirques surrounding Ushuaia to 13.5 ka (SD 1.3) and 14.3 ka (SD 0.2) (mean ages).

6.2.4 Late Pleistocene / Early Holocene transition: 12 – 10 ka

In some valleys, there are minimum-limiting ^{14}C ages that morphostratigraphically relate to the moraines, and lie in the Northern Hemisphere Younger Dryas chronozone (e.g., Marden and Clapperton, 1995; Mercer, 1968, 1976; Strelin and Malagnino, 2000; Wenzens, 1999). At Lago Argentino, the Herminita moraine system is dated to 12.2 cal. ka BP (Strelin et al., 2011). There are often not enough dates or ^{14}C data are minimum-limiting, or it is in general not clear how such stillstands or advances relate specifically to the Younger Dryas events in the Northern Hemisphere. Furthermore, in valleys mapped with sufficient resolution, numerous cross-valley moraines, post-dating maximum ACR ice position, are identified (e.g. Martin et al., 2019). This is indicative of active recession, with glaciers frequently stabilising and forming moraines. The post-ACR moraines dated to 10 – 11 ka around the Northern Patagonian Icefield and the Nef valley (Glasser et al., 2012) could be part of this active recession, or a dynamic response to palaeolake drainage as ice dams receded past key cols and spillways during a period of rapid regional warming. The early to mid-Holocene Tempanos Moraine from Laguna San Rafael also indicate a period of ice-margin stabilisation and moraine formation post-dating the ACR in the Early Holocene (Harrison et al., 2012).

Paleoclimate data from onshore and immediately offshore along the Taitao Peninsula suggest that the Younger Dryas chronozone was an event characterised by cooler and drier conditions (Massaferro and Brooks, 2002; Siani et al., 2010), but, according to pollen records, did not represent a significant climate reversal as reported further north in the Chilean Lake District. In southern Patagonia, Moreno et al. (2009)

inferred that after the ACR, conditions were slightly warmer but still cold and variable until the start of the Holocene early thermal maximum.

The alpine glaciers in cirques surrounding Ushuaia also contain the only record of glacier activity of Younger Dryas age in that part of southernmost Patagonia, represented by a single recessional moraine dated to 12.38 - 12.01 ka (Menounos et al., 2013). Palaeoenvironmental evidence for Younger Dryas cooling in the Strait of Magellan has been the subject of great debate, with a particular focus on whether cooling was climate-driven or by other factors (Heusser and Rabassa, 1987; Heusser et al., 2000; Markgraf, 1993; McCulloch and Davies, 2001). Evidence from Fiordo Marinelli in Cordillera Darwin supports highly restricted ice extent from 8 cal. ka BP, during the Early Holocene (Hall et al., 2019).

6.2.5 Mid-Holocene: 6 – 4 ka

Figure 36A, B and C reveals a consistent set of moraine ages indicating a mid-Holocene neoglaciation, and the first major glacier stabilisation since the end of the ACR. They include mean ^{10}Be ages of 5.4 ka (SD 0.2) in front of Lago Colonia (47.3°S) (Nimick et al., 2016). The first deglaciation of the Glaciar Gualas lagoon occurred by 5.3 ± 0.2 cal. ka BP, indicating ice extent near this point until the mid-Holocene (Fernandez et al., 2012). For MSL, a mean age of 5.7 ka (SD 0.1) was obtained on the RT6 moraines of Tranquilo Glacier (47.5°S) (Sagredo et al., 2016). An overridden tree within moraines surrounding an eastward-flowing outlet glacier of MSL provide a maximum age for glacial advance of 5.3 ± 0.7 cal. ka BP (Mercer, 1976). Lichenometric data further supports a period of glacier stabilisation and moraine formation for Glacier San Lorenzo and Glaciar Rio Lacteo at 5.8 to 4.5 ka (Garibotti and Villalba, 2017).

Around the Southern Patagonian Icefield, moraines have ^{10}Be exposure ages ranging from 5.2 ± 0.4 to 4.6 ± 0.4 ka on the outer Pearson moraines near Lago Argentino (49.9°S), and ranging from 5.7 ± 0.5 to 4.5 ± 0.4 ka on the Herminita Peninsula at 50.0°S (Kaplan et al., 2016; Strelin et al., 2014). In the most south-westerly part of the Lago Argentino basin, Holocene moraines date to around 6.1 to 5.7 ka around Lago Frias (50.6°S) (Kaplan et al., 2016; Strelin et al., 2014). Just to the north of Lago Viedma, Glacier Torres has a sequence of progressively inset moraines with mean ^{10}Be ages of 6.9 ka (SD 0.1), 6.2 ka (SD 0.2) and 4.5 ka (SD 0.1) (Reynhout et al., 2019). These ^{10}Be ages agree with the more widespread limiting ^{14}C ages that indicate ice margins close to the most recent 0.5 – 0.2 ka maximum extent before or by 5 ka. For example, radiocarbon ages of 3.6 ± 0.2 and 4.8 ± 0.5 cal. ka BP inside moraines from Río Condor and Río Guanaco, respectively, constrain a mid-Holocene ice advance east of the Southern Patagonian Icefield (Wenzens, 1999). For Cordillera Darwin, there is strong evidence of glacier advances at 6.7 – 5.4 cal. ka BP, synchronous with ice advances reported in the Southern Patagonian Icefield (Hall et al., 2019).

In all these cases, these mid-Holocene moraines are close to, but just larger than, moraines with ages of 1 – 2 ka or 0.2 – 0.5 ka. Recent findings, especially in Lago Argentino and at San Lorenzo, support earlier work by Mercer (1968) or inferred larger middle than Late-Holocene limits. The exception are the Leones Moraine, west of the NPI, which does show significant differences between the 0.5 – 0.2 ka and early to mid-Holocene advances (Harrison et al., 2008). It is highly likely that moraines of mid-Holocene age are more widespread in Patagonia, but limited work dating these advances has been carried out, and many of these moraines may have been re-occupied by glaciers during the last few centuries. However, unlike glaciers in the Northern Hemisphere, which reached their maximum extent during the "Little Ice Age" (cf. Ivy-Ochs et al., 2009; Solomina et al., 2015), this mid (or early)-Holocene advance is likely to be the greatest since the end of the ACR, with relatively more subdued ice advances during the last millennium. Similar Neoglacial mid-Holocene advances have been observed at this time in the sub-Antarctic islands (Hall, 2009) and in New Zealand (Bravo et al., 2015; Schaefer et al., 2009).

Kaplan et al. (2016) suggested that the 6 – 4 ka mid-Holocene advance is due to a northward expansion of the SWW at this time, bringing colder polar/subpolar air. Moreno et al. (2018) showed that the Mid-Holocene was a time of pervasive or persistent negative SAM-like conditions of cold and wet climate, which forced glacier growth. Using PMIP2 climate model simulations, Bravo et al. (2015) suggest that during the mid-Holocene (6 ka), there were cooler conditions during the austral summer (-0.2°C), autumn (-0.5°C) and winter (-0.4°C), with slightly warmer conditions during the spring (+0.2°C). This was accompanied by a seasonal shift in precipitation, with increased precipitation from October to April. This resulted in an ELA that was 15 – 33 m lower during the mid-Holocene than at 1750 AD, resulting in slightly larger glacier extents at this time (Bravo et al., 2015). These Neoglacial glacier expansions were followed by warming and glacier recession that drove glacier recession and ice limits similar to present (Moreno et al., 2018).

6.2.6 Last two millennia: 1 – 2 ka

Figure 36 shows consistent evidence of a Neoglacial readvance at 1 – 2 ka, when colder conditions are recorded in Antarctic ice cores (Cuffey et al., 2016). Some of these late Holocene advances are also constrained by OSL or radiocarbon dating. These include moraines dated to 1.1 ± 0.2 ka by OSL and ^{10}Be at Glacier Leon, an outlet glacier of the Northern Patagonian Icefield (Harrison et al., 2008) (46.7°S); the Lago Onelli moraine at the head of Lago Argentino (1.4 ± 0.1 ka), moraines on the Herminita Peninsula at 50°S (^{10}Be ages are 1.2 ± 0.1 ka; 2.1 ± 0.2 ka; 1.4 ± 0.1 ka), and moraines from nearby Lago Pearson dating from 1.6 ± 0.1 and 1.3 ± 0.1 ka (Kaplan et al., 2016; Strelin et al., 2014). A series of radiocarbon ages indicate a similar late Holocene readvance in the nearby Agassiz Este Valley (Strelin et al., 2014). Radiocarbon ages indicate a later readvance that predates the 0.5 – 0.2 ka advance at Soler Glacier (Glasser et al., 2002).

Finally, radiocarbon ages indicate a late Holocene advance during the last two millennia in Cordillera Darwin, using bracketing inside-outside ages to constrain moraine limits to *ca* 2 ka (Kuylenstierna et al., 1996). Radiocarbon ages from Fiordo Marinelli, Cordillera Darwin, indicate Late Holocene advances at 1.3-1.1 cal. ka BP and 3.8 – 2.4 cal. ka BP (Hall et al., 2019).

Further work is needed to firmly establish glacier limits before a region-wide reconstruction can be attempted for this late Holocene readvance. However, the proximity of dated limits to those dated to 5 ka and the 0.5 – 0.2 ka advance suggest that this ice advance was of a similar magnitude to those occurring in the mid and late Holocene, although this may have varied depending on glacier size or other factors.

6.2.7 Late Holocene: 0.5 – 0.2 ka

A final near-recent Neoglacial readvance is evidenced by historical documents (e.g. Araneda et al., 2007; Casassa et al., 1997; Rivera et al., 2012b), dendrochronology (e.g. Masiokas et al., 2009b; Winchester and Harrison, 2000; Winchester et al., 2001, 2014), lichenometry (Harrison et al., 2007; Garibotti and Villalba, 2009, 2017), and ^{10}Be dating (Kaplan et al., 2016; Reynhout et al., 2019). The most recent moraines and trimlines, generally assumed to date from the period 0.5 – 0.2 ka, show distinctive differences to older Holocene moraines in terms of vegetation and degradation on satellite imagery (Davies and Glasser, 2012; Glasser et al., 2011a).

In the Isla de Chiloé and Archipiélago de los Chonos sector, lichenometric dating of Glaciar Torrecillas suggests a series of consecutively stratigraphically younger moraines date from 1735 AD to 1934 AD (Garibotti and Villalba, 2009).

At the Northern Patagonian Icefield, chronostratigraphic data record a readvance of Glaciar San Rafael into the lagoon at 1871 AD, followed by recession to present-day limits at 1675 and 1766 AD (Araneda et al., 2007; Winchester and Harrison, 1996). Dendrochronological records indicate advance of Glaciar Benito of the Northern Patagonian Icefield to prominent nearby moraines at 1860 AD (Winchester et al., 2014). On the eastern Northern Patagonian Icefield, Glaciar Nef formed prominent moraines at 1863 AD (Winchester et al., 2001), and moraine crests around Lago Arco date an advance of glacier NPI-24 at 1881 AD (Winchester and Harrison, 2000). In this case, this signifies a significant difference in distance between Mid-Holocene moraines dated to 5.4 ± 0.3 ka (Nimick et al., 2016) and near-recent moraines for Glaciar Colonia. For Monte San Lorenzo, lichenometric dating indicates ice-margin stabilisation at *ca* 1925 AD (Glaciar Rio Lacteo) and 1795 – 1955 AD (Glaciar San Lorenzo) (Garibotti and Villalba, 2017).

For the Southern Patagonian Icefield, historical documents provide evidence of a substantial advance of Glacier Jorge Montt relative to present at 1898 AD (Rivera et al., 2012a). Glacier O'Higgins likewise advanced into Lago O'Higgins at 1896 AD (Casassa et al., 1997). On the eastern Southern Patagonian Icefield, dendrochronology indicates glacier advance to prominent moraines at 1626 to 1850 AD (Masiokas et al., 2009b). Moraines near Huemul Glaciar are dated from 1481 to 1886 AD by lichenometry (Garibotti and Villalba, 2009).

On the Herminita Peninsula, a number of moraines, just inside the mid-Holocene and last two millennia moraines described above, are dated using ^{10}Be dating to *ca* 0.2 to 0.6 ka (Kaplan et al., 2016; Strelin et al., 2014). Moraines just inside those of Mid-Holocene age at Glacier Torres have ^{10}Be exposure ages of 0.5 ka (Reynhout et al., 2019). In the south-western Lago Argentino basin, moraines inside the mid-Holocene limits document an advance of Grande Glacier at 0.2 to 0.5 ka (Kaplan et al., 2016). A Late Holocene advance of the Gran Campo Nevado ice cap is recorded by dendrochronology on glacier moraines dating from AD 1628 to AD 1886 (Koch and Kilian, 2005). An advance of glaciers at Cordillera Darwin is recorded in Fiordo Marinelli, where two advances are dated to ~480 and ~750 years BP. The most recent of these reached Narrows Moraine (Figure 32), where it remained until historical times (Hall et al., 2019).

Many of the moraines dating from the mid- and late-Holocene are morphologically similar to moraines dated to the last few centuries by dendrochronology, lichenometry, historical documents or geological data. While in some cases a series of inset moraines are present, independently dated to ~6 – 5 ka, ~1 – 2 ka and ~0.3 ka (Kaplan et al., 2016; Strelin et al., 2014), in other places, the same moraines may have been repeatedly occupied. Additionally, some moraines assumed to date from the last two centuries may have initially been formed much earlier. Further work is therefore required to untangle these complex relationships, and we are presently unable to definitively separate out ice extent through these Mid- and Late-Holocene advances at a continental scale.

6.2.8 Latitudinal variations in timings of key advances

The large latitudinal transect covered by the former PIS allows examination of the spatial variation in timings of ice-marginal stabilisation and recession (summarised in Table 7). This in turn can be used to investigate palaeoclimatic controls driving ice sheet dynamics. However, while some of these fluctuations are clearly related to large-scale climatic drivers, it is possible that some ice-marginal fluctuations could have been driven by glaciodynamic processes, especially changes in glaciomarine or glaciolacustrine calving, as glaciers receded into embayments or created large glacier lakes at their termini (Bendle et al., 2017a; Lovell et al., 2012; Darvill et al., 2017; Davies et al. 2018; Thorndycraft et al., 2019). We also note that thermal regime

could evolve or switch as ice volume changed, which could influence glacier response time and lag times between climate and ice extent or dynamics (Glasser and Jansson, 2005). Further work and detailed numerical modelling is required to further investigate the internal versus external drivers of former ice margin variability.

In the Chilean Lake District (38 – 42°S), the piedmont lobe glaciers advanced repeatedly at 33.6, 30.8, 26.9, and 26.0 cal. ka BP (Moreno et al., 2015). On Isla Grande de Chiloé, an ice-dammed lake dated to 26.8 ± 0.2 cal. ka BP indicates that the Golfo de Corcovado outlet lobe was near its maximum extent at that time (Denton et al., 1999). In the central sector of Isla Grande de Chiloé, at Dalcahue, the most extensive advance occurred at 17 – 18 cal. ka BP. The Lago GCBA and Lago CP outlet lobes of the Northern Patagonian Icefield record maximum extents with mean moraine ages of 28.0 ka (SD 1.8) (Douglass et al., 2006) and 29.9 ka (SD 3.0) (Hein et al., 2010) (Table 7). Therefore, the available evidence suggests that from 38°S to 46°S, the LLGM was reached at ca. 33 – 28 ka.

Further south, in the Southern Patagonian Icefield, the LLGM was reached earlier, with the oldest moraines of the Torres del Paine/Río Coyle Lobe pertaining to the last glaciation dated to 47.0 ka (SD 0.6) (Garcia et al., 2018). Associated lateral moraines yielded a mean age of 39.2 ka (SD 3.3) to 35.1 ka (SD 1.2). Similarly, the UE/BV Lobe yielded maximum LLGM ages of 47.1 ka (SD 1.8) (Garcia et al., 2018; Sagredo et al., 2011). Inboard of this, the Aracuco moraines yielded mean ages of 33.0 ka (SD 2.8). Together, these show that the LLGM was reached in the region of 48°S to 52°S during MIS 3, at ca. 47 ka. At 53°S, the Magellan Lobe was extensive at 27.7 ka (SD 1.0) (Kaplan et al., 2008), although the maximum LLGM ice extent may have been reached even earlier, at ~60 – 70 ka, during MIS 4 (Peltier et al., 2016). Cosmogenic dating of outwash gravels from the Bahía Inútil-San Sebastián Lobe (53°S) suggests that ice was extensive here at ~45.6 ka, and confidently before 30.1 ka (Darvill et al., 2015). We therefore suggest that the currently available evidence also supports an LLGM in this region at 47 ka, or possibly earlier in the last glacial cycle.

The timing of the onset of deglaciation, which we define as when glacier recession accelerated, also varies latitudinally. In the Chilean Lake District, rapid deglaciation was initiated after *ca* 18 ka, with glaciers retreating into the mountains by 16.8 cal. ka BP. Limited data after that time is available in the sector from 42 – 46°S. In the Northern Patagonian Icefield, the outlet lobes had only minor recession from the LGM until 17 – 18 ka (Lago GCBA) and 21 ka (Lago CP), with deglaciation after this time, similar to the Río Cisnes valley (García et al., 2019). The tephra-constrained FCMC17 varve record at Lago GCBA indicates a phase of ice-lobe recession beginning at 18.1 ± 0.2 cal. ka BP followed by accelerated recession coinciding with calving dynamics from 17.3 ± 0.1 cal. ka BP (Bendle et al., 2017a; 2019). There is limited data around the Southern Patagonian Icefield, though moraines around the margin of Lago del Toro yield a mean age of 21.3 ka (SD

1.7), suggesting deglaciation after this time. Deglaciation began at ca 19 – 20 ka in the Gran Campo Nevado and Cordillera Darwin regions (52°S – 56°S; Table 7).

Evidence for an ACR glacier stabilisation is absent from 38°S to 46°S, but there is strong evidence of an advance from 14 – 13 ka around the Northern and Southern Patagonian icefields. In that sector (46°S – 52°S), ice remained reasonably extensive until after the ACR, with large ice-dammed lakes forming in front of the icefields. An ACR advance also occurred around Cordillera Darwin. However, glaciation at that time may have been smaller scale, and restricted to upland cirque glacier advance.

Mid-Holocene readvances are well documented around the Northern and Southern Patagonian icefields. A Late-Holocene advance at ~2 ka is also observed between 46°S and 56°S. Further work is required to establish whether the northern parts of Patagonia underwent Neoglacial advances at this time. Finally, a Late Holocene advance synchronous with the Northern Hemisphere "Little Ice Age" at 0.5 – 0.2 ka is well documented across the latitudinal gradient of Patagonia.

We note that there is a synchronous response to substantial climate changes such as that seen during the period 0.5 – 0.2 ka and at the beginning of the 21st century (cf. Meier et al., 2018). This suggests that for larger global climate changes, there is a synchronous response.

2625 *Table 7. Summary of evidence of the timing of key advances and during key climatic transitions across the Patagonian latitudinal transect.*

Location	**Latitude**	**Local LGM**	**Global LGM (23 – 19 ka)**	**Onset of deglaciation**	**ACR (14.6 – 12.8 ka)**	**Early Holocene (12 – 10 ka)**	**Mid-Holocene readvance**	**Readvances in the last two millennia**	**Late Holocene advance at 0.5 – 0.2 ka**
Chilean Lake District	38°S – 42°S	33.6 – 26.0 ka	Limited data	After 17.7 ka	Strong recession; limited data	Strong recession; limited data	Limited data	Limited data	Advance at 0.5 – 0.2 ka
Isla de Chiloe and Archipiélago de los Chonos	42°S – 46°S	26.8 ka	Limited data	Limited data; recession in Cisnes from 20.1 ka	Limited data, no evidence for advance	No evidence for advance	Limited data	Limited data	Advance at 0.5 – 0.2 ka
Northern Patagonian Icefield	46°S to 48°S	28.0 to 29.9 ka	Moraines near LLGM at 23.3 to 21 ka	After 17.3 ka	13.8 – 13.3 ka	Inset moraines at 11.4 ka. San Rafael moraines 9.3 – 9.7 ka	San Rafael: 7.7, 5.7 ka Gualas: 5.4 – 4.1 ka MSL: 5.7 ka	Leones: 2.5 ka	Advance at 0.5 – 0.2 ka
Southern Patagonian Icefield	48°S– 52°S	O'Higgins: 34.9 ka Rio Coyle: 47 ka UE/BV: 47.1 ka	TDP I moraine 21.3 ka, near LLGM extent	Lago del Toro: after 21 ka	13.3 – 14.1 ka Torres del Paine: 14 ka. Puerto Bandera ~13 ka	Limited data. Glaciar Torre (10 – 9.5 ka)	Glaciar Torre: Multiple small advances 6 – 4 ka. Sierra de Sangra: 4.9 ka	Herminita: 3 – 2 ka; 1.4 – 1.5 ka	Advance at 0.6 – 0.2 ka
Gran Campo Nevado	52°S – 53°S	27.7 ka, though ice may have been more extensive earlier	Limited data	Magellan: after 19.4 ka	Limited data	Limited data	Limited data	Limited data	Advance at 0.5 – 0.2 ka
Cordillera Darwin	53°S – 56°S	45.6 ka	Limited data	After 19.4 - 19.9 ka	Ushuaia: 13.5 – 14.3 ka; small advances. Fiordo Marinelli shows restricted ice extent.	Restricted ice extent, similar to present	6.7 – 5.4 cal. Ka BP	3.8 – 2.4 cal. ka BP 1.3 – 1.1 cal. Ka BP	Advance at 0.5 – 0.2 ka

2626

6.3 Glacier and ice-dammed palaeolake area and volume change

6.3.1 Glacier area and volume change

Our calculated area and volume for the PIS at each time-slice is presented in Table 8 and Figure 37. The reconstructed maximum glacierised area is the best estimate to date of ice-sheet extent through time, although uncertainties remain, particularly at 10 and 5 ka (Figure 34). Ice extent at 0.5 to 0.2 ka and present day (2011 AD) takes into account previous estimates (Davies and Glasser, 2012; Glasser et al., 2011a), but has been updated with our new glaciological mapping. The annualised rate of change between each time slice is an average over the entire time-slice and does not consider periods of time when rates of recession may have been more rapid. It is therefore a useful guide to average rates of change.

Calculated ice volumes (Table 8) are dependent on volume-area scaling, using different power laws for ice sheets, ice fields, glaciers and dome-shaped mountain ice caps (see Section 3.3.5). Vertical constraints on ice-sheet thickness are limited (e.g. Boex et al., 2013), meaning that ice volume estimates remain challenging. Though crude, our calculations provide insights into volume change of the PIS and its contribution to sea level change through the late glacial. Present-day ice volume is from Carrivick et al. (2016) using a more sophisticated method, and adjusted for ice volume below sea level. Ice volume at 0.2 ka is likely within errors of the estimate for present-day.

The PIS reached its maximum extent during MIS 3, and was relatively stable from 35 to 30 ka. From a local LGM maximum extent, initial recession and deposition of inboard moraines began by 25 ka (Figure 37), during a period of slight cooling in the Antarctic ice cores (Cuffey et al., 2016; Wais Divide Project Members, 2013) (Figure 37C), and perhaps highlighting the role of atmospheric circulation changes (such as changes in the SWW) in driving ice-sheet dynamics. The maximum extent of the PIS thus preceded the global LGM. To some degree, this may be because the global LGM is defined by $\delta^{18}O$, which is a function of the large ice sheets, which take longer to reach a maximum size, compared with the relatively small and dynamic PIS. An earlier LLGM may also highlight the role of regional atmospheric and oceanic circulation changes in driving ice-sheet dynamics to large extents well before the Laurentide and other ice sheets reached their maxima.

*Table 8. Estimated area and volume of the Patagonian Ice Sheet and associated ice fields, glaciers and mountain ice caps, at each time-slice, and calculated annualised rates of recession. *Present-day ice volume and SLE was estimated by Carrivick et al. (2016). Volume-area scaling estimates the 2011 extent to be 2.2 x 10^3 Gt. SLE = Sea level equivalent. 0.2 ka ice volume is within errors of present-day ice volume. See also Figure 37.*

Time Slice	Total ice-covered area (km^2)	Difference (km^2)	Rate of change (km^2/yr)	% area change	% area change per annum (% a^{-1})	Volume (Gt)	SLE (mm)
35 ka	492.6×10^3		0	0	0	541.2×10^3	1496
30 ka	491.3×10^3	1.3×10^3	0.27	0.3%	0.000%	539.8×10^3	1492
25 ka	465.3×10^3	26.0×10^3	5.20	5.3%	0.001%	503.5×10^3	1392
20 ka	359.6×10^3	105.7×10^3	21.14	22.7%	0.005%	367.2×10^3	1015
15 ka	121.8×10^3	237.7×10^3	47.55	66.1%	0.013%	144.8×10^3	400
13 ka	116.7×10^3	5.1×10^3	2.57	4.2%	0.002%	134.2×10^3	371
10 ka	63.8×10^3	53.1×10^3	10.61	45.5%	0.009%	51.0×10^3	141
5 ka	31.1×10^3	32.5×10^3	6.50	51.1%	0.010%	21.7×10^3	60
0.2 ka	27.9×10^3	3.2×10^3	0.66	10.4%	0.002%	5.5×10^3	14.7 ± 2.9
2011 AD*	23.3×10^3	4.6×10^3	32.90	16.5%	0.118%	5.5×10^3	14.7 ± 2.9

Figure 37. A. Area of the PIS at each time-slice (see Table 8). Grey line represents glaciated area of the PIS (km^2). The black line represents the annualised rate of change (km^2/year) between each time-slice. B. As A, but with percentage area change per annum (% a^{-1}). C. Surface air temperatures from West Antarctica (Cuffey et al., 2016). D. Global ice volume sea-level equivalent, with timing of global ice-volume maximum highlighted (from Harrison et al., 2019). Timings of significant Patagonian glacier advances are highlighted in vertical blue bars. Meltwater pulses (MWP) 1A and 1B are highlighted in pink bars.

Particularly rapid recession and widespread deglaciation occurred after ~18 ka at the end of the late glacial, during a period of rapid Antarctic warming (Cuffey et al., 2016; Wais Divide Project Members, 2013) (Figure 37C), and rapid sea level rise (Figure 6) (Guilderson et al., 2000; Harrison et al., 2019). Rapid retreat in the Lago GCBA Lobe has also been attributed to abrupt southward migration of the SWW, which may have enhanced ablation at the ice sheet surface (Bendle et al., 2019). The PIS potentially contributed ca 615 mm to global eustatic sea level rise between 20 and 15 ka, when we estimate that it shrank from 359.6 to 121.8 × 10^3 km^2 (Table 8). Glaciers stabilised or re-advanced during the ACR (Figure 37), although the PIS was by then significantly smaller than during the LLGM at 116.7 × 10^3 km^2.

Rates of ice recession slowed through the Holocene until after 0.2 ka (with the caveat that some time-slices are highly uncertain). Absolute recession rates (km^2 a^{-1}) over recent decades rival those seen between 20 and 15 ka for an ice sheet more than two orders of magnitude larger, and relative average rates of recession (% a^{-1}) are higher between 0.2 ka and 2011 AD than at any time observed in our reconstruction (Table 8). However, more rapid rates of recession are possible during deglaciation, given the 5 kyr resolution of our reconstruction. It is likely that there were periods of time with especially rapid rates of recession during the last glacial-interglacial transition, when many outlet lobes were calving into large, deep, ice-dammed lakes; however, the published chronologies and our compilation are currently not able to capture this.

There are fewer degrees of freedom for ice extent and volume changes during the Holocene than earlier time slices. Ice margins stabilised not far from present-day positions by the early Holocene, and dated moraines suggest that Holocene neoglacial advances were largely similar to advance at 0.2 ka in size. Thus we argue that average rates of ice-marginal recession are currently faster than at any time observed in the Holocene, in line with recent temperature increases observed in Antarctica and Patagonia, following a sustained period of relative stability, and when glacial lake area remains fairly constant (Figure 37C, Table 9; see below). Since observations indicate that rates of recession in Patagonia have accelerated in recent decades, from 34.3 km^2 a^{-1} (0.14 % a^{-1}) for 1986 – 2001 AD to 51.2 km^2 a^{-1} (0.22 % a^{-1}) for 2001 – 2011 AD (Davies and Glasser, 2012), this is especially concerning.

6.3.2 Ice-dammed palaeolake area change

Table 9 presents calculated ice-dammed lake areas and volumes for 23 palaeolakes for each of the key timeslices. During the LGM, the PIS blocked drainage of palaeolakes to the Pacific, and they drained instead towards the Atlantic Ocean. The ACR was characterised by large ice-dammed palaeolakes filling glacial over-deepenings within the LGM terminal moraines, and the start of the fragmentation of the PIS into the modern-day icefields, ice caps and glaciers. During the ACR, glacier recession had allowed some lakes around the Northern Patagonian Icefield to drain towards the Pacific (Thorndycraft et al, 2019a).

Glacial lake area peaked at ~13 ka with an estimated area of 13,999 km^2 (Table 9), with the enlargement of palaeolakes Chelenko, Tar and Tehuelche-Puerto Consuelo. This is substantially larger than previous estimates of palaeolake area at this time (7,400 km^2; Glasser et al., 2016; Harrison et al., 2019). These large ice-dammed lakes likely exerted a strong control on glacial recession, as evidenced over the short 17.3 - 17.0 ka period at the end of the FCMC17 varve record (Bendle et al., 2017a), and would have contributed to the rapid absolute rates of recession observed at that time (Figure 37).

Glacial lake area minimum was reached at 10 ka (assuming that all lakes are mapped and known at this time slice; Figure 38). Rapid recession of glaciers from the end of the ACR to *ca* 10 ka led to many of these lakes reaching their current spatial extent and volume. As ice dams receded, this cold, fresh water may have been released suddenly into the Pacific (Thorndycraft et al, 2019a), possibly affecting regional climate (Glasser et al., 2016b). Thorndycraft et al. (2019) noted that opening drainage pathways to the Pacific through separation of ice fields and ice caps in the Northern Patagonian Icefield region led to a ~1.0 x 10^5 km^2 increase in watershed drainage area to the Pacific.

Glacial lake area at 5 ka and during the 0.5 to 0.2 ka advance was similar to the present day and is not calculated separately due to the low confidence in most ice margins at 5 ka. In some basins, parts of these palaeolakes remain as the modern proglacial lakes. In addition to these larger glacial lakes, Wilson et al. (2018) mapped 4204 current glacier lakes in our study region, equating to 1,178 km^2 in addition to the glacial lakes noted in Table 9 below.

The remaining lake water today, from lakes that were within the footprint of the palaeolakes, is 6,823.6 km^2. Overall, between the maximum lake extent at 13 ka and today, there has been a reduction in glacial lake area of 7,175.6 km^2. It is important to note that although glacial lake area remained relatively constant during the Holocene (Figure 38), rates of glacier recession (percentage change per annum) observed in the 20^{th} century are currently far higher than have been observed or reconstructed at any time in the last 10,000 years.

2733 *Table 9. Calculated glacier lake area (km^2). Present-day glacial lake area is also provided for those palaeolakes that still remain today in some form. Palaeolake*
2734 *Magellan-Bahia Inútil likely existed for some time between 20 and 15 ka, but is not included here due to uncertainties in timing.*

Sector	Latitude (°S)	Palaeolake Name	Area (km^2)							Present-day (remaining lake waters)	
			35 ka	30 ka	25 ka	20 ka	15 ka	13 ka	10 ka	Present-day status of glacial lakes	Area (km^2)
Chilean Lake District	41.0	**Nahuel Huapi**	-	-	-	-	-	239.8	576	Lago Nahuel Huapi	538.1
	41.1	**Elpapfquen**	-	-	-	-	472.2	-	-	Lago Nahuel Huapi	
Isla de Chiloé-Archipiélago de los Chonos region	42.2	**Epuyen**	-	-	-	114.9	0	0	0	Drained completely	0
	42.2	**Golfo de Ancud**	-	-	319.2	366.3	0	0	0	Drained completely	0
	42.5	**Cholia**	-	-	-	233.35	0	0	0	Drained completely	0
	45.0	**Cisnes-Nirehuao**	-	-	-	743.1	1126.5	1126.5	0	Drained completely	0
	45.7	**Frio**	-	-	-	50.4	4.1	4.1	4.1	Small remnant lakes; Lago Frío	4.1
	45.6	**Lago Castor**	-	-	70.8	Palaeolake Frío; 13.01	13.01	13.01	13.01	Small remnant lakes; Lago Castor and Lago Pollux	13.01
	45.9	**Balmaceda**	-	-	102.6	345.3	0	0	0	Drained completely	0
Northern Patagonian Icefield	47.3	**CP-Chacabuco**	120	120.1	153.7	155.23	1965.7	Palaeolake Chelenko	348.8	Lago CP	348.77
	46.5	**Deseado**	-	-	-	-	3151.5	Palaeolake Chelenko	1803.2	Lago GCBA	1803.15
	46.8	**Chelenko**	-	-	-	-	-	4740.5	-	Evolved into Lago GCBA/CP	
	47.4	**Tranquilo**	-	-	-	-	-	20.3	0	Drained completely	0
Southern Patagonian Icefield	49.7	**Tar**	409.0	409.0	514.5	567.2	797.3	981	711	Lago O'Higgins / San Martin / Tar	1054.2
	51.1	**Tehuelche**	-	52.2	276.6	829.4	-	-	-		
	51.9	**Consuelo**	-	-	89.6	217.9	-	-	-		
	51.6	**Tehuelche-Puerto Consuelo**	-	-	-	-	1369.7	1369.7	269.7	Small remnant lakes; Lago del Toro and Balmaceda	269.7
	49.7	**Viedma**	-	-	-	-	661.9	662.2	766.2	Lago Viedma	1200.8
	50.2	**Argentino**	-	-	-	-	124.9	713.2	1083.3	Lago Argentino	1479.5
	50.5	**Southern Lago Argentino**	-	-	-	-	-	-	248	Joined with Lago Argentino	0
Gran Campo Nevado	52.4	**Blanca**	-	-	466.9	551.5	112.3	112.3	112.3	Laguna Blanca	112.3
	52.8	**Magellan**	-	-	1618.7	2162.6	0	0	0	Marine fjord	0
	52.6	**Skyring**	-	-	-	-	1564	1564	0	Marine fjord	0

Cordillera Darwin	53.1	**Otway**	-	-	-	-	2452.6	2452.6	0	Marine fjord	0
		Total	529.0	581.3	3,612.6	6,350.2	13,815.7	13,999.2	5,935.6		6,823.6

Figure 38. Change in glacier lake area in Patagonia from the LGM to present, visualising data from Table 9.

6.4 Key future research agendas

We suggest the Patagonian research community focus on the following six key priority areas in order to improve future empirical reconstructions of the PIS:

(1) A major remaining limitation for empirical reconstructions of PIS dynamics is constraints on vertical ice extent, and we call on future studies to target vertical transects constraining the timing of ice-surface elevation lowering (cf. Mackintosh et al., 2007).
(2) Ice dynamics during the Holocene remain poorly understood, apart from a small number of well constrained outlet lobes. In order to contextualise current change and extend the empirical record of observations of glacier length, further analyses of ice extent in the last few millennia are required.
(3) The synchronicity of recession from north to south remains challenging to ascertain in the absence of comparable and detailed records detailing the timing of the LLGM, Late Glacial advances and Holocene neoglaciations dynamics. The eastern Chilean Lake District, most outlet lobes in the Isla Grande de Chiloé sector, south-central and western Patagonia through the archipelago and numerous outlet lobes of the Southern Patagonian Ice Field remain poorly dated and poorly understood.
(4) Detailed studies in different sectors of Patagonia are also required to further untangle the complex interplays between climatic controls on ice dynamics (including the behaviour of the SWW) and local dynamic controls, such as calving and topography. In many places, a strong influence of topography and water depth is expected in influencing ice marginal positions and retreat dynamics, but few studies have attempted to analyse these. Detailed analysis of lacustrine varves offers an opportunity to provide high-resolution studies of outlet lobe recession, building on pioneering early work (Caldenius, 1932). Numerical modelling may also be able to test the links between palaeoclimate and ice-mass behaviour by linking mass-balance sensitivities, topography and ice flow parameters with variations in temperature and precipitation.
(5) The direction of ice flow and the extent to which flow was topographically controlled is poorly constrained in areas of thickest ice, and the location of the ice divide in these places remains uncertain. The direction of ice flow in extensive areas that are currently not glacierised also remains uncertain.

(6) Large parts of western Patagonia remain unknown in terms of extent and timing of ice advance and retreat, with limited geomorphological data from the onshore (being well hidden and inaccessible in dense vegetation) or offshore environment. A greater understanding of western-flowing glaciers is a research priority, as these were likely some of the largest and most important outlet lobes of the LGM ice sheet, and formed an important ice-ocean interface.

(7) We are still largely unable to resolve whether deglacial ice limits result from significant stabilisation or re-advance of glaciers, or a combination of the two over time. Numerical modelling work is needed to establish the likely dynamic behaviour of the ice lobes under complex topographic and climatic conditions.

7 Summary and Conclusions

We present the first 2D ice-sheet scale reconstruction of PIS evolution at 5 kyr intervals, from 35 ka to 2011 AD, with additional time-slices at the ACR (13 ka) and late Holocene (0.5 - 0.2 ka). The reconstruction is empirically constrained by the PATICE database, a new compilation of published geomorphology (moraines, perched delta terraces, trimlines, bathymetric troughs, palaeochannels, shorelines, glacial lineations, alluvial fans, sandar, cirques) and recalibrated published ages. Our chronological database includes radiocarbon ages, cosmogenic nuclide surface exposure ages (^{10}Be, ^{26}Al, ^{36}Cl, ^{3}He), cosmogenic depth profiles, OSL, lichenometry, dendrochronology, tephrochronology, varve ages and historical documents. Each age is assigned a reliability rating based on well-defined criteria to aid our pan-ice sheet reconstruction. This new PATICE database thus generates an unprecedented assessment of materials pertinent to southern Patagonia.

At its last maximum, the PIS was 350 km wide, 2091 km long, and covered 492.6 x 10^3 km^2, with a sea-level equivalent of 1,496 mm. Our reconstruction envisages an ice sheet 12% larger than previous reconstructions. It was arranged along the spine of the Andean mountain chain, with prominent outlet lobes flowing orthogonally from the ice divide. The western, Pacific margin of the PIS was likely grounded at the continental shelf edge and outlet lobes here calved into deep water. The emergence of the broad Argentinian continental shelf resulted in an enlarged expanse of land east and towards the Atlantic Ocean. Outlet lobes extended onto this continental plain, following existing topography and often with limited interaction between lobes. Some of the largest outlet lobes satisfy some of the criteria to be considered topographically constrained ice streams.

The timing of the local LGM varied latitudinally, occurring at *ca* 33 to 28 ka in the Chilean Lake District and around the Northern Patagonian Icefield (38°S to 46°S). Further south, the LLGM was reached earlier, at *ca* 47 ka (48°S to 56°S). Maximum ice extent was followed by a period of stabilisation until ~20 ka, with a period

of moraine formation and outlet lobe stabilisation at 18 – 19 ka. However, again this varied latitudinally, with ice persisting later in the north and deglaciation beginning earlier, at 20 ka, in the Gran Campo Nevado and Cordillera Darwin sectors.

After 18 ka, rapid recession and thinning occurred during a phase of fast warming observed in Antarctic ice cores. The rapid recession observed in the post-LGM period in the sector south of 46°S was closely associated with palaeolake formation and development, with outlet lobes calving into large, deep lakes. These palaeolakes were likely pivotal in terms of shaping glacial behaviour. Glaciers then stabilised or readvanced during the ACR, before once again receding. Some glaciers may have responded to Younger Dryas cooling, with a minor stabilisation at *ca* 12 – 11 ka. It is also possible that some late glacial moraines formed in response to ice-margin stabilisation due to palaeolake drainage and the cessation of lacustrine calving rather than climatic deterioration. There is currently no evidence for ice readvance during the ACR or Younger Dryas periods in the northernmost Chilean Lake District and Isla Grande de Chiloé sectors of the PIS (38°S to 46°S), or in Cordillera Darwin, south of 54°S, with the exception of a small independent terrestrial glacier in Tierra del Fuego (Menounos et al., 2013). Potentially ice limits could still be offshore in this area during the ACR, or perhaps advances were only small scale here. Further work is needed to investigate this.

A number of well-dated moraines across Patagonia constrain stillstands or readvances at *ca* 5 ka and 2 – 1 ka across our latitudinal transect, usually slightly larger than the 0.5 – 0.2 ka advance. Holocene ice advances were likely more subdued in Cordillera Darwin. This was possibly in response to changes in the core belt of the SWW, as Antarctic ice cores do not record a substantial period of cooling at this time. However, across the study region, glacial chronologies are generally sparse for this time period. Late Holocene glacial limits at 0.5 – 0.2 ka are synchronous with the Northern Hemisphere “Little Ice Age”. However, unlike in the Northern Hemisphere, ice was likely more extensive at *ca* 5 ka than during this period (cf. Mercer, 1968). These data indicate that the PIS generally seems to have responded to climate signals observed in Antarctica, such as the ACR, with some glaciodynamic controls, such as palaeolake drainage. It also highlights the critical role that the SWW, and centennial-scale climatic oscillations, such as the SAM, played in driving glacier advance and recession. Variations in the core belt of the SWW were responsible for the latitudinal gradients observed in the timings and locations of key glacier advances in Patagonia.

Our empirical reconstruction of the PIS and its evolution through time demonstrates that rates of net recession were generally slow through the Holocene, with limited evidence for large-scale advances or extensive glacier recession. However, observations of glacier recession for the last few decades rival rates seen much earlier, for a much larger ice sheet that was calving into large, deep, ice-dammed lakes. This rapid recession is in line with recent temperature increases observed in Patagonia and in Antarctic ice cores, and documents a step-change in rates of recession.

2834 We provide these data (shapefiles and data tables of geomorphology and ice and palaeolake extent;
2835 shapefiles and data tables of recalibrated ages, confidence levels in ice margins) as supplementary
2836 information in the hope that this will drive forwards data-calibrated numerical modelling of the PIS.
2837 Numerical models should be calibrated in locations with *high confidence* in ice-margin position and should
2838 integrate calving dynamics in ice-dammed lakes and offshore regions. Our reconstructions highlight regions
2839 where ice limits are less well constrained, and these should be used to prioritise future field campaigns.

2840 Our reconstruction highlights key priorities for future research. Data informing the timing of vertical ice
2841 sheet thinning as well as improved sea level estimates would better constrain calculations of ice volume, a
2842 parameter that remains difficult to assess reliably. We are still largely unable to resolve whether deglacial ice
2843 limits result from stabilisation or re-advance of glaciers, or a combination of the two over time. A lack of
2844 detailed chronological data across the latitudinal transect makes it challenging to assess variations that may
2845 be related to changes in the SWW, and to unpick palaeoclimatic controls on deglaciation. More work is
2846 needed to constrain the extent of the Patagonian icefields during the Holocene, including times of reduced
2847 ice extent, and to distinguish 0.2 - 0.5 ka and other mid/late Holocene neoglaciations. While there are
2848 sufficient data to emphasise confidently ice-sheet stabilisation or glacier advances during the ACR and at 5
2849 ka, 2 – 1 ka and 0.5 – 0.2 ka, there are too few dated moraines at this stage to attempt ice-sheet wide
2850 reconstructions for all these time periods in addition to our 5 kyr time-slices.

2851

2852 ## Acknowledgements

2853 We thank all other researchers who shared or clarified their data with us. We thank Eñaut Izzagirre for
2854 sharing shapefiles of geomorphology around northern Cordillera Darwin. Bethan Davies, Varyl Thorndycraft
2855 and Julian Martin acknowledge additional Patagonian fieldwork funding support from the Quaternary
2856 Research Association. Bethan Davies and Varyl Thorndycraft also acknowledge support from the Royal
2857 Holloway Research Strategy Fund, British Society for Geomorphology and Geologists' Association for this
2858 project. Julian Dowdeswell thanks the Servicio Hidrográfico y Oceanográfico de la Armada de Chile (SHOA)
2859 for access to their swath-bathymetric data from Chilean fjords. Jacob Bendle acknowledges NERC Doctoral
2860 Training Grant NE/L501803/1. Monika Mendelova thanks NERC Doctoral Training Grant NE/L002558/1 and
2861 the University of Edinburgh for her PhD studentship. Andy Hein acknowledges NERC CIAF awards 9167/0416,
2862 9036/0407, and the Scottish Alliance for Geoscience, Environment and Society (SAGES). Julian Martin
2863 acknowledges NERC Doctoral Training Grant NE/L002485/1. Christopher Darvill acknowledges previous NERC
2864 studentship NE/j500215/1 at Durham University, NERC CIAF awards 9127/1012 and 9140/1013, University of
2865 Manchester SEED Strategic Research Fund ECR Award, University of Manchester Geography Research Fund,
2866 plus fieldwork support from an Explorers Club Exploration Grant, Quaternary Research Association NRW

Award, Santander Mobility Grant, and Durham University. Neil Glasser acknowledges funding from NERC (NER/B/S/2002/00282, NE/G00952X/1, NE/N020693/1) and the Leverhulme Trust, plus NERC CIAF awards 9186-0418, 9166.0416 and 9086.0410. Esteban Sagredo acknowledges the Millennium Science Initiative of the Ministry of Economy, Development and Tourism, grant "Millennium Nuclei Palaeoclimate", and FONDECYT Grants #1160488 and #1180717. Juan-Luis García acknowledges FONDECYT grant #1161110. Michael Kaplan acknowledges the National Science Foundation specifically NSF BCS 1263474 and NSF EAR-0902363. We thank all Patagonian landowners for allowing access to their property during fieldwork. ASTER GDEM is a product of METI and NASA. We acknowledge GEBCO for the bathymetry data (GEBCO Compilation Group (2019) GEBCO 2019 Grid (doi:10.5285/836f016a-33be-6ddc-e053-6c86abc0788e). We thank Dr Jeremy Ely and two anonymous reviewers whose helpful and constructive comments improved the manuscript. This is LEDO contribution number #XXXX.

Data availability

The Supplementary Information comprises:

- PATICE logo
- Supplementary Methods
- Animated GIF of glacier extent.

All data used in the PATICE database is available in the Mendeley Data repository, which comprises:

- Full Excel tables of recalibrated published ages (including all data required to rerun the calculations).
- ESRI Shapefiles of each dating technique and compiled geomorphology.
- ESRI Shapefiles of outlines of ice extent and uncertainty in the ice margin.
- ESRI Shapefile of ice flow and ice divide at the LLGM.
- ESRI Shapefile of names of outlet lobes.

List of Figures

List of Tables

References

Ackert, R.P., Becker, R.A., Singer, B.S., Kurz, M.D., Caffee, M.W., Mickelson, D.M., 2008. Patagonian Glacier Response During the Late Glacial–Holocene Transition. Science 321, 392-395.

Adhikary, S., Yamaguchi, Y., Ogawa, K., 2002. Estimation of snow ablation under a dust layer covering a wide range of albedo. Hydrological processes 16, 2853-2865.

Álvarez, D., Fagel, N., Araneda, A., Jana-Pinninghoff, P., Keppens, E., Urrutia, R., 2015. Late Holocene climate variability on the eastern flank of the Patagonian Andes (Chile): A δ18O record from mollusks in Lago Cisnes (47 S). The Holocene 25, 1220-1230.

Andersen, B., Denton, G.H., Lowell, T.V., 1999. Glacial geomorphologic maps of Llanquihue drift in the area of the southern Lake District, Chile. Geografiska Annaler: Series A, Physical Geography 81, 155-166.

Anderson, D.M., Archer, R.B., 1999. Preliminary evidence of early deglaciation in southern Chile. Palaeogeography, Palaeoclimatology, Palaeoecology 146, 295-301.

Aniya, M., 1999. Recent glacier variations of the Hielos Patagonicos, South America, and their contribution to sea-level change. Arctic, Antarctic, Alpine Research 31, 165–173.

Aniya, M., Enomoto, H., 1986. Glacier variations and their causes in the Northern Patagonia Icefield, Chile, since 1944. Arctic and Alpine Research 18, 307–316.

Araos, J.M., Le Roux, J.P., Kaplan, M.R., Spagnolo, M., 2018. Factors controlling alpine glaciations in the Sierra Baguales Mountain Range of southern Patagonia (50° S), inferred from the morphometric analysis of glacial cirques. Andean Geology 45, 357–378.

Araneda, A., Torrejon, F., Aguayo, M., Torres, L., Cruces, F., Cisternas, M., Urrutia, R., 2007. Historical records of San Rafael glacier advances (North Patagonian Icefield): another clue to 'Little Ice Age' timing in southern Chile? Holocene 17, 987-998.

Aravena, J.C., Luckman, B.H., 2009. Spatio-temporal rainfall patterns in Southern South America. International Journal of Climatology 29, 2106-2120.

Araya-Vergara, J., 2008. 2.2. The submarine geomorphology of the Chilean Patagonian fjords and piedmonts, in: Silva, N., Palma, S. (Eds.), Progress in the oceanographic knowledge of Chilean interior waters, from Puerto Montt to Cape Horn. Comité Oceanográfico Nacional - Pontificia Universidad Católica de Valparaíso, Valparaíso, pp. 25-27.

Ariztegui, D., Bianchi, M.M., Masaferro, J., Lafargue, E., Niessen, F., 1997. Interhemispheric synchrony of Late-glacial climatic instability as recorded in proglacial Lake Mascardi, Argentina. Journal of Quaternary Science: Published for the Quaternary Research Association 12, 333-338.

Ashworth, A.C., Markgraf, V., Villagran, C., 1991. Late Quaternary climatic history of the Chilean Channels based on fossil pollen and beetle analyses, with an analysis of the modern vegetation and pollen rain. Journal of Quaternary Science 6, 279-291.

Bahr, D.B., 2014. Estimation of glacier volume and volume change by scaling methods, Encyclopedia of Snow, Ice and Glaciers. Springer, pp. 278-280.

Bahr, D.B., Pfeffer, W.T., Kaser, G., 2014a. Glacier volume estimation as an ill-posed inversion. Journal of Glaciology 60, 922-934.

3140 Bahr, D.B., Pfeffer, W.T., Kaser, G., 2014b. A Review of Volume-Area Scaling of Glaciers. Reviews of
3141 Geophysics.

3142 Barr, I.D., Lovell, H., 2014. A review of topographic controls on moraine distribution. Geomorphology 226,
3143 44-64.

3144 Bassett, S.E., Milne, G.A., Mitrovica, J.X., Clark, P.U., 2005. Ice sheet and solid earth influences on far-field
3145 sea-level histories. Science 309, 925-928.

3146 Batchelor, C., Dowdeswell, J., 2014. The physiography of High Arctic cross-shelf troughs. Quaternary Science
3147 Reviews 92, 68-96.

3148 Bell, C., 2008. Punctuated drainage of an ice-dammed Quaternary lake in Southern South America.
3149 Geografiska Annaler: Series A, Physical Geography 90, 1-17.

3150 Bell, C.M., 2009. Quaternary lacustrine braid deltas on Lake General Carrera in southern Chile. Andean
3151 Geology 36, 51-65.

3152 Bendle, J.M., Palmer, A.P., Thorndycraft, V.R., Matthews, I.P., 2017a. High-resolution chronology for
3153 deglaciation of the Patagonian Ice Sheet at Lago Buenos Aires (46.5°S) revealed through varve chronology
3154 and Bayesian age modelling. Quaternary Science Reviews 177, 314-339.

3155 Bendle, J.M., Palmer, A.P., Thorndycraft, V.R., Matthews, I.P., 2019. Phased Patagonian Ice Sheet response to
3156 Southern Hemisphere atmospheric and oceanic warming between 18 and 17 ka. Scientific Reports 9, 4133.

3157 Bendle, J.M., Thorndycraft, V.R., Palmer, A.P., 2017b. The glacial geomorphology of the Lago Buenos Aires
3158 and Lago Pueyrredón ice lobes of central Patagonia. Journal of Maps 13, 654-673.

3159 Benito, G. and Thorndycraft, V.R. 2020. Catastrophic glacial lake outburst flooding of the Patagonian Ice
3160 Sheet. Earth-Science Reviews 200, 102996.

3161 Benn, D.I., Clapperton, C.M., 2000. Pleistocene glacitectonic landforms and sediments around central
3162 Magellan Strait, southernmost Chile: evidence for fast outlet glaciers with cold-based margins. Quaternary
3163 Science Reviews 19, 591-612.

3164 Bennett, K.D., Haberle, S.G., Lumley, S.H., 2000. The last glacial-Holocene transition in southern Chile.
3165 Science 290, 325-328.

3166 Bentley, M.J., 1996. The role of lakes in moraine formation, Chilean Lake District. Earth Surface Processes
3167 and Landforms 21, 493-507.

3168 Bentley, M.J., 1997. Relative and radiocarbon chronology of two former glaciers in the Chilean Lake District.
3169 Journal of Quaternary Science 12, 25-33.

3170 Bentley, M.J., McCulloch, R.D., 2005. Impact of neotectonics on the record of glacier and sea level
3171 fluctuations, strait of magellan, southern Chile. Geografiska Annaler: Series A, Physical Geography 87, 393-
3172 402.

3173 Bentley, M.J., Ó Cofaigh, C., Anderson, J.B., Conway, H., Davies, B., Graham, A.G.C., Hillenbrand, C.-D.,
3174 Hodgson, D.A., Jamieson, S.S.R., Larter, R.D., Mackintosh, A., Smith, J.A., Verleyen, E., Ackert, R.P., Bart, P.J.,
3175 Berg, S., Brunstein, D., Canals, M., Colhoun, E.A., Crosta, X., Dickens, W.A., Domack, E., Dowdeswell, J.A.,
3176 Dunbar, R., Ehrmann, W., Evans, J., Favier, V., Fink, D., Fogwill, C.J., Glasser, N.F., Gohl, K., Golledge, N.R.,
3177 Goodwin, I., Gore, D.B., Greenwood, S.L., Hall, B.L., Hall, K., Hedding, D.W., Hein, A.S., Hocking, E.P.,

3178 Jakobsson, M., Johnson, J.S., Jomelli, V., Jones, R.S., Klages, J.P., Kristoffersen, Y., Kuhn, G., Leventer, A.,
3179 Licht, K., Lilly, K., Lindow, J., Livingstone, S.J., Massé, G., McGlone, M.S., McKay, R.M., Melles, M., Miura, H.,
3180 Mulvaney, R., Nel, W., Nitsche, F.O., O'Brien, P.E., Post, A.L., Roberts, S.J., Saunders, K.M., Selkirk, P.M.,
3181 Simms, A.R., Spiegel, C., Stolldorf, T.D., Sugden, D.E., van der Putten, N., van Ommen, T., Verfaillie, D.,
3182 Vyverman, W., Wagner, B., White, D.A., Witus, A.E., Zwartz, D., 2014. A community-based geological
3183 reconstruction of Antarctic Ice Sheet deglaciation since the Last Glacial Maximum. Quaternary Science
3184 Reviews 100, 1-9.

3185 Bentley, M.J., Sugden, D.E., Hulton, N.R.J., McCullough, R.D., 2005. The landforms and pattern of
3186 deglaciation in the Strait of Magellan and Bahìa Inùtil, southernmost South America. Geografiska Annaler
3187 87A, 313-333.

3188 Beraza, L., Vilas, J., 1989. Paleomagnetism and relative age from Pleistocenic end moraines at Río Pico valley,
3189 Patagonia, Argentina., International geological congress. International Geological Congress, Washington DC,
3190 pp. 128-129.

3191 Bertrand, S., Charlet, F., Charlier, B., Renson, V., Fagel, N., 2008. Climate variability of southern Chile since
3192 the Last Glacial Maximum: a continuous sedimentological record from Lago Puyehue (40 S). Journal of
3193 Paleolimnology 39, 179-195.

3194 Bertrand, S., Hughen, K.A., Lamy, F., Stuut, J.-B., Torrejon, F., Lange, C.B., 2012. Precipitation as the main
3195 driver of Neoglacial fluctuations of Gualas glacier, Northern Patagonian Icefield. Climate of the Past 8, 519.

3196 Bertrand, S., Lange, C.B., Pantoja, S., Hughen, K., Van Tornhout, E., Wellner, J.S., 2017. Postglacial
3197 fluctuations of Cordillera Darwin glaciers (southernmost Patagonia) reconstructed from Almirantazgo fjord
3198 sediments. Quaternary Science Reviews 177, 265-275.

3199 Biester, H., Martinez-Cortizas, A., Birkenstock, S., Kilian, R., 2003. Effect of peat decomposition and mass loss
3200 on historic mercury records in peat bogs from Patagonia. Environmental science & technology 37, 32-39.

3201 Björck, S., Rundgren, M., Ljung, K., Unkel, I., Wallin, Å., 2012. Multi-proxy analyses of a peat bog on Isla de los
3202 Estados, easternmost Tierra del Fuego: a unique record of the variable Southern Hemisphere Westerlies
3203 since the last deglaciation. Quaternary Science Reviews 42, 1-14.

3204 Blomdin, R., Murray, A., Thomsen, K.J., Buylaert, J.-P., Sohbati, R., Jansson, K.N., Alexanderson, H., 2012.
3205 Timing of the deglaciation in southern Patagonia: Testing the applicability of K-Feldspar IRSL. Quaternary
3206 Geochronology 10, 264-272.

3207 Blunier, T., Schwander, J., Stauffer, B., Stocker, T., Dällenbach, A., Indermühle, A., Tschumi, J., Chappellaz, J.,
3208 Raynaud, D., Barnola, J.M., 1997. Timing of the Antarctic Cold Reversal and the atmospheric CO_2 increase
3209 with respect to the Younger Dryas Event. Geophysical Research Letters 24, 2683-2686.

3210 Boex, J., Fogwill, C., Harrison, S., Glasser, N.F., Hein, A., Schnabel, C., Xu, S., 2013. Rapid thinning of the late
3211 Pleistocene Patagonian Ice Sheet followed migration of the Southern Westerlies. Scientific Reports 3, 1-6.

3212 Borchers, B., Marrero, S., Balco, G., Caffee, M., Goehring, B., Lifton, N., Nishiizumi, K., Phillips, F., Schaefer, J.,
3213 Stone, J., 2016. Geological calibration of spallation production rates in the CRONUS-Earth project.
3214 Quaternary Geochronology 31, 188-198.

3215 Boulton, G., Clark, C., 1990. A highly mobile Laurentide ice sheet revealed by satellite images of glacial
3216 lineations. Nature 346, 813.

3217 Bourgois, J., Cisternas, M.E., Braucher, R., Bourlès, D., Frutos, J., 2016. Geomorphic Records along the
3218 General Carrera (Chile)–Buenos Aires (Argentina) Glacial Lake (46°–48° S), Climate Inferences, and Glacial
3219 Rebound for the Past 7–9 ka. The Journal of Geology 124, 27-53.

3220 Bown, F., Rivera, A., 2007. Climate changes and recent glacier behaviour in the Chilean Lake District. Global
3221 and Planetary Change 59, 79-86.

3222 Bown, F., Rivera, A., Zenteno, P., Bravo, C., Cawkwell, F., 2014. First Glacier Inventory and Recent Glacier
3223 Variation on Isla Grande de Tierra Del Fuego and Adjacent Islands in Southern Chile, in: Kargel, J.S., Leonard,
3224 G.J., Bishop, M.P., Kääb, A., Raup, B.H. (Eds.), Global Land Ice Measurements from Space. Springer Berlin
3225 Heidelberg, pp. 661-674.

3226 Boyd, B.L., Anderson, J.B., Wellner, J.S., Fernández, R.A., 2008. The sedimentary record of glacial retreat,
3227 Marinelli Fjord, Patagonia: Regional correlations and climate ties. Marine Geology 255, 165-178.

3228 Braun, M.H., Malz, P., Sommer, C., Farías-Barahona, D., Sauter, T., Casassa, G., Soruco, A., Skvarca, P.,
3229 Seehaus, T.C., 2019. Constraining glacier elevation and mass changes in South America. Nature Climate
3230 Change 9, 130-136.

3231 Breuer, S., Kilian, R., Schörner, D., Weinrebe, W., Behrmann, J., Baeza, O., 2013. Glacial and tectonic control
3232 on fjord morphology and sediment deposition in the Magellan region (53°S), Chile. Marine Geology 346, 31-
3233 46.

3234 Briggs, R.D., Pollard, D., Tarasov, L., 2014. A data-constrained large ensemble analysis of Antarctic evolution
3235 since the Eemian. Quaterny Science Reviews 103, 91–115.

3236 Bujalesky, G., Coronato, A., Isla, F., 2001. Ambientes glacifluviales y litorales Cuaternarios de la region del Rio
3237 Chico, Tierra del Fuego, Argentina. Revista de la Asociación Geológica Argentina 56, 73-90.

3238 Bujalesky, G.G., Heusser, C.J., Coronato, A.M., Roig, C.E., Rabassa, J.O., 1997. Pleistocene glaciolacustrine
3239 sedimentation at Lago Fagnano, Andes of Tierra del Fuego, Southernmost South America. Quaternary
3240 Science Reviews 16, 767-778.

3241 Cai, J., Powell, R.D., Cowan, E.A., Carlson, P.R., 1997. Lithofacies and seismic-reflection interpretation of
3242 temperate glacimarine sedimentation in Tarr Inlet, Glacier Bay, Alaska. Marine Geology 143, 5-37.

3243 Caldenius, C.C., 1932. Las glaciaciones cuaternarias en la Patagonia y Tierra del Fuego. Geografiska Annaler
3244 14, 1-164.

3245 Caniupán, M., Lamy, F., Lange, C.B., Kaiser, J., Arz, H., Kilian, R., Baeza Urrea, O., Aracena, C., Hebbeln, D.,
3246 Kissel, C., Laj, C., Mollenhauer, G., Tiedemann, R., 2011. Millennial-scale sea surface temperature and
3247 Patagonian Ice Sheet changes off southernmost Chile (53°S) over the past ~60 kyr. Paleoceanography 26 (3).

3248 Carrivick, J.L., Davies, B.J., James, W.H.M., Quincey, D.J., Glasser, N.F., 2016. Distributed ice thickness and
3249 glacier volume in southern South America. Global and Planetary Change 146, 122-132.

3250 Casassa, G., Brecher, H., Rivera, A., Aniya, M., 1997. A century-long recession record of Glaciar O'Higgins,
3251 Chilean Patagonia. Annals of Glaciology 24, 106-110.

3252 Chandler, B.M.P., Lovell, H., Boston, C.M., Lukas, S., Barr, I.D., Benediktsson, Í.Ö., Benn, D.I., Clark, C.D.,
3253 Darvill, C.M., Evans, D.J.A., Ewertowski, M.W., Loibl, D., Margold, M., Otto, J.-C., Roberts, D.H., Stokes, C.R.,
3254 Storrar, R.D., Stroeven, A.P., 2018. Glacial geomorphological mapping: A review of approaches and
3255 frameworks for best practice. Earth-Science Reviews 185, 806-846.

3256 Charlet, F., De Batist, M., Chapron, E., Bertrand, S., Pino, M., Urrutia, R., 2008. Seismic stratigraphy of Lago
3257 Puyehue (Chilean Lake District): new views on its deglacial and Holocene evolution. Journal of
3258 Paleolimnology 39, 163-177.

3259 Clague, J.J., Barendregt, R.W., Menounos, B., Roberts, N.J., Rabassa, J., Martinez, O., Ercolano, B., Corbella,
3260 H., Hemming, S.R., 2020. Pliocene and Early Pleistocene glaciation and landscape evolution on the
3261 Patagonian Steppe, Santa Cruz province, Argentina. Quaternary Science Reviews 227, 105992.

3262 Clapperton, C.M., 1989. Asymmetrical drumlins in Patagonia, Chile. Sedimentary Geology 62, 387-398.

3263 Clapperton, C.M., 1993. Nature of environmental changes in South America at the Last Glacial Maximum.
3264 Palaeogeography, Palaeoclimatology, Palaeoecology 101, 189-208.

3265 Clapperton, C.M., 1995. Fluctuations of local glaciers at the termination of the Pleistocene: 18-8 ka BP.
3266 Quaternary International 28, 41-50.

3267 Clapperton, C.M., Clapperton, C., 1993. Quaternary geology and geomorphology of South America. Elsevier
3268 Amsterdam etc.

3269 Clapperton, C.M., Sugden, D.E., Kaufman, D.S., McCulloch, R.D., 1995. The Last Glaciation in Central
3270 Magellan Strait, Southernmost Chile. Quaternary Research 44, 133-148.

3271 Clark, C.D., 1993. Mega-scale Glacial Lineations and Cross-cutting Ice-flow Landforms. Earth Surface
3272 Processes and Landforms 18, 1-29.

3273 Clark, C.D., 1997. Reconstructing the evolutionary dynamics of former ice sheets using multi-temporal
3274 evidence, remote sensing and GIS. Quaternary Science Reviews 16, 1067-1092.

3275 Clark, C.D., Ely, J.C., Greenwood, S.L., Hughes, A.L.C., Meehan, R., Barr, I.D., Bateman, M.D., Bradwell, T.,
3276 Doole, J., Evans, D.J.A., Jordan, C.J., Monteys, X., Pellicer, X.M., Sheehy, M., 2018. BRITICE Glacial Map,
3277 version 2: a map and GIS database of glacial landforms of the last British–Irish Ice Sheet. Boreas 47, 11-e18.

3278 Clark, C.D., Hughes, A.L.C., Greenwood, S.L., Jordan, C., Sejrup, H.P., 2012. Pattern and timing of retreat of
3279 the last British-Irish Ice Sheet. Quaternary Science Reviews 44, 112-146.

3280 Clark, P.U., Dyke, A.S., Shakun, J.D., Carlson, A.E., Clark, J., Wohlfarth, B., Mitrovica, J.X., Hostetler, S.W.,
3281 McCabe, A.M., 2009. The Last Glacial Maximum. Science 325, 710-714.

3282 Cogez, A., Herman, F., Pelt, É., Reuschlé, T., Morvan, G., Darvill, C.M., Norton, K.P., Christl, M., Märki, L. and
3283 Chabaux, F., 2018. U-Th and ^{10}Be constraints on sediment recycling in proglacial settings, Lago Buenos Aires,
3284 Patagonia. Earth Surface Dynamics, 6(1), 121-140.

3285 Coronato, A., Martínez, O., Rabassa, J., 2004. Glaciations in Argentine Patagonia, southern South America.
3286 Developments in Quaternary Sciences 2, 49-67.

3287 Coronato, A., Rabassa, J., 2011. Chapter 51 - Pleistocene Glaciations in Southern Patagonia and Tierra del
3288 Fuego, in: Jürgen Ehlers, P.L.G., Philip, D.H. (Eds.), Developments in Quaternary Sciences. Elsevier, pp. 715-
3289 727.

3290 Coronato, A., Seppälä, M., Ponce, J., Rabassa, J., 2009. Glacial geomorphology of the Pleistocene lake
3291 Fagnano ice lobe, Tierra del Fuego, southern South America. Geomorphology 112, 67-81.

3292 Cronin, T.M., 2012. Rapid sea level rise. Quaternary Science Reviews 56, 11-30.

3293 Cuffey, K.M., Clow, G.D., Steig, E.J., Buizert, C., Fudge, T., Koutnik, M., Waddington, E.D., Alley, R.B.,
3294 Severinghaus, J.P., 2016. Deglacial temperature history of West Antarctica. Proceedings of the National
3295 Academy of Sciences 113, 14249-14254.

3296 Curran-Everett, D., Benos, D.J., 2004. Guidelines for reporting statistics in journals published by the American
3297 Physiological Society. AJP - Gastrointestinal and Liver Physiology 287(2):G307.

3298 Darvill, C.M., Bentley, M.J., Stokes, C.R., 2015a. Geomorphology and weathering characteristics of erratic
3299 boulder trains on Tierra del Fuego, southernmost South America: Implications for dating of glacial deposits.
3300 Geomorphology 228, 382-397.

3301 Darvill, C.M., Bentley, M.J., Stokes, C.R., Hein, A.S., Rodés, Á., 2015b. Extensive MIS 3 glaciation in
3302 southernmost Patagonia revealed by cosmogenic nuclide dating of outwash sediments. Earth and Planetary
3303 Science Letters 429, 157-169.

3304 Darvill, C.M., Bentley, M.J., Stokes, C.R., Shulmeister, J., 2016. The timing and cause of glacial advances in the
3305 southern mid-latitudes during the last glacial cycle based on a synthesis of exposure ages from Patagonia
3306 and New Zealand. Quaternary Science Reviews 149, 200-214.

3307 Darvill, C.M., Stokes, C.R., Bentley, M.J., Evans, D.J.A., Lovell, H., 2017. Dynamics of former ice lobes of the
3308 southernmost Patagonian Ice Sheet based on a glacial landsystems approach. Journal of Quaternary Science
3309 32, 857-876.

3310 Darvill, C.M., Stokes, C.R., Bentley, M.J., Lovell, H., 2014. A glacial geomorphological map of the
3311 southernmost ice lobes of Patagonia: the Bahía Inútil–San Sebastián, Magellan, Otway, Skyring and Río
3312 Gallegos lobes. Journal of Maps 10, 500-520.

3313 DaSilva, J.L., Anderson, J.B., Stravers, J., 1997. Seismic facies changes along a nearly continuous 24°
3314 latitudinal transect: the fjords of Chile and the northern Antarctic Peninsula. Marine Geology 143, 103-123.

3315 Davies, B.J., Glasser, N.F., 2012. Accelerating recession in Patagonian glaciers from the "Little Ice Age" (c. AD
3316 1870) to 2011. Journal of Glaciology 58, 1063-1084.

3317 Davies, B.J., Hambrey, M.J., Smellie, J.L., Carrivick, J.L., Glasser, N.F., 2012. Antarctic Peninsula Ice Sheet
3318 evolution during the Cenozoic Era. Quaternary Science Reviews 31, 30-66.

3319 Davies, B.J., Thorndycraft, V.R., Fabel, D., Martin, J.R.V., 2018. Asynchronous glacier dynamics during the
3320 Antarctic Cold Reversal in central Patagonia. Quaternary Science Reviews 200, 287-312.

3321 Dalziel, I.W., de Wit, M.J., Palmer, K.F., 1974. Fossil marginal basin in the southern Andes. Nature 250, 291-
3322 294.

3323 de Agostini, A.M., 1956. Treinta años en Tierra del Fuego. Elefante Blanco, Buenos Aires.

3324 de Gasperi, G.B., 1922. Scritti vari di geografia e geologia; pubblicazione postuma.

3325 Del Valle, R.A., Lirio, J.M., Nunez, H.J., Tatur, A., Rinaldi, C.A., 2000. Sedimentary cores from Mascardi Lake,
3326 Argentina: a key site to study Elpalafquen paleolake, in: Southern Hemisphere Paleo-and Neoclimates.
3327 Springer, pp. 275–286.

De Muro, S., Brambati, A., Tecchiato, S., Porta, M., Ibba, A., 2017. Geomorphology of marine and transitional terraces and raised shorelines between Punta Paulo and Porvenir, Tierra del Fuego, Straits of Magellan – Chile. Journal of Maps 13, 311-321.

De Muro, S., Tecchiato, S., Porta, M., Buosi, C., Ibba, A., 2018. Geomorphology of marine and glacio-lacustrine terraces and raised shorelines in the northern sector of Península Brunswick, Patagonia, Straits of Magellan, Chile AU - De Muro, Sandro. Journal of Maps 14, 135-143.

de Porras, M.E., Maldonado, A., Abarzúa, A.M., Cárdenas, M.L., Francois, J.P., Martel-Cea, A., Stern, C.R., Méndez, C., Reyes, O., 2012. Postglacial vegetation, fire and climate dynamics at Central Chilean Patagonia (Lake Shaman, 44 S). Quaternary Science Reviews 50, 71-85.

de Porras, M.E., Maldonado, A., Quintana, F., Martel Cea, A., Reyes, O., Méndez Melgar, C., 2014. Environmental and climatic changes in Central Chilean Patagonia since the Late Glacial (Mallín El Embudo, 44 S).

Denton, G.H., Lowell, T.V., Heusser, C.J., Schlüchter, C., Andersen, B.G., Heusser, L.E., Moreno, P.I., Marchant, D.R., 1999. Geomorphology, Stratigraphy, and Radiocarbon Chronology of LlanquihueDrift in the Area of the Southern Lake District, Seno Reloncaví, and Isla Grande de Chiloé, Chile. Geografiska Annaler: Series A, Physical Geography 81, 167-229.

Doughty, A. M., Schaefer, J. M., Putnam, A. E., Denton, G. H., Kaplan, M. R., Barrell, D. J. A., Andersen, B.G., Finkel, R.C., Schwartz, R. 2015. Mismatch of glacier extent and summer insolation in Southern Hemisphere mid-latitudes. Geology, 43(5), 407–410.

Douglass, D., Singer, B., Kaplan, M., Mickelson, D., Caffee, M., 2006. Cosmogenic nuclide surface exposure dating of boulders on last-glacial and late-glacial moraines, Lago Buenos Aires, Argentina: interpretive strategies and paleoclimate implications. Quaternary Geochronology 1, 43-58.

Douglass, D.C., Singer, B.S., Kaplan, M.R., Ackert, R.P., Mickelson, D.M., Caffee, M.W., 2005. Evidence of early Holocene glacial advances in southern South America from cosmogenic surface-exposure dating. Geology 33, 237-240.

Dowdeswell, J.A., Canals, M., Jakobsson, M., Todd, B.J., Dowdeswell, E.K., Hogan, K.A., 2016a. The variety and distribution of submarine glacial landforms and implications for ice-sheet reconstruction. Geological Society, London, Memoirs 46, 519-552.

Dowdeswell, J.A., Dowdeswell, E.K., Rodrigo, C., 2016b. Pockmarks in the fjords of Chilean Patagonia. Geological Society, London, Memoirs 46, 109-110.

Dowdeswell, J.A., Dowdeswell, E.K., Rodrigo, C., Diaz, J., 2016c. Assemblage of glacial and related landforms in the fjords of southern Chile. Geological Society, London, Memoirs 46, 131-134.

Dowdeswell, J.A., Forsberg, C.F., 1992. The size and frequency of icebergs and bergy bits derived from tidewater glaciers in Kongsfjorden, northwest Spitsbergen. Polar Research 11, 81-91.

Dowdeswell, J.A., Vásquez, M., 2013. Submarine landforms in the fjords of southern Chile: implications for glacimarine processes and sedimentation in a mild glacier-influenced environment. Quaternary Science Reviews 64, 1-19.

Elbert, J., Wartenburger, R., von Gunten, L., Urrutia, R., Fischer, D., Fujak, M., Hamann, Y., Greber, N.D., Grosjean, M., 2013. Late Holocene air temperature variability reconstructed from the sediments of Laguna Escondida, Patagonia, Chile (45° 30’ S). Palaeogeography, Palaeoclimatology, Palaeoecology 369, 482-492.

3368 Ely, J. C., Clark, C. D., Hindmarsh, R. C. A., Hughes, A. L. C., Greenwood, S. L., Bradley, S. L., Gasson, E.,
3369 Gregoire, L., Gandy, N., Stokes, C. R., Small, D. 2019. Recent progress on combining geomorphological and
3370 geochronological data with ice sheet modelling, demonstrated using the last British–Irish Ice Sheet. Journal
3371 of Quaternary Science.

3372 Ercolano, B., Coronato, A., Tiberi, P., Corbella, H., Marderwald, G., 2016. Glacial geomorphology of the
3373 tableland east of the Andes between the Coyle and Gallegos river valleys, Patagonia, Argentina. Journal of
3374 Maps 12, 304-313.

3375 Ercolano, B., Mazzoni, E., Vazquez, M., Rabassa, J., 2004. Drumlins and drumlinoid forms of the Lower
3376 Pleistocene in southern Patagonia, Province of Santa Cruz. Rev. Asoc. Geol. Argent 59, 771-777.

3377 Evenson, E.B., Burkhart, P.A., Gosse, J.C., Baker, G.S., Jackofsky, D., Meglioli, A., Dalziel, I., Kraus, S., Alley,
3378 R.B., Berti, C., 2009. Enigmatic boulder trains, supraglacial rock avalanches, and the origin of “Darwin's
3379 boulders,” Tierra del Fuego. GSA Today 19, 4-10.

3380 Falaschi, D., Bravo, C., Masiokas, M., Villalba, R., Rivera, A., 2013. First Glacier Inventory and Recent Changes
3381 in Glacier Area in the Monte San Lorenzo Region (47°S), Southern Patagonian Andes, South America. Arctic,
3382 Antarctic, and Alpine Research 45, 19-28.

3383 Fernandez, R., Anderson, J., Bertrand, S., Wellner, J., 2012. Gualas Glacier sedimentary record of climate and
3384 environmental change, Golfo Elefantes, Western Patagonia (46.5° S). The Holocene 22, 451-463.

3385 Fernández, R., Gulick, S., Rodrigo, C., Domack, E., Leventer, A., 2017. Seismic stratigraphy and glacial cycles in
3386 the inland passages of the Magallanes región of Chile, southernmost South America. Marine Geology 386,
3387 19-31.

3388 Fernandez, R.A., Anderson, J.B., Wellner, J.S., Hallet, B., 2011. Timescale dependence of glacial erosion rates:
3389 a case study of Marinelli Glacier, Cordillera Darwin, southern Patagonia. Journal of Geophysical Research:
3390 Earth Surface 116.

3391 Feruglio, E., 1933. I terrazzi marini della Patagonia. Cooperativa Tip. Edit. Paolo Galeati.

3392 Fick, S.E., Hijmans, R.J., 2017. WorldClim 2: new 1-km spatial resolution climate surfaces for global land
3393 areas. International Journal of Climatology 37, 4302-4315.

3394 Fildani, A., Hessler, A.M., 2005. Stratigraphic record across a retroarc basin inversion: Rocas Verdes–
3395 Magallanes basin, Patagonian Andes, Chile. Geological Society of America Bulletin 117, 1596-1614.

3396 Fletcher, M.-S., Moreno, P.I., 2012. Have the Southern Westerlies changed in a zonally symmetric manner
3397 over the last 14,000 years? A hemisphere-wide take on a controversial problem. Quaternary International
3398 253, 32-46.

3399 Fogwill, C.J., Kubik, P.W., 2005. A Glacial Stage Spanning the Antarctic Cold Reversal in Torres del Paine
3400 (51°S), Chile, Based on Preliminary Cosmogenic Exposure Ages. Geografiska Annaler. Series A, Physical
3401 Geography 87, 403-408.

3402 Forsyth, R., Prior, D., 1992. Cenozoic continental geology of South America and its relations to the evolution
3403 of the Chile triple junction. Proceedings of the Ocean Drilling Program, Initial Reports 141, 23-31.

3404 García, J.-L., Hall, B.L., Kaplan, M.R., Vega, R.M., Strelin, J.A., 2014. Glacial geomorphology of the Torres del
3405 Paine region (southern Patagonia): Implications for glaciation, deglaciation and paleolake history.
3406 Geomorphology 204, 599-616.

García, J.-L., Hein, A.S., Binnie, S.A., Gómez, G.A., González, M.A., Dunai, T.J., 2018. The MIS 3 maximum of the Torres del Paine and Última Esperanza ice lobes in Patagonia and the pacing of southern mountain glaciation. Quaternary Science Reviews 185, 9-26.

García, J.L., 2012. Late Pleistocene ice fluctuations and glacial geomorphology of the Archipiélago de Chiloé, southern Chile. Geografiska Annaler: Series A, Physical Geography 94, 459-479.

García, J.L., Kaplan, M.R., Hall, B.L., Schaefer, J.M., Vega, R.M., Schwartz, R., Finkel, R., 2012. Glacier expansion in southern Patagonia throughout the Antarctic Cold Reversal. Geology 40, 859-862.

García, J.-L., Maldonado, A., de Porras, M.E., Delaunay, A.N., Reyes, O., Ebensperger, C.A., Binnie, S.A., Lüthgens, C., Méndez, C., 2019. Early deglaciation and paleolake history of Río Cisnes Glacier, Patagonian Ice Sheet (44° S). Quaternary Research 91, 194–217.

Garcia, J.-L., Strelin, J.A., Vega, R.M., Hall, B.L., Stern, C.R., 2015. Deglacial ice-marginal glaciolacustrine environments and structural moraine building in Torres del Paine, Chilean southern Patagonia. Andean Geology 42 (2), 190-212.

Gardner, A.S., Moholdt, G., Cogley, J.G., Wouters, B., Arendt, A.A., Wahr, J., Berthier, E., Hock, R., Pfeffer, W.T., Kaser, G., Ligtenberg, S.R.M., Bolch, T., Sharp, M.J., Hagen, J.O., van den Broeke, M.R., Paul, F., 2013. A Reconciled Estimate of Glacier Contributions to Sea Level Rise: 2003 to 2009. Science 340, 852–857.

Garreaud, R., 2007. Precipitation and circulation covariability in the extratropics. Journal of Climate 20, 4789-4797.

Garreaud, R., Lopez, P., Minvielle, M., Rojas, M., 2013. Large-Scale Control on the Patagonian Climate. Journal of Climate 26, 215-230.

Garreaud, R.D., Vuille, M., Compagnucci, R., Marengo, J., 2009. Present-day South American climate. Palaeogeography Palaeoclimatology Palaeoecology 281, 180-195.

Garibotti, I.A., Villalba, R., 2009. Lichenometric dating using Rhizocarpon subgenus Rhizocarpon in the Patagonian Andes, Argentina. Quaternary Research 71, 271–283.

Garibotti, I.A., Villalba, R., 2017. Colonization of mid- and late-Holocene moraines by lichens and trees in the Magellanic sub-Antarctic province. Polar Biology 1–15

GEBCO Compilation Group, 2019. GEBCO 2019 Grid (doi:10.5285/836f016a-33be-6ddc-e053-6c86abc0788e) Available at http://www.gebco.net.

Glasser, N., Jansson, K., 2008. The Glacial Map of southern South America. Journal of Maps 4, 175-196.

Glasser, N.F., Ghiglione, M.C., 2009. Structural, tectonic and glaciological controls on the evolution of fjord landscapes. Geomorphology 105, 291-302.

Glasser, N.F., Hambrey, M.J., Aniya, M., 2002. An advance of Soler Glacier, North Patagonian Icefield, at c. AD 1222-1342. Holocene 12, 113-120.

Glasser, N.F., Harrison, S., 2005. Sediment distribution around glacially abraded bedrock landforms (whalebacks) at Lago Tranquilo, Chile. Geografiska Annaler Series A-Physical Geography 87A, 421-430.

3442 Glasser, N.F., Harrison, S., Ivy-Ochs, S., Duller, G.A.T., Kubik, P.W., 2006a. Evidence from the Rio Bayo valley
3443 on the extent of the North Patagonian Icefield during the Late Pleistocene - Holocene transition. Quaternary
3444 Research 65, 70-77.

3445 Glasser, N.F., Harrison, S., Jansson, K.N., 2009. Topographic controls on glacier sediment-landform
3446 associations around the temperate North Patagonian Icefield. Quaternary Science Reviews 28, 2817-2832.

3447 Glasser, N.F., Harrison, S., Jansson, K.N., Anderson, K., Cowley, A., 2011a. Global sea-level contribution from
3448 the Patagonian Icefields since the Little Ice Age maximum. Nature Geoscience 4, 303-307.

3449 Glasser, N.F., Harrison, S., Schnabel, C., Fabel, D., Jansson, K.N., 2012. Younger Dryas and early Holocene age
3450 glacier advances in Patagonia. Quaternary Science Reviews 58, 7-17.

3451 Glasser, N.F., Holt, T.O., Evans, Z.D., Davies, B.J., Pelto, M., Harrison, S., 2016a. Recent spatial and temporal
3452 variations in debris cover on Patagonian glaciers. Geomorphology 273, 202-216.

3453 Glasser, N.F., Jansson, K., Mitchell, W.A., Harrison, S., 2006b. The geomorphology and sedimentology of the
3454 'Tempanos' moraine at Laguna San Rafael, Chile. Journal of Quaternary Science 21, 629-643.

3455 Glasser, N.F., Jansson, K.N., 2005. Fast-flowing outlet glaciers of the Last Glacial Maximum Patagonian
3456 Icefield. Quaternary Research 63, 206-211.

3457 Glasser, N.F., Jansson, K.N., Duller, G.A.T., Singarayer, J., Holloway, M., Harrison, S., 2016b. Glacial lake
3458 drainage in Patagonia (13-8 kyr) and response of the adjacent Pacific Ocean. Scientific Reports 6, 21064.

3459 Glasser, N.F., Jansson, K.N., Goodfellow, B.W., de Angelis, H., Rodnight, H., Rood, D.H., 2011b. Cosmogenic
3460 nuclide exposure ages for moraines in the Lago San Martin Valley, Argentina. Quaternary Research 75, 636-
3461 646.

3462 Glasser, N.F., Jansson, K.N., Harrison, S., Kleman, J., 2008. The glacial geomorphology and Pleistocene history
3463 of South America between 38°S and 56°S. Quaternary Science Reviews 27, 365-390.

3464 Glasser, N.F., Jansson, K.N., Harrison, S., Rivera, A., 2005. Geomorphological evidence for variations of the
3465 North Patagonian Icefield during the Holocene. Geomorphology 71, 263-277.

3466 Golledge, N.R., Mackintosh, A.N., Anderson, B.M., Buckley, K.M., Doughty, A.M., Barrell, D.J.A., Denton, G.H.,
3467 Vandergoes, M.J., Andersen, B.G., Schaefer, J.M., 2012. Last Glacial Maximum climate in New Zealand
3468 inferred from a modelled Southern Alps icefield. Quaternary Science Reviews 46, 30-45.

3469 Golledge, N.R., Menviel, L., Carter, L., Fogwill, C.J., England, M.H., Cortese, G., Levy, R.H., 2014. Antarctic
3470 contribution to meltwater pulse 1A from reduced Southern Ocean overturning. Nature Communications 5,
3471 5107.

3472 Gordillo, S., Bujalesky, G.G., Pirazzoli, P.A., Rabassa, J.O., Saliège, J.-F., 1992. Holocene raised beaches along
3473 the northern coast of the Beagle Channel, Tierra del Fuego, Argentina. Palaeogeography, Palaeoclimatology,
3474 Palaeoecology 99, 41-54.

3475 Gourlet, P., Rignot, E., Rivera, A., Casassa, G., 2016. Ice thickness of the northern half of the Patagonia
3476 Icefields of South America from high-resolution airborne gravity surveys. Geophysical Research Letters 43,
3477 241–249.

3478 Graham, A.G.C., Fretwell, P.T., Larter, R.D., Hodgson, D.A., Wilson, C.K., Tate, A.J., Morris, P., 2008. A new
3479 bathymetric compilation highlighting extensive paleo–ice sheet drainage on the continental shelf, South
3480 Georgia, sub-Antarctica. Geochemistry, Geophysics, Geosystems 9, Q07011.

3481 Guilderson, T., Burckle, L., Hemming, S., Peltier, W., 2000. Late Pleistocene sea level variations derived from
3482 the Argentine Shelf. Geochemistry, Geophysics, Geosystems 1.

3483 Haberle, S., Bennett, K., 2004. Postglacial formation and dynamics of North Patagonian Rainforest in the
3484 Chonos Archipelago, southern Chile. Quaternary Science Reviews 23, 2433-2452.

3485 Haberzettl, T., Anselmetti, F.S., Bowen, S.W., Fey, M., Mayr, C., Zolitschka, B., Ariztegui, D., Mauz, B.,
3486 Ohlendorf, C., Kastner, S., 2009. Late Pleistocene dust deposition in the Patagonian steppe-extending and
3487 refining the paleoenvironmental and tephrochronological record from Laguna Potrok Aike back to 55 ka.
3488 Quaternary Science Reviews 28, 2927-2939.

3489 Hajdas, I., Bonani, G., Moreno, P.I., Ariztegui, D., 2003. Precise radiocarbon dating of Late-Glacial cooling in
3490 mid-latitude South America. Quaternary Research 59, 70-78.

3491 Hall, B., Denton, G., Lowell, T., Bromley, G., Putnam, A., 2017. Retreat of the Cordillera Darwin icefield during
3492 Termination I. Cuadernos de Investigación Geográfica 43, 751-766.

3493 Hall, B.L., 2009. Holocene glacial history of Antarctica and the sub-Antarctic islands. Quaternary Science
3494 Reviews 28, 2213-2230.

3495 Hall, B.L., Porter, C.T., Denton, G.H., Lowell, T.V., Bromley, G.R.M., 2013. Extensive recession of Cordillera
3496 Darwin glaciers in southernmost South America during Heinrich Stadial 1. Quaternary Science Reviews 62,
3497 49-55.

3498 Hall, B.L., Lowell, T. V, Bromley, G.R.M., Denton, G.H., Putnam, A.E., 2019. Holocene glacier fluctuations on
3499 the northern flank of Cordillera Darwin, southernmost South America. Quaternary Science Reviews 222,
3500 105904.

3501 Harrison, S., Glasser, N.F., 2011. Chapter 54 - The Pleistocene Glaciations of Chile, in: Jürgen Ehlers, P.L.G.,
3502 Philip, D.H. (Eds.), Developments in Quaternary Sciences. Elsevier, pp. 739–756.

3503 Harrison, S., Glasser, N., Winchester, V., Haresign, E., Warren, C., Duller, G.A.T., Bailey, R., Ivy-Ochs, S.,
3504 Jansson, K., Kubik, P., 2008. Glaciar Leon, Chilean Patagonia: late-Holocene chronology and geomorphology.
3505 Holocene 18, 643-652.

3506 Harrison, S., Glasser, N.F., Duller, G.A.T., Jansson, K.N., 2012. Early and mid-Holocene age for the Tempanos
3507 moraines, Laguna San Rafael, Patagonian Chile. Quaternary Science Reviews 31, 82-92.

3508 Harrison, S., Smith, D.E., Glasser, N.F., 2019. Late Quaternary meltwater pulses and sea level change. Journal
3509 of Quaternary Science 34, 1–15.

3510 Harrison, S., Winchester, V., Glasser, N., 2007. The timing and nature of recession of outlet glaciers of Hielo
3511 Patagonico Norte, Chile, from their Neoglacial IV (Little Ice Age) maximum positions. Global and Planetary
3512 Change 59, 67-78.

3513 Hatté, C., Jull, A.J.T., 2013. RADIOCARBON DATING | ^{14}C of Plant Macrofossils, in: Elias, S.A., Mock, C.J.B.T.-E.
3514 of Q.S. (Second E. (Eds.), . Elsevier, Amsterdam, pp. 361–367.

3515 Hein, A.S., Cogez, A., Darvill, C.M., Mendelova, M., Kaplan, M.R., Herman, F., Dunai, T.J., Norton, K., Xu, S.,
3516 Christl, M., 2017. Regional mid-Pleistocene glaciation in central Patagonia. Quaternary Science Reviews 164,
3517 77-94.

3518 Hein, A.S., Dunai, T.J., Hulton, N.R.J., Xu, S., 2011. Exposure dating outwash gravels to determine the age of
3519 the greatest Patagonian glaciations. Geology 39, 103-106.

3520 Hein, A.S., Hulton, N.R., Dunai, T.J., Sugden, D.E., Kaplan, M.R., Xu, S., 2010. The chronology of the Last
3521 Glacial Maximum and deglacial events in central Argentine Patagonia. Quaternary Science Reviews 29, 1212-
3522 1227.

3523 Hein, A.S., Hulton, N.R.J., Dunai, T.J., Schnabel, C., Kaplan, M.R., Naylor, M., Xu, S., 2009. Middle Pleistocene
3524 glaciation in Patagonia dated by cosmogenic-nuclide measurements on outwash gravels. Earth and Planetary
3525 Science Letters 286, 184-197.

3526 Heirman, K., De Batist, M., Charlet, F., Moernaut, J., Chapron, E., Brümmer, R., Pino, M., Urrutia, R., 2011.
3527 Detailed seismic stratigraphy of Lago Puyehue: implications for the mode and timing of glacier retreat in the
3528 Chilean Lake District. Journal of Quaternary Science 26, 665-674.

3529 Henríquez, W.I., Villa-Martínez, R., Vilanova, I., De Pol-Holz, R., Moreno, P.I., 2017. The last glacial
3530 termination on the eastern flank of the central Patagonian Andes (47 ° S). Climate of the Past 13, 879-895.

3531 Hervé, F., Pankhurst, R., Trouw, R., Fanning, C., Dzogolyk, E., Solari, M., Suárez, M., 2003. Geological
3532 Observations at the Western Portion of the Scotia–South America plate Boundary: results of the “Penguin”
3533 2003 Cruise, X Congreso Geológico Chileno. CD ROM.

3534 Hervé, F., Pankhurst, R.J., Fanning, C.M., Calderón, M., Yaxley, G.M., 2007. The South Patagonian batholith:
3535 150 my of granite magmatism on a plate margin. Lithos 97, 373-394.

3536 Heusser, C., 1999. 14 C Age of Glaciation in Estrecho De Magallanes–Bahía Inútil, Chile. Radiocarbon 41, 287-
3537 293.

3538 Heusser, C., Heusser, L., Hauser, A., 1989. A 12,000 yr BP tephra layer at Bahia Inutil (Tierra del Fuego, Chile).
3539 Anales del Instituto de la Patagonia 19, 39-49.

3540 Heusser, C.J., Heusser, L.E., Lowell, T. V, 1999. Paleoecology of the southern Chilean Lake District-Isla Grande
3541 de Chiloé during middle–late Llanquihue glaciation and deglaciation. Geografiska Annaler Series A, Physical
3542 Geography 81, 231–284.

3543 Heusser, C., Rabassa, J., 1987. Cold climatic episode of Younger Dryas age in Tierra del Fuego. Nature 328,
3544 609.

3545 Heusser, C.J., 1974. Vegetation and climate of the southern Chilean Lake District during and since the last
3546 interglaciation. Quaternary Research 4, 290-315.

3547 Heusser, C.J., 1989. Climate and chronology of Antarctica and adjacent South America over the past 30,000
3548 yr. Palaeogeography, Palaeoclimatology, Palaeoecology 76, 31-37.

3549 Heusser, C.J., 1998. Deglacial paleoclimate of the American sector of the Southern Ocean: Late Glacial–
3550 Holocene records from the latitude of Canal Beagle (55°S), Argentine Tierra del Fuego. Palaeogeography,
3551 Palaeoclimatology, Palaeoecology 141, 277-301.

3552 Heusser, C.J., 2003. Ice Age Southern Andes. Elsevier.

3553 Heusser, C.J., Denton, G.H., Hauser, A., Andersen, B.G., Lowell, T.V., 1995. Quaternary pollen records from
3554 the Archipiélago de Chiloé in the context of glaciation and climate. Andean Geology 22, 25-46.

3555 Heusser, C.J., Heusser, L.E., Lowell, T.V., 1999. Paleoecology of the southern Chilean Lake District-Isla Grande
3556 de Chiloé during middle–late Llanquihue glaciation and deglaciation. Geografiska Annaler: Series A, Physical
3557 Geography 81, 231-284.

3558 Heusser, C.J., Heusser, L.E., Lowell, T.V., 2000. Deglacial palaeoclimate at Puerto del Hambre, subantarctic
3559 Patagonia, Chile. Journal of Quaternary Science 15, 101-114.

3560 Hidy, A.J., Gosse, J.C., Pederson, J.L., Mattern, J.P., Finkel, R.C., 2010. A geologically constrained Monte Carlo
3561 approach to modeling exposure ages from profiles of cosmogenic nuclides: An example from Lees Ferry,
3562 Arizona. Geochemistry, Geophysics, Geosystems 11.

3563 Hillenbrand, C.-D., Bentley, M.J., Stolldorf, T.D., Hein, A.S., Kuhn, G., Graham, A.G.C., Fogwill, C.J.,
3564 Kristoffersen, Y., Smith, J.A., Anderson, J.B., Larter, R.D., Melles, M., Hodgson, D.A., Mulvaney, R., Sugden,
3565 D.E., 2014. Reconstruction of changes in the Weddell Sea sector of the Antarctic Ice Sheet since the Last
3566 Glacial Maximum. Quaternary Science Reviews 100, 111-136.

3567 Hodgson, D.A., Graham, A.G.C., Roberts, S.J., Bentley, M.J., Ó Cofaigh, C., Verleyen, E., Vyverman, W.,
3568 Jomelli, V., Favier, V., Brunstein, D., Verfaillie, D., Colhoun, E.A., Saunders, K.M., Selkirk, P.M., Mackintosh,
3569 A., Hedding, D.W., Nel, W., Hall, K., McGlone, M.S., Van der Putten, N., Dickens, W.A., Smith, J.A., 2014.
3570 Terrestrial and submarine evidence for the extent and timing of the Last Glacial Maximum and the onset of
3571 deglaciation on the maritime-Antarctic and sub-Antarctic islands. Quaternary Science Reviews 100, 137-158.

3572 Hogg, A.G., Hua, Q., Blackwell, P.G., Niu, M., Buck, C.E., Guilderson, T.P., Heaton, T.J., Palmer, J.G., Reimer,
3573 P.J., Reimer, R.W., Turney, C.S.M., Zimmerman, S.R.H., 2013. SHCal13 Southern Hemisphere Calibration, 0–
3574 50,000 Years cal BP. Radiocarbon 55, 1889-1903.

3575 Holmlund, P., Fuenzalida, H., 1995. Anomalous glacier responses to 20th century climatic changes in Darwin
3576 Cordillera, southern Chile. Journal of Glaciology 41, 465-473.

3577 Horta, L.R., Belardi, J.B., Georgieff, S.M., Carballo Marina, F., 2019. Paleogeographic reconstruction of the Tar
3578 – San Martín lacustrine system during late Pleistocene to early Holocene: Landscape availability and hunter-
3579 gatherer circulation (Santa Cruz, Argentina). Quaternary International 512, 45-51.

3580 Hubbard, A., Hein, A.S., Kaplan, M.R., Hulton, N.R.J., Glasser, N., 2005. A modelling reconstruction of the Last
3581 Glacial Maximum ice sheet and its deglaciation in the vicinity of the Northern Patagonian Icefield, South
3582 America. Geografiska Annaler 87, 375-391.

3583 Hughes, A.L., Gyllencreutz, R., Lohne, Ø.S., Mangerud, J., Svendsen, J.I., 2016. The last Eurasian ice sheets–a
3584 chronological database and time-slice reconstruction, DATED-1. Boreas 45, 1-45.

3585 Hughes, P.D., Gibbard, P.L., Ehlers, J., 2013. Timing of glaciation during the last glacial cycle: evaluating the
3586 concept of a global 'Last Glacial Maximum' (LGM). Earth-Science Reviews 125, 171-198.

3587 Hulton, N.R., Sugden, D.E., Payne, A., Clapperton, C., 1994. Glacier modeling and the climate of Patagonia
3588 during the Last Glacial Maximum. Quaternary Research 42, 1-19.

3589 Hulton, N.R.J., Purves, R.S., McCulloch, R.D., Sugden, D.E., Bentley, M.J., 2002. The Last Glacial Maximum and
3590 deglaciation in southern South America. Quaternary Science Reviews 21, 233-241.

3591 Huss, M., Hock, R., 2018. Global-scale hydrological response to future glacier mass loss. Nature Climate
3592 Change 8, 135–140.

3593 Iglesias, V., Markgraf, V., Whitlock, C., 2016. 17,000 years of vegetation, fire and climate change in the
3594 eastern foothills of the Andes (lat. 44° S). Palaeogeography, Palaeoclimatology, Palaeoecology 457, 195-208.

3595 Isla, F.I., 2013. The flooding of the San Matías Gulf: The Northern Patagonia sea-level curve. Geomorphology
3596 203, 60–65.

3597 Ivy-Ochs, S., Kerschner, H., Maisch, M., Christl, M., Kubik, P.W., Schlüchter, C., 2009. Latest Pleistocene and
3598 Holocene glacier variations in the European Alps. Quaternary Science Reviews 28, 2137-2149.

3599 Izagirre, E., Darvill, C.M., Rada, C., Aravena, J.C., 2018. Glacial geomorphology of the Marinelli and Pigafetta
3600 glaciers, Cordillera Darwin Icefield, southernmost Chile. Journal of Maps 14, 269-281.

3601 Jaber, W.A., Floricioiu, D., Rott, H., 2016. Geodetic mass balance of the Patagonian Icefields derived from
3602 SRTM and TanDEM-X data, 2016 IEEE International Geoscience and Remote Sensing Symposium (IGARSS),
3603 pp. 342-345.

3604 Jansson, K.N., Glasser, N.F., 2005. Using Landsat 7 ETM+ imagery and Digital Terrain Models for mapping
3605 glacial lineaments on former ice sheet beds. International Journal of Remote Sensing 26, 3931-3941.

3606 Jomelli, V., Favier, V., Vuille, M., Braucher, R., Martin, L., Blard, P.H., Colose, C., Brunstein, D., He, F., Khodri,
3607 M., Bourles, D.L., Leanni, L., Rinterknecht, V., Grancher, D., Francou, B., Ceballos, J.L., Fonseca, H., Liu, Z.,
3608 Otto-Bliesner, B.L., 2014. A major advance of tropical Andean glaciers during the Antarctic cold reversal.
3609 Nature 513(7517), 224-228.

3610 Kaiser, J., Lamy, F., Arz, H.W., Hebbeln, D., 2007. Dynamics of the millennial-scale sea surface temperature
3611 and Patagonian Ice Sheet fluctuations in southern Chile during the last 70 kyr (ODP Site 1233). Quaternary
3612 International 161, 77-89.

3613 Kaplan, M., Schaefer, J., Strelin, J., Denton, G., Anderson, R., Vandergoes, M., Finkel, R., Schwartz, R., Travis,
3614 S., Garcia, J., 2016. Patagonian and southern South Atlantic view of Holocene climate. Quaternary Science
3615 Reviews 141, 112-125.

3616 Kaplan, M.R., Ackert, R.P., Singer, B.S., Douglass, D.C., Kurz, M.D., 2004. Cosmogenic nuclide chronology of
3617 millennial-scale glacial advances during O-isotope stage 2 in Patagonia. GSA Bulletin 116, 308-321.

3618 Kaplan, M.R., Coronato, A., Hulton, N.R.J., Rabassa, J.O., Kubik, P.W., Freeman, S.P.H.T., 2007. Cosmogenic
3619 nuclide measurements in southernmost South America and implications for landscape change.
3620 Geomorphology 87, 284-301.

3621 Kaplan, M.R., Douglass, D.C., Singer, B.S., Ackert, R.P., Caffee, M.W., 2005. Cosmogenic nuclide chronology of
3622 pre-last glacial maximum moraines at Lago Buenos Aires, 46°S, Argentina. Quaternary Research 63, 301-315.

3623 Kaplan, M.R., Fogwill, C.J., Sugden, D.E., Hulton, N.R.J., Kubik, P.W., Freeman, S.P.H.T., 2008. Southern
3624 Patagonian glacial chronology for the Last Glacial period and implications for Southern Ocean climate.
3625 Quaternary Science Reviews 27, 284-294.

3626 Kaplan, M.R., Hein, A.S., Hubbard, A., Lax, S.M., 2009. Can glacial erosion limit the extent of glaciation?
3627 Geomorphology 103, 172-179.

3628 Kaplan, M.R., Strelin, J.A., Schaefer, J.M., Denton, G.H., Finkel, R.C., Schwartz, R., Putnam, A.E., Vandergoes,
3629 M.J., Goehring, B.M., Travis, S.G., 2011. In-situ cosmogenic 10Be production rate at Lago Argentino,
3630 Patagonia: Implications for late-glacial climate chronology. Earth and Planetary Science Letters 309, 21-32.

3631 Kilian, R., Baeza, O., Breuer, S., Ríos, F., Arz, H., Lamy, F., Wirtz, J., Baque, D., Korf, P., Kremer, K., 2013a.
3632 Evolución paleogeográfica y paleoecológica del Sistema de fiordos del Seno Skyring y Seno Otway en la
3633 region de Magallanes durante el Tardiglacial y Holoceno. Anales del Instituto de la Patagonia 41, 5-26.

3634 Kilian, R., Baeza, O., Breuer, S., Ríos, F., Arz, H., Lamy, F., Wirtz, J., Baque, D., Korf, P., Kremer, K., 2013b. Late
3635 Glacial and Holocene palaeogeographical and palaeoecological evolution of the Seno Skyring and Otway
3636 fjord systems in the Magellan Region. Anales del Instituto de la Patagonia 41, 5-26.

3637 Kilian, R., Baeza, O., Steinke, T., Arevalo, M., Rios, C., Schneider, C., 2007a. Late Pleistocene to Holocene
3638 marine transgression and thermohaline control on sediment transport in the western Magellanes fjord
3639 system of Chile (53 S). Quaternary International 161, 90-107.

3640 Kilian, R., Hohner, M., Biester, H., Wallrabe-Adams, H.J., Stern, C.R., 2003. Holocene peat and lake sediment
3641 tephra record from the southernmost Chilean Andes (53-55 S). Revista geologica de Chile 30, 23-37.

3642 Kilian, R., Lamy, F., 2012. A review of Glacial and Holocene paleoclimate records from southernmost
3643 Patagonia (49–55°S). Quaternary Science Reviews 53, 1-23.

3644 Kilian, R., Lamy, F., Arz, H., 2013c. Late Quaternary variations of the southern westerly wind belt and its
3645 influences on aquatic ecosystems and glacier extend within the southernmost Andes [Spätquartäre
3646 Variationen der südhemisphärischen Westwindzone und deren Einfluss auf aquatische Ökosysteme sowie
3647 Gletscherausdehnung in den südlichen Anden]. Zeitschrift der Deutschen Gesellschaft für
3648 Geowissenschaften 164, 279-294.

3649 Kilian, R., Schneider, C., Koch, J., Fesq-Martin, M., Biester, H., Casassa, G., Arévalo, M., Wendt, G., Baeza, O.,
3650 Behrmann, J., 2007b. Palaeoecological constraints on late Glacial and Holocene ice retreat in the Southern
3651 Andes (53°S). Global and Planetary Change 59, 49-66.

3652 Kelley, S. E., Kaplan, M. R., Schaefer, J. M., Andersen, B. G., Barrell, D. J. A., Putnam, A. E., Denton, G.H.,
3653 Schwartz, R., Finkel, R.C., Doughty, A. M. 2014. High-precision ^{10}Be chronology of moraines in the Southern
3654 Alps indicates synchronous cooling in Antarctica and New Zealand 42,000 years ago. Earth and Planetary
3655 Science Letters, 405, 194–206.

3656 Koch, J., Kilian, R., 2005. 'Little Ice Age' glacier fluctuations, Gran Campo Nevado, southernmost Chile.
3657 Holocene 15, 20-28.

3658 Kohfeld, K., Graham, R., De Boer, A., Sime, L., Wolff, E., Le Quéré, C., Bopp, L., 2013. Southern Hemisphere
3659 westerly wind changes during the Last Glacial Maximum: paleo-data synthesis. Quaternary Science Reviews
3660 68, 76-95.

3661 Kuylenstierna, J.L., Rosqvist, G.C., Holmlund, P., 1996. Late-Holocene glacier variations in the Cordillera
3662 Darwin, Tierra del Fuego, Chile. The Holocene 6, 353-358.

3663 Lal, D., 1991. Cosmic ray labeling of erosion surfaces: in situ nuclide production rates and erosion models.
3664 Earth and Planetary Science Letters 104, 424-439.

Lamy, F., Kaiser, J., Ninnemann, U., Hebbeln, D., Arz, H.W., Stoner, J., 2004. Antarctic timing of surface water changes off Chile and Patagonian ice sheet response. Science 304, 1959-1962.

Lamy, F., Kilian, R., Arz, H.W., Francois, J.-P., Kaiser, J., Prange, M., Steinke, T., 2010. Holocene changes in the position and intensity of the southern westerly wind belt. Nature Geoscience 3, 695-699.

Lamy, F., Arz, H.W., Kilian, R., Lange, C.B., Lembke-Jene, L., Wengler, M., Kaiser, J., Baeza-Urrea, O., Hall, I.R., Harada, N., Tiedemann, R., 2015. Glacial reduction and millennial-scale variations in Drake Passage throughflow. Proceedings of the National Academy of Sciences 112, 13496 LP – 13501.

Lapido, O., 2000. Carta Geológica de la República Argentina, Escala 1:250.000., Gobernador Costa 4572-II/I. Edición Cartográfica Preliminar. Servicio Geológico Nacional, Buenos Aires.

Larter, R.D., Anderson, J.B., Graham, A.G.C., Gohl, K., Hillenbrand, C.-D., Jakobsson, M., Johnson, J.S., Kuhn, G., Nitsche, F.O., Smith, J.A., Witus, A.E., Bentley, M.J., Dowdeswell, J.A., Ehrmann, W., Klages, J.P., Lindow, J., Ó Cofaigh, C., Spiegel, C., 2014. Reconstruction of changes in the Amundsen Sea and Bellingshausen Sea sector of the West Antarctic Ice Sheet since the Last Glacial Maximum. Quaternary Science Reviews 100, 55-86.

Lastras, G., Dowdeswell, J., 2016. Terminal and recessional moraines in the fjords of southern Chile. Geological Society, London, Memoirs 46, 65-66.

Lawrence, D.B., Lawrence, E.G., 1959. Recent glacier variations in southern South America. American Geographical Society New York.

Lenaerts, J.T., Van Den Broeke, M.R., van Wessem, J.M., van de Berg, W.J., van Meijgaard, E., van Ulft, L.H., Schaefer, M., 2014. Extreme precipitation and climate gradients in Patagonia revealed by high-resolution regional atmospheric climate modeling. Journal of climate 27, 4607-4621.

López-Martínez, J., Muñoz, A., Dowdeswell, J.A., Linés, C., Acosta, J., 2011. Relict sea-floor ploughmarks record deep-keeled Antarctic icebergs to 45 S on the Argentine margin. Marine Geology 288, 43-48.

Loriaux, T., Casassa, G., 2013. Evolution of glacial lakes from the Northern Patagonia Icefield and terrestrial water storage in a sea-level rise context. Global and Planetary Change 102, 33–40.

Lovell, H., Stokes, C.R., Bentley, M.J., 2011. A glacial geomorphological map of the Seno Skyring-Seno Otway-Strait of Magellan region, southernmost Patagonia. Journal of maps 7, 318-339.

Lovell, H., Stokes, C.R., Bentley, M.J., Benn, D.I., 2012. Evidence for rapid ice flow and proglacial lake evolution around the central Strait of Magellan region, southernmost Patagonia. Journal of Quaternary Science 27, 625-638.

Lowe, J.J., Walker, M.J.C., 2015. Reconstructing Quaternary Environments. Routledge, Abingdon, Oxon.

Lowell, T., Heusser, C., Andersen, B., Moreno, P., Hauser, A., Heusser, L., Schlüchter, C., Marchant, D., Denton, G., 1995. Interhemispheric correlation of late Pleistocene glacial events. Science 269, 1541-1549.

Lozano, J.G., Tassone, A., Bran, D.M., Lodolo, E., Menichetti, M., Cerredo, M.E., Esteban, F., Ormazabal, J.P., Ísola, J., Baradello, L., 2018. Glacial-related morphology and sedimentary setting of a high-latitude lacustrine basin: The Lago Chepelmut (Tierra del Fuego, Argentina). Journal of South American Earth Sciences 86, 259-270.

3702 Ludbrook, J., 2008. The presentation of statistics in Clinical and Experimental Pharmacology and Physiology.
3703 Clinical and Experimental Pharmacology and Physiology 35, 1271–1274.

3704 Lumley, S.H., Switsur, R., 1993. Late Quaternary chronology of the Taitao Peninsula, southern Chile. Journal
3705 of Quaternary Science 8, 161-165.

3706 Mackintosh, A., White, D., Fink, D., Gore, D.B., Pickard, J., Fanning, P.C., 2007. Exposure ages from mountain
3707 dipsticks in Mac. Robertson Land, East Antarctica, indicate little change in ice-sheet thickness since the Last
3708 Glacial Maximum. Geology 35, 551–554.

3709 Malz, P., Meier, W., Casassa, G., Jaña, R., Skvarca, P., Braun, M., 2018. Elevation and mass changes of the
3710 Southern Patagonia Icefield derived from TanDEM-X and SRTM data. Remote Sensing 10, 188.

3711 Mancini, M., Paez, M., Prieto, A., Stutz, S., Tonello, M., Vilanova, I., 2005. Mid-Holocene climatic variability
3712 reconstruction from pollen records (32–52 S, Argentina). Quaternary International 132, 47-59.

3713 Mansilla, C.A., McCulloch, R.D., Morello, F., 2016. Palaeoenvironmental change in Southern Patagonia during
3714 the Lateglacial and Holocene: Implications for forest refugia and climate reconstructions. Palaeogeography,
3715 Palaeoclimatology, Palaeoecology 447, 1-11.

3716 Marden, C.J., Clapperton, C.M., 1995. Fluctuations of the South Patagonian Ice-field during the last glaciation
3717 and the Holocene. Journal of Quaternary Science 10, 197-209.

3718 Margold, M., Stokes, C. R., & Clark, C. D. (2018). Reconciling records of ice streaming and ice margin retreat
3719 to produce a palaeogeographic reconstruction of the deglaciation of the Laurentide Ice Sheet. Quaternary
3720 Science Reviews, 189, 1–30.

3721 Markgraf, V., 1993. Paleoenvironments and paleoclimates in Tierra del Fuego and southernmost Patagonia,
3722 South America. Palaeogeography, Palaeoclimatology, Palaeoecology 102, 53-68.

3723 Martin, D., Cornford, S., Peter, S., Le Brocq, A., Payne, A., Lipscomb, W., Ng, E., 2013. Resolving Grounding
3724 Line Dynamics with the BISICLES Adaptive Mesh, EGU General Assembly Conference Abstracts, p. 12083.

3725 Martin, J.R.V., Davies, B.J., Thorndycraft, V.R., 2019. Glacier dynamics during a phase of Late Quaternary
3726 warming in Patagonia reconstructed from sediment-landform associations. Geomorphology 337, 111-133.

3727 Martínez, O., Coronato, A., Rabassa, J., 2011. Chapter 52 - Pleistocene Glaciations in Northern Patagonia,
3728 Argentina: An Updated Review, in: Jürgen Ehlers, P.L.G., Philip, D.H. (Eds.), Developments in Quaternary
3729 Sciences. Elsevier, pp. 729-734.

3730 Martinod, J., Regard, V., Riquelme, R., Aguilar, G., Guillaume, B., Carretier, S., Cortés-Aranda, J., Leanni, L.,
3731 Hérail, G., 2016. Pleistocene uplift, climate and morphological segmentation of the Northern Chile coasts (24
3732 S–32 S): Insights from cosmogenic 10Be dating of paleoshorelines. Geomorphology 274, 78-91.

3733 Masiokas, M., Luckman, B., Villalba, R., Delgado, S., Skvarca, P., Ripalta, A., 2009a. Little Ice Age fluctuations
3734 of small glaciers in the Monte Fitz Roy and Lago del Desierto areas, south Patagonian Andes, Argentina.
3735 Palaeogeography, Palaeoclimatology, Palaeoecology 281, 351-362.

3736 Masiokas, M.H., Rivera, A., Espizua, L.E., Villalba, R., Delgado, S., Aravena, J.C., 2009b. Glacier fluctuations in
3737 extratropical South America during the past 1000 years. Palaeogeography, Palaeoclimatology, Palaeoecology
3738 281, 242-268.

3739 Masiokas, M.H., Villalba, R., Luckman, B.H., Lascano, M.E., Delgado, S., Stepanek, P., 2008. 20th-century
3740 glacier recession and regional hydroclimatic changes in northwestern Patagonia. Global and Planetary
3741 Change 60, 85-100.

3742 Massaferro, J., Brooks, S.J., 2002. Response of chironomids to Late Quaternary environmental change in the
3743 Taitao Peninsula, southern Chile. Journal of Quaternary Science 17, 101-111.

3744 Massaferro, J., Larocque-Tobler, I., Brooks, S.J., Vandergoes, M., Dieffenbacher-Krall, A., Moreno, P., 2014.
3745 Quantifying climate change in Huelmo mire (Chile, Northwestern Patagonia) during the Last Glacial
3746 Termination using a newly developed chironomid-based temperature model. Palaeogeography,
3747 Palaeoclimatology, Palaeoecology 399, 214-224.

3748 Massaferro, J.I., Moreno, P.I., Denton, G.H., Vandergoes, M., Dieffenbacher-Krall, A., 2009. Chironomid and
3749 pollen evidence for climate fluctuations during the Last Glacial Termination in NW Patagonia. Quaternary
3750 Science Reviews 28, 517-525.

3751 Mayr, C., Wille, M., Haberzettl, T., Fey, M., Janssen, S., Lücke, A., Ohlendorf, C., Oliva, G., Schäbitz, F.,
3752 Schleser, G.H., Zolitschka, B., 2007. Holocene variability of the Southern Hemisphere westerlies in
3753 Argentinean Patagonia (52°S). Quaternary Science Reviews 26, 579–584.

3754 Mayr, C., Lücke, A., Wagner, S., Wissel, H., Ohlendorf, C., Haberzettl, T., Oehlerich, M., Schäbitz, F., Wille, M.,
3755 Zhu, J., 2013. Intensified Southern Hemisphere Westerlies regulated atmospheric CO_2 during the last
3756 deglaciation. Geology 41, 831-834.

3757 McCulloch, R.D., Bentley, M.J., 1998. Late glacial ice advances in the Strait of Magellan, southern Chile.
3758 Quaternary Science Reviews 17, 775-787.

3759 McCulloch, R.D., Bentley, M.J., Purves, R.S., Hulton, N.R.J., Sugden, D.E., Clapperton, C.M., 2000. Climatic
3760 inferences from glacial and palaeoecological evidence at the last glacial termination, southern South
3761 America. Journal of Quaternary Science 15, 409-417.

3762 McCulloch, R.D., Bentley, M.J., Tipping, R.M., Clapperton, C.M., 2005a. Evidence for Late-Glacial ice-dammed
3763 lakes in the central Strait of Magellan and Bahìa Inùtil, southernmost South America. Geografiska Annaler:
3764 Series A, Physical Geography 87, 335-362.

3765 McCulloch, R.D., Davies, S.J., 2001. Late-glacial and Holocene palaeoenvironmental change in the central
3766 Strait of Magellan, southern Patagonia. Palaeogeography, Palaeoclimatology, Palaeoecology 173, 143-173.

3767 McCulloch, R.D., Fogwill, C.J., Sugden, D.E., Bentley, M.J., Kubik, P.W., 2005b. Chronology of the Last
3768 Glaciation in Central Strait of Magellan and Bahía Inútil, Southernmost South America. Geografiska Annaler.
3769 Series A, Physical Geography 87, 289-312.

3770 Meglioli, A., 1992. Glacial geology and chronology of southernmost Patagonia and Tierra del Fuego,
3771 Argentina and Chile. Lehigh University, Bethlehem, p. 298.

3772 Meier, W.J.-H., Grießinger, J., Hochreuther, P., Braun, M.H., 2018. An updated multi-temporal glacier
3773 inventory for the Patagonian Andes with changes between the Little Ice Age and 2016. Frontiers in Earth
3774 Science 6 (62), 1-21.

3775 Mendelova, M., Hein, A., McCulloch, R., Davies, B., 2017. The Last Glacial Maximum and deglaciation in
3776 central Patagonia, 44° S–49° S. Cuadernos de Investigación Geográfica.

3777 Menounos, B., Clague, J.J., Osborn, G., Davis, P.T., Ponce, F., Goehring, B., Maurer, M., Rabassa, J., Coronato,
3778 A., Marr, R., 2013. Latest Pleistocene and Holocene glacier fluctuations in southernmost Tierra del Fuego,
3779 Argentina. Quaternary Science Reviews 77, 70-79.

3780 Mercer, J.H., 1965. Glacier Variations in Southern Patagonia. Geographical Review 55, 390-413.

3781 Mercer, J.H., 1968. Variations of some Patagonian glaciers since the Late-Glacial. American Journal of Science
3782 266, 91-109.

3783 Mercer, J.H., 1970. Variations of some Patagonian glaciers since the Late-Glacial; II. American Journal of
3784 Science 269, 1-25.

3785 Mercer, J.H., 1972. Chilean glacial chronology 20,000 to 11,000 carbon-14 years ago: some global
3786 comparisons. Science 176, 1118-1120.

3787 Mercer, J.H., 1976. Glacial history of southernmost South America. Quaternary Research 6, 125-166.

3788 Mercer, J.H., Ager, T., 1983. Glacial and floral changes in Southern Argentina since 14,000 years ago. National
3789 Geographic Society Research Reports 15, 457-477.

3790 Milner, A.M., Khamis, K., Battin, T.J., Brittain, J.E., Barrand, N.E., Füreder, L., Cauvy-Fraunié, S., Gíslason,
3791 G.M., Jacobsen, D., Hannah, D.M., Hodson, A.J., Hood, E., Lencioni, V., Ólafsson, J.S., Robinson, C.T., Tranter,
3792 M., Brown, L.E., 2017. Glacier shrinkage driving global changes in downstream systems. Proceedings of the
3793 National Academy of Sciences 114(37), 9770-9778.

3794 Miranda, C., Moreno, P., Vilanova, I., Villa-Martínez, R., 2013. Glacial fluctuations in the Coyhaique-
3795 Balmaceda sector of central Patagonia (45S-46S) during the last glacial termination. Bollettino di Geofisica
3796 54, 268-271.

3797 Möller, M., Schneider, C., 2008. Climate sensitivity and mass-balance evolution of Gran Campo Nevado ice
3798 cap, southwest Patagonia. Annals of Glaciology 48, 32-42.

3799 Möller, M., Schneider, C., Kilian, R., 2007. Glacier change and climate forcing in recent decades at Gran
3800 Campo Nevado, southernmost Patagonia. Annals of Glaciology 46, 136-144.

3801 Montade, V., Nebout, N.C., Kissel, C., Haberle, S.G., Siani, G., Michel, E., 2013. Vegetation and climate
3802 changes during the last 22,000 yr from a marine core near Taitao Peninsula, southern Chile.
3803 Palaeogeography, Palaeoclimatology, Palaeoecology 369, 335-348.

3804 Montade, V., Peyron, O., Favier, C., Francois, J.P., Haberle, S.G., 2019. A pollen–climate calibration from
3805 western Patagonia for palaeoclimatic reconstructions. Journal of Quaternary Science 34, 76-86.

3806 Moreno, P.I., 1998. Termination of the last ice age in mid-latitudes of South America. University of Maine, p.
3807 187.

3808 Moreno, P.I., 2004. Millennial-scale climate variability in northwest Patagonia over the last 15 000 yr. Journal
3809 of Quaternary Science 19, 35-47.

3810 Moreno, P.I., Denton, G.H., Moreno, H., Lowell, T.V., Putnam, A.E., Kaplan, M.R., 2015. Radiocarbon
3811 chronology of the Last Glacial Maximum and its termination in northwestern Patagonia. Quaternary Science
3812 Reviews 122, 233-249.

3813 Moreno, P.I., Jacobson Jr, G.L., Lowell, T.V., Denton, G.H., 2001. Interhemispheric climate links revealed by a
3814 late-glacial cooling episode in southern Chile. Nature 409, 804.

3815 Moreno, P.I., Kaplan, M.R., François, J.P., Villa-Martínez, R., Moy, C.M., Stern, C.R., Kubik, P.W., 2009.
3816 Renewed glacial activity during the Antarctic Cold Reversal and persistence of cold conditions until 11.5 ka in
3817 southwestern Patagonia. Geology 37, 375-378.

3818 Moreno, P.I., Lowell, T.V., Jacobson Jr, G.L., Denton, G.H., 1999. Abrupt Vegetation and Climate Changes
3819 During the Last Glacial Maximumand Last Termination in The Chilean Lake District: A Case Study from Canal
3820 De La Puntilla (41° S). Geografiska Annaler: Series A, Physical Geography 81, 285-311.

3821 Moreno, P.I., Videla, J., Valero-Garcés, B., Alloway, B.V. and Heusser, L.E., 2018. A continuous record of
3822 vegetation, fire-regime and climatic changes in northwestern Patagonia spanning the last 25,000 years.
3823 Quaternary Science Reviews 198, 15-36.

3824 Moreno, P.I., Videla, J., 2016. Centennial and millennial-scale hydroclimate changes in northwestern
3825 Patagonia since 16,000 yr BP. Quaternary Science Reviews 149, 326-337.

3826 Moreno, P.I., Vilanova, I., Villa-Martínez, R., Dunbar, R.B., Mucciarone, D.A., Kaplan, M.R., Garreaud, R.D.,
3827 Rojas, M., Moy, C.M., De Pol-Holz, R., 2018. Onset and evolution of southern annular mode-like changes at
3828 centennial timescale. Scientific Reports 8, 3458.

3829 Mouginot, J., Rignot, E., 2015. Ice motion of the Patagonian Icefields of South America: 1984-2014.
3830 Geophysical Research Letters, 2014GL062661.

3831 Murdie, R., Pugh, D., Styles, P., 1998. A lightweight, portable, digital probe for measuring the thermal
3832 gradient in shallow water sediments, with examples from Patagonia. Geo-Marine Letters 18, 315-320.

3833 Nimick, D.A., McGrath, D., Mahan, S.A., Friesen, B.A., Leidich, J., 2016. Latest Pleistocene and Holocene
3834 glacial events in the Colonia valley, Northern Patagonia Icefield, southern Chile. Journal of Quaternary
3835 Science 31, 551-564.

3836 Ó Cofaigh, C., Davies, B.J., Livingstone, S.J., Smith, J.A., Johnson, J.S., Hocking, E.P., Hodgson, D.A., Anderson,
3837 J.B., Bentley, M.J., Canals, M., Domack, E., Dowdeswell, J.A., Evans, J., Glasser, N.F., Hillenbrand, C.-D., Larter,
3838 R.D., Roberts, S.J., Simms, A.R., 2014. Reconstruction of ice-sheet changes in the Antarctic Peninsula since
3839 the Last Glacial Maximum. Quaternary Science Reviews 100, 87-110.

3840 Ó Cofaigh, C., Justin, T., Julian A, D., Carol J, P., 2003. Palaeo-ice streams, trough mouth fans and high-
3841 latitude continental slope sedimentation. Boreas 32, 37-55.

3842 Ó Cofaigh, C., Larter, R.D., Dowdeswel, J.A., Hillenbrand, C.-D., Pudsey, C.J., Evans, J., Morris, P., 2005. Flow
3843 of the West Antarctic Ice Sheet on the continental margin of the Bellingshausen Sea at the Last Glacial
3844 Maximum. Journal of Geophysical Research 110, B11103.

3845 Oehlerich, M., Mayr, C., Gussone, N., Hahn, A., Hölzl, S., Lücke, A., Ohlendorf, C., Rummel, S., Teichert, B.,
3846 Zolitschka, B., 2015. Lateglacial and Holocene climatic changes in south-eastern Patagonia inferred from
3847 carbonate isotope records of Laguna Potrok Aike (Argentina). Quaternary science reviews 114, 189-202.

3848 Ortlieb, L., Vargas, G., Saliège, J.-F., 2011. Marine radiocarbon reservoir effect along the northern Chile–
3849 southern Peru coast (14–24°S) throughout the Holocene. Quaternary Research 75, 91-103.

3850 Paterson, W., 1994. The physics of glaciers, 480 pp. Pergamon, New York.

Patton, H., Hubbard, A., Andreassen, K., Auriac, A., Whitehouse, P.L., Stroeven, A.P., Shackleton, C., Winsborrow, M., Heyman, J., Hall, A.M., 2017. Deglaciation of the Eurasian ice sheet complex. Quaternary Science Reviews 169, 148-172.

Patton, H., Hubbard, A., Andreassen, K., Winsborrow, M., Stroeven, A.P., 2016. The build-up, configuration, and dynamical sensitivity of the Eurasian ice-sheet complex to Late Weichselian climatic and oceanic forcing. Quaternary Science Reviews 153, 97-121.

Pattyn, F., Favier, L., Sun, S., Durand, G., 2017. Progress in numerical modeling of Antarctic ice-sheet dynamics. Current Climate Change Reports 3, 174–184.

Paul, F., Mölg, N., 2014. Hasty retreat of glaciers in northern Patagonia from 1985-2011. Journal of Glaciology 60, 1033-1043.

Pedro, J.B., Bostock, H.C., Bitz, C.M., He, F., Vandergoes, M.J., Steig, E.J., Chase, B.M., Krause, C.E., Rasmussen, S.O., Markle, B.R., 2016. The spatial extent and dynamics of the Antarctic Cold Reversal. Nature Geoscience 9, 51-55.

Pedro, J.B., Jochum, M., Buizert, C., He, F., Barker, S., Rasmussen, S.O., 2018. Beyond the bipolar seesaw: Toward a process understanding of interhemispheric coupling. Quaternary Science Reviews 192, 27-46.

Peltier, C., Kaplan, M.R., Schaefer, J.M., Soteres, R., Sagredo, E.A., Aravena, J.C., 2016. A Glacial Chronology of the Strait of Magellan. AGU Fall Meeting Abstracts.

Peltier, W.R., Drummond, R., 2002. A “broad-shelf effect” upon postglacial relative sea level history. Geophysical Research Letters 29, 10-11-10-14.

Pollard, D., DeConto, R.M., Alley, R.B., 2015. Potential Antarctic Ice Sheet retreat driven by hydrofracturing and ice cliff failure. Earth Planetary Science Lettres 412, 112–121.

Ponce, J.F., Guillot, M.G., Martinez, O., Balocchi, L.D., 2018. Geomorphological evidences of paleosurge activity in Lake Viedma Lobe, Patagonia, Argentina. Geomorphology 327, 511-522.

Ponce, J.F., Rabassa, J., Coronato, A., Borromei, A., 2011. Palaeogeographical evolution of the Atlantic coast of Pampa and Patagonia from the last glacial maximum to the Middle Holocene. Biological Journal of the Linnean Society 103, 363-379.

Ponce, J.F., Rabassa, J., Serrat, D., Martínez, O.A., 2013. El campo de drumlins, flutes y megaflutes de lago Viedma, Pleistoceno Tardío, provincia de Santa Cruz. Revista de la Asociación Geológica Argentina 70, 115-127.

Porter, C., Santana, A., 2003. Rapid 20th century retreat of Ventisquero Marinelli in the Cordillera Darwin icefield. Anales del Instituto de la Patagonia 31.

Porter, S.C., 2000. Onset of Neoglaciation in the Southern Hemisphere. Journal of Quaternary Science 15, 395–408.

Porter, S.C., 1990. Character and ages of Pleistocene drifts in a transect across the Strait of Magellan. Quaternary of South America and Antarctic Peninsula 7, 35-50.

Porter, S.C., Clapperton, C., Sugden, D., 1992. Chronology and dynamics of deglaciation along and near the Strait of Magellan, southernmost South America. SGU series Ca. Research paper, 233-239.

3888 Porter, S.C., 1981. Pleistocene glaciation in the southern Lake District of Chile. Quaternary Research 16, 263-
3889 292.

3890 Porter, S.C., Stuiver, M., Heusser, C.J., 1984. Holocene sea-level changes along the Strait of Magellan and
3891 Beagle Channel, southernmost South America. Quaternary Research 22, 59-67.

3892 Powell, R.D., Molnia, B.F., 1989. Glacimarine sedimentary processes, facies and morphology of the south-
3893 southeast Alaska shelf and fjords. Marine Geology 85, 359-390.

3894 Quade, J., Kaplan, M. R., 2017. Lake-level stratigraphy and geochronology revisited at Lago (Lake) Cardiel,
3895 Argentina, and changes in the Southern Hemispheric Westerlies over the last 25 ka. Quaternary Science
3896 Reviews 177, 173–188.

3897 Rabassa, J., 2008. Late Cenozoic glaciations in Patagonia and Tierra del Fuego. Developments in quaternary
3898 sciences 11, 151-204.

3899 Rabassa, J., Clapperton, C.M., 1990. Quaternary glaciations of the southern Andes. Quaternary Science
3900 Reviews 9, 153-174.

3901 Rabassa, J., Coronato, A., Bujalesky, G., Salemme, M., Roig, C., Meglioli, A., Heusser, C., Gordillo, S., Roig, F.,
3902 Borromei, A., Quattrocchio, M., 2000. Quaternary of Tierra del Fuego, Southernmost South America: an
3903 updated review. Quaternary International 68–71, 217-240.

3904 Rabassa, J., Coronato, A., Martinez, O., 2011. Late Cenozoic glaciations in Patagonia and Tierra del Fuego: an
3905 updated review. Biological Journal of the Linnean Society 103, 316-335.

3906 Rabassa, J., Heusser, C., Roig, C., Coronato, A., Bujalesky, G., 1998. Palaeoenvironmental conditions during
3907 the termination of a glacial stadial in Lago Fagnano, Isla Grande de Tierra del Fuego, Argentina, Actas VII
3908 Congreso Argentino de PaleontologmHa y BioestratigrafmHa, p. 132.

3909 Rapela, C.W., Pankhurst, R.J., 1992. The granites of northern Patagonia and the Gastre Fault System in
3910 relation to the break-up of Gondwana. Geological Society, London, Special Publications 68, 209-220.

3911 Rapela, C.W., Pankhurst, R.J., Fanning, C., Herve, F., 2005. Pacific subduction coeval with the Karoo mantle
3912 plume: the Early Jurasssic Subcordilleran belt of northwestern Patagonia. Geological Society, London, Special
3913 Publications 246, 217-239.

3914 Rau, F., Mauz, F., Vogt, S., Khalsa, S.J.S., Raup, B., 2005. Illustrated GLIMS Glacier Classification Manual,
3915 Version 1.0. GLIMS (Global Land Ice Measurement from Space), NSIDC, GLIMS Regional Centre, 'Antarctic
3916 Peninsula'.

3917 Raup, B., Khalsa, S.J.S., 2010. GLIMS Analysis Tutorial. GLIMS, Global Land Ice Measurements from Space,
3918 NSIDC, www.GLIMS.org.

3919 Raup, B., Racoviteanu, A., Khalsa, S.J.S., Helm, C., Armstrong, R., Arnaud, Y., 2007. The GLIMS geospatial
3920 glacier database: A new tool for studying glacier change. Global and Planetary Change 56, 101-110.

3921 Recasens, C., Ariztegui, D., Gebhardt, C., Gogorza, C., Haberzettl, T., Hahn, A., Kliem, P., Lisé-Pronovost, A.,
3922 Lücke, A., Maidana, N., 2012. New insights into paleoenvironmental changes in Laguna Potrok Aike, southern
3923 Patagonia, since the Late Pleistocene: the PASADO multiproxy record. The Holocene 22, 1323-1335.

Reimer, P.J., Bard, E., Bayliss, A., Beck, J.W., Blackwell, P.G., Ramsey, C.B., Buck, C.E., Cheng, H., Edwards, R.L., Friedrich, M., 2013. IntCal13 and Marine13 radiocarbon age calibration curves 0–50,000 years cal BP. Radiocarbon 55, 1869-1887.

Reinthaler, J., Paul, F., Granados, H. D., Rivera, A., & Huggel, C. 2019. Area changes of glaciers on active volcanoes in Latin America between 1986 and 2015 observed from multi-temporal satellite imagery. Journal of Glaciology, 65(252), 542–556.

Reynhout, S., Sagredo, E.A., Kaplan, M.R., Aravena, J.C., Martini, M.A., Moreno, P.I., Rojas, M., Schwartz, R., Schaefer, J.M., 2019. Holocene glacier fluctuations in Patagonia are modulated by summer insolation intensity and paced by Southern Annular Mode-like variability. Quaternary Science Reviews 220, 178-187.

Rignot, E., Mouginot, J., Scheuchl, B., van den Broeke, M., van Wessem, M. J., & Morlighem, M. (2019). Four decades of Antarctic Ice Sheet mass balance from 1979–2017. Proceedings of the National Academy of Sciences, 116(4), 1095–1103. https://doi.org/10.1073/pnas.1812883116

Rivera, A., Benham, T., Casassa, G., Bamber, J., Dowdeswell, J.A., 2007. Ice elevation and areal changes of glaciers from the Northern Patagonia Icefield, Chile. Global and Planetary Change 59, 126-137.

Rivera, A., Bown, F., Casassa, G., Acuña, C., Clavero, J., 2005. Glacier shrinkage and negative mass balance in the Chilean Lake District (40° S)/Rétrécissement glaciaire et bilan massique négatif dans la Région des Lacs du Chili (40° S). Hydrological Sciences Journal 50.

Rivera, A., Bown, F., Mella, R., Wendt, J., Casassa, G., Acuña, C., Rignot, E., Clavero, J., Brock, B., 2006. Ice volumetric changes on active volcanoes in southern Chile. Annals of Glaciology 43, 111-122.

Rivera, A., Corripio, J., Bravo, C., Cisternas, S., 2012a. Glaciar Jorge Montt (Chilean Patagonia) dynamics derived from photos obtained by fixed cameras and satellite image feature tracking. Annals of Glaciology 53, 147-155.

Rivera, A., Koppes, M., Bravo, C., Aravena, J.C., 2012b. Little Ice Age advance and retreat of Glaciar Jorge Montt, Chilean Patagonia. Climate of the Past 8, 403-414.

Rodbell, D.T., Smith, J.A., Mark, B.G., 2009. Glaciation in the Andes during the Lateglacial and Holocene. Quaternary Science Reviews 28, 2165-2212.

Roig, F., Roig, C., Rabassa, J., Boninsegna, J., 1996. Fuegian floating tree-ring chronology from subfossil Nothofagus wood. The Holocene 6, 469-476.

Rosenau, M., Melnick, D., Echtler, H., 2006. Kinematic constraints on intra-arc shear and strain partitioning in the southern Andes between 38 S and 42 S latitude. Tectonics 25.

Rutt, I.C., Hagdorn, M., Hulton, N.R.J., Payne, A.J., 2009. The Glimmer community ice sheet model. Journal of Geophysical Research 114, F02004.

Sagredo, E.A., Kaplan, M.R., Araya, P.S., Lowell, T.V., Aravena, J.C., Moreno, P.I., Kelly, M.A., Schaefer, J.M., 2018. Trans-pacific glacial response to the Antarctic Cold Reversal in the southern mid-latitudes. Quaternary Science Reviews 188, 160-166.

Sagredo, E.A., Lowell, T.V., Kelly, M.A., Rupper, S., Aravena, J.C., Ward, D.J., Malone, A.G., 2016. Equilibrium line altitudes along the Andes during the Last millennium: Paleoclimatic implications. The Holocene 27, 1019 - 1033.

3962 Sagredo, E.A., Moreno, P.I., Villa-Martínez, R., Kaplan, M.R., Kubik, P.W., Stern, C.R., 2011. Fluctuations of
3963 the Última Esperanza ice lobe (52°S), Chilean Patagonia, during the last glacial maximum and termination 1.
3964 Geomorphology 125, 92-108.

3965 Schäbitz, F., Wille, M., Francois, J.-P., Haberzettl, T., Quintana, F., Mayr, C., Lücke, A., Ohlendorf, C., Mancini,
3966 V., Paez, M.M., 2013. Reconstruction of palaeoprecipitation based on pollen transfer functions–the record of
3967 the last 16 ka from Laguna Potrok Aike, southern Patagonia. Quaternary Science Reviews 71, 175-190.

3968 Schaefer, J.M., Denton, G.H., Kaplan, M., Putnam, A., Finkel, R.C., Barrell, D.J.A., Andersen, B.G., Schwartz, R.,
3969 Mackintosh, A., Chinn, T., SchlÃ¼chter, C., 2009. High-Frequency Holocene Glacier Fluctuations in New
3970 Zealand Differ from the Northern Signature. Science 324, 622–625.

3971 Schaefer, M., Machguth, H., Falvey, M., Casassa, G., Rignot, E., 2015. Quantifying mass balance processes on
3972 the Southern Patagonia Icefield. The Cryosphere 9, 25-35.

3973 Schellmann, G., Radtke, U., 2010. Timing and magnitude of Holocene sea-level changes along the middle and
3974 south Patagonian Atlantic coast derived from beach ridge systems, littoral terraces and valley-mouth
3975 terraces. Earth-Science Reviews 103, 1-30.

3976 Schenk, C.J., Viger, R.J., Anderson, C.P., 1997. Map showing oil and gas fields and geologic provinces of South
3977 America. U.S. Geological Survey, pp. 1-12.

3978 Schneider, C., Gies, D., 2004. Effects of El Niño–southern oscillation on southernmost South America
3979 precipitation at 53 S revealed from NCEP–NCAR reanalyses and weather station data. International Journal
3980 of Climatology 24, 1057–1076.

3981 Schneider, C., Schnirch, M., Acuña, C., Casassa, G., Kilian, R., 2007. Glacier inventory of the Gran Campo
3982 Nevado Ice Cap in the Southern Andes and glacier changes observed during recent decades. Global and
3983 Planetary Change 59, 87-100.

3984 Siani, G., Colin, C., Michel, E., Carel, M., Richter, T., Kissel, C., Dewilde, F., 2010. Late Glacial to Holocene
3985 terrigenous sediment record in the Northern Patagonian margin: Paleoclimate implications.
3986 Palaeogeography, Palaeoclimatology, Palaeoecology 297, 26-36.

3987 Siddall, M., Rohling, E.J., Thompson, W.G., Waelbroeck, C., 2008. Marine isotope stage 3 sea level
3988 fluctuations: Data synthesis and new outlook. Reviews of Geophysics 46.

3989 Sime, L.C., Kohfeld, K.E., Le Quéré, C., Wolff, E.W., de Boer, A.M., Graham, R.M. and Bopp, L., 2013. Southern
3990 Hemisphere westerly wind changes during the Last Glacial Maximum: model-data comparison. Quaternary
3991 Science Reviews, 64, 104-120.

3992 Singer, B.S., Ackert, R.P., Guillou, H., 2004a. $^{40}Ar/^{39}Ar$ and K-Ar chronology of Pleistocene glaciations in
3993 Patagonia. Geological Society of America Bulletin 116, 434-450.

3994 Singer, B.S., Brown, L.L., Rabassa, J.O., Guillou, H., 2004b. $^{40}Ar/^{39}Ar$ chronology of late Pliocene and Early
3995 Pleistocene geomagnetic and glacial events in southern Argentina. Timescales of the paleomagnetic field,
3996 175-190.

3997 Small, D., Clark, C.D., Chiverrell, R.C., Smedley, R.K., Bateman, M.D., Duller, G.A.T., Ely, J.C., Fabel, D.,
3998 Medialdea, A., Moreton, S.G., 2017. Devising quality assurance procedures for assessment of legacy
3999 geochronological data relating to deglaciation of the last British-Irish Ice Sheet. Earth-Science Reviews 164,
4000 232-250.

4001 Smedley, R., Glasser, N., Duller, G., 2016. Luminescence dating of glacial advances at Lago Buenos Aires (~
4002 46° S), Patagonia. Quaternary Science Reviews 134, 59-73.

4003 Solari, M.A., Le Roux, J.P., Hervé, F., Airo, A., Calderón, M., 2012. Evolution of the Great Tehuelche Paleolake
4004 in the Torres del Paine National Park of Chilean Patagonia during the Last Glacial Maximum and Holocene.
4005 Andean Geology 39, 1-21.

4006 Solomina, O.N., Bradley, R.S., Hodgson, D.A., Ivy-Ochs, S., Jomelli, V., Mackintosh, A.N., Nesje, A., Owen, L.A.,
4007 Wanner, H., Wiles, G.C., Young, N.E., 2015. Holocene glacier fluctuations. Quaternary Science Reviews 111,
4008 9-34.

4009 Steig, E., Brook, E., White, J., Sucher, C., Bender, M., Lehman, S., Morse, D., Waddington, E., Clow, G., 1998.
4010 Synchronous climate changes in Antarctica and the North Atlantic. Science 282, 92-95.

4011 Stern, C., 1992. Tefrocronologia de Magallanes: nuevos datos e implicaciones, Anales del Instituto de la
4012 Patagonia, pp. 129-141.

4013 Stern, C., 2011. Evolution of ice-dammed proglacial lakes in Última Esperanza, Chile: implications from the
4014 late-glacial R1 eruption of Reclús volcano, Andean Austral Volcanic Zone.

4015 Stern, C.R., 1990. Tephrochronology of southernmost Patagonia. National Geographic Society Research 6,
4016 110-126.

4017 Stern, C.R., 2008. Holocene tephrochronology record of large explosive eruptions in the southernmost
4018 Patagonian Andes. Bulletin of Volcanology 70, 435-454.

4019 Stern, C.R., de Porras, M.E., Maldonado, A., 2015. Tephrochronology of the upper Río Cisnes valley (44 S),
4020 southern Chile. Andean Geology 42.

4021 Stern, C.R., Moreno, P.I., Henríquez, W.I., Villa-Martínez, R., Sagredo, E., Aravena, J.C., de Pol-Holz, R., 2016.
4022 Holocene tephrochronology around Cochrane (~ 47 S), southern Chile. Andean Geology 43.

4023 Stokes, C.R., Clark, C.D., 1999. Geomorphological criteria for identifying Pleistocene ice streams. Annals of
4024 Glaciology 28, 67-74.

4025 Stokes, C.R., Tarasov, L., 2010. Ice streaming in the Laurentide Ice Sheet: A first comparison between data-
4026 calibrated numerical model output and geological evidence. Geophysical Research Letters 37, L01501.

4027 Stokes, C.R., Tarasov, L., Blomdin, R., Cronin, T.M., Fisher, T.G., Gyllencreutz, R., Hättestrand, C., Heyman, J.,
4028 Hindmarsh, R.C.A., Hughes, A.L.C., Jakobsson, M., Kirchner, N., Livingstone, S.J., Margold, M., Murton, J.B.,
4029 Noormets, R., Peltier, W.R., Peteet, D.M., Piper, D.J.W., Preusser, F., Renssen, H., Roberts, D.H., Roche, D.M.,
4030 Saint-Ange, F., Stroeven, A.P., Teller, J.T., 2015. On the reconstruction of palaeo-ice sheets: Recent advances
4031 and future challenges. Quaternary Science Reviews 125, 15-49.

4032 Stone, J.O., 2000. Air pressure and cosmogenic isotope production. Journal of Geophysical Research 105,
4033 23753–23759.

4034 Strand, P. D., Schaefer, J. M., Putnam, A. E., Denton, G. H., Barrell, D. J. A., Koffman, T. N. B., & Schwartz, R.
4035 2019. Millennial-scale pulsebeat of glaciation in the Southern Alps of New Zealand. Quaternary Science
4036 Reviews, 220, 165–177.

4037 Strelin, J., Casassa, G., Rosqvist, G., Holmlund, P., 2008. Holocene glaciations in the Ema glacier valley, Monte
4038 Sarmiento massif, Tierra del Fuego. Palaeogeography, Palaeoclimatology, Palaeoecology 260, 299-314.

4039 Strelin, J., Denton, G., Vandergoes, M., Ninnemann, U., Putnam, A., 2011. Radiocarbon chronology of the
4040 late-glacial Puerto Bandera moraines, southern Patagonian Icefield, Argentina. Quaternary Science Reviews
4041 30, 2551-2569.

4042 Strelin, J.A., Kaplan, M.R., Vandergoes, M.J., Denton, G.H., Schaefer, J.M., 2014. Holocene glacier history of
4043 the Lago Argentino basin, southern Patagonian Icefield. Quaternary Science Reviews 101, 124-145.

4044 Strelin, J.A., Malagnino, E.C., 2000. Late-glacial history of Lago Argentino, Argentina, and age of the Puerto
4045 Bandera moraines. Quaternary Research 54, 339-347.

4046 Stuefer, M., Rott, H., Skvarca, P., 2007. Glaciar Perito Moreno, Patagonia: climate sensitivities and glacier
4047 characteristics preceding the 2003/04 and 2005/06 damming events. Journal of Glaciology 53, 3-16.

4048 Stuiver, M., Reimer, P.J., Reimer, R.W., 2009. CALIB 5.0.1. Program and Documentation.
4049 http://www.calib.qub.ac.uk/.

4050 Sugden, D.E., Bentley, M.J., Fogwill, C.J., Hulton, N.R.J., McCulloch, R.D., Purves, R.S., 2005. Late-glacial
4051 glacier events in southernmost South America: a blend of 'Northern' and 'Southern' hemispheric climate
4052 signals? Geografiska Annaler: Series A, Physical Geography 87, 273-288.

4053 Syvitski, J.P.M., 1989. On the deposition of sediment within glacier-influenced fjords: oceanographic
4054 controls. Marine Geology 85, 301-329.

4055 Syvitski, J.P.M., Burrell, D.C., Skei, J.M., 1987. Fjords: processes and products. Springer Science & Business
4056 Media, Berlin.

4057 Tarasov, L., Dyke, A.S., Neal, R.M., Peltier, W., 2012. A data-calibrated distribution of deglacial chronologies
4058 for the North American ice complex from glaciological modeling. Earth and Planetary Science Letters 315,
4059 30-40.

4060 Tatur, A., del Valle, R., Bianchi, M.-M., Outes, V., Villarosa, G., Niegodzisz, J., Debaene, G., 2002. Late
4061 Pleistocene palaeolakes in the Andean and Extra-Andean Patagonia at mid-latitudes of South America.
4062 Quaternary International 89, 135–150.

4063 Thorndycraft, V.R., Bendle, J.M., Benito, G., Davies, B.J., Sancho, C., Palmer, A.P., Fabel, D., Medialdea, A.,
4064 Martin, J.R.V., 2019a. Glacial lake evolution and Atlantic-Pacific drainage reversals during deglaciation of the
4065 Patagonian Ice Sheet. Quaternary Science Reviews 203, 102-127.

4066 Thorndycraft, V.R., Bendle, J.M., Matthews, I.P., Palmer, A.P., Benito, G., Davies, B.J., Sancho, C., Pike, J.H.,
4067 Martin, J.R. V, Fabel, D., 2019. Reply to comments by Bourgois et al.(2019) on:" Glacial lake evolution and
4068 Atlantic-Pacific drainage reversals during deglaciation of the Patagonia Ice Sheet". Quaternary Science
4069 Reviews 213, 171–177.

4070 Toggweiler, J.R., 2009. Shifting Westerlies. Science 323, 1434-1435.

4071 Tonello, M.S., Mancini, M.V., Seppä, H., 2009. Quantitative reconstruction of Holocene precipitation changes
4072 in southern Patagonia. Quaternary Research 72, 410-420.

4073 Turner, K., Fogwill, C., McCulloch, R., Sugden, D.E., 2005. Deglaciation of the eastern flank of the North
4074 Patagonian Icefield and associated continental-scale lake diversions. Geografiska Annaler: Series A, Physical
4075 Geography 87, 363-374.

4076 Tweed, F., 2011. Ice-Dammed Lakes, Encyclopedia of Snow, Ice and Glaciers. Springer, pp. 619-621.

4077 Uribe, P., 1982. Deglaciación en el sector central del Estrecho de Magallanes; consideraciones
4078 geomorfológicas y cronológicas, Anales del Instituto de la Patagonia. El Instituto, pp. 103-111.

4079 Van Daele, M., Bertrand, S., Meyer, I., Moernaut, J., Vandoorne, W., Siani, G., Tanghe, N., Ghazoui, Z., Pino,
4080 M., Urrutia, R., 2016. Late Quaternary evolution of Lago Castor (Chile, 45.6° S): Timing of the deglaciation in
4081 northern Patagonia and evolution of the southern westerlies during the last 17 kyr. Quaternary Science
4082 Reviews 133, 130-146.

4083 Vanneste, H., De Vleeschouwer, F., Martínez-Cortizas, A., von Scheffer, C., Piotrowska, N., Coronato, A., Le
4084 Roux, G., 2015. Late-glacial elevated dust deposition linked to westerly wind shifts in southern South
4085 America. Scientific Reports 5.

4086 Villa-Martínez, R., Moreno, P.I., Valenzuela, M.A., 2012. Deglacial and postglacial vegetation changes on the
4087 eastern slopes of the central Patagonian Andes (47°S). Quaternary Science Reviews 32, 86-99.

4088 Villagran, C., 1988. Late quaternary vegetation of southern Isla Grande de Chiloé, Chile. Quaternary Research
4089 29, 294-306.

4090 Wais Divide Project Members, 2013. Onset of deglacial warming in West Antarctica driven by local orbital
4091 forcing. Nature 500, 440.

4092 Waldmann, N., Ariztegui, D., Anselmetti, F.S., Coronato, A., Austin Jr, J.A., 2010. Geophysical evidence of
4093 multiple glacier advances in Lago Fagnano (54°S), southernmost Patagonia. Quaternary Science Reviews 29,
4094 1188-1200.

4095 Warren, C., Aniya, M., 1999. The calving glaciers of southern South America. Global and Planetary Change
4096 22, 59-77.

4097 Warren, C.R., 1993. Rapid recent fluctuations of the calving San Rafael glacier, Chilean Patagonia: climatic or
4098 non-climatic? Geografiska Annaler. Series A. Physical Geography, 111-125.

4099 Warren, C.R., Glasser, N.F., Harrison, S., Winchester, V., Kerr, A.R., Rivera, A., 1995. Characteristics of tide-
4100 water calving at Glaciar San Rafael, Chile. Journal of glaciology 41, 273-289.

4101 Weller, D., Miranda, C., Moreno, P., Villa-Martínez, R., Stern, C., 2015. Tephrochronology of the
4102 southernmost Andean southern volcanic zone, Chile. Bulletin of Volcanology 77, 107.

4103 Weller, D.J., de Porras, M.E., Maldonado, A., Méndez, C., Stern, C.R., 2017. Holocene tephrochronology of
4104 the lower Río Cisnes valley, southern Chile. Andean Geology 44, 229-248.

4105 Wenzens, G., 1999. Fluctuations of outlet and valley glaciers in the Southern Andes (Argentina) during the
4106 past 13,000 years. Quaternary Research 51, 238-247.

4107 Wenzens, G., 2003. Comment on:'The Last Glacial Maximum and deglaciation in southern South America': by
4108 NRJ Hulton, RS Purves, RD McCulloch, DE Sugden, MJ Bentley [Quaternary Science Reviews 21 (2002) 233–
4109 241]. Quaternary science reviews 22, 751-754.

4110 Wenzens, G., 2005. Glacier advances east of the Southern Andes between the Last Glacial Maximum and
4111 5,000 BP compared with lake terraces of the endorrheic Lago Cardiel (49 S, Patagonia, Argentina). Zeitschrift
4112 für Geomorphologie, NF, 433-454.

4113 Wenzens, G., 2006. Terminal Moraines, Outwash Plains, and Lake Terraces in the Vicinity of Lago Cardiel
4114 (49°S; Patagonia, Argentina)—Evidence for Miocene Andean Foreland Glaciations. Arctic, Antarctic, and
4115 Alpine Research 38, 276-291.

4116 Wilson, R., Glasser, N.F., Reynolds, J.M., Harrison, S., Anacona, P.I., Schaefer, M., Shannon, S., 2018. Glacial
4117 lakes of the Central and Patagonian Andes. Global and Planetary Change 162, 275-291.

4118 Winchester, V., Harrison, S., 1996. Recent Oscillations of the San Quintin and San Rafael Glaciers, Patagonian
4119 Chile. Geografiska Annaler: Series A, Physical Geography 78, 35-49.

4120 Winchester, V., Harrison, S., 2000. Dendrochronology and lichenometry: colonization, growth rates and
4121 dating of geomorphological events on the east side of the North Patagonian Icefield, Chile. Geomorphology
4122 34, 181-194.

4123 Winchester, V., Harrison, S., Warren, C.R., 2001. Recent retreat Glaciar Nef, Chilean Patagonia, dated by
4124 lichenometry and dendrochronology. Arctic Antarctic and Alpine Research 33, 266-273.

4125 Winchester, V., Sessions, M., Cerda, J.V., Wündrich, O., Clemmens, S., Glasser, N.F., Nash, M., 2014. Post-
4126 1850 changes in Glacier Benito, North Patagonian Icefield, Chile. Geografiska Annaler: Series A, Physical
4127 Geography 96, 43-59.

4128 Winkelmann, R., Martin, M.A., Haseloff, M., Albrecht, T., Bueler, E., Khroulev, C., Levermann, A., 2011. The
4129 Potsdam Parallel Ice Sheet Model (PISM-PIK) – Part 1: Model description. The Cryosphere 5, 715-726.

4130 Wolff, I.W., Glasser, N.F., Hubbard, A., 2013. The reconstruction and climatic implication of an independent
4131 palaeo ice cap within the Andean rain shadow east of the former Patagonian ice sheet, Santa Cruz Province,
4132 Argentina. Geomorphology 185, 1-15.

4133 Zemp, M., Huss, M., Thibert, E., Eckert, N., McNabb, R., Huber, J., Barandun, M., Machguth, H., Nussbaumer,
4134 S.U., Gärtner-Roer, I., 2019. Global glacier mass changes and their contributions to sea-level rise from 1961
4135 to 2016. Nature 568, 382-386.

4136

4137

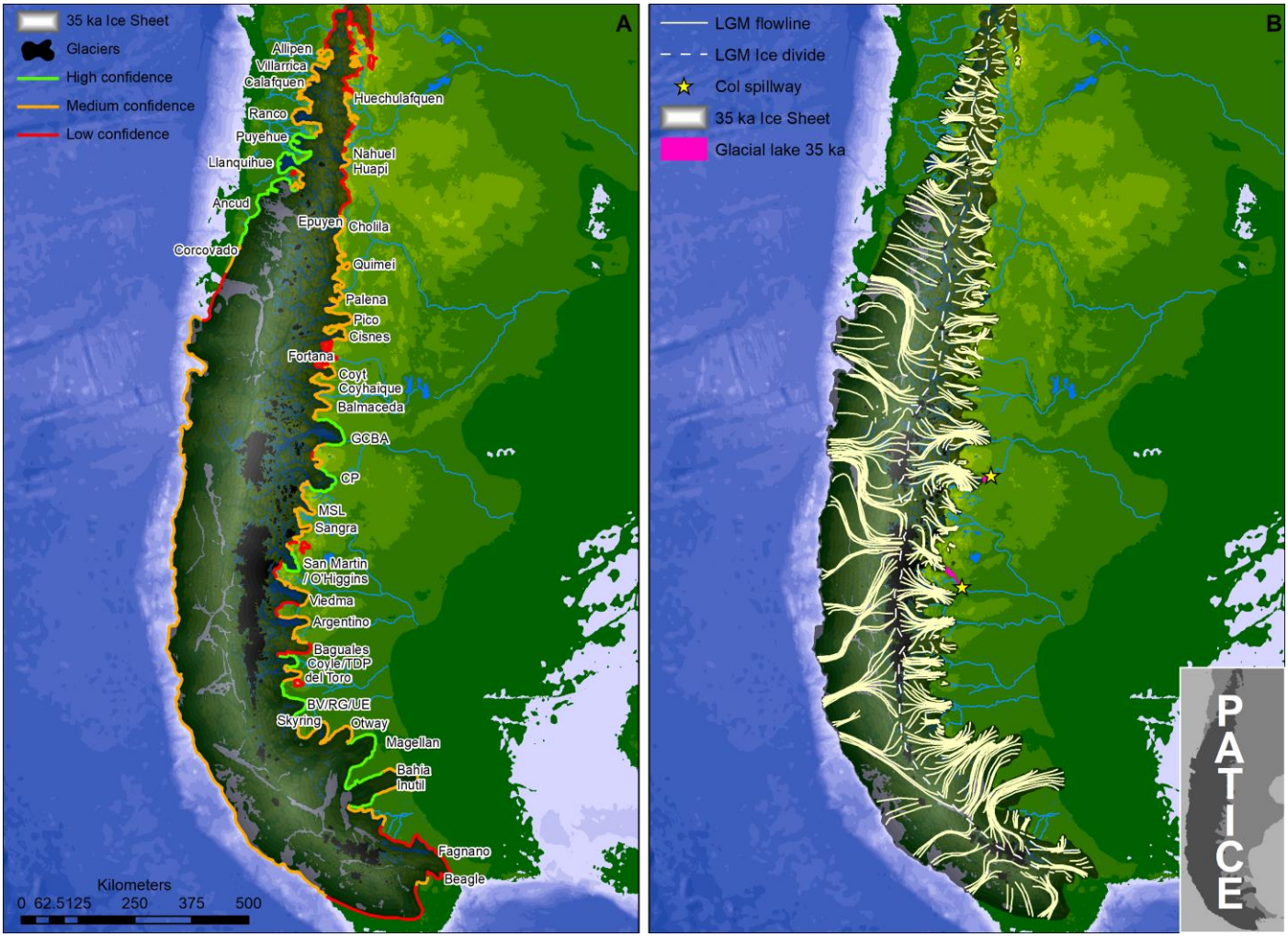

Graphical Abstract

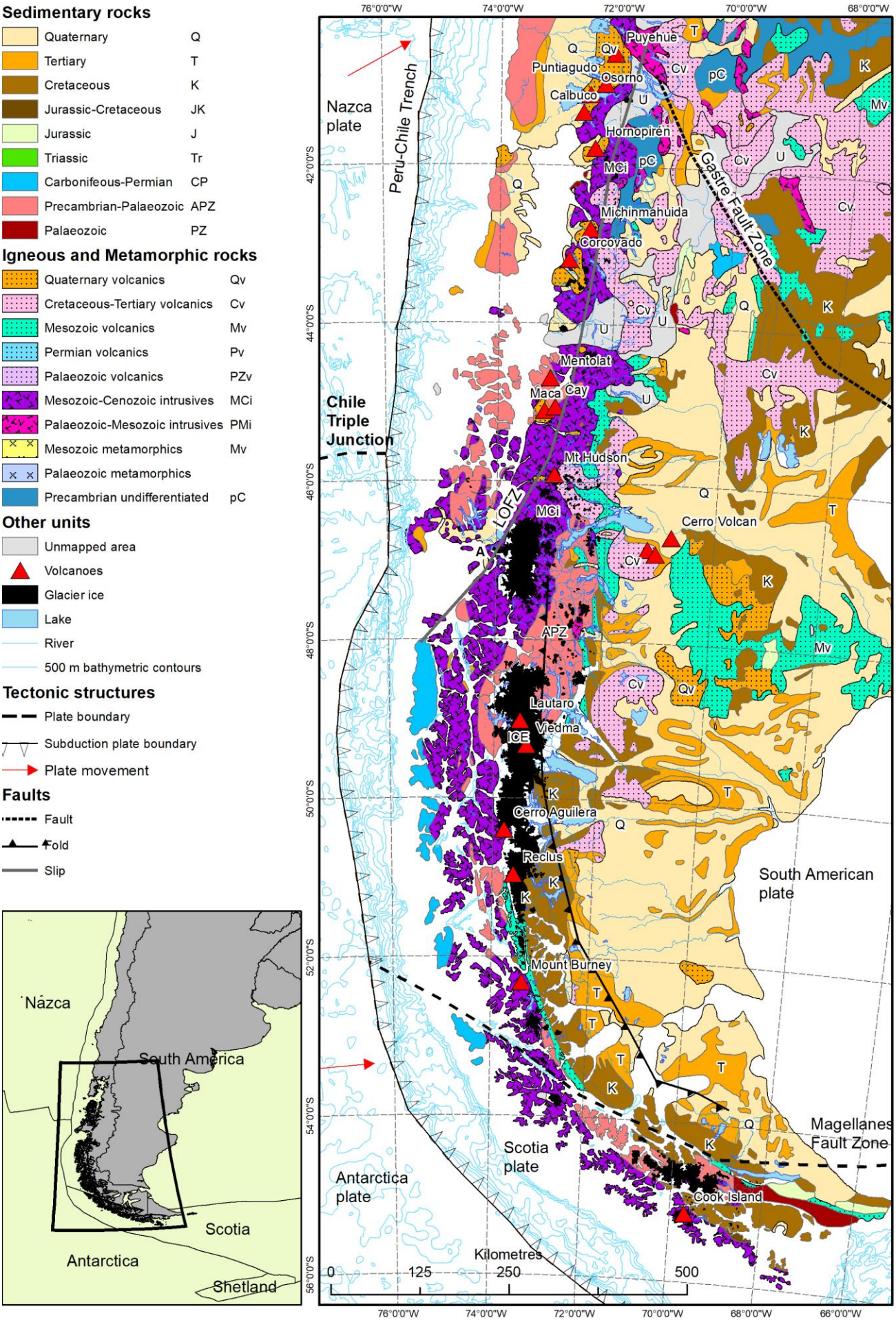
Sedimentary rocks
Quaternary Q
Tertiary T
Cretaceous K
Jurassic-Cretaceous JK
Jurassic J
Triassic Tr
Carbonifeous-Permian CP
Precambrian-Palaeozoic APZ
Palaeozoic PZ
Igneous and Metamorphic rocks
Quaternary volcanics Qv
Cretaceous-Tertiary volcanics Cv
Mesozoic volcanics Mv
Permian volcanics Pv
Palaeozoic volcanics PZv
Mesozoic-Cenozoic intrusives MCi
Palaeozoic-Mesozoic intrusives PMi
Mesozoic metamorphics Mv
Palaeozoic metamorphics
Precambrian undifferentiated pC
Other units
Unmapped area
Volcanoes
Glacier ice
Lake
River
500 m bathymetric contours
Tectonic structures
Plate boundary
Subduction plate boundary
Plate movement
Faults
Fault
Fold
Slip
Nazca
South America
Scotia
Antarctica
Shetland
76°0'0"W
74°0'0"W
72°0'0"W
70°0'0"W
68°0'0"W
66°0'0"W
42°0'0"S
44°0'0"S
46°0'0"S
48°0'0"S
50°0'0"S
52°0'0"S
54°0'0"S
56°0'0"S
Nazca plate
Peru-Chile Trench
Chile Triple Junction
Gastre Fault Zone
LOFZ
Puyehue
Puntiagudo
Osorno
Calbuco
Hornopirén
Michinmahuida
Corcovado
Mentolat
Maca
Cay
Mt Hudson
Cerro Volcan
Lautaro
Viedma
ICE
Cerro Aguilera
Reclus
Mount Burney
South American plate
Scotia plate
Antarctica plate
Magellanes Fault Zone
Cook Island
Kilometres
0
125
250
500

Figure 1.

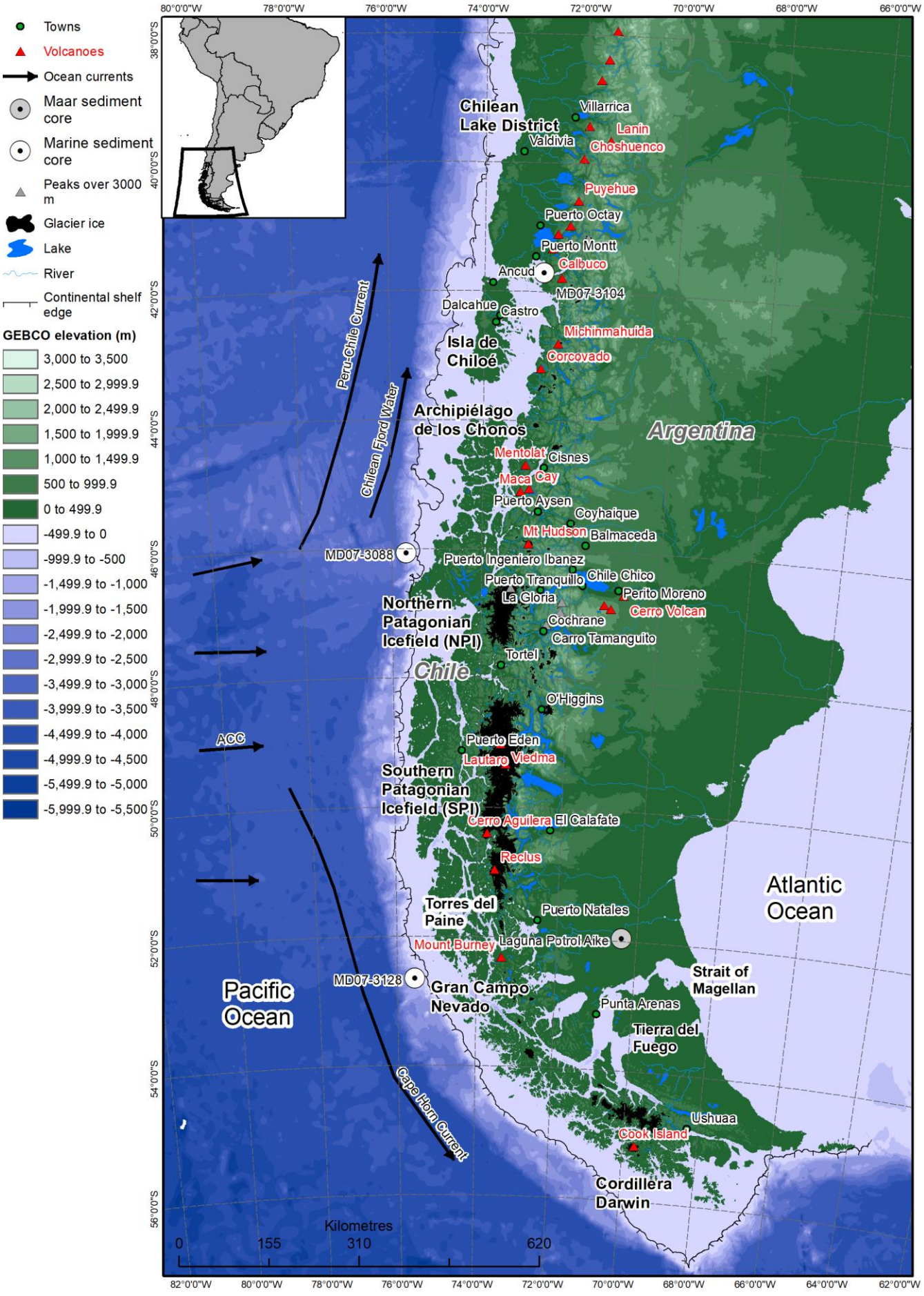
Towns
Volcanoes
Ocean currents
Maar sediment core
Marine sediment core
Peaks over 3000 m
Glacier ice
Lake
River
Continental shelf edge
GEBCO elevation (m)
3,000 to 3,500
2,500 to 2,999.9
2,000 to 2,499.9
1,500 to 1,999.9
1,000 to 1,499.9
500 to 999.9
0 to 499.9
-499.9 to 0
-999.9 to -500
-1,499.9 to -1,000
-1,999.9 to -1,500
-2,499.9 to -2,000
-2,999.9 to -2,500
-3,499.9 to -3,000
-3,999.9 to -3,500
-4,499.9 to -4,000
-4,999.9 to -4,500
-5,499.9 to -5,000
-5,999.9 to -5,500
80°0'0"W
78°0'0"W
76°0'0"W
74°0'0"W
72°0'0"W
70°0'0"W
68°0'0"W
66°0'0"W
38°0'0"S
40°0'0"S
42°0'0"S
44°0'0"S
46°0'0"S
48°0'0"S
50°0'0"S
52°0'0"S
54°0'0"S
56°0'0"S
82°0'0"W
80°0'0"W
78°0'0"W
76°0'0"W
74°0'0"W
72°0'0"W
70°0'0"W
68°0'0"W
66°0'0"W
64°0'0"W
62°0'0"W
Chilean Lake District
Villarrica
Lanin
Valdivia
Choshuenco
Puyehue
Puerto Octay
Puerto Montt
Calbuco
Ancud
MD07-3104
Dalcahue
Castro
Michinmahuida
Isla de Chiloé
Corcovado
Peru-Chile Current
Chilean Fjord Water
Archipiélago de los Chonos
Argentina
Mentolat
Cisnes
Maca
Cay
Puerto Aysen
Coyhaique
Mt Hudson
Balmaceda
MD07-3088
Puerto Ingeniero Ibanez
Chile Chico
Puerto Tranquilo
Perito Moreno
La Gloria
Cerro Volcan
Northern Patagonian Icefield (NPI)
Cochrane
Carro Tamanguito
Tortel
Chile
O'Higgins
ACC
Puerto Eden
Lautaro
Viedma
Southern Patagonian Icefield (SPI)
Cerro Aguilera
El Calafate
Reclus
Torres del Paine
Puerto Natales
Mount Burney
Laguna Potrol Aike
Atlantic Ocean
Pacific Ocean
MD07-3128
Gran Campo Nevado
Strait of Magellan
Punta Arenas
Tierra del Fuego
Cape Horn Current
Ushuaa
Cook Island
Cordillera Darwin
Kilometres
0
155
310
620

Figure 2.

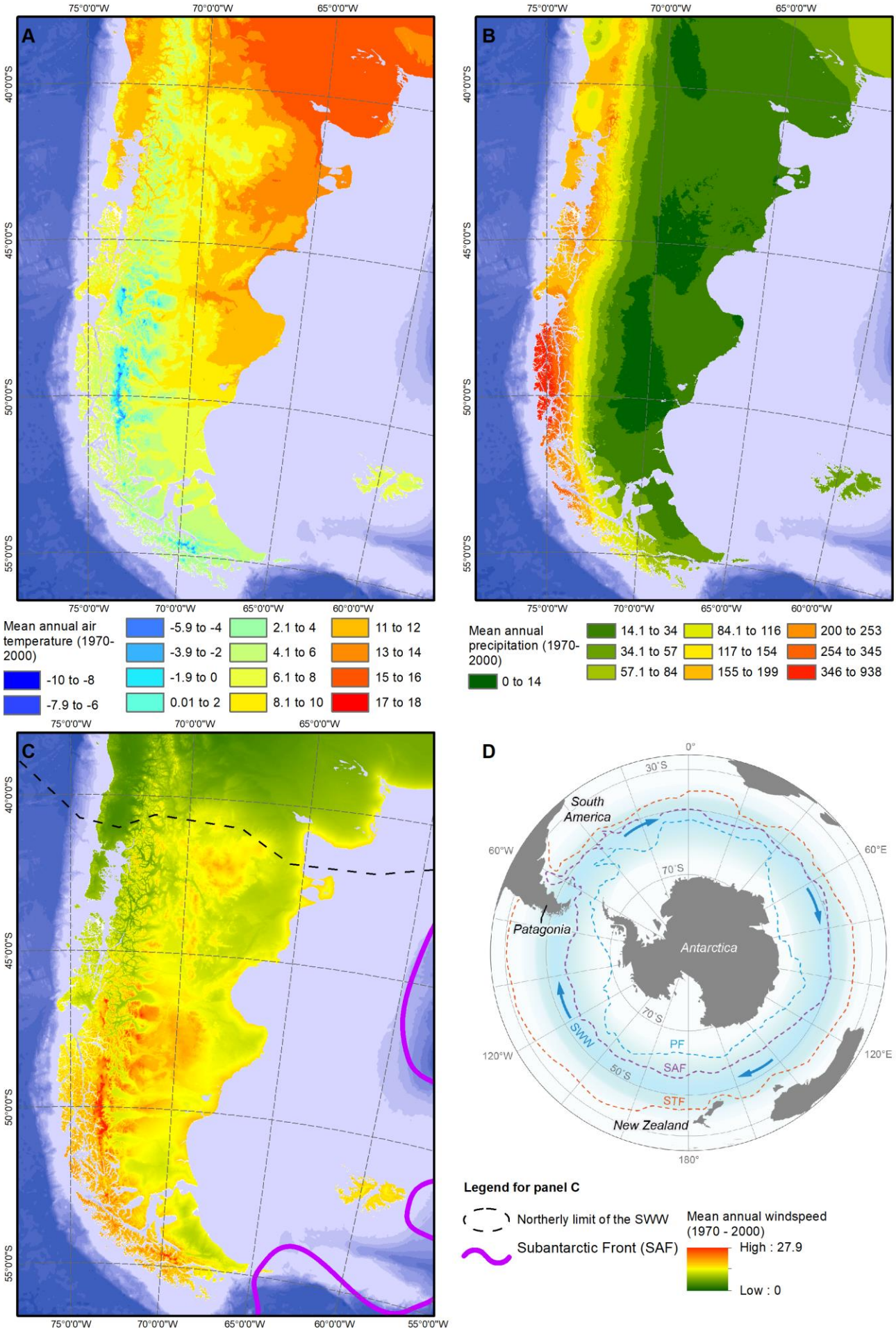
A
B
C
D
75°0'0"W
70°0'0"W
65°0'0"W
60°0'0"W
55°0'0"W
40°0'0"S
45°0'0"S
50°0'0"S
55°0'0"S
Mean annual air temperature (1970-2000)
-10 to -8
-7.9 to -6
-5.9 to -4
-3.9 to -2
-1.9 to 0
0.01 to 2
2.1 to 4
4.1 to 6
6.1 to 8
8.1 to 10
11 to 12
13 to 14
15 to 16
17 to 18
Mean annual precipitation (1970-2000)
0 to 14
14.1 to 34
34.1 to 57
57.1 to 84
84.1 to 116
117 to 154
155 to 199
200 to 253
254 to 345
346 to 938
0°
30°S
60°W
60°E
70°S
120°W
120°E
180°
South America
Patagonia
Antarctica
New Zealand
SWW
PF
SAF
STF
50°S
Legend for panel C
Northerly limit of the SWW
Subantarctic Front (SAF)
Mean annual windspeed (1970 - 2000)
High : 27.9
Low : 0

Figure 3.

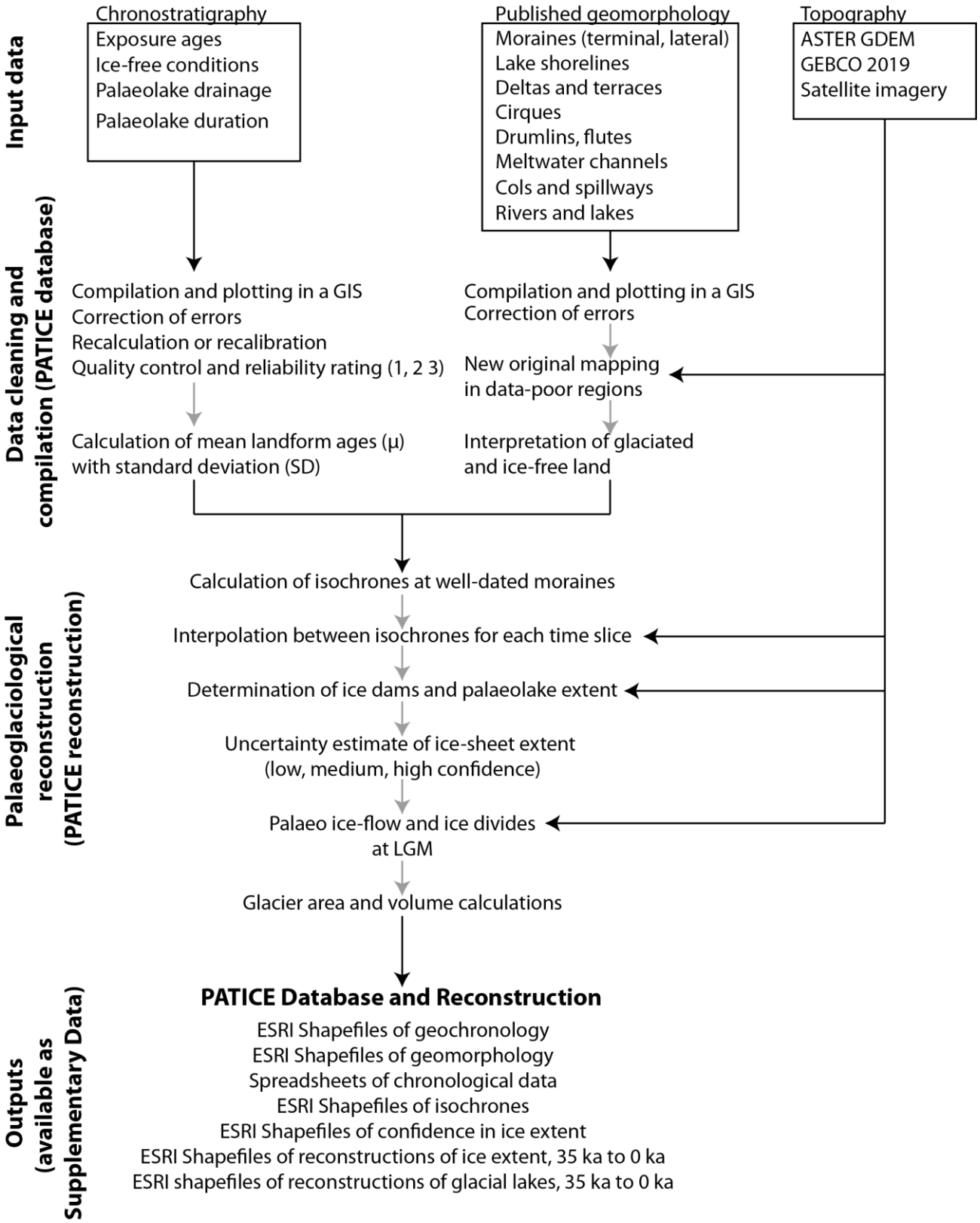
Input data
Chronostratigraphy
Exposure ages
Ice-free conditions
Palaeolake drainage
Palaeolake duration
Published geomorphology
Moraines (terminal, lateral)
Lake shorelines
Deltas and terraces
Cirques
Drumlins, flutes
Meltwater channels
Cols and spillways
Rivers and lakes
Topography
ASTER GDEM
GEBCO 2019
Satellite imagery
Data cleaning and compilation (PATICE database)
Compilation and plotting in a GIS
Correction of errors
Recalculation or recalibration
Quality control and reliability rating (1, 2 3)
Compilation and plotting in a GIS
Correction of errors
New original mapping in data-poor regions
Calculation of mean landform ages (μ) with standard deviation (SD)
Interpretation of glaciated and ice-free land
Palaeoglaciological reconstruction (PATICE reconstruction)
Calculation of isochrones at well-dated moraines
Interpolation between isochrones for each time slice
Determination of ice dams and palaeolake extent
Uncertainty estimate of ice-sheet extent (low, medium, high confidence)
Palaeo ice-flow and ice divides at LGM
Glacier area and volume calculations
Outputs (available as Supplementary Data)
PATICE Database and Reconstruction
ESRI Shapefiles of geochronology
ESRI Shapefiles of geomorphology
Spreadsheets of chronological data
ESRI Shapefiles of isochrones
ESRI Shapefiles of confidence in ice extent
ESRI Shapefiles of reconstructions of ice extent, 35 ka to 0 ka
ESRI shapefiles of reconstructions of glacial lakes, 35 ka to 0 ka

Figure 4

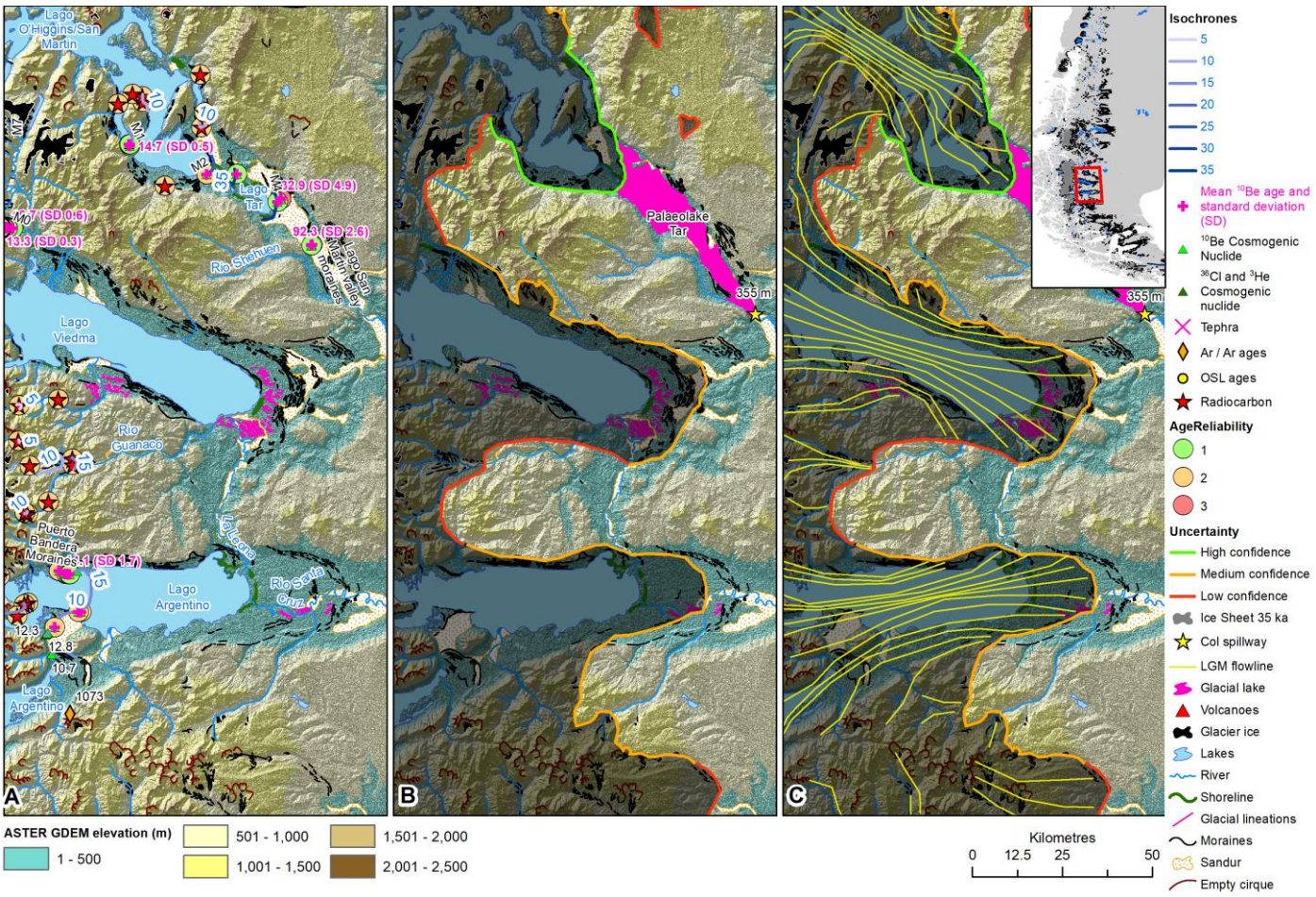

Figure 5.

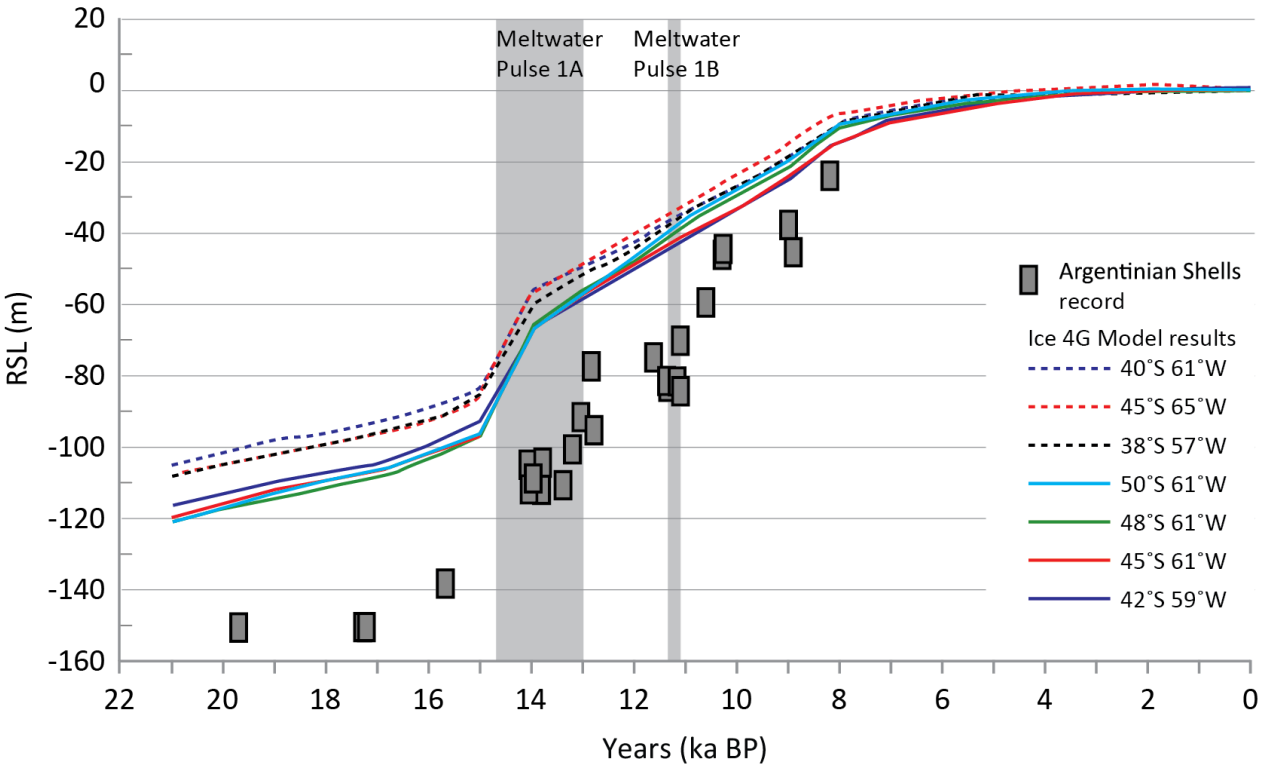

Figure 6.

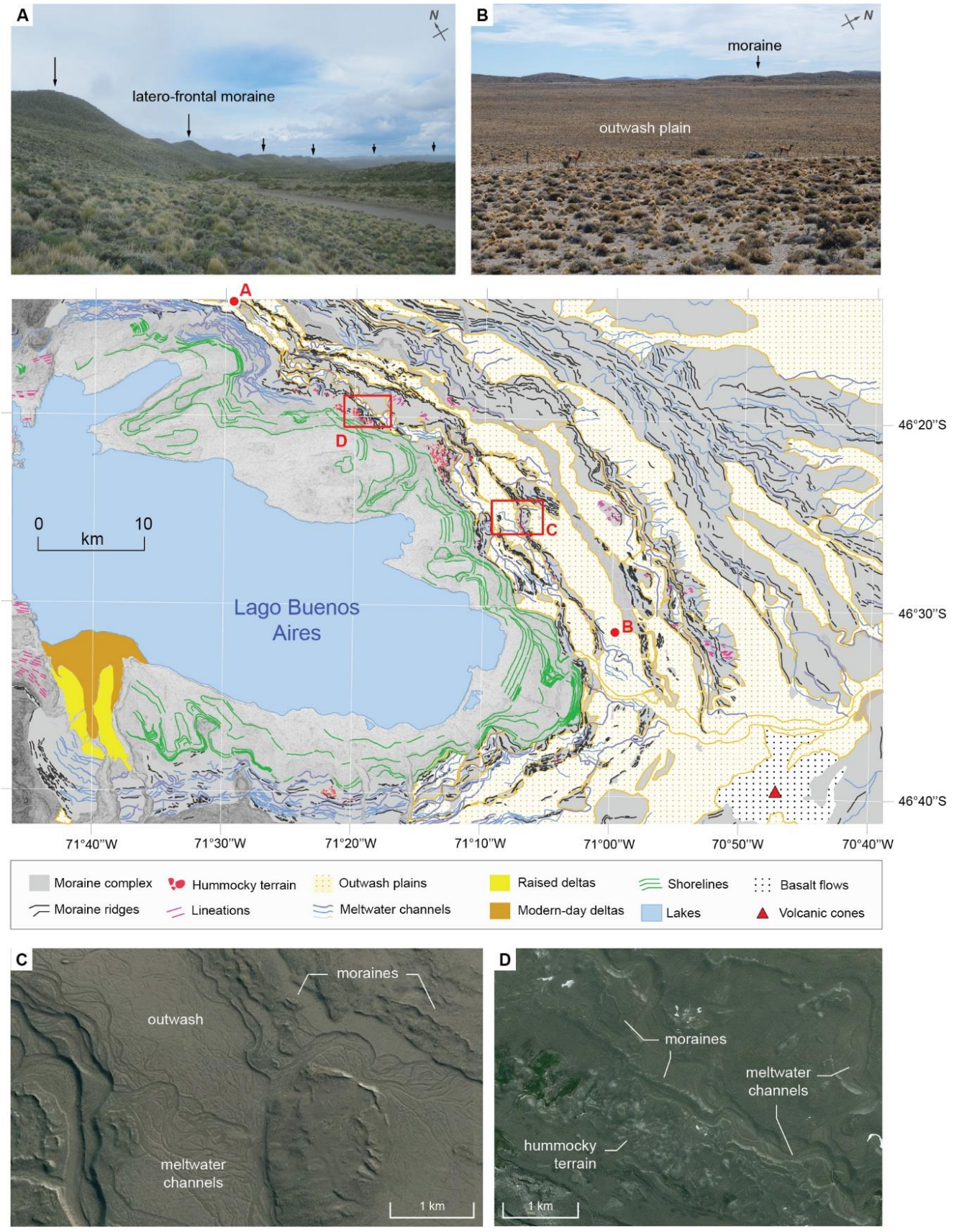
A
N
latero-frontal moraine
B
N
moraine
outwash plain
A
D
C
B
0
10
km
Lago Buenos
Aires
46°20"S
46°30"S
46°40"S
71°40"W
71°30"W
71°20"W
71°10"W
71°00"W
70°50"W
70°40"W
Moraine complex
Hummocky terrain
Outwash plains
Raised deltas
Shorelines
Basalt flows
Moraine ridges
Lineations
Meltwater channels
Modern-day deltas
Lakes
Volcanic cones
C
moraines
outwash
meltwater
channels
1 km
D
moraines
meltwater
channels
hummocky
terrain
1 km

Figure 7.

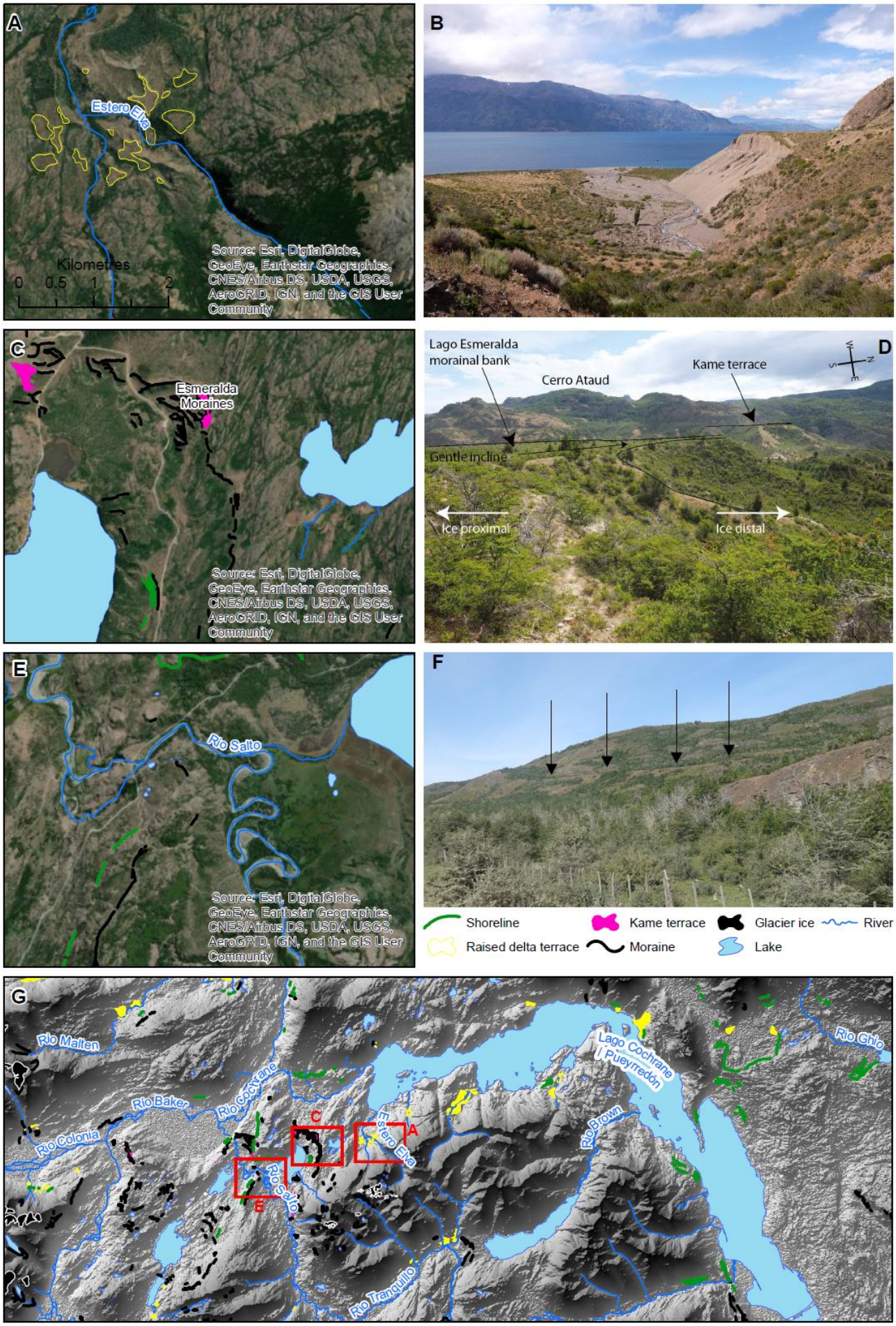
A
Estero Elsa
Kilometres
0 0.5 1 2
Source: Esri, DigitalGlobe, GeoEye, Earthstar Geographics, CNES/Airbus DS, USDA, USGS, AeroGRID, IGN, and the GIS User Community
B
C
Esmeralda Moraines
Source: Esri, DigitalGlobe, GeoEye, Earthstar Geographics, CNES/Airbus DS, USDA, USGS, AeroGRID, IGN, and the GIS User Community
D
Lago Esmeralda morainal bank
Cerro Ataud
Kame terrace
Gentle incline
Ice proximal
Ice distal
E
Rio Salto
Source: Esri, DigitalGlobe, GeoEye, Earthstar Geographics, CNES/Airbus DS, USDA, USGS, AeroGRID, IGN, and the GIS User Community
F
Shoreline
Kame terrace
Glacier ice
River
Raised delta terrace
Moraine
Lake
G
Rio Malten
Rio Baker
Rio Cochrane
Rio Colonia
Lago Cochrane / Pueyrredon
Rio Ghio
Rio Brown
Rio Salto
Rio Tranquilo

Figure 8.

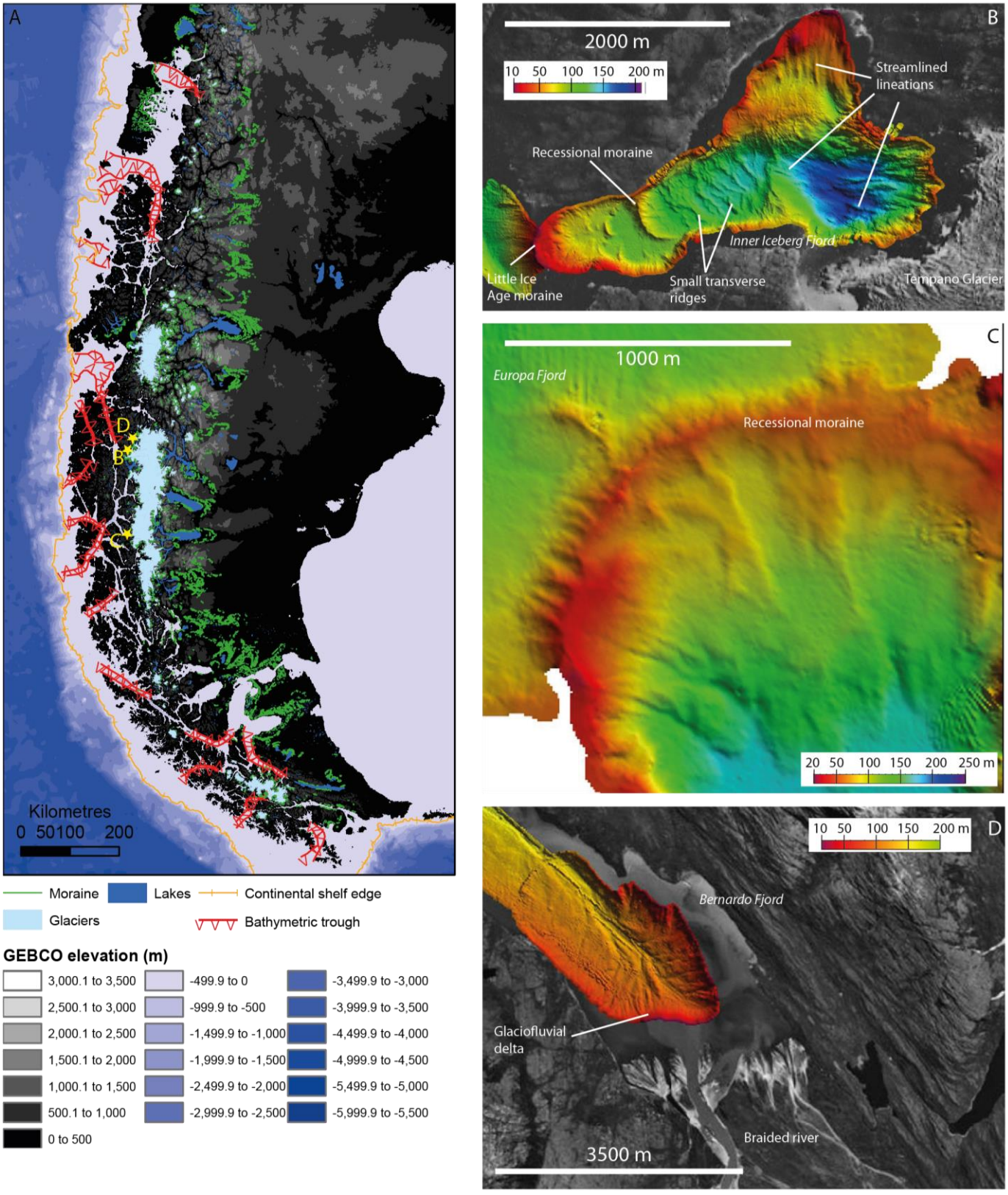
A
Kilometres
0 50100 200
D
B
C
Moraine
Lakes
Continental shelf edge
Glaciers
Bathymetric trough
GEBCO elevation (m)
3,000.1 to 3,500
2,500.1 to 3,000
2,000.1 to 2,500
1,500.1 to 2,000
1,000.1 to 1,500
500.1 to 1,000
0 to 500
-499.9 to 0
-999.9 to -500
-1,499.9 to -1,000
-1,999.9 to -1,500
-2,499.9 to -2,000
-2,999.9 to -2,500
-3,499.9 to -3,000
-3,999.9 to -3,500
-4,499.9 to -4,000
-4,999.9 to -4,500
-5,499.9 to -5,000
-5,999.9 to -5,500
B
2000 m
10 50 100 150 200 m
Streamlined lineations
Recessional moraine
Inner Iceberg Fjord
Little Ice Age moraine
Small transverse ridges
Tempano Glacier
C
1000 m
Europa Fjord
Recessional moraine
20 50 100 150 200 250 m
D
10 50 100 150 200 m
Bernardo Fjord
Glaciofluvial delta
Braided river
3500 m

Figure 9.

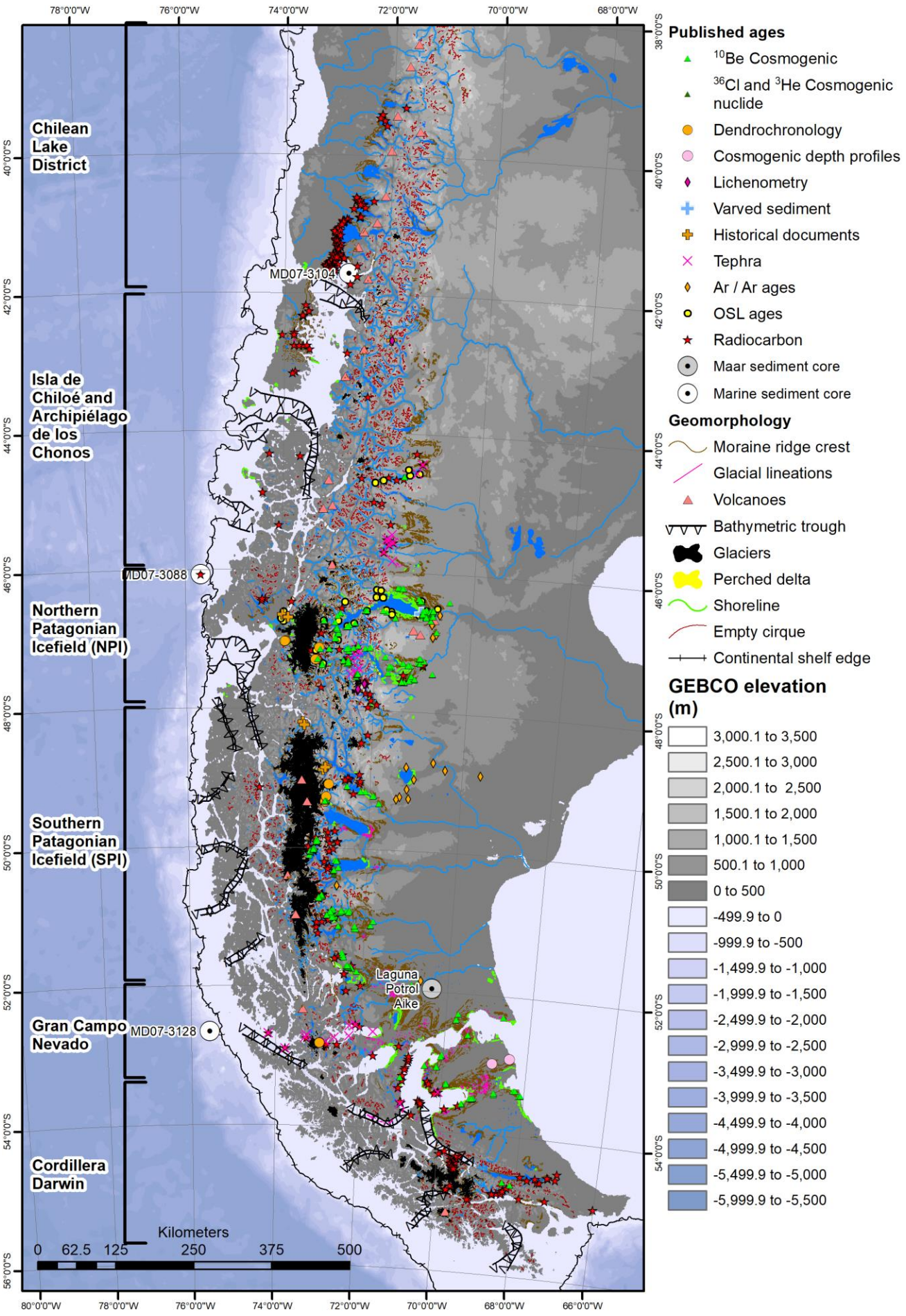
Chilean Lake District
Isla de Chiloé and Archipiélago de los Chonos
Northern Patagonian Icefield (NPI)
Southern Patagonian Icefield (SPI)
Gran Campo Nevado
Cordillera Darwin
MD07-3104
MD07-3088
MD07-3128
Laguna Potrol Aike
Kilometers
0 62.5 125 250 375 500
Published ages
10Be Cosmogenic
36Cl and 3He Cosmogenic nuclide
Dendrochronology
Cosmogenic depth profiles
Lichenometry
Varved sediment
Historical documents
Tephra
Ar / Ar ages
OSL ages
Radiocarbon
Maar sediment core
Marine sediment core
Geomorphology
Moraine ridge crest
Glacial lineations
Volcanoes
Bathymetric trough
Glaciers
Perched delta
Shoreline
Empty cirque
Continental shelf edge
GEBCO elevation (m)
3,000.1 to 3,500
2,500.1 to 3,000
2,000.1 to 2,500
1,500.1 to 2,000
1,000.1 to 1,500
500.1 to 1,000
0 to 500
-499.9 to 0
-999.9 to -500
-1,499.9 to -1,000
-1,999.9 to -1,500
-2,499.9 to -2,000
-2,999.9 to -2,500
-3,499.9 to -3,000
-3,999.9 to -3,500
-4,499.9 to -4,000
-4,999.9 to -4,500
-5,499.9 to -5,000
-5,999.9 to -5,500

Figure 10.

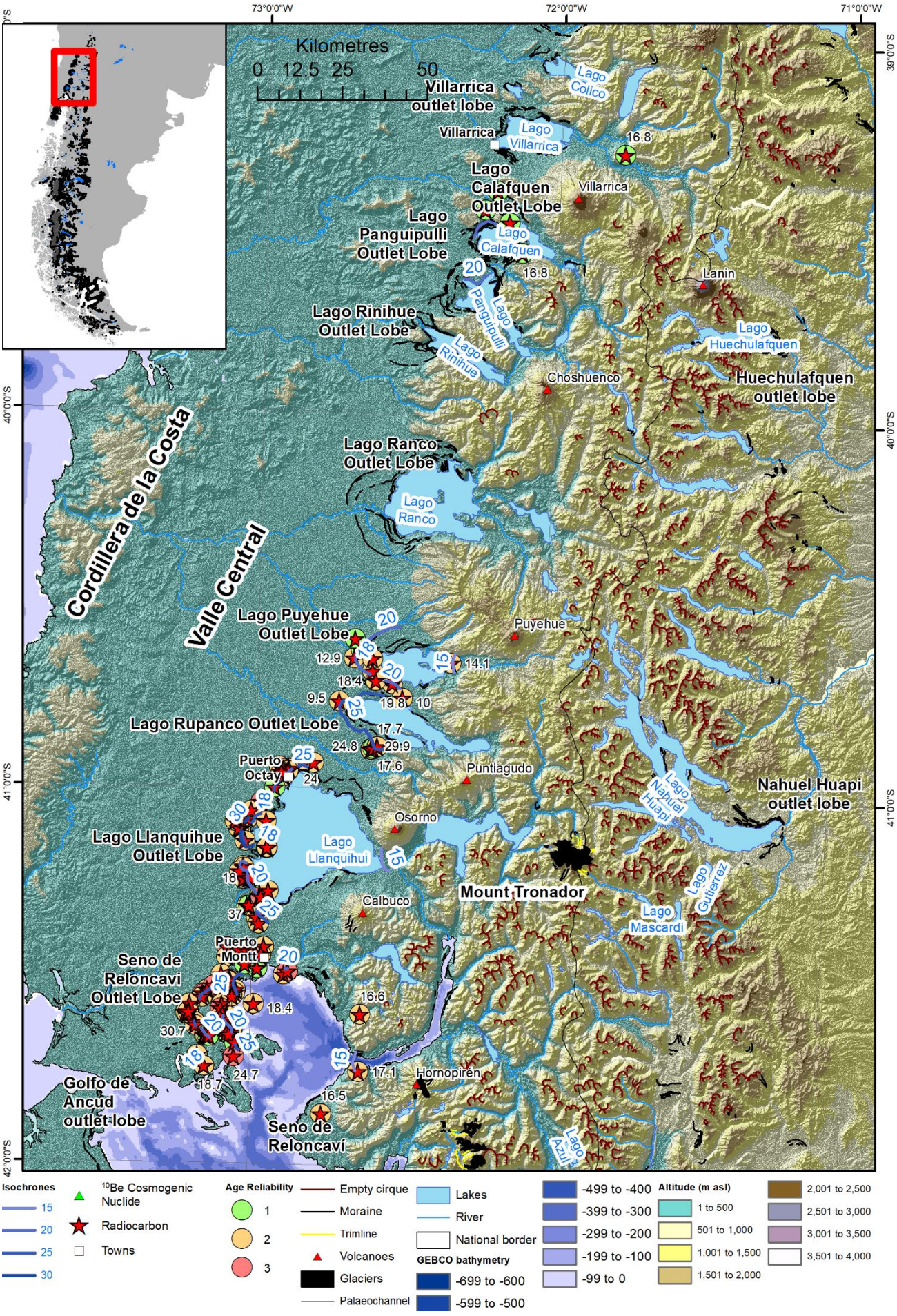
Kilometres
0 12.5 25 50
73°0'0"W
72°0'0"W
71°0'0"W
39°0'0"S
40°0'0"S
41°0'0"S
42°0'0"S
Villarrica outlet lobe
Lago Colico
Villarrica
Lago Villarrica
16.8
Lago Calafquen Outlet Lobe
Lago Panguipulli Outlet Lobe
Lago Calafquen
Lanin
Lago Panguipulli
Lago Rinihue Outlet Lobe
Lago Rinihue
Lago Huechulafquen
Choshuenco
Huechulafquen outlet lobe
Lago Ranco Outlet Lobe
Lago Ranco
Cordillera de la Costa
Valle Central
Lago Puyehue Outlet Lobe
Puyehue
12.9
14.1
18.4
19.8
9.5
Lago Rupanco Outlet Lobe
17.7
24.8
29.9
17.6
Puerto Octay
Puntiagudo
Nahuel Huapi outlet lobe
Lago Nahuel Huapi
Osorno
Lago Llanquihue Outlet Lobe
Lago Llanquihui
Mount Tronador
Lago Gutierrez
Calbuco
Lago Mascardi
Puerto Montt
Seno de Reloncavi Outlet Lobe
16.6
18.4
30.7
24.7
18.7
16.5
17.1
Hornopirén
Golfo de Ancud outlet lobe
Seno de Reloncaví
Lago Azul
Isochrones
15
20
25
30
10Be Cosmogenic Nuclide
Radiocarbon
Towns
Age Reliability
1
2
3
Empty cirque
Moraine
Trimline
Volcanoes
Glaciers
Palaeochannel
Lakes
River
National border
GEBCO bathymetry
-699 to -600
-599 to -500
-499 to -400
-399 to -300
-299 to -200
-199 to -100
-99 to 0
Altitude (m asl)
1 to 500
501 to 1,000
1,001 to 1,500
1,501 to 2,000
2,001 to 2,500
2,501 to 3,000
3,001 to 3,500
3,501 to 4,000

Figure 11.

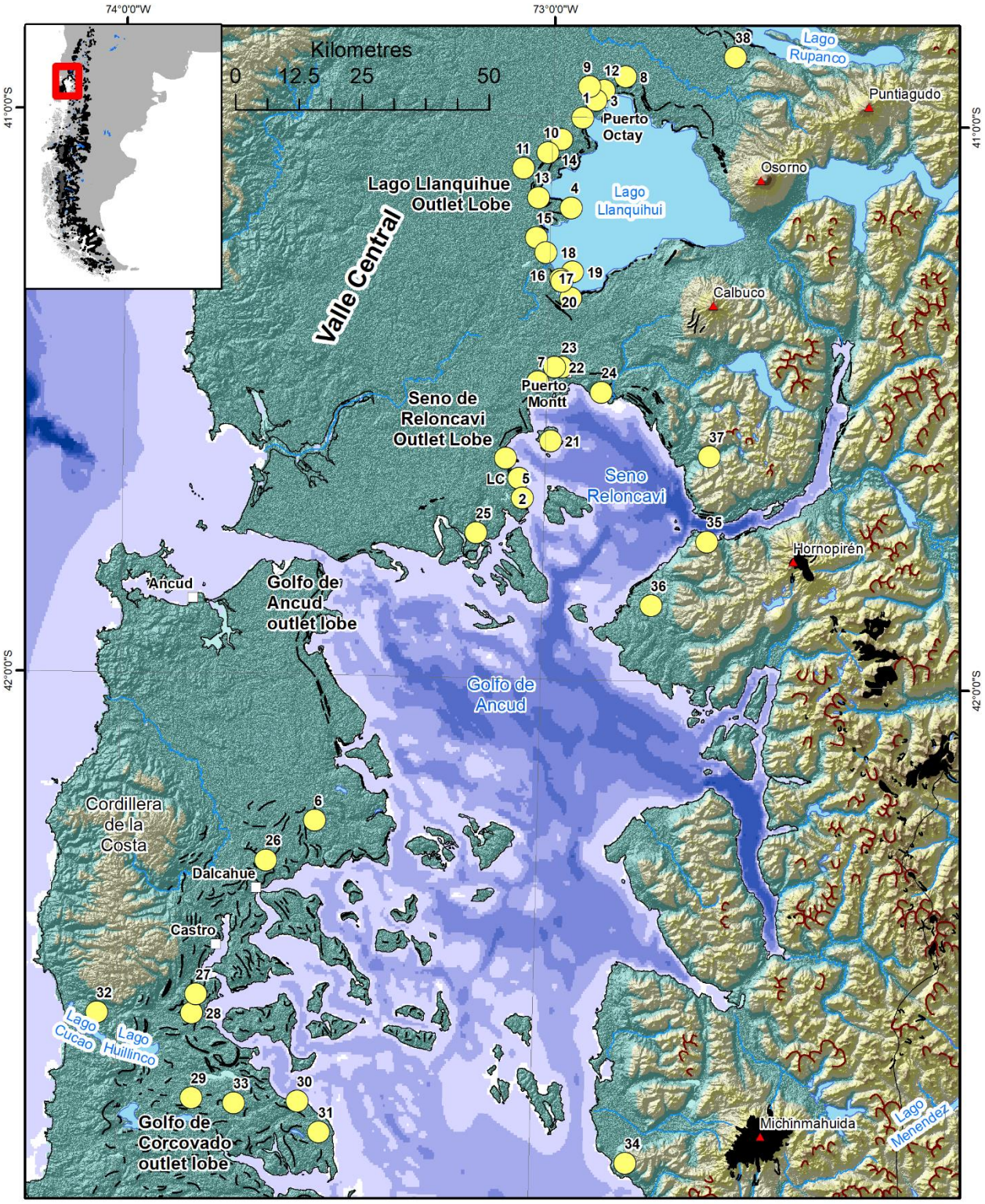

Number	Name	Number	Name	Number	Name	Number	Name
1	Canal de la Puntilla	11	Frutilla Alto	21	Isla Maillen	30	Lago Tahui
2	Huelmo	12	Canal de Chanchan	22	No name	31	Lago Melli
3	Puerto Octay	13	No Name	23	Lago Lepue	32	Lago Taruman
4	Bahia Frutiilla Bajo	14	Fundo Linea Pantanosa	24	Punta Penas, upper	33	Lago Lepue
5	Seno Reloncavi, top of organic bed	15	Fundo Llanquihue	25	Near Calbuco, reworked clast in till	34	Chaiten, base of organic bed
6	Teguaco, top of organic bed	16	Puerto Varas Railroad Bridge, lower	26	Dalcahue, top of organic bed	35	Caleta Puelche, base of organic bed
7	Puerto Montt	17	Bella Vista Bluff	27	Mayol	36	Lago Proschle
8	Organic clast reworked into Llanquihue outwash	18	Llaniquihue	28	Esteri Huitanque	37	Lago Reflejos
9	Organic clast reworked into Llanquihue outwash	19	Northwest Bluff	29	Unnamed bog	38	Lago Bonita
10	Organic clast reworked into Llanquihue outwash	20	Calla Santa Rosa, Puerto Varas			LC	Lago Condorito

Figure 12

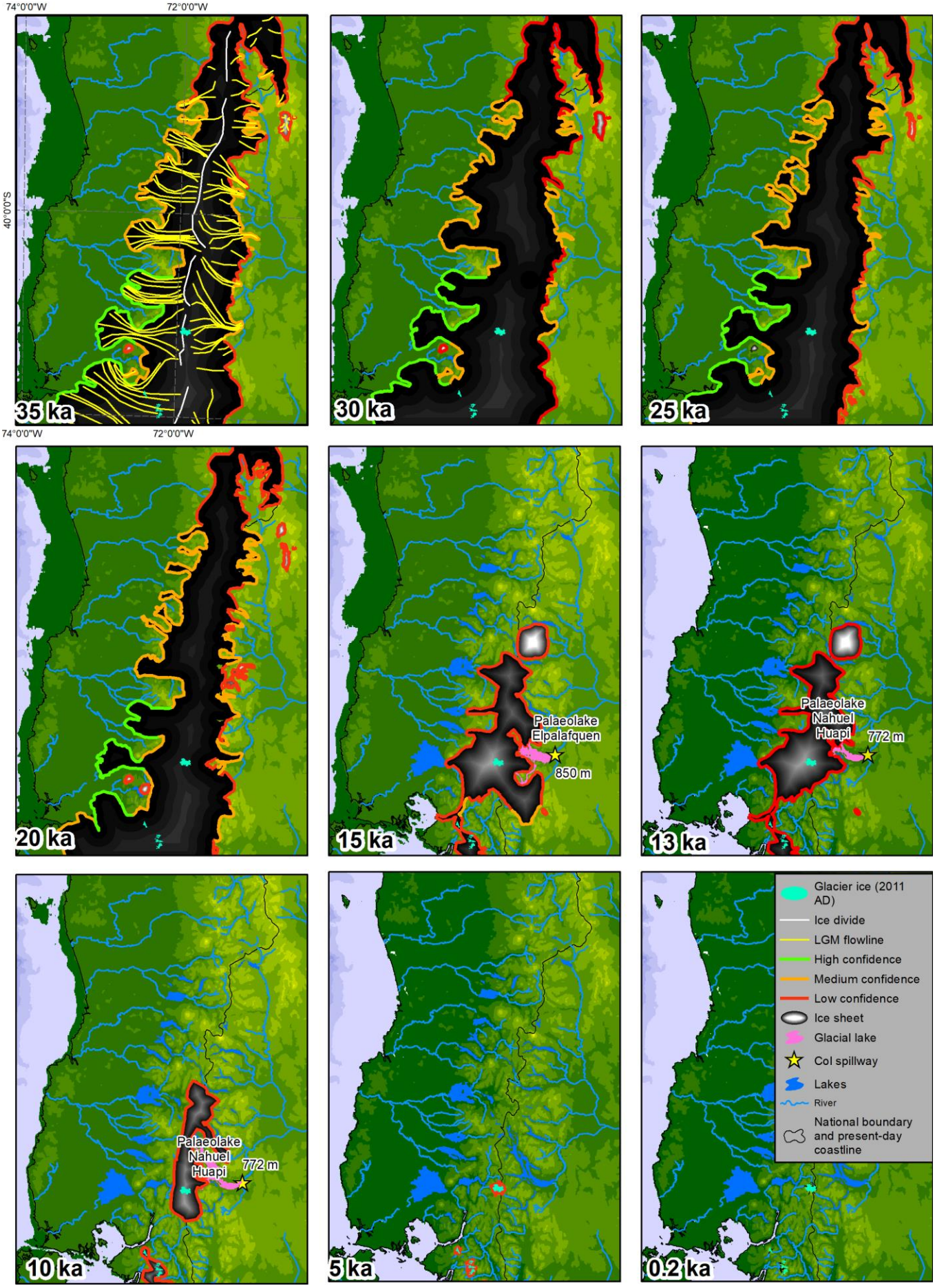
74°0'0"W
72°0'0"W
40°0'0"S
35 ka
30 ka
25 ka
20 ka
15 ka
13 ka
10 ka
5 ka
0.2 ka
Palaeolake Elpalafquen
850 m
Palaeolake Nahuel Huapi
772 m
Glacier ice (2011 AD)
Ice divide
LGM flowline
High confidence
Medium confidence
Low confidence
Ice sheet
Glacial lake
Col spillway
Lakes
River
National boundary and present-day coastline

Figure 13.

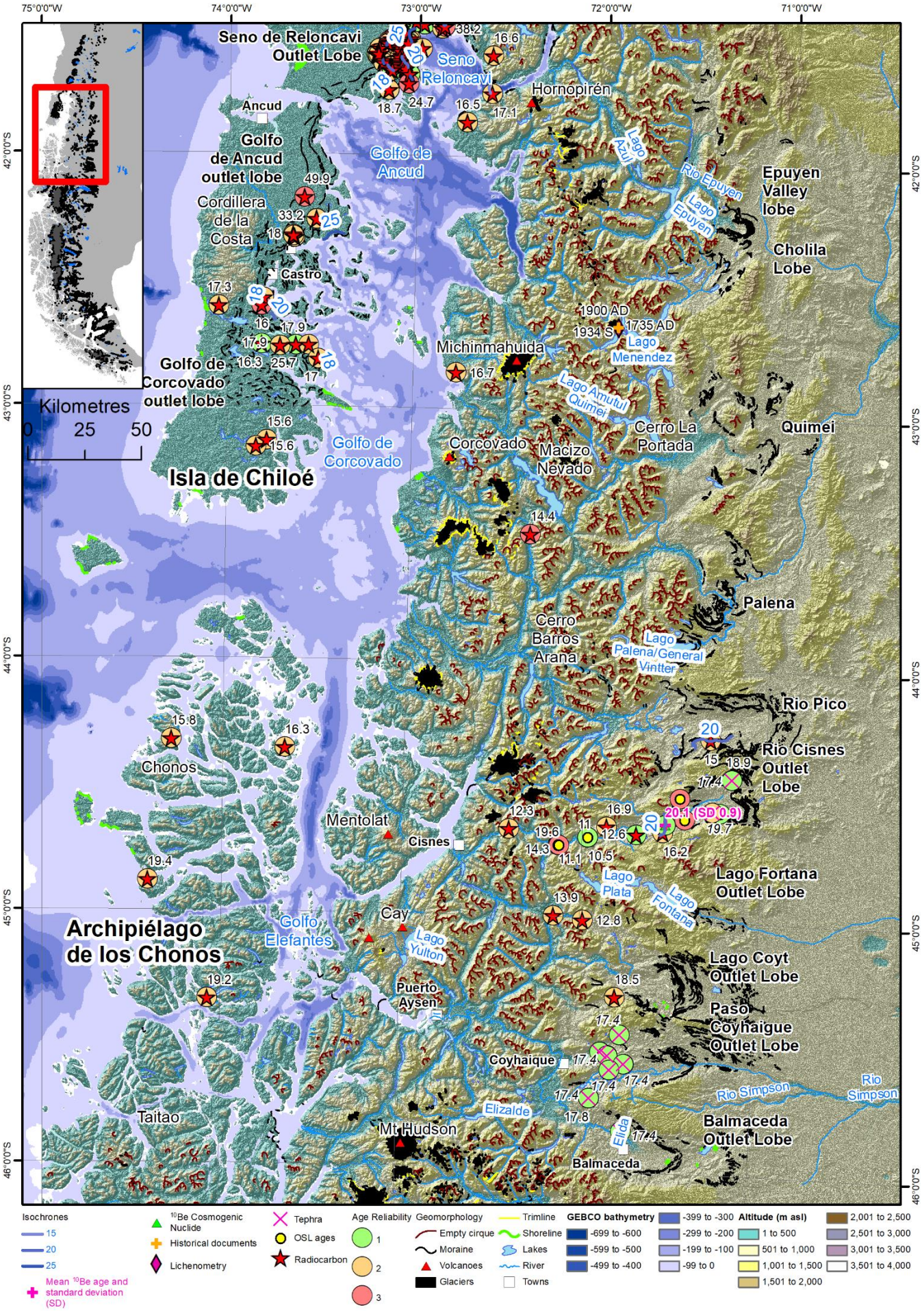
75°0'0"W
74°0'0"W
73°0'0"W
72°0'0"W
71°0'0"W
42°0'0"S
43°0'0"S
44°0'0"S
45°0'0"S
46°0'0"S
Seno de Reloncavi Outlet Lobe
Seno Reloncavi
Hornopirén
Ancud
Golfo de Ancud outlet lobe
Golfo de Ancud
Cordillera de la Costa
Castro
Golfo de Corcovado outlet lobe
Golfo de Corcovado
Isla de Chiloé
Kilometres
0 25 50
Lago Azul
Rio Epuyen
Lago Epuyen
Epuyen Valley lobe
Cholila Lobe
1900 AD
1934 S
1735 AD
Lago Menendez
Michinmahuida
Lago Amutui Quimei
Quimei
Cerro La Portada
Corcovado
Macizo Nevado
Palena
Cerro Barros Arana
Lago Palena/General Vintter
Rio Pico
Rio Cisnes Outlet Lobe
20.1 (SD 0.9)
Chonos
Mentolat
Cisnes
Lago Fontana Outlet Lobe
Lago Plata
Lago Fontana
Archipiélago de los Chonos
Golfo Elefantes
Cay
Lago Yulton
Puerto Aysen
Lago Coyt Outlet Lobe
Paso Coyhaigue Outlet Lobe
Coyhaique
Rio Simpson
Elizalde
Taitao
Mt Hudson
Balmaceda Outlet Lobe
Balmaceda
Isochrones
15
20
25
Mean 10Be age and standard deviation (SD)
10Be Cosmogenic Nuclide
Historical documents
Lichenometry
Tephra
OSL ages
Radiocarbon
Age Reliability
1
2
3
Geomorphology
Empty cirque
Moraine
Volcanoes
Glaciers
Trimline
Shoreline
Lakes
River
Towns
GEBCO bathymetry
-399 to -300
-299 to -200
-199 to -100
-99 to 0
-699 to -600
-599 to -500
-499 to -400
Altitude (m asl)
1 to 500
501 to 1,000
1,001 to 1,500
1,501 to 2,000
2,001 to 2,500
2,501 to 3,000
3,001 to 3,500
3,501 to 4,000

Figure 14.

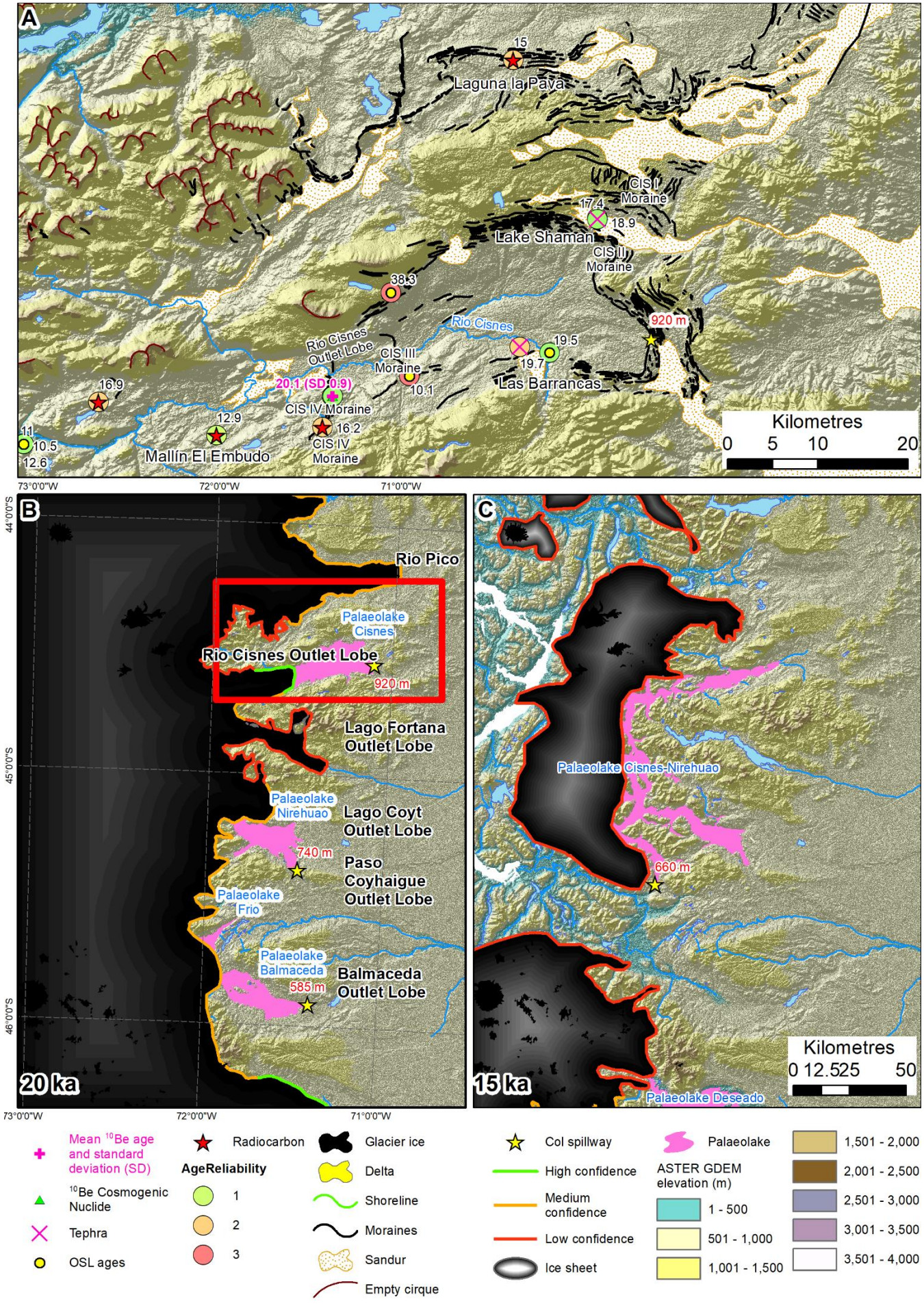
A
15
Laguna la Paya
CIS I Moraine
17.4
18.9
Lake Shaman
CIS II Moraine
38.3
Rio Cisnes
920 m
Rio Cisnes Outlet Lobe
CIS III Moraine
19.5
19.7
Las Barrancas
16.9
20.1 (SD 0.9)
10.1
CIS IV Moraine
12.9
16.2
11
10.5
12.6
Mallín El Embudo
CIS IV Moraine
Kilometres
0 5 10 20
73°0'0"W
72°0'0"W
71°0'0"W
B
Rio Pico
Palaeolake Cisnes
Rio Cisnes Outlet Lobe
920 m
Lago Fortana Outlet Lobe
Palaeolake Nirehuao
Lago Coyt Outlet Lobe
740 m
Paso Coyhaigue Outlet Lobe
Palaeolake Frio
Palaeolake Balmaceda
585 m
Balmaceda Outlet Lobe
20 ka
44°0'0"S
45°0'0"S
46°0'0"S
73°0'0"W
72°0'0"W
71°0'0"W
C
Palaeolake Cisnes-Nirehuao
660 m
Kilometres
0 12.525 50
15 ka
Palaeolake Deseado
Mean 10Be age and standard deviation (SD)
10Be Cosmogenic Nuclide
Tephra
OSL ages
Radiocarbon
AgeReliability
1
2
3
Glacier ice
Delta
Shoreline
Moraines
Sandur
Empty cirque
Col spillway
High confidence
Medium confidence
Low confidence
Ice sheet
Palaeolake
ASTER GDEM elevation (m)
1 - 500
501 - 1,000
1,001 - 1,500
1,501 - 2,000
2,001 - 2,500
2,501 - 3,000
3,001 - 3,500
3,501 - 4,000

Figure 15.

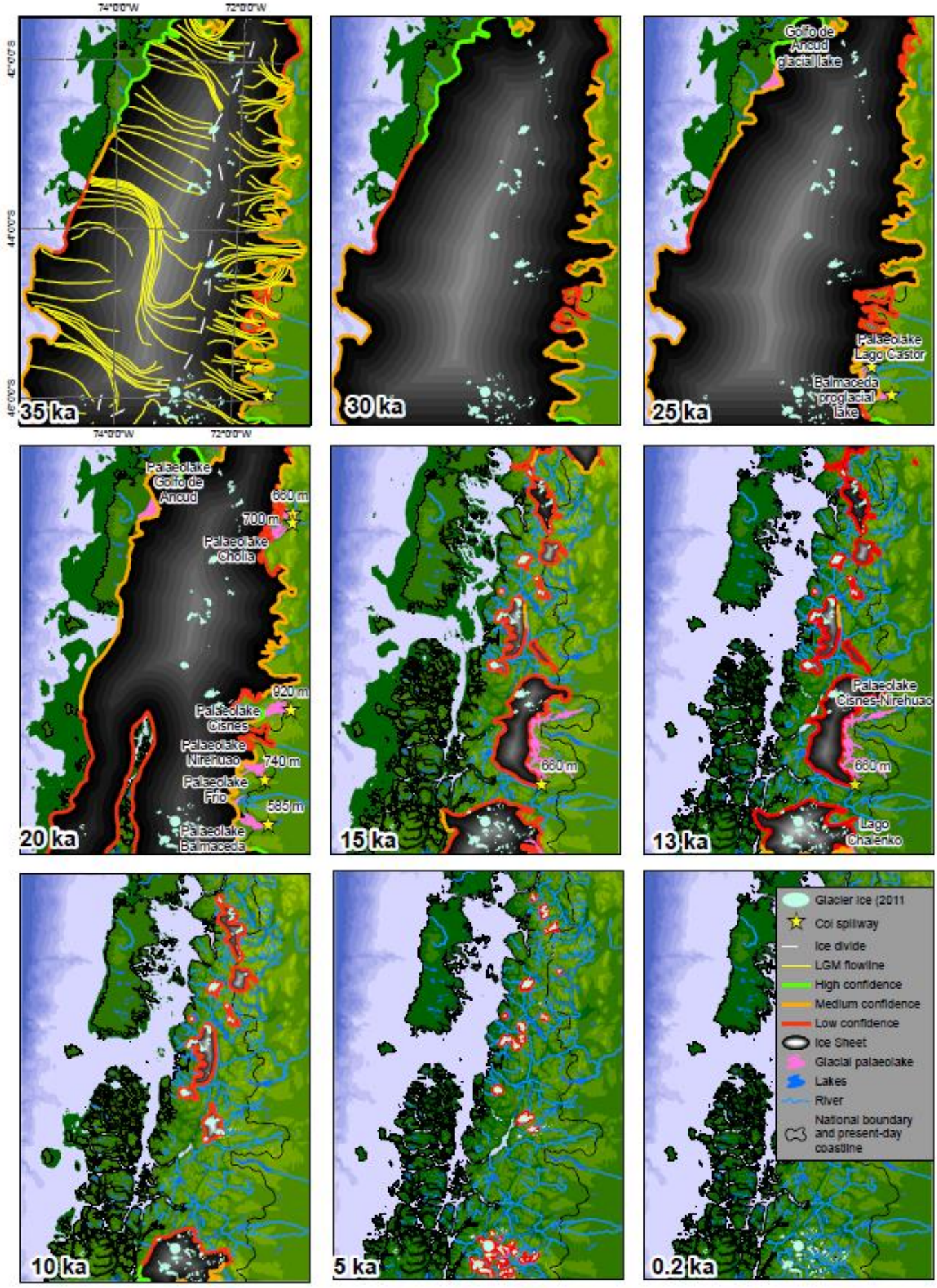
74°0'0"W
72°0'0"W
43°0'0"S
44°0'0"S
45°0'0"S
35 ka
30 ka
Golfo de Ancud glacial lake
Palaeolake Lago Castor
Balmaceda proglacial lake
25 ka
Palaeolake Golfo de Ancud
680 m
700 m
Palaeolake Cholia
920 m
Palaeolake Cisnes
Palaeolake Nirehuao
740 m
Palaeolake Frio
585 m
Palaeolake Balmaceda
20 ka
680 m
15 ka
Palaeolake Cisnes-Nirehuao
680 m
Lago Chalenko
13 ka
10 ka
5 ka
0.2 ka
Glacier ice (2011
Col spillway
Ice divide
LGM flowline
High confidence
Medium confidence
Low confidence
Ice Sheet
Glacial palaeolake
Lakes
River
National boundary and present-day coastline

Figure 16.

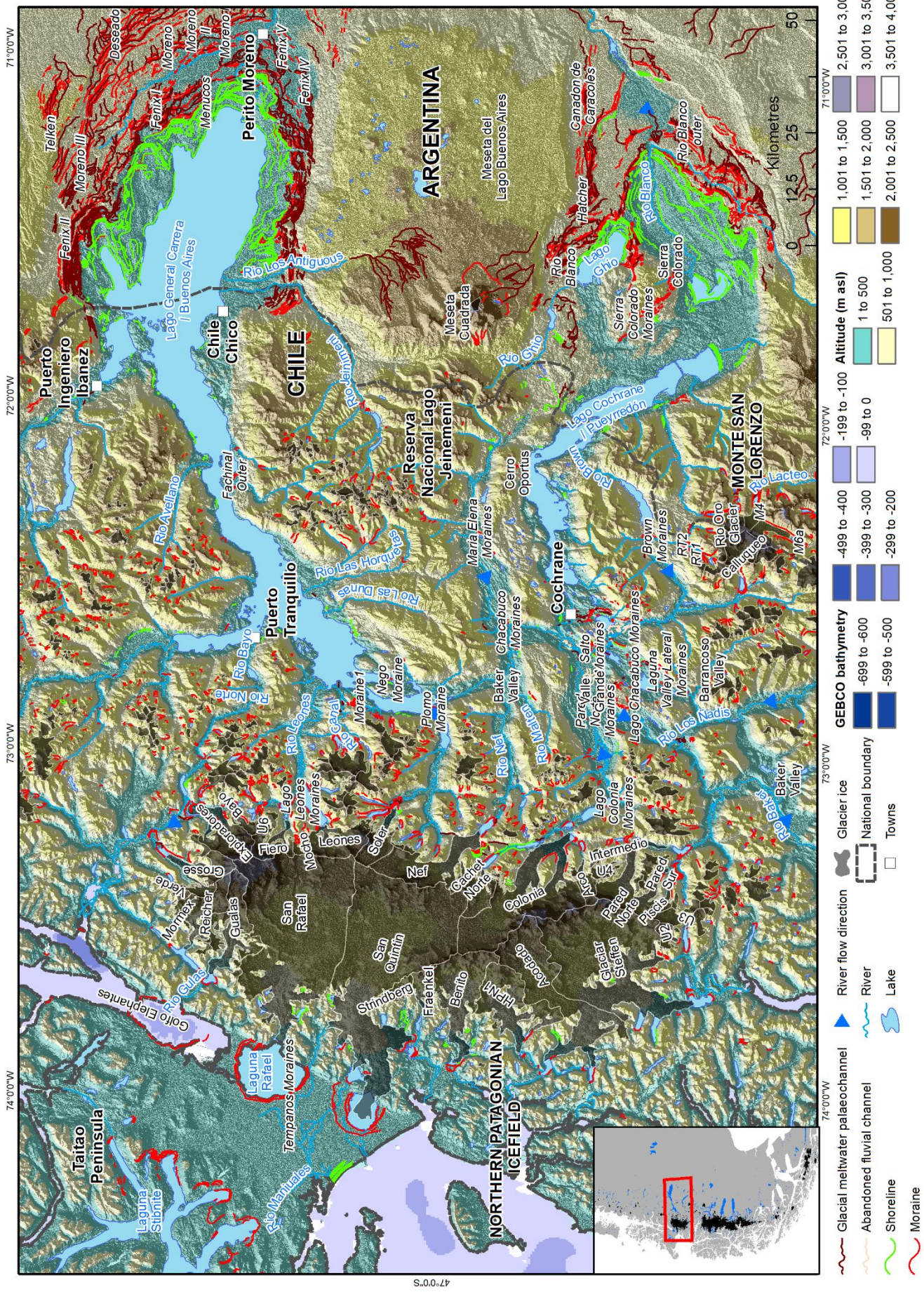
ARGENTINA
CHILE
NORTHERN PATAGONIAN ICEFIELD
Taitao Peninsula
Puerto Ingeniero Ibanez
Chile Chico
Puerto Tranquillo
Perito Moreno
Cochrane
MONTE SAN LORENZO
Reserva Nacional Lago Jeinemeni
Meseta del Lago Buenos Aires
Meseta Cuadrada
Canadon de Caracoles
Lago General Carrera / Buenos Aires
Lago Cochrane / Pueyrredon
Rio Los Antiguous
Rio Jeinemeni
Rio Ghio
Rio Blanco
Rio Avellano
Rio Bayo
Rio Norte
Rio Leones
Rio Las Horquetas
Rio Las Dunas
Rio Nef
Rio Maiten
Rio Los Nadis
Rio Oro
Rio Lacteo
Rio Baker
Rio Mantuales
Rio Gulas
Laguna Sibinite
Laguna Rafael
Golfo Elefantes
Fachinal Outer
Lago Leones
Lago Colonia
Lago Chacabuco
Glacier ice
River flow direction
River
National boundary
Towns
Lake
GEBCO bathymetry
-499 to -400
-399 to -300
-299 to -200
-199 to -100
-99 to 0
-699 to -600
-599 to -500
Altitude (m asl)
1 to 500
501 to 1,000
1,001 to 1,500
1,501 to 2,000
2,001 to 2,500
2,501 to 3,000
3,001 to 3,500
3,501 to 4,000
Glacial meltwater palaeochannel
Abandoned fluvial channel
Shoreline
Moraine
Kilometres
0
12.5
25
50
71°0'0"W
72°0'0"W
73°0'0"W
74°0'0"W
47°0'0"S

Figure 17.

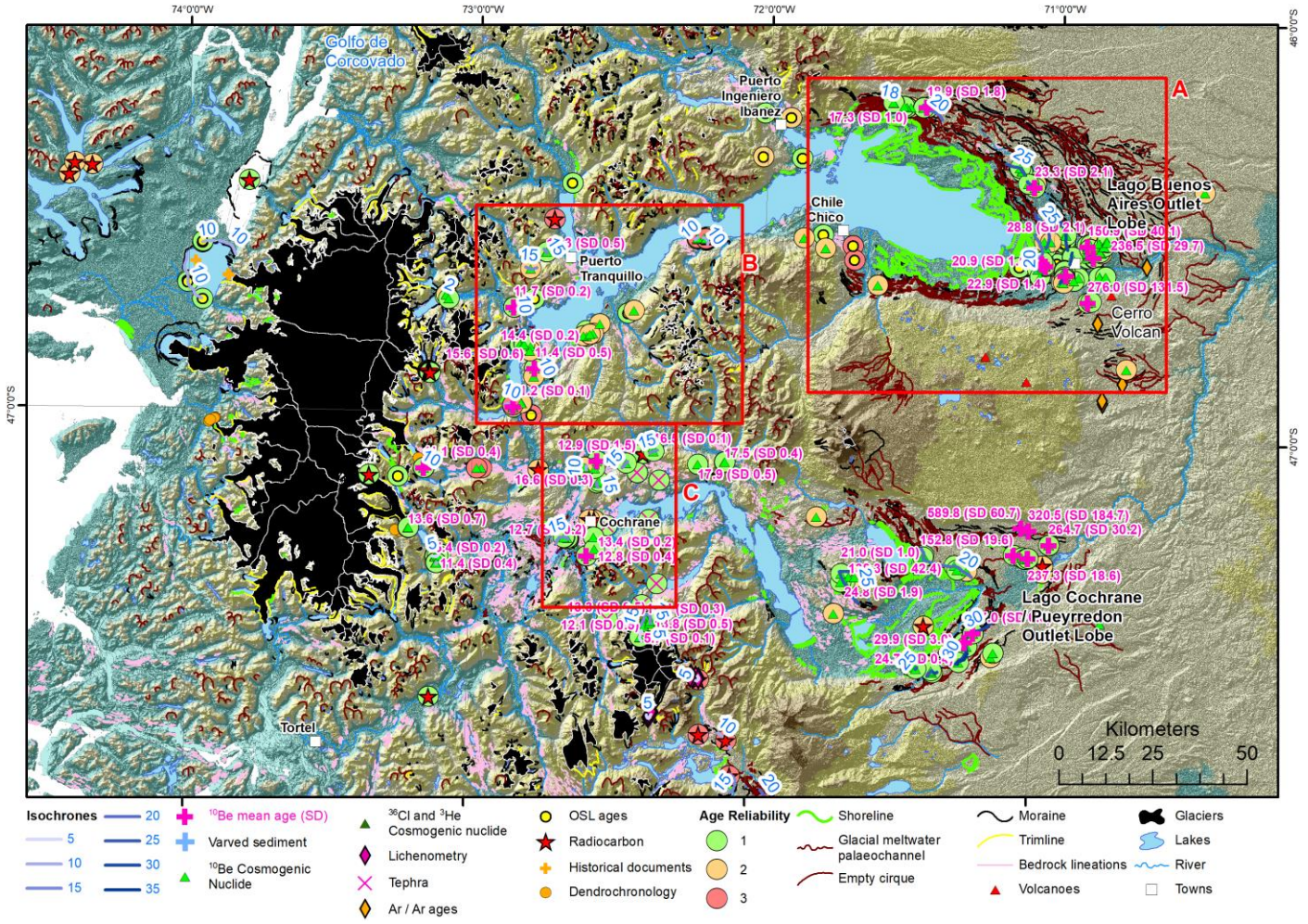
74°0'0"W
73°0'0"W
72°0'0"W
71°0'0"W
46°0'0"S
47°0'0"S
Golfo de Corcovado
Puerto Ingeniero Ibanez
Chile Chico
Puerto Tranquillo
Cochrane
Tortel
Lago Buenos Aires Outlet Lobe
Cerro Volcan
Lago Cochrane / Pueyrredon Outlet Lobe
A
B
C
Kilometers
0 12.5 25 50
Isochrones
5
10
15
20
25
30
35
10Be mean age (SD)
Varved sediment
10Be Cosmogenic Nuclide
36Cl and 3He Cosmogenic nuclide
Lichenometry
Tephra
Ar / Ar ages
OSL ages
Radiocarbon
Historical documents
Dendrochronology
Age Reliability
1
2
3
Shoreline
Glacial meltwater palaeochannel
Empty cirque
Moraine
Trimline
Bedrock lineations
Volcanoes
Glaciers
Lakes
River
Towns

Figure 18.

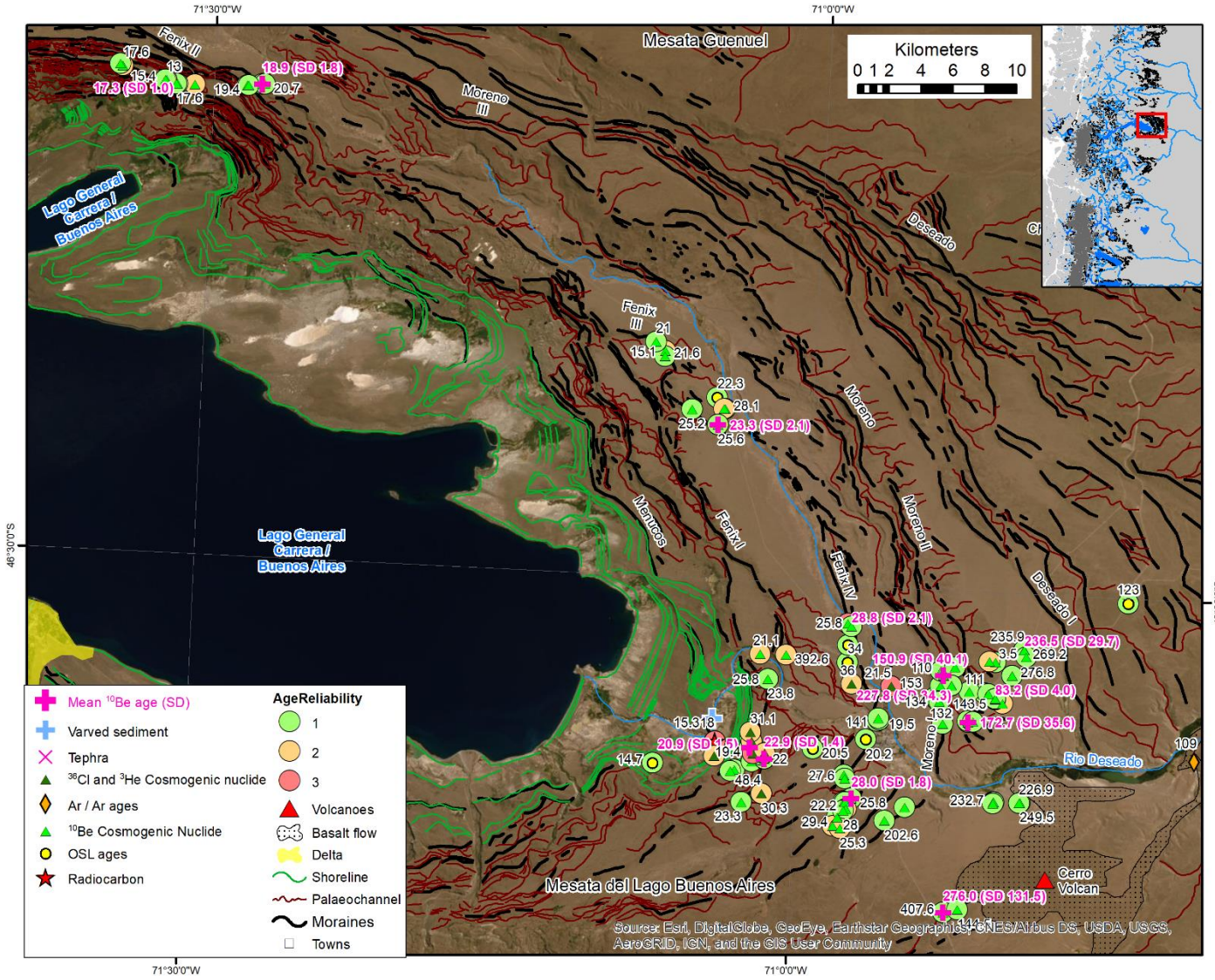
71°30'0"W
71°0'0"W
46°30'0"S
Mesata Guenuel
Kilometers
0 1 2 4 6 8 10
Fenix II
Moreno III
Lago General Carrera / Buenos Aires
Deseado
Fenix III
Moreno
Meniques
Fenix I
Fenix IV
Moreno II
Deseado I
Rio Deseado
Mesata del Lago Buenos Aires
Cerro Volcan
Source: Esri, DigitalGlobe, GeoEye, Earthstar Geographics, CNES/Airbus DS, USDA, USGS, AeroGRID, IGN, and the GIS User Community
Mean 10Be age (SD)
Varved sediment
Tephra
36Cl and 3He Cosmogenic nuclide
Ar / Ar ages
10Be Cosmogenic Nuclide
OSL ages
Radiocarbon
AgeReliability
1
2
3
Volcanoes
Basalt flow
Delta
Shoreline
Palaeochannel
Moraines
Towns

Figure 19.

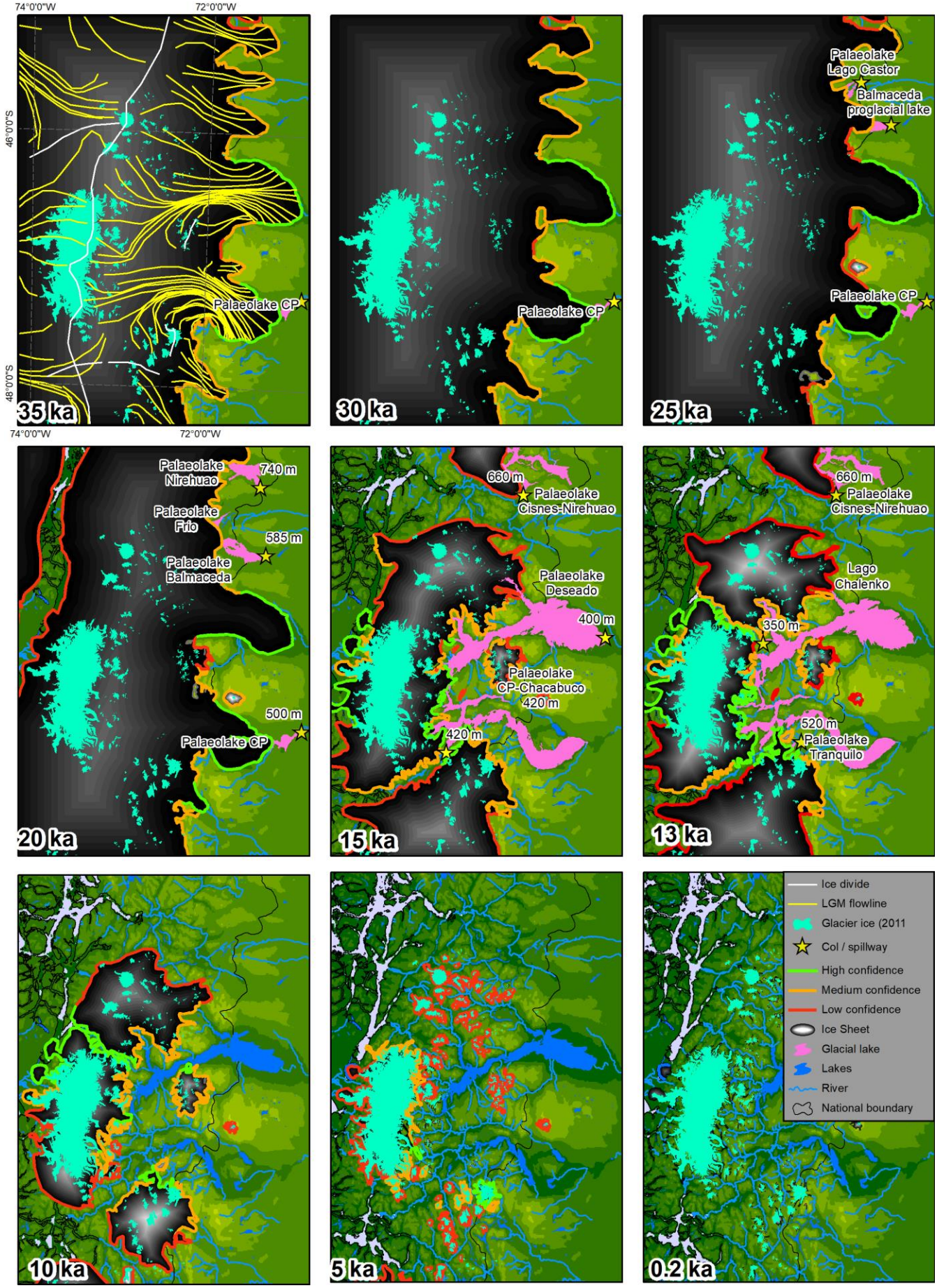
74°0'0"W
72°0'0"W
46°0'0"S
48°0'0"S
Palaeolake CP
35 ka
Palaeolake CP
30 ka
Palaeolake Lago Castor
Balmaceda proglacial lake
Palaeolake CP
25 ka
Palaeolake Nirehuao
740 m
Palaeolake Frío
585 m
Palaeolake Balmaceda
500 m
Palaeolake CP
20 ka
660 m
Palaeolake Cisnes-Nirehuao
Palaeolake Deseado
400 m
Palaeolake CP-Chacabuco
420 m
420 m
15 ka
660 m
Palaeolake Cisnes-Nirehuao
Lago Chalenko
350 m
520 m
Palaeolake Tranquilo
13 ka
10 ka
5 ka
0.2 ka
Ice divide
LGM flowline
Glacier ice (2011
Col / spillway
High confidence
Medium confidence
Low confidence
Ice Sheet
Glacial lake
Lakes
River
National boundary

Figure 20.

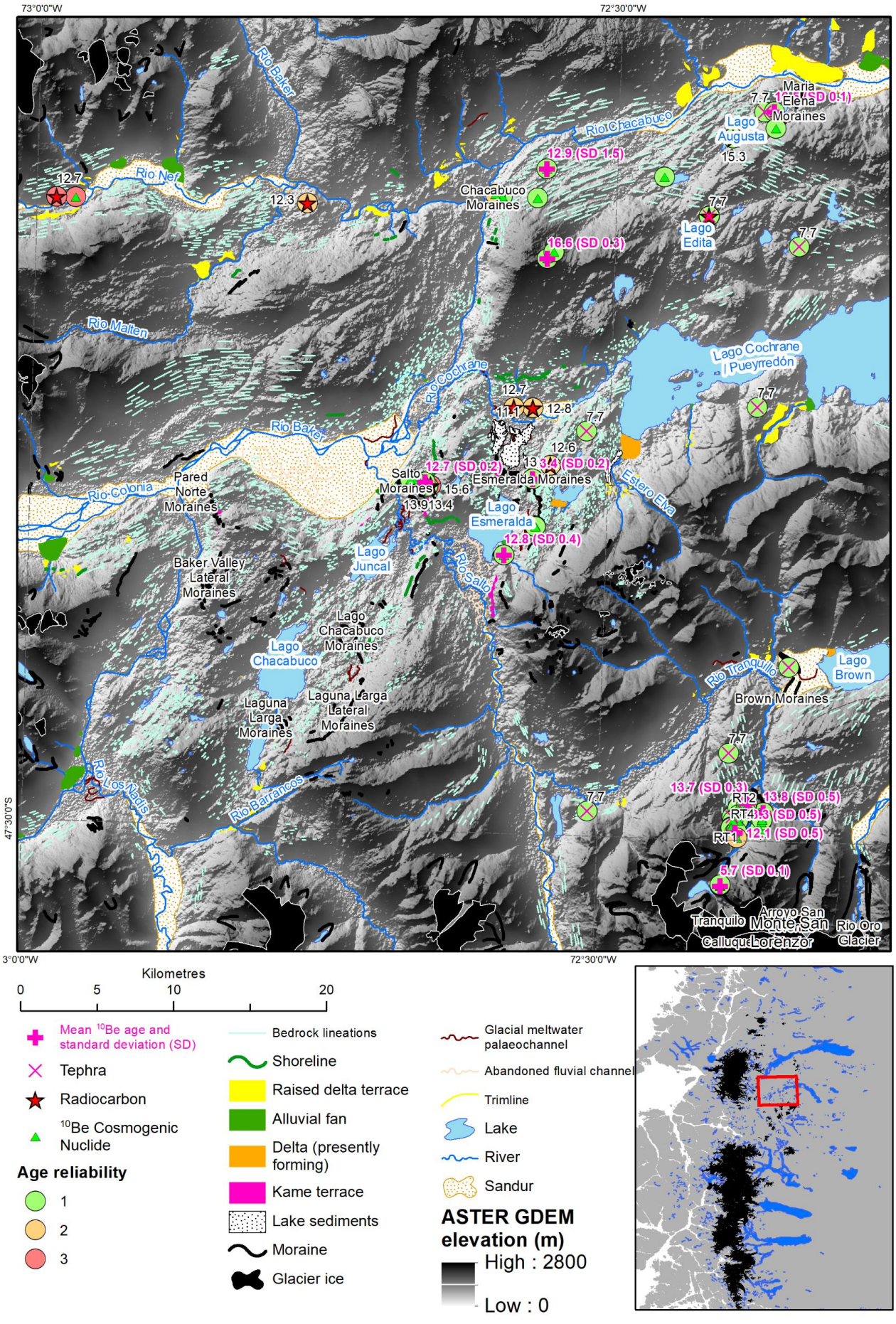
73°0'0"W
72°30'0"W
47°30'0"S
3°0'0"W
72°30'0"W
Río Baker
Río Nef
Río Chacabuco
Río Maitén
Río Cochrane
Río Colonia
Río Salto
Río Tranquilo
Río Los Nadis
Río Barrancos
Lago Cochrane / Pueyrredón
Lago Augusta
Lago Edita
Lago Esmeralda
Lago Juncal
Lago Chacabuco
Lago Brown
Estero Elva
Chacabuco Moraines
Salto Moraines
Esmeralda Moraines
Pared Norte Moraines
Baker Valley Lateral Moraines
Laguna Larga Moraines
Laguna Larga Lateral Moraines
Brown Moraines
Maria Elena Moraines
Arroyo Tranquilo
San Lorenzo
Monte San Valluque
Río Oro Glacier
12.9 (SD 1.5)
16.6 (SD 0.3)
12.7 (SD 0.2)
13.4 (SD 0.2)
12.8 (SD 0.4)
13.7 (SD 0.3)
13.8 (SD 0.5)
13.3 (SD 0.5)
12.1 (SD 0.5)
5.7 (SD 0.1)
Kilometres
0 5 10 20
Mean 10Be age and standard deviation (SD)
Tephra
Radiocarbon
10Be Cosmogenic Nuclide
Age reliability
1
2
3
Bedrock lineations
Shoreline
Raised delta terrace
Alluvial fan
Delta (presently forming)
Kame terrace
Lake sediments
Moraine
Glacier ice
Glacial meltwater palaeochannel
Abandoned fluvial channel
Trimline
Lake
River
Sandur
ASTER GDEM elevation (m)
High : 2800
Low : 0

Figure 21.

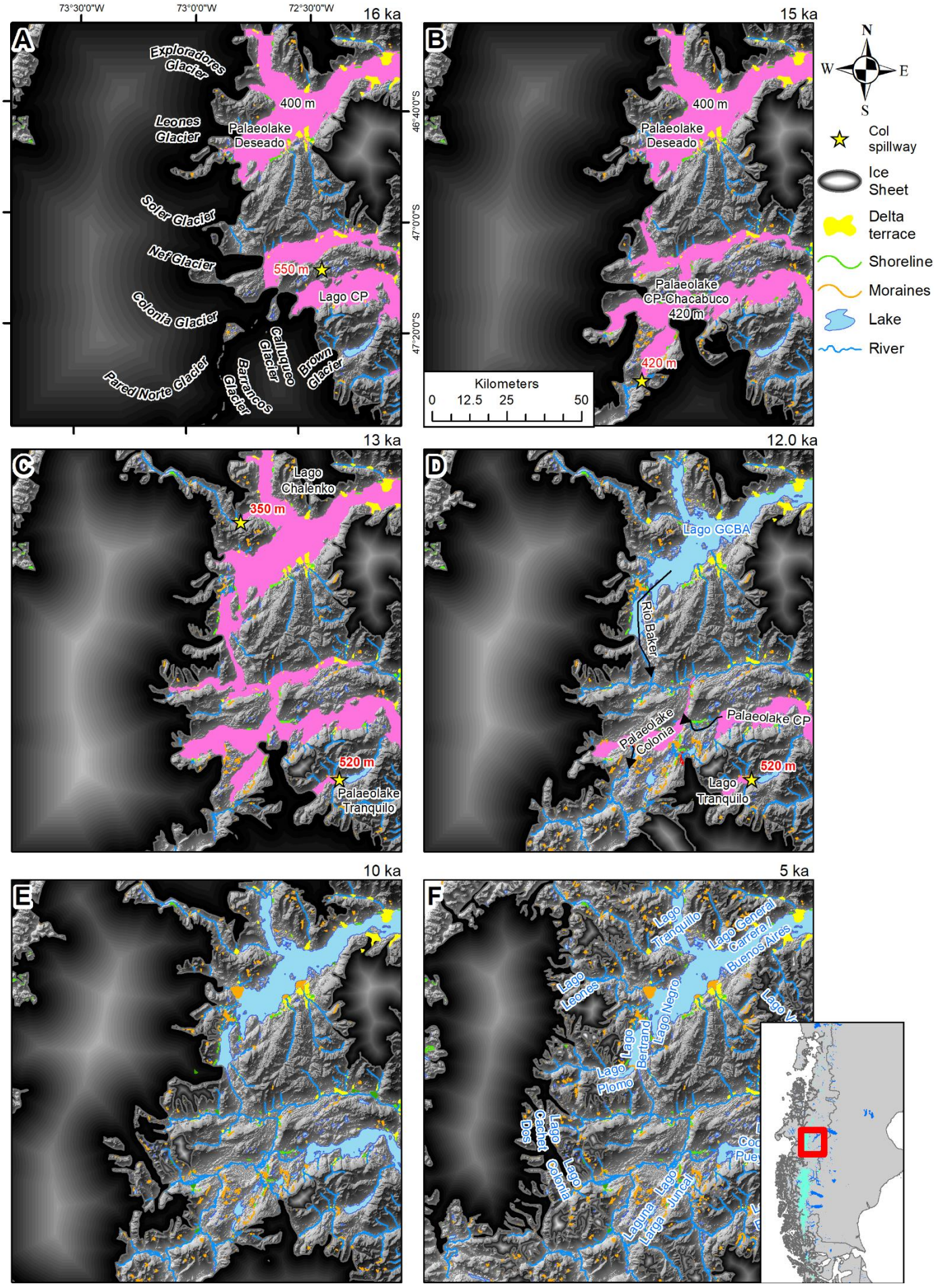
73°30'0"W
73°0'0"W
72°30'0"W
46°40'0"S
47°0'0"S
47°20'0"S
16 ka
A
Exploradores Glacier
Leones Glacier
Soler Glacier
Nef Glacier
Colonia Glacier
Pared Norte Glacier
Barrancos Glacier
Calluqueo Glacier
Brown Glacier
400 m
Palaeolake Deseado
550 m
Lago CP
15 ka
B
400 m
Palaeolake Deseado
Palaeolake CP-Chacabuco
420 m
420 m
Kilometers
0 12.5 25 50
N
W
E
S
Col spillway
Ice Sheet
Delta terrace
Shoreline
Moraines
Lake
River
13 ka
C
Lago Chalenko
350 m
520 m
Palaeolake Tranquilo
12.0 ka
D
Lago GCBA
Río Baker
Palaeolake Colonia
Palaeolake CP
520 m
Lago Tranquilo
10 ka
E
5 ka
F
Lago Tranquilo
Lago General Carrera / Buenos Aires
Lago Leones
Lago Negro
Lago Bertrand
Lago Plomo
Lago Cachet Dos
Lago Colonia
Laguna Larga
Lago Juncal

Figure 22.

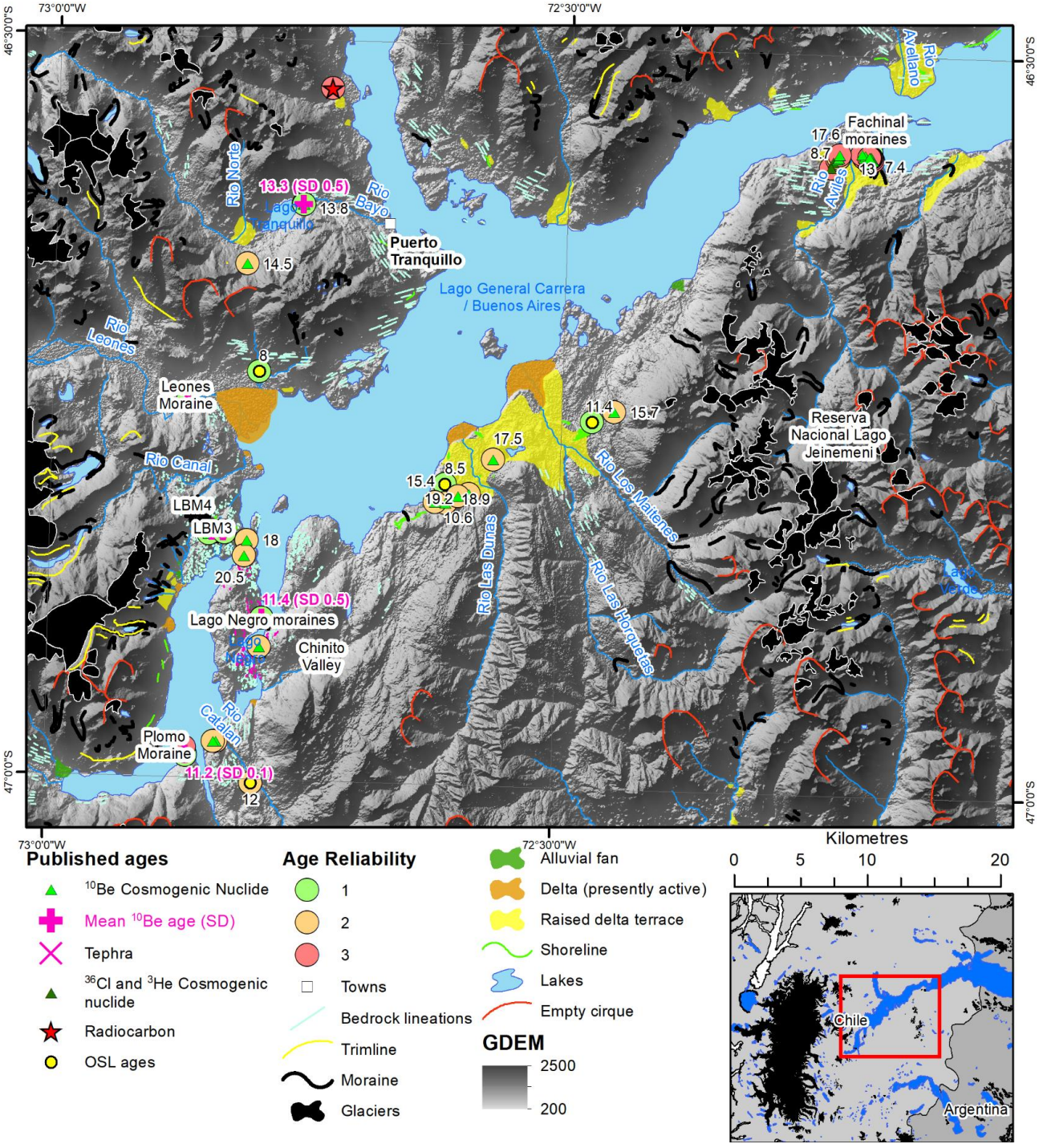
73°0'0"W
72°30'0"W
46°30'0"S
47°0'0"S
Río Norte
Río Bayo
Río Leones
Río Canal
Río Avellano
Río Aviles
Río Los Maitenes
Río Las Dunas
Río Las Horquetas
Río Cañadón
Lago Tranquilo
Puerto Tranquillo
Lago General Carrera / Buenos Aires
Lago Verde
Fachinal moraines
Leones Moraine
Lago Negro moraines
Chinito Valley
Plomo Moraine
Reserva Nacional Lago Jeinemeni
LBM4
LBM3
13.3 (SD 0.5)
13.8
14.5
8
18
20.5
11.4 (SD 0.5)
11.2 (SD 0.1)
12
17.6
8.7
13
7.4
11.4
15.7
17.5
15.4
8.5
19.2
18.9
10.6
Published ages
10Be Cosmogenic Nuclide
Mean 10Be age (SD)
Tephra
36Cl and 3He Cosmogenic nuclide
Radiocarbon
OSL ages
Age Reliability
1
2
3
Towns
Bedrock lineations
Trimline
Moraine
Glaciers
Alluvial fan
Delta (presently active)
Raised delta terrace
Shoreline
Lakes
Empty cirque
GDEM
2500
200
Kilometres
0
5
10
20
Chile
Argentina

Figure 23.

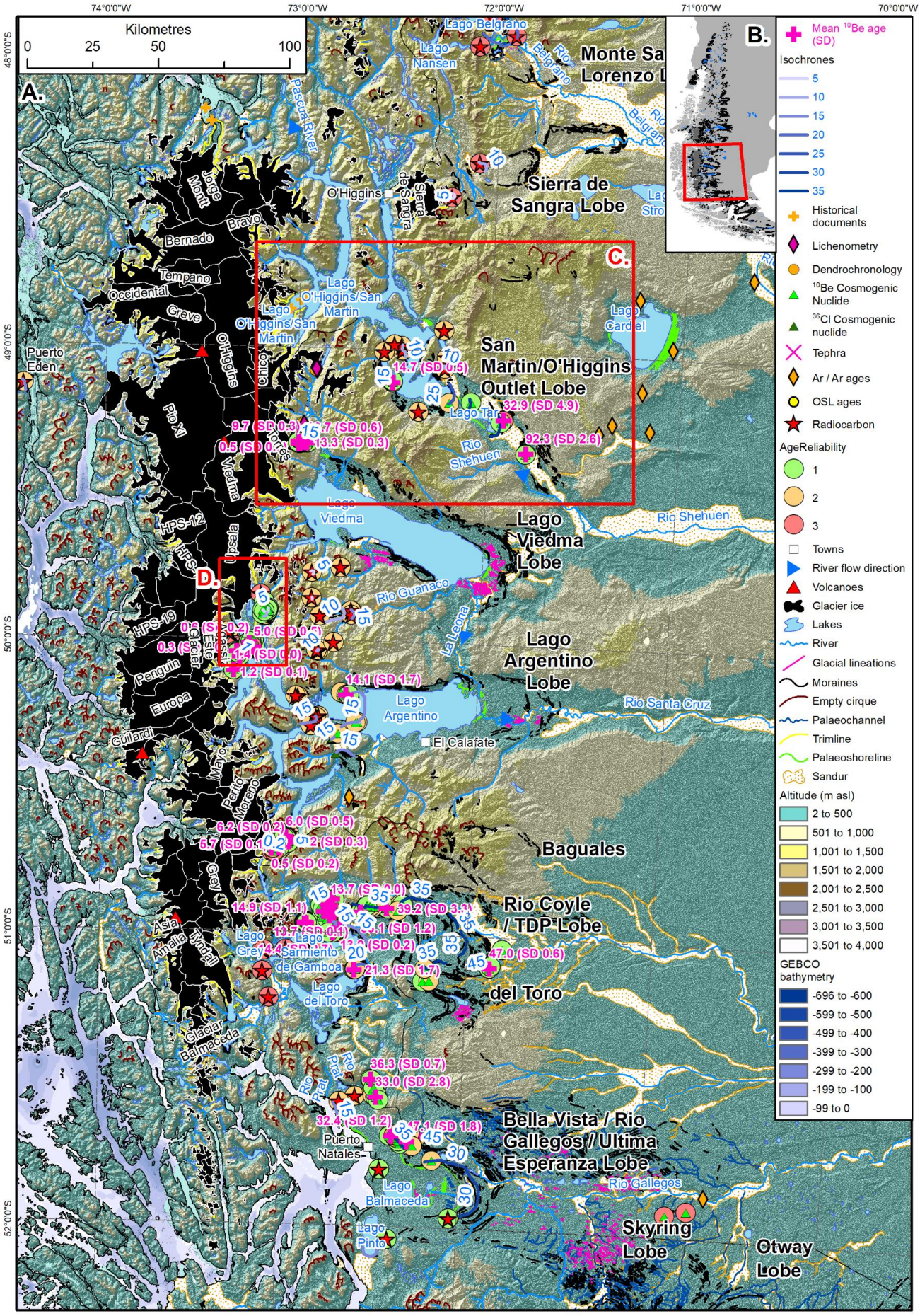
74°0'0"W
73°0'0"W
72°0'0"W
71°0'0"W
70°0'0"W
48°0'0"S
49°0'0"S
50°0'0"S
51°0'0"S
52°0'0"S
Kilometres
0
25
50
100
A.
B.
C.
D.
Monte San Lorenzo
Sierra de Sangra Lobe
San Martin/O'Higgins Outlet Lobe
Lago Viedma Lobe
Lago Argentino Lobe
Baguales
Rio Coyle / TDP Lobe
del Toro
Bella Vista / Rio Gallegos / Ultima Esperanza Lobe
Skyring Lobe
Otway Lobe
Lago Belgrano
Lago Nansen
Lago O'Higgins/San Martin
Lago Cardiel
Lago Tar
Rio Shehuen
Lago Viedma
Rio Guanaco
Lago Argentino
El Calafate
Rio Santa Cruz
Lago Sarmiento
Lago del Toro
Lago Balmaceda
Lago Pinto
Puerto Natales
Rio Gallegos
Puerto Eden
Pascua River
Rio Belgrano
Rio Pinturas
Rio Ibanez
Rio Tranquilo
Rio Baker
Rio Pascua
Rio Chico
Rio Penitente
Rio Serrano
Rio Grey
Rio Paine
Rio Prat
Rio Vizcachas
Rio Las Chinas
Rio Las Vueltas
Rio Coyle
Rio Turbio
Rio Gallegos
Rio Shehuen
Rio Santa Cruz
Rio Guanaco
La Leona
Monte San Lorenzo
Sierra de Sangra
O'Higgins
Bernardo O'Higgins
Monte San Valentin
Brazo Occidental
Tempano
Greve
Chico
Viedma
Upsala
HPS-12
HPS
HPS-19
Glaciar Upsala
Glaciar Este
Glaciar Penguin
Europa
Guillardi
Mayo
Perito Moreno
Grey
Asia
Amalia
Tyndall
Glaciar Balmaceda
Glaciar Pinto
Mean 10Be age (SD)
Isochrones
5
10
15
20
25
30
35
Historical documents
Lichenometry
Dendrochronology
10Be Cosmogenic Nuclide
36Cl Cosmogenic nuclide
Tephra
Ar / Ar ages
OSL ages
Radiocarbon
AgeReliability
1
2
3
Towns
River flow direction
Volcanoes
Glacier ice
Lakes
River
Glacial lineations
Moraines
Empty cirque
Palaeochannel
Trimline
Palaeoshoreline
Sandur
Altitude (m asl)
2 to 500
501 to 1,000
1,001 to 1,500
1,501 to 2,000
2,001 to 2,500
2,501 to 3,000
3,001 to 3,500
3,501 to 4,000
GEBCO bathymetry
-696 to -600
-599 to -500
-499 to -400
-399 to -300
-299 to -200
-199 to -100
-99 to 0

Figure 24.

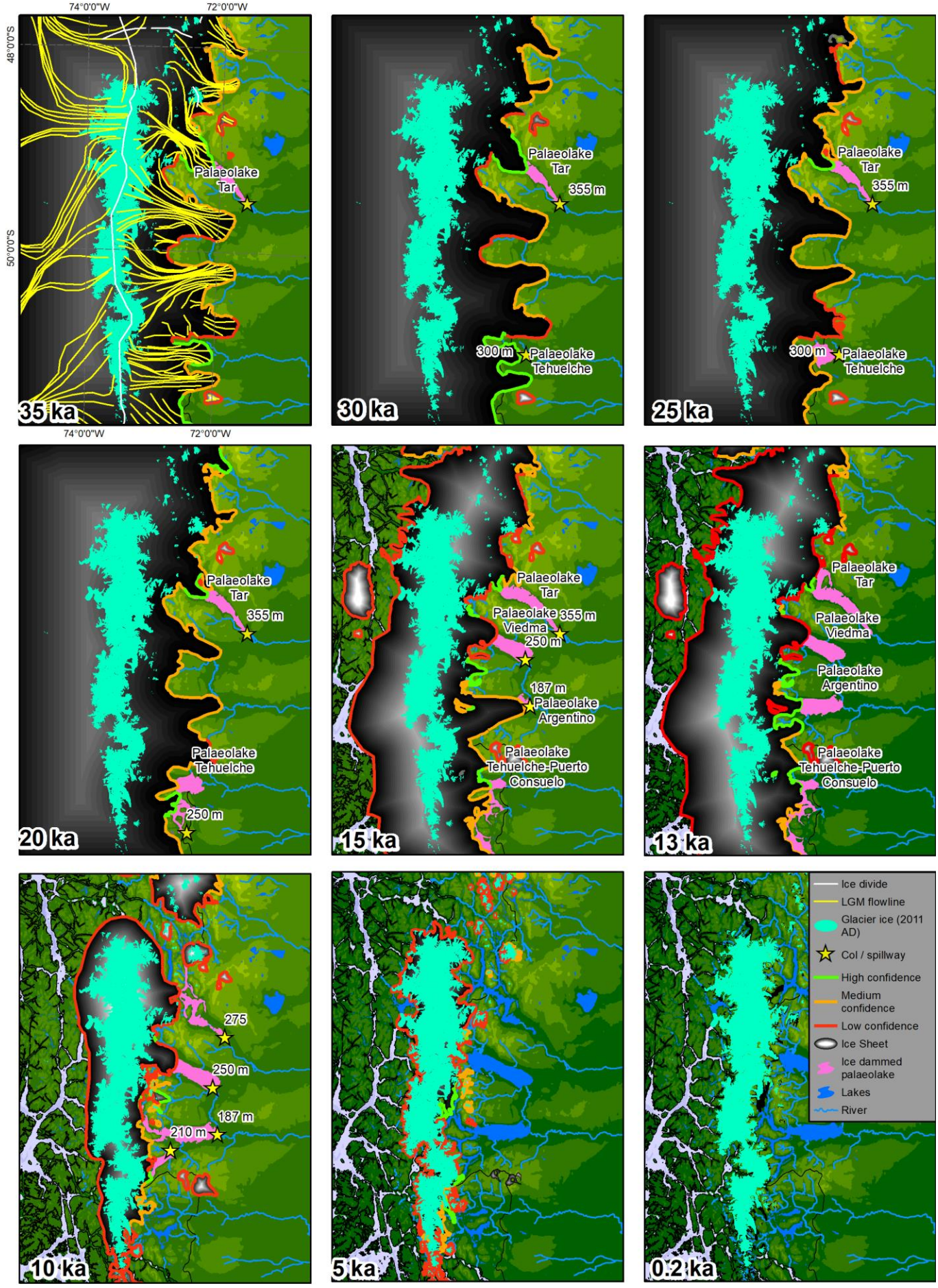
74°0'0"W
72°0'0"W
48°0'0"S
50°0'0"S
Palaeolake Tar
35 ka
355 m
300 m
Palaeolake Tehuelche
30 ka
25 ka
Palaeolake Viedma
Palaeolake Argentino
Palaeolake Tehuelche-Puerto Consuelo
250 m
187 m
20 ka
15 ka
13 ka
275
210 m
10 ka
5 ka
0.2 ka
Ice divide
LGM flowline
Glacier ice (2011 AD)
Col / spillway
High confidence
Medium confidence
Low confidence
Ice Sheet
Ice dammed palaeolake
Lakes
River

Figure 25

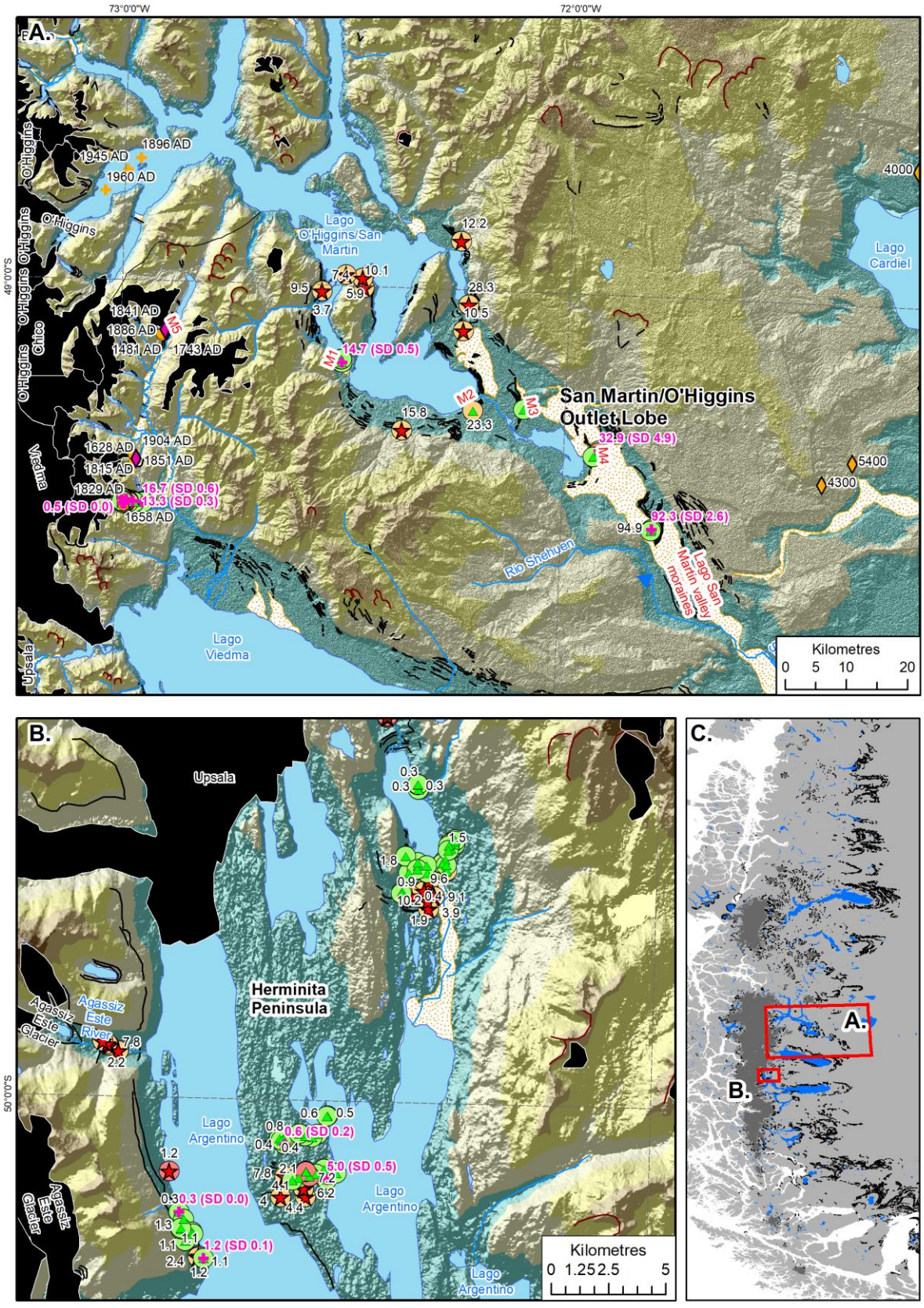
A.
B.
C.
73°0'0"W
72°0'0"W
49°0'0"S
50°0'0"S
1896 AD
1945 AD
1960 AD
O'Higgins
Lago O'Higgins/San Martin
12.2
7.4
10.1
9.5
5.9
3.7
28.3
10.5
184.1 AD
1886 AD
1481 AD
1743 AD
M5
M1
14.7 (SD 0.5)
Chico
15.8
M2
23.3
M3
San Martin/O'Higgins Outlet Lobe
32.9 (SD 4.9)
M4
1628 AD
1904 AD
1851 AD
1815 AD
1829 AD
16.7 (SD 0.6)
13.3 (SD 0.3)
0.5 (SD 0.0)
1658 AD
Viedma
4000
Lago Cardiel
5400
4300
92.3 (SD 2.6)
94.9
Rio Shehuen
Lago San Martin valley moraines
Lago Viedma
Upsala
Kilometres
0 5 10 20
0.3
0.3
0.3
1.5
1.8
0.9
9.6
10.2
0.4
9.1
1.9
3.9
Herminita Peninsula
Agassiz Este Glacier
Agassiz Este River
7.8
2.2
Lago Argentino
0.6
0.5
0.8
0.6 (SD 0.2)
0.4
0.4
1.2
7.8
2.1
5.0 (SD 0.5)
4.1
7.2
4
4.4
6.2
0.3
0.3 (SD 0.0)
1.3
1.1
1.1
1.2 (SD 0.1)
2.4
1.1
1.2
Kilometres
0 1.252.5 5

Figure 26.

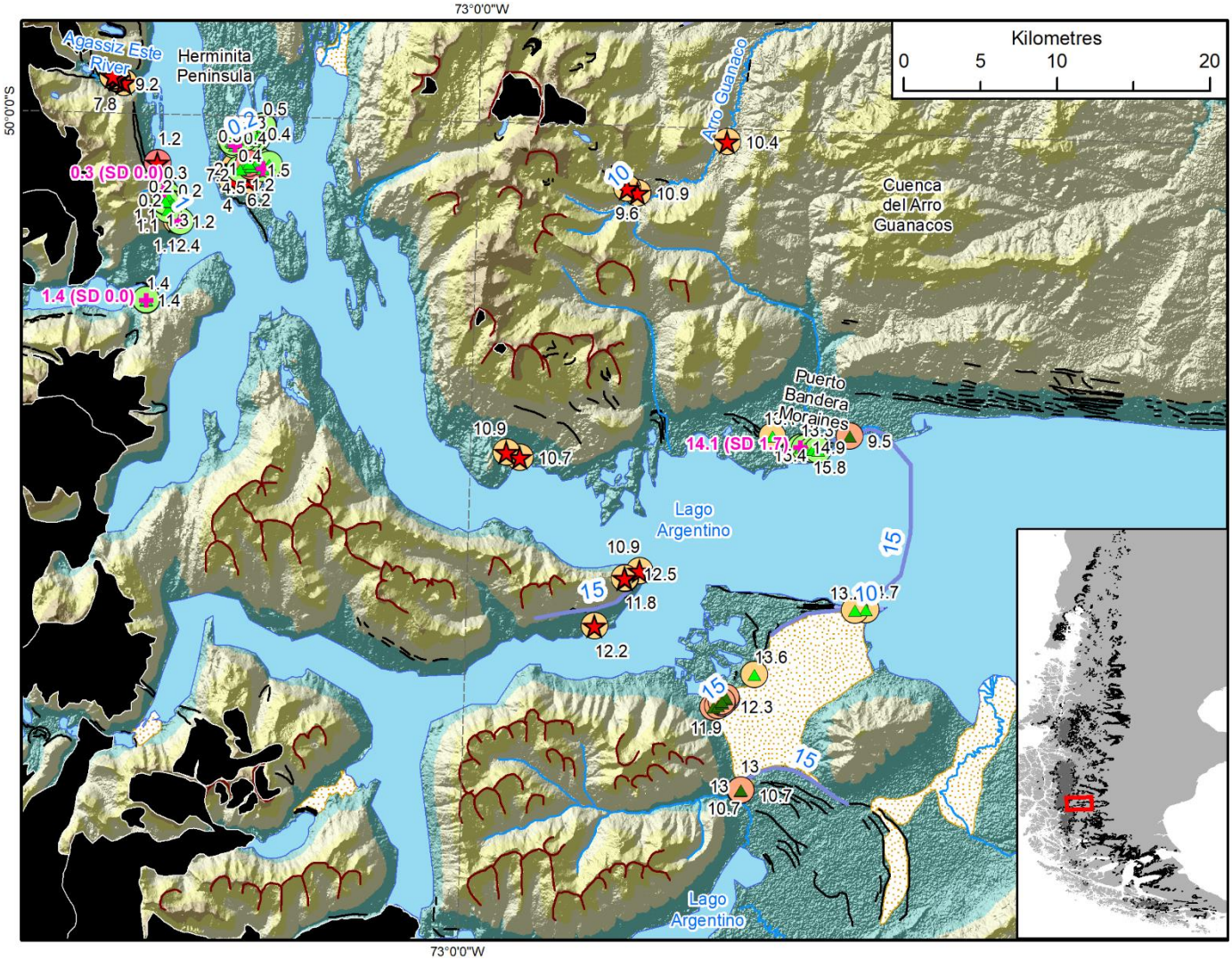
73°0'0"W
50°0'0"S
Kilometres
0
5
10
20
Agassiz Este River
Herminita Peninsula
Arro Guanaco
Cuenca del Arro Guanacos
Puerto Bandera
Moraines
Lago Argentino
Lago Argentino
0.3 (SD 0.0)
1.4 (SD 0.0)
14.1 (SD 1.7)
10
15
15
15
15
73°0'0"W

Figure 27.

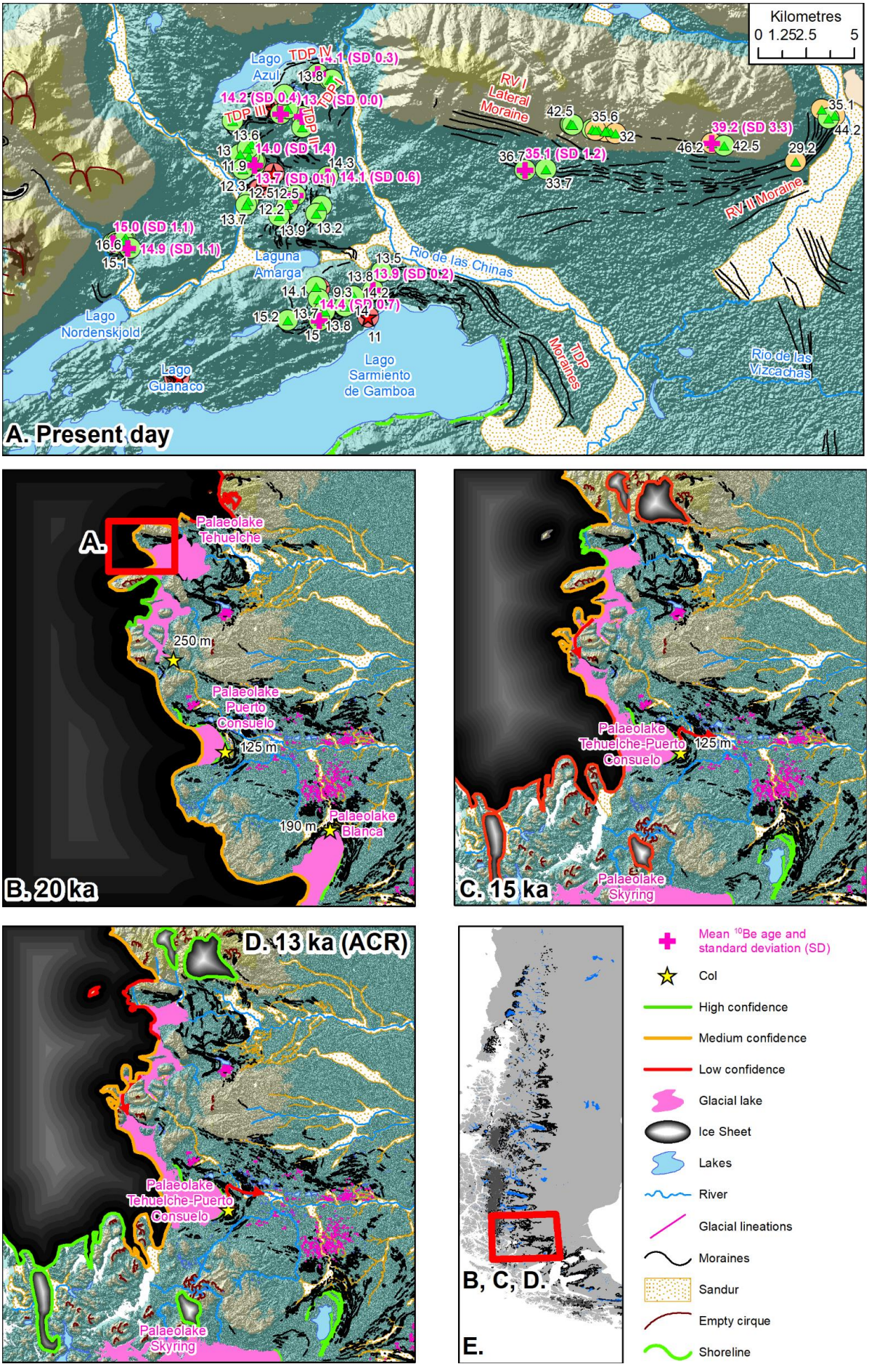
Kilometres
0 1.252.5 5
A. Present day
Lago Azul
TDP IV
14.1 (SD 0.3)
13.8
14.2 (SD 0.4)
13.4
TDP III
(SD 0.0)
TDP II
13.6
13
14.0 (SD 1.4)
11.9
14.3
13.7 (SD 0.1)
14.1 (SD 0.6)
12.3
12.5
12.5
12.2
13.7
13.9
13.2
15.0 (SD 1.1)
16.6
14.9 (SD 1.1)
15.1
Laguna Amarga
13.5
Rio de las Chinas
13.8
13.9 (SD 0.2)
14.1
9.3
14.2
14.4 (SD 0.7)
15.2
13.7
14
13.8
15
11
Lago Nordenskjold
Lago Guanaco
Lago Sarmiento de Gamboa
RV I Lateral Moraine
42.5
35.6
32
39.2 (SD 3.3)
46.2
42.5
35.1
44.2
29.2
36.7
35.1 (SD 1.2)
33.7
RV II Moraine
TDP Moraines
Rio de las Vizcachas
A.
Palaeolake Tehuelche
250 m
Palaeolake Puerto Consuelo
125 m
190 m
Palaeolake Blanca
B. 20 ka
Palaeolake Tehuelche-Puerto Consuelo
125 m
C. 15 ka
Palaeolake Skyring
D. 13 ka (ACR)
Palaeolake Tehuelche-Puerto Consuelo
Palaeolake Skyring
B, C, D.
E.
Mean 10Be age and standard deviation (SD)
Col
High confidence
Medium confidence
Low confidence
Glacial lake
Ice Sheet
Lakes
River
Glacial lineations
Moraines
Sandur
Empty cirque
Shoreline

Figure 28.

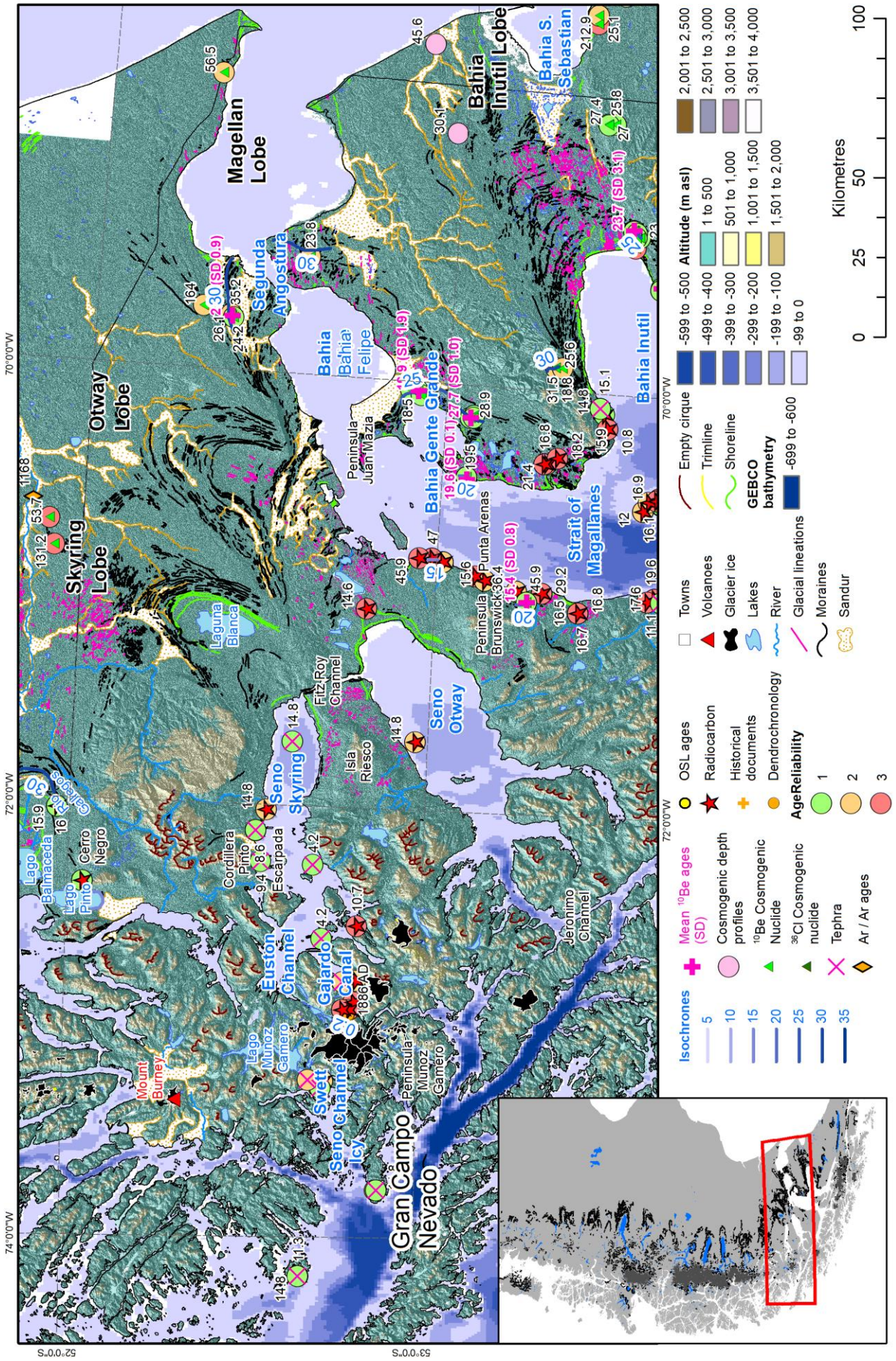
Otway Lobe
Skyring Lobe
Magellan Lobe
Bahia Inutil Lobe
Bahia Inutil
Bahia Gente Grande
Bahia Felipe
Segunda Angostura
Bahia S. Sebastian
Strait of Magallanes
Seno Otway
Seno Skyring
Seno Swett
Euston Channel
Gajardo Channel
Fitz Roy Channel
Jeronimo Channel
Icy
Gran Campo Nevado
Punta Arenas
Peninsula Brunswick
Peninsula Juan Mazia
Peninsula Munoz Gamero
Laguna Blanca
Lago Balmaceda
Lago Pinto
Lago Munoz Gamero
Cerro Negro
Cerro Sota
Cordillera Pinto
Escarpada
Isla Riesco
Mount Burney
1886AD
74°0'0"W
72°0'0"W
70°0'0"W
52°0'0"S
53°0'0"S
Isochrones
5
10
15
20
25
30
35
Mean 10Be ages (SD)
Cosmogenic depth profiles
10Be Cosmogenic Nuclide
36Cl Cosmogenic nuclide
Tephra
Ar / Ar ages
OSL ages
Radiocarbon
Historical documents
Dendrochronology
AgeReliability
1
2
3
Towns
Volcanoes
Glacier ice
Lakes
River
Glacial lineations
Moraines
Sandur
Empty cirque
Trimline
Shoreline
GEBCO bathymetry
-699 to -600
-599 to -500
-499 to -400
-399 to -300
-299 to -200
-199 to -100
-99 to 0
Altitude (m asl)
1 to 500
501 to 1,000
1,001 to 1,500
1,501 to 2,000
2,001 to 2,500
2,501 to 3,000
3,001 to 3,500
3,501 to 4,000
Kilometres
0
25
50
100

Figure 29.

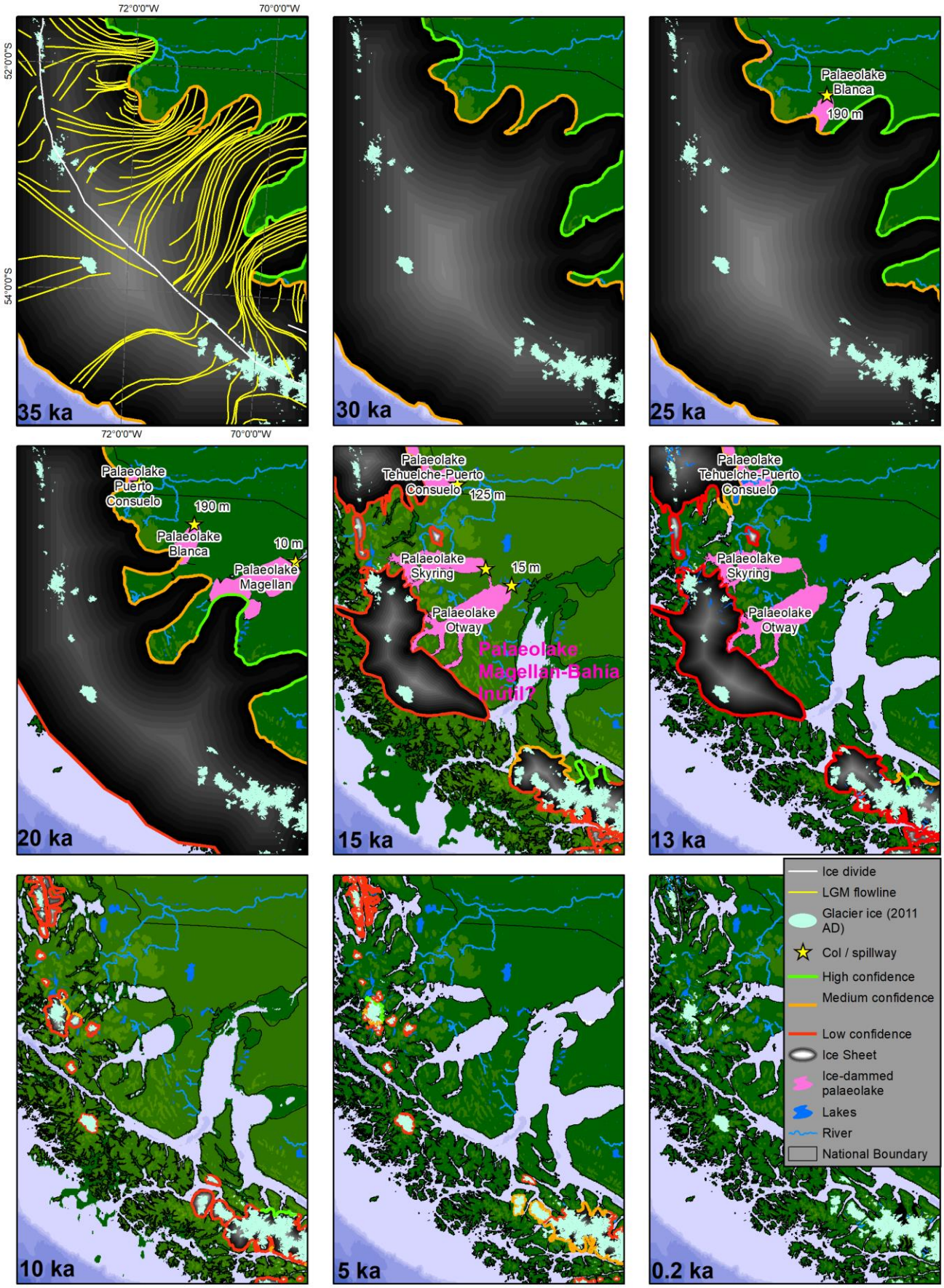
72°0'0"W
70°0'0"W
52°0'0"S
54°0'0"S
35 ka
30 ka
25 ka
Palaeolake Blanca
190 m
Palaeolake Puerto Consuelo
190 m
Palaeolake Blanca
10 m
Palaeolake Magellan
20 ka
Palaeolake Tehuelche-Puerto Consuelo
125 m
Palaeolake Skyring
15 m
Palaeolake Otway
Palaeolake Magellan-Bahía Inútil?
15 ka
Palaeolake Tehuelche-Puerto Consuelo
Palaeolake Skyring
Palaeolake Otway
13 ka
10 ka
5 ka
0.2 ka
Ice divide
LGM flowline
Glacier ice (2011 AD)
Col / spillway
High confidence
Medium confidence
Low confidence
Ice Sheet
Ice-dammed palaeolake
Lakes
River
National Boundary

Figure 30.

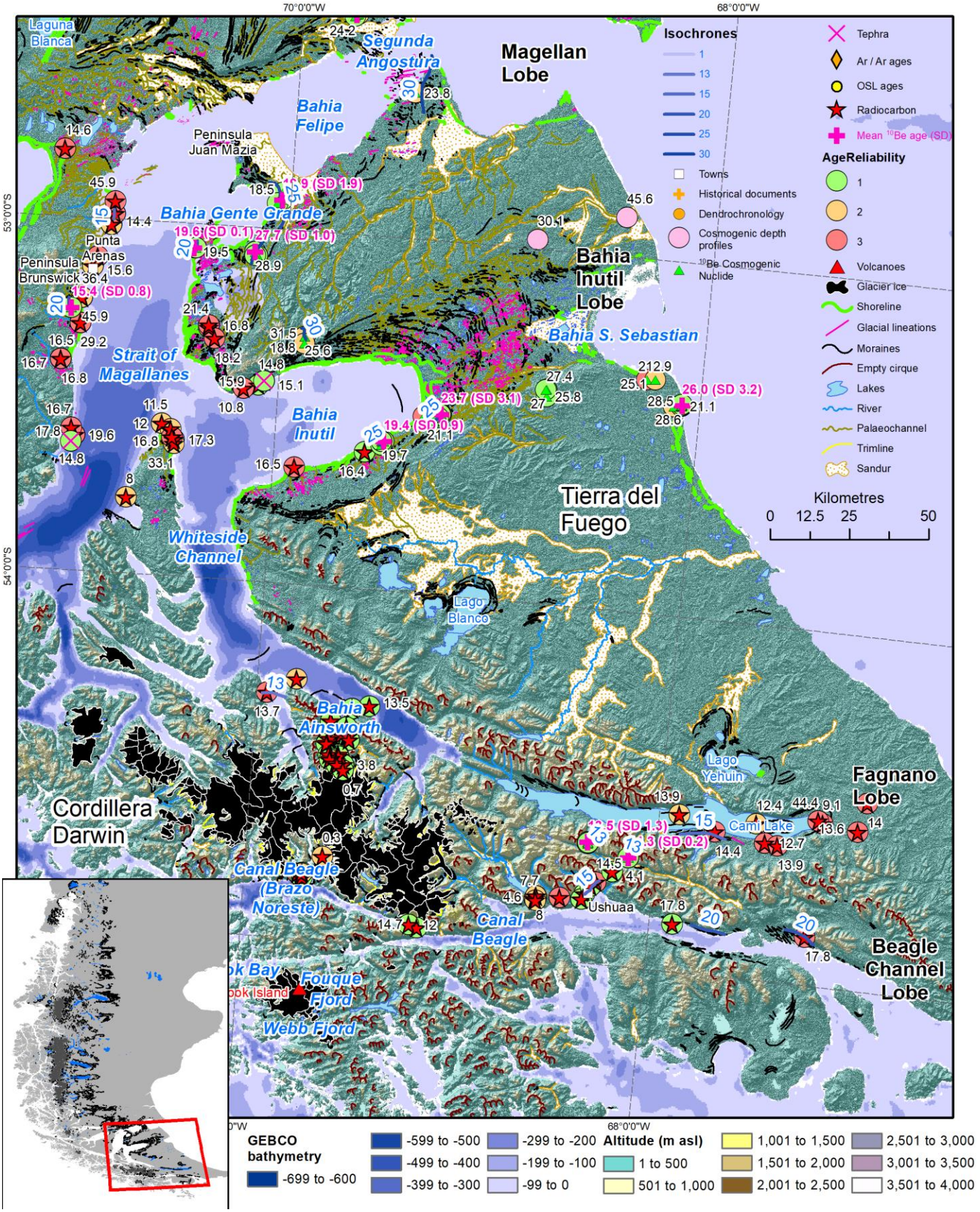
70°0'0"W
68°0'0"W
53°0'0"S
54°0'0"S
Laguna Blanca
Segunda Angostura
Magellan Lobe
Bahia Felipe
Peninsula Juan Mazia
Bahia Gente Grande
Punta Arenas
Peninsula Brunswick
Strait of Magallanes
Bahia Inutil Lobe
Bahia S. Sebastian
Bahia Inutil
Tierra del Fuego
Whiteside Channel
Lago Blanco
Bahia Ainsworth
Cordillera Darwin
Canal Beagle (Brazo Noreste)
Canal Beagle
Lago Yehuin
Fagnano Lobe
Cami Lake
Ushuaia
Beagle Channel Lobe
Fouque Fjord
Webb Fjord
Isochrones
1
13
15
20
25
30
Towns
Historical documents
Dendrochronology
Cosmogenic depth profiles
10Be Cosmogenic Nuclide
Tephra
Ar / Ar ages
OSL ages
Radiocarbon
Mean 10Be age (SD)
AgeReliability
1
2
3
Volcanoes
Glacier Ice
Shoreline
Glacial lineations
Moraines
Empty cirque
Lakes
River
Palaeochannel
Trimline
Sandur
Kilometres
0 12.5 25 50
GEBCO bathymetry
-699 to -600
-599 to -500
-499 to -400
-399 to -300
-299 to -200
-199 to -100
-99 to 0
Altitude (m asl)
1 to 500
501 to 1,000
1,001 to 1,500
1,501 to 2,000
2,001 to 2,500
2,501 to 3,000
3,001 to 3,500
3,501 to 4,000

Figure 31.

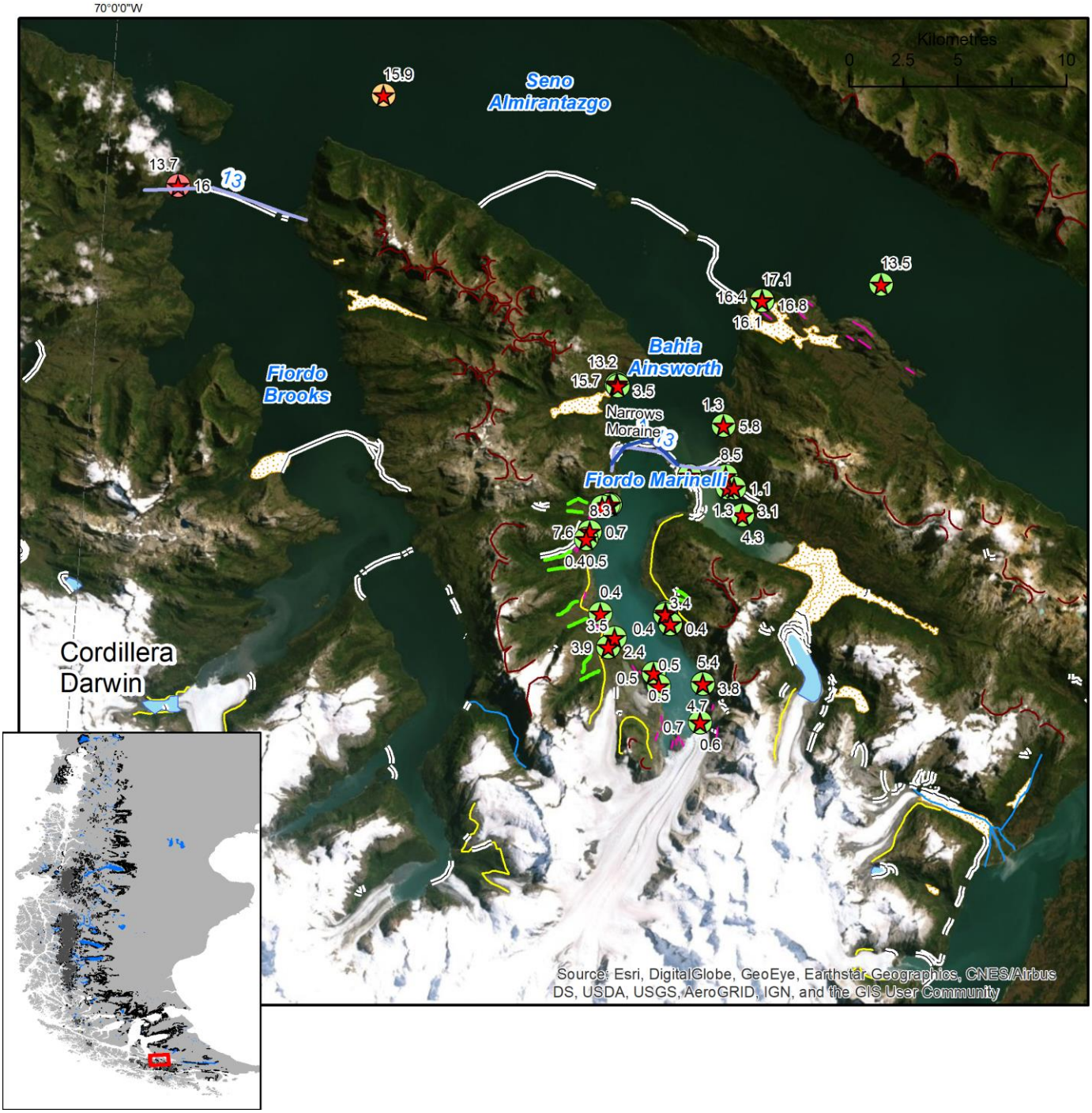
70°0'0"W
Kilometres
0 2.5 5 10
Seno Almirantazgo
Fiordo Brooks
Bahia Ainsworth
Narrows Moraine
Fiordo Marinelli
Cordillera Darwin
15.9
13.7
16
13
17.1
16.4
16.8
16.1
13.5
13.2
15.7
3.5
1.3
5.8
8.5
1.1
1.3
3.1
4.3
8.3
7.6
0.7
0.4
0.5
0.4
3.4
3.5
0.4
0.4
3.9
2.4
0.5
5.4
0.5
3.8
0.5
4.7
0.7
0.6
Source: Esri, DigitalGlobe, GeoEye, Earthstar Geographics, CNES/Airbus DS, USDA, USGS, AeroGRID, IGN, and the GIS User Community

Figure 32

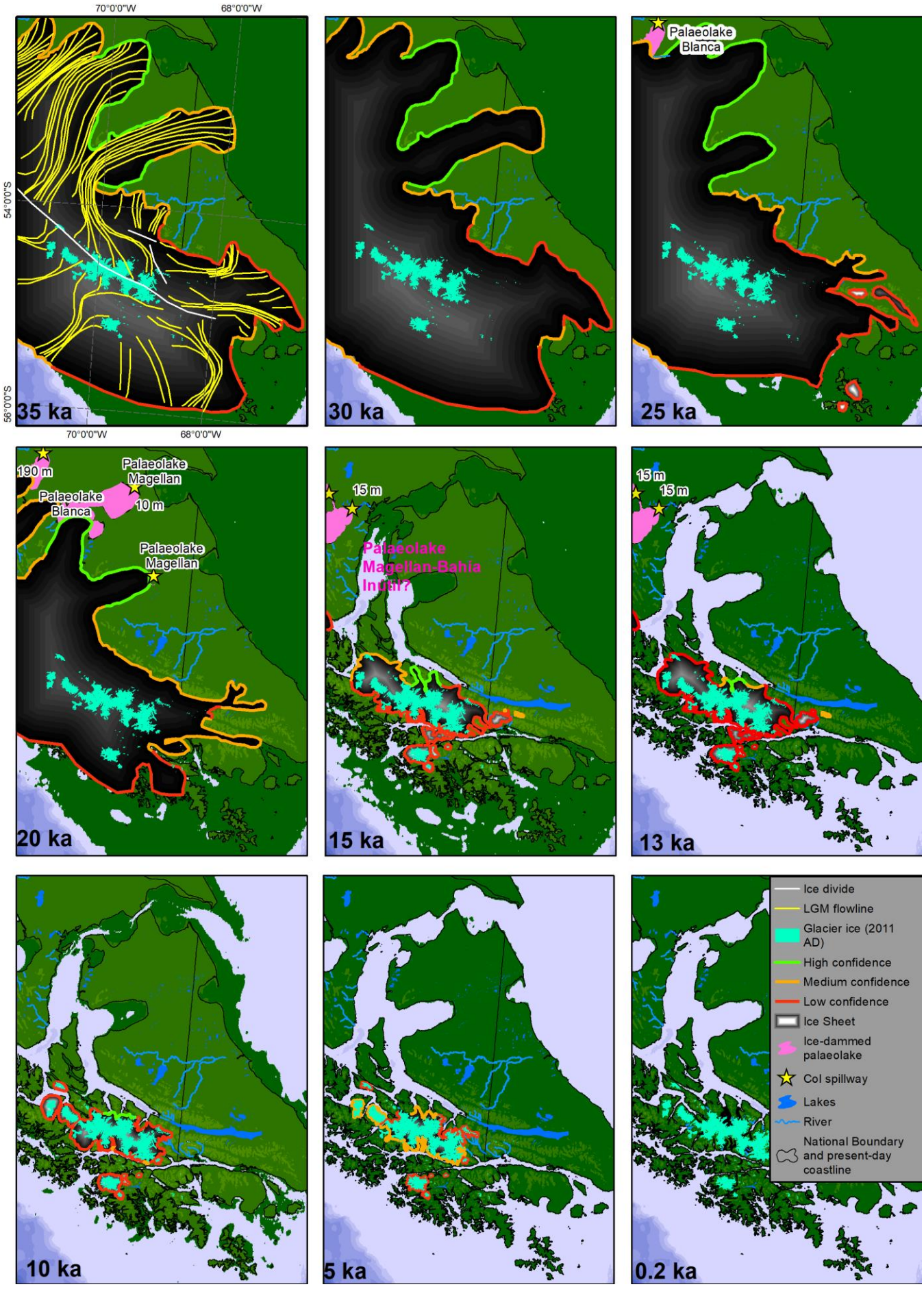
70°0'0"W
68°0'0"W
54°0'0"S
56°0'0"S
35 ka
30 ka
Palaeolake Blanca
25 ka
190 m
Palaeolake Magellan
Palaeolake Blanca
10 m
Palaeolake Magellan
20 ka
15 m
Palaeolake Magellan-Bahia Inutil?
15 ka
15 m
15 m
13 ka
10 ka
5 ka
0.2 ka
Ice divide
LGM flowline
Glacier ice (2011 AD)
High confidence
Medium confidence
Low confidence
Ice Sheet
Ice-dammed palaeolake
Col spillway
Lakes
River
National Boundary and present-day coastline

Figure 33.

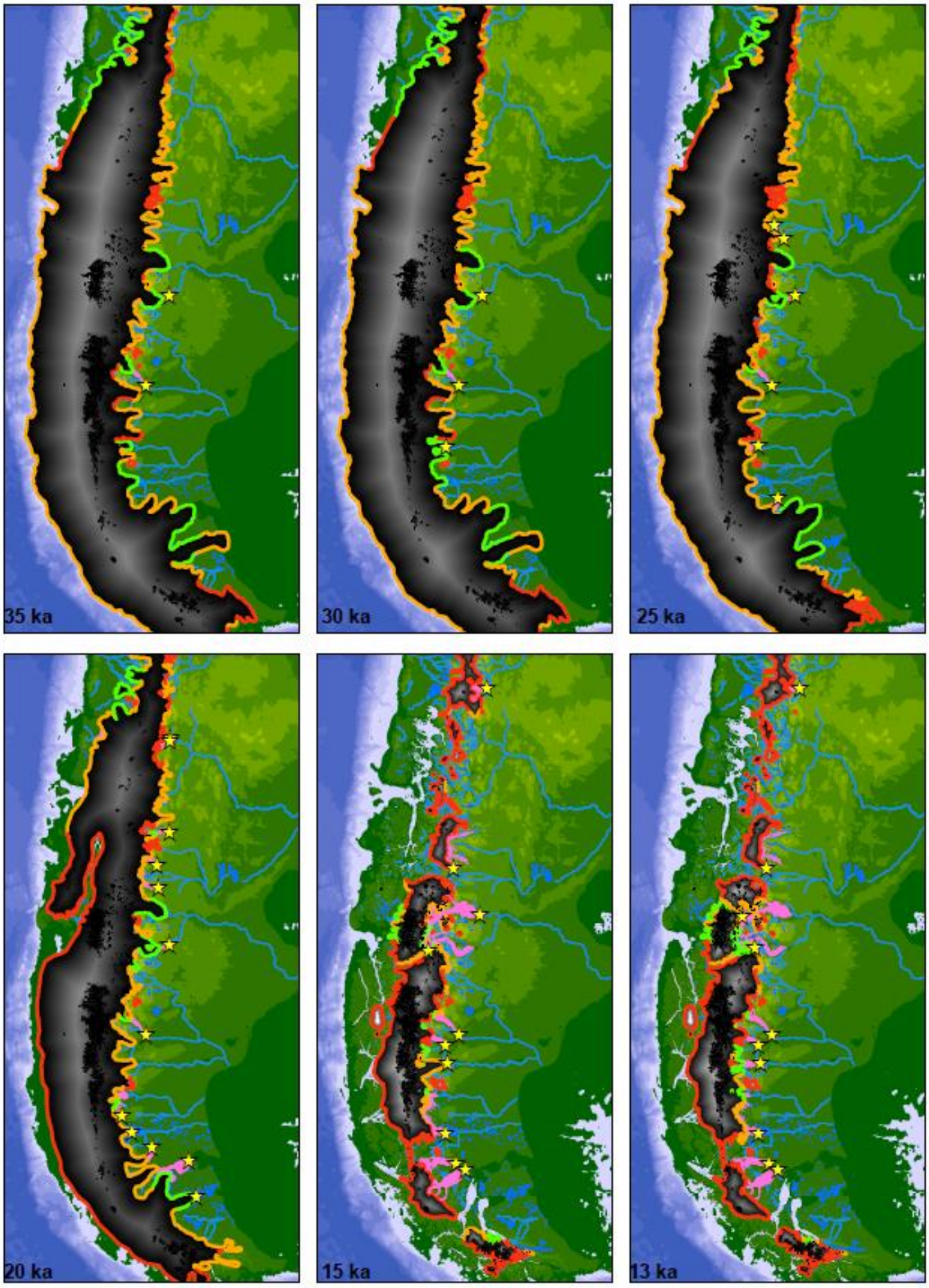
35 ka
30 ka
25 ka
20 ka
15 ka
13 ka

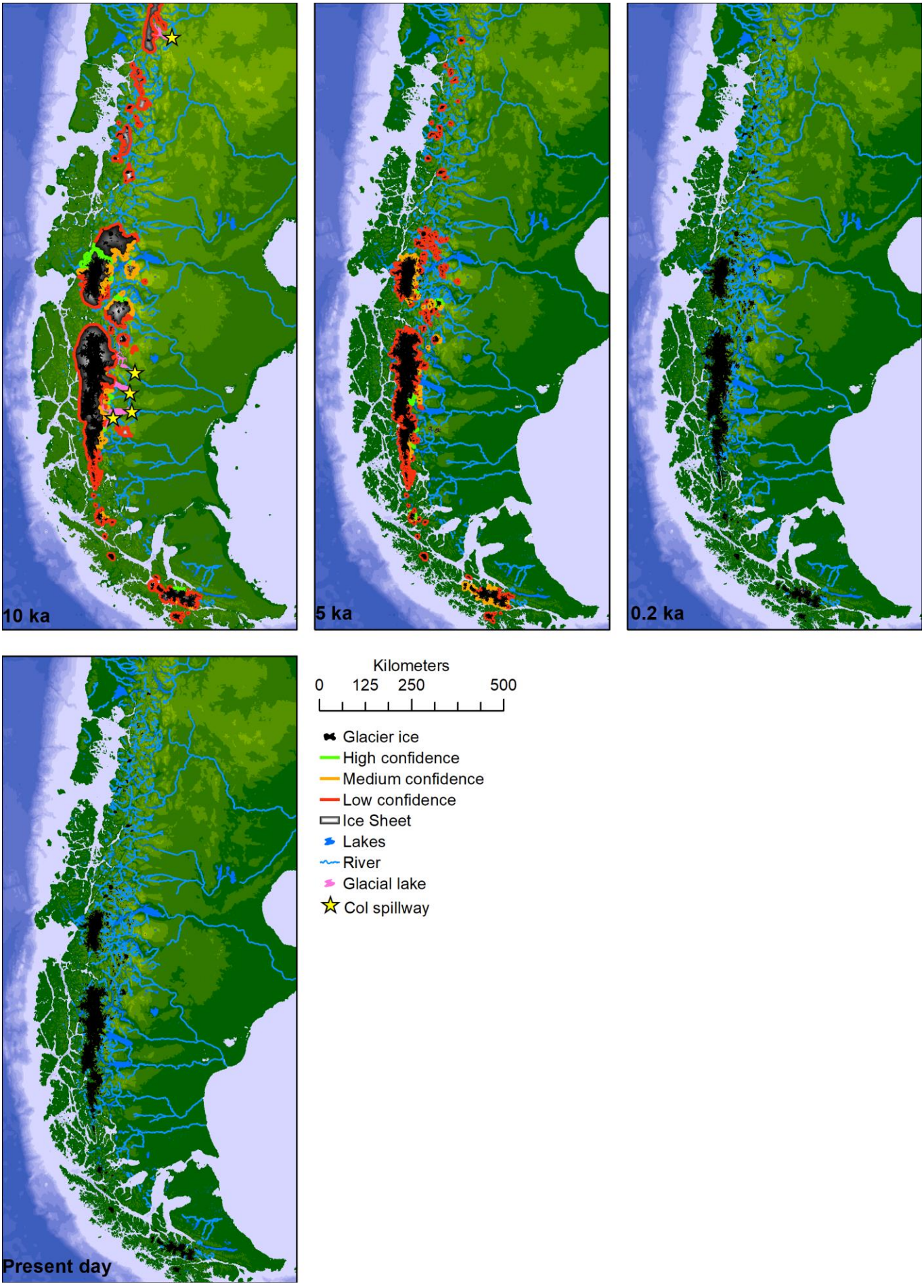
10 ka
5 ka
0.2 ka
Present day
Kilometers
0 125 250 500
Glacier ice
High confidence
Medium confidence
Low confidence
Ice Sheet
Lakes
River
Glacial lake
Col spillway

Figure 34.

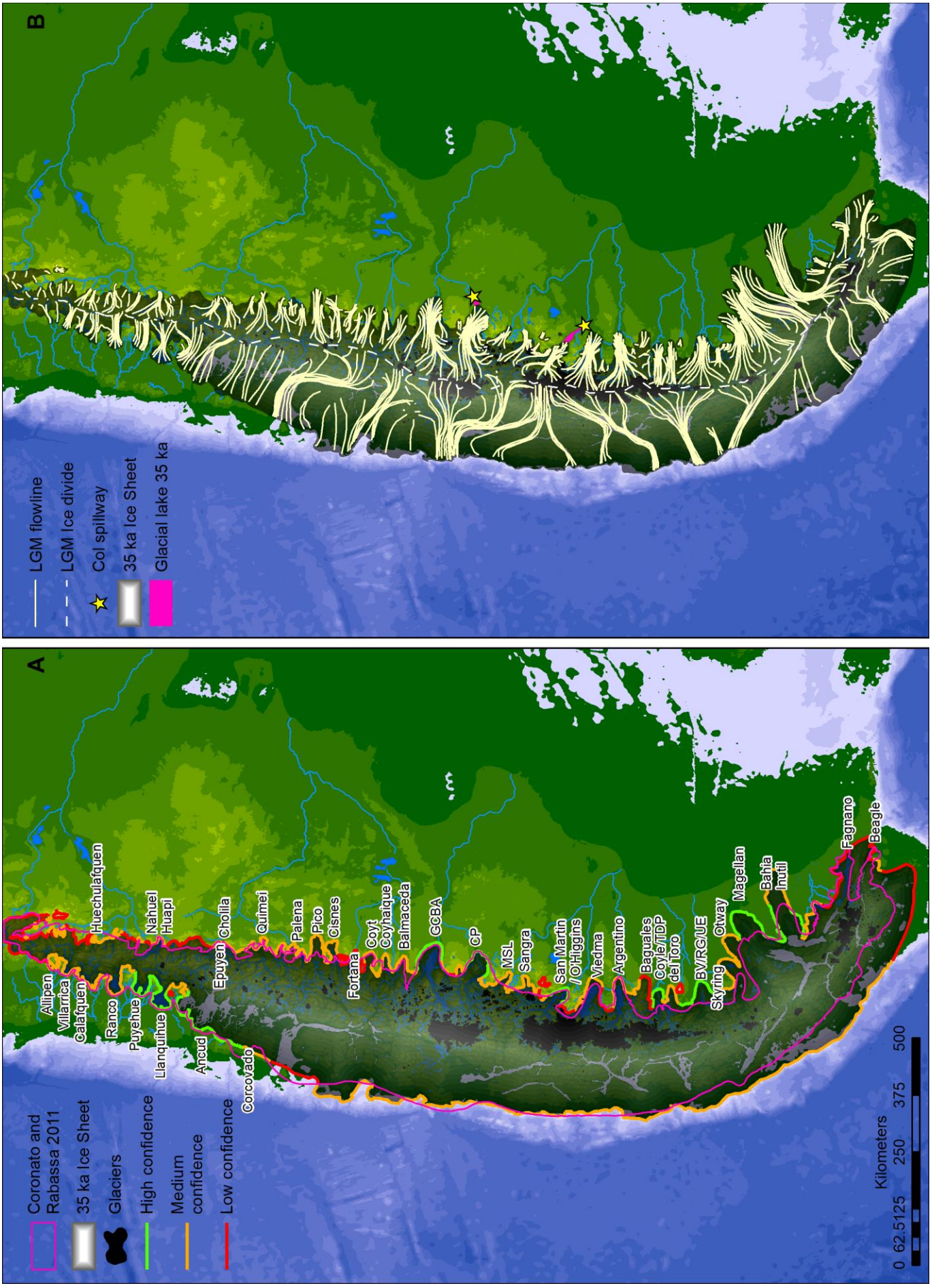
A
B
Coronato and Rabassa 2011
35 ka Ice Sheet
Glaciers
High confidence
Medium confidence
Low confidence
Kilometers
0 62.5125 250 375 500
Allipen
Villarrica
Calafquen
Huechulafquen
Ranco
Puyehue
Nahuel Huapi
Llanquihue
Ancud
Corcovado
Epuyen
Cholila
Quimei
Palena
Pico
Cisnes
Fontana
Coyt
Coyhaique
Balmaceda
CCBA
CP
MSL
Sangra
San Martin
/O'Higgins
Medma
Argentino
Baguales
Coyle/TDP
del Toro
BV/RG/UE
Skyring
Otway
Magellan
Bahia Inutil
Fagnano
Beagle
LGM flowline
LGM Ice divide
Col spillway
35 ka Ice Sheet
Glacial lake 35 ka

Figure 35.

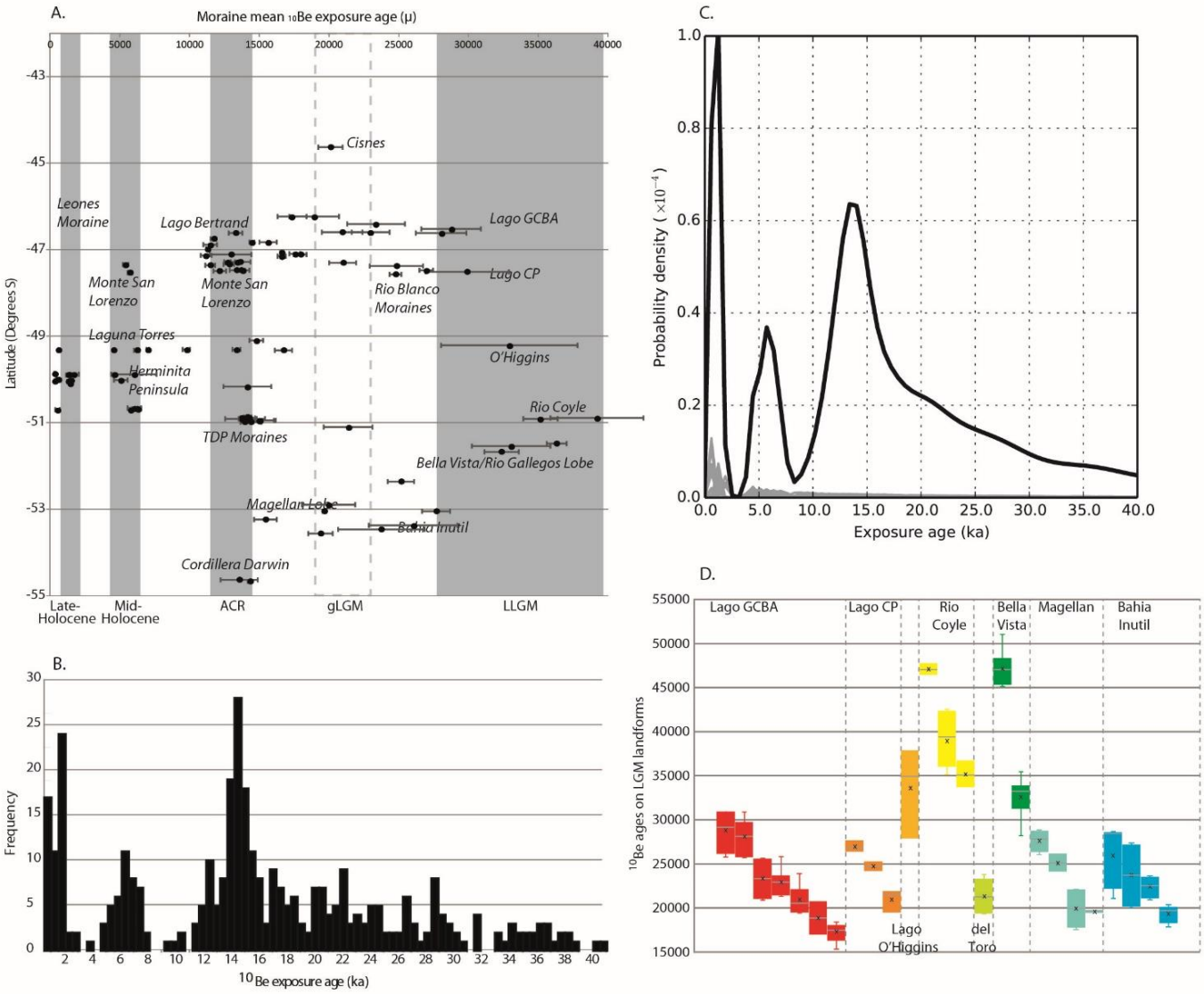
A.
Moraine mean ¹⁰Be exposure age (μ)
Latitude (Degrees S)
Cisnes
Leones Moraine
Lago Bertrand
Lago GCBA
Monte San Lorenzo
Monte San Lorenzo
Lago CP
Rio Blanco Moraines
Laguna Torres
O'Higgins
Herminita Peninsula
Rio Coyle
TDP Moraines
Bella Vista/Rio Gallegos Lobe
Magellan Lobe
Bahia Inutil
Cordillera Darwin
Late-Holocene
Mid-Holocene
ACR
gLGM
LLGM
B.
Frequency
¹⁰Be exposure age (ka)
C.
Probability density (×10⁻⁴)
Exposure age (ka)
D.
¹⁰Be ages on LGM landforms
Lago GCBA
Lago CP
Rio Coyle
Bella Vista
Magellan
Bahia Inutil
Lago O'Higgins
del Toro

Figure 36.

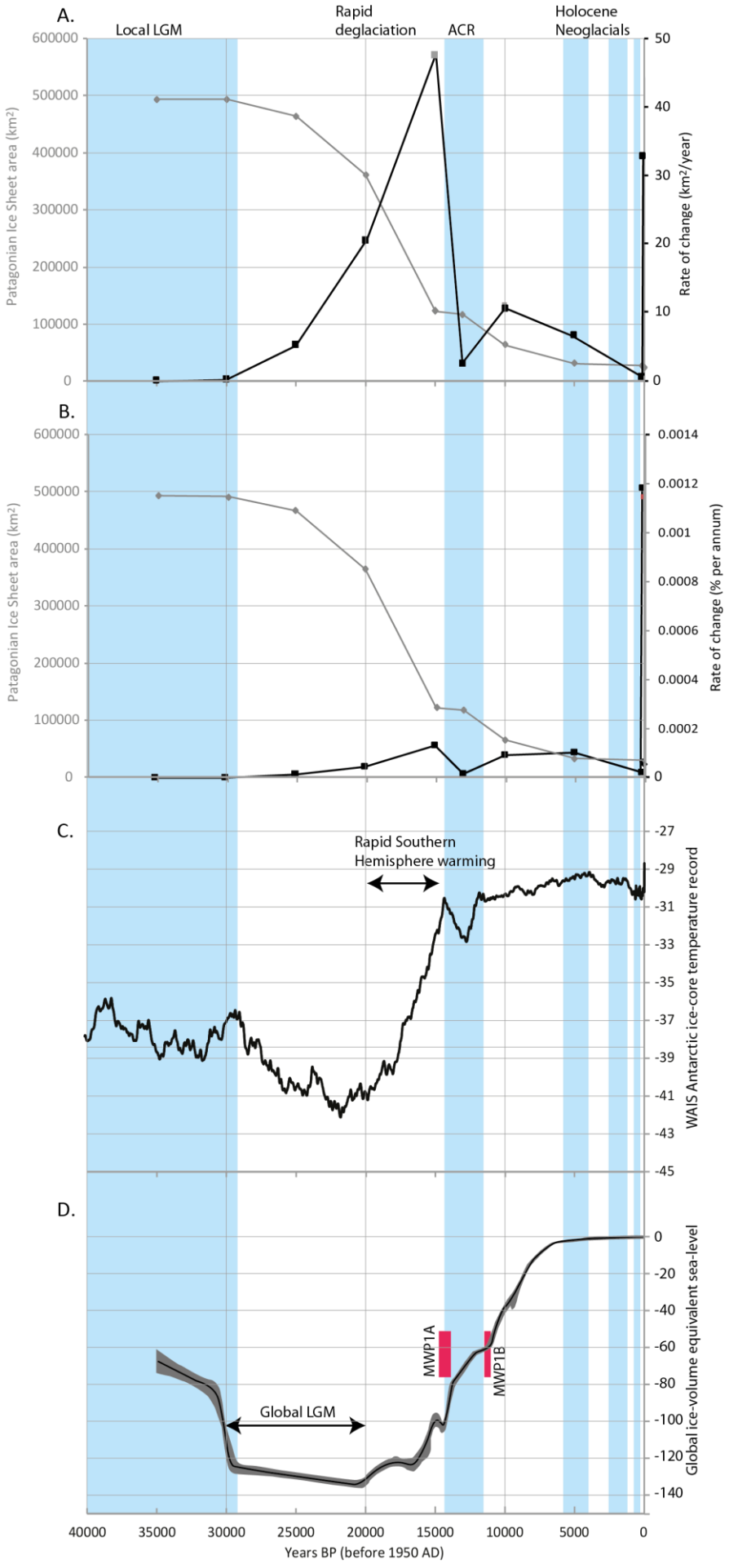
A.
Local LGM
Rapid deglaciation
ACR
Holocene Neoglacials
Patagonian Ice Sheet area (km²)
Rate of change (km²/year)
B.
Patagonian Ice Sheet area (km²)
Rate of change (% per annum)
C.
Rapid Southern Hemisphere warming
WAIS Antarctic ice-core temperature record
D.
MWP1A
MWP1B
Global LGM
Global ice-volume equivalent sea-level
Years BP (before 1950 AD)

Figure 37.

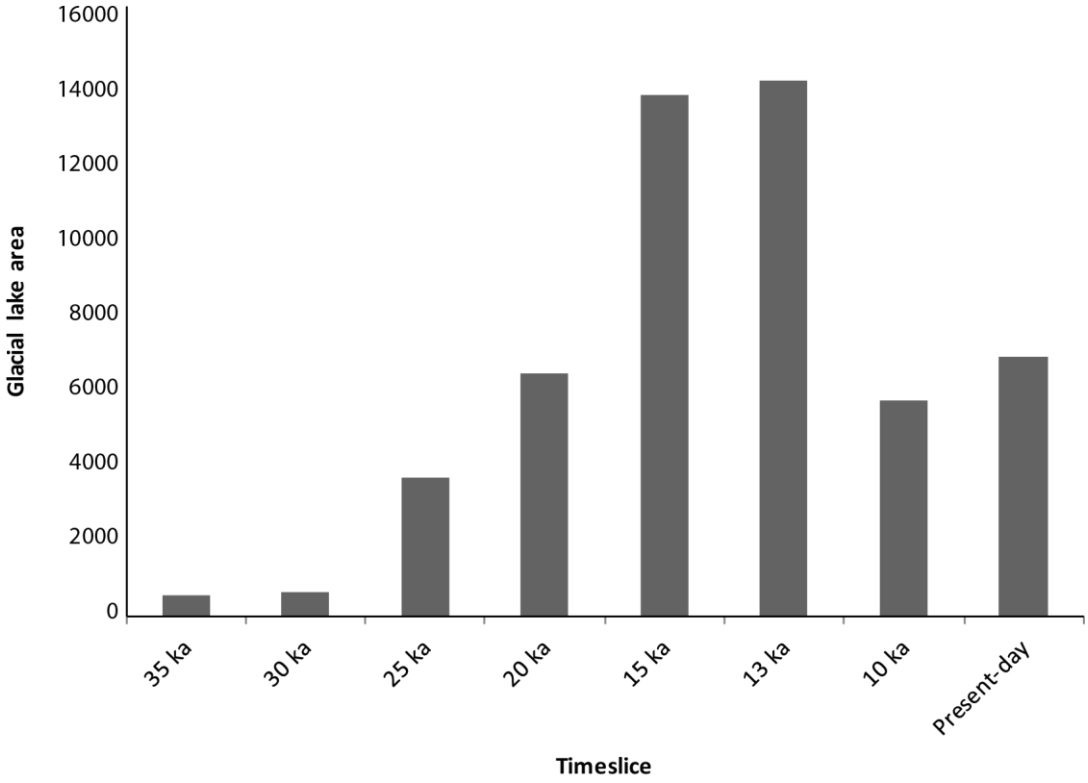
16000
14000
12000
10000
8000
6000
4000
2000
0
Glacial lake area
35 ka
30 ka
25 ka
20 ka
15 ka
13 ka
10 ka
Present-day
Timeslice

Figure 38.

The Patagonian Ice Sheet from the last glacial cycle to the Present Day: Supplementary Methods

1 Logo

Here, we present a logo, to be used with all uses of the PATICE data and PATICE reconstructions.

Figure 1. PATICE logo, with the new empirical reconstruction of the Patagonian Ice Sheet (38°S – 56°S) at 35 ka.

2 Chronological methodologies

2.1 Ar/Ar ages

$^{40}Ar/^{39}Ar$ dating of basaltic lava sequences interbedded with moraines around Lago GCBA provides a chronological framework for Pleistocene glaciations (Singer et al., 2004a). These ages data basalt lava flows from Cerro Volcán to 760 ± 14 ka and 109 ± 3 ka, with the older age underlying six moraines, and the older age overlying and burying the moraines. Other $^{40}Ar/^{39}Ar$ ages in our database are located 520 km south of Lago GCBA, where a 3 m thick basaltic lava flow crops out south of Río Gallegos, east of Estancia Bella Vista (Singer et al., 2004a). This lava flow underlies glacial drift derived from the easternmost and oldest glacial deposit in the area. Finally, K-Ar and $^{40}Ar/^{39}Ar$ dating from the basaltic lava sequence atop Cerro del Fraile, Argentina, date seven glacial tills interbedded with lavas associated with the Réunion event (Singer et al., 2004b). Note that several ages from Singer et al. (2004b) date from Pliocene or early Quaternary, and are not shown or included in this compilation.

The PATICE shapefile comprises:

1. Unique ID (>1)
2. Reference
3. Site Name

4. Sample ID
5. Location Comments
6. Dating material
7. Latitude (decimal degrees)
8. Longitude (decimal degrees)
9. Description
10. Age as given in publication
11. Further comments
12. Age (ka)

2.2 Radiocarbon ages

2.2.1 Calibration of terrestrial radiocarbon ages

Radiocarbon ages gleaned from the published literature and existing databases were recalibrated using OxCal (Bronk Ramsey, 2009) and the SHCal13 dataset (Hogg et al., 2013). Ages are presented in the Supplementary Information as a 2 σ range (95.4% confidence interval). Following convention (Reimer et al., 2013), uncalibrated ages are referred to as ^{14}C ka BP and calibrated ages as cal. ka BP. Given the broad scale of our reconstruction, we present calibrated median ages (± 2σ) on our maps. Some studies use an age-depth model through multiple ages in a sediment core to establish an estimate for basal age (a minimum age for the onset of deglaciation at that location). Including these modelled ages in our compilation is problematic since different studies use various modelling approaches and include/exclude ages for different reasons. As a compromise, in cases where multiple ages from one core are presented in stratigraphic order, the oldest age is included in our compilation. Oldest ages give an indication of the timing of the onset of organic sedimentation, but we add the significant caveat that such ages may over- or under-estimate the true onset of deglaciation given factors such as detrital contamination or undated core sections.

Radiocarbon ages without published δ^{13}C, age uncertainty, or clear geographical or geomorphological context are assigned a low reliability in the compilation. Stratigraphically consistent or multiple ages from the same core are given the highest quality rating. In some older publications, limited metadata is provided for radiocarbon ages, making it challenging to assess the age's reliability. Otherwise, quality control follows the guidelines given in the main manuscript.

Radiocarbon ages from freshwater taxa from lakes or bogs should be avoided (Hatté and Jull, 2013), and so receive a low rating in our analysis of ages. This is because aquatic cells photosynthesise subaquatically, and build carbon from the dissolved inorganic carbon in the water. The dissolved inorganic carbon is influenced by exchange with the atmospheric CO_2 reservoir, decomposition of organic matter, dissolved carbonate from

surrounding rocks, and the residence time of the lake or bog water. The dissolved inorganic carbon is therefore highly spatially variable. The ^{14}C does not reflect atmospheric carbon, but is ^{14}C depleted, resulting in an artificial aging, which can show wide variation (Hatté and Jull, 2013).

2.2.2 Calibration of marine radiocarbon ages

Radiocarbon dating of marine materials (32 samples in our database) requires correction for a global marine reservoir effect (*R*), which varies spatially and temporally in response to changes in oceanic and atmospheric circulation (Ortlieb et al., 2011). Because oceanic carbon is not in isotopic equilibrium with the atmospheric carbon reservoir, radiocarbon ages from marine materials provides older apparent ages than terrestrial counterparts. Deep ocean masses with low radiocarbon concentrations may yield ages older by several hundred years. Global marine reservoir values have been estimated for the last 22,000 years at a decadal resolution, with a current *R* value of 400 years (Hughen et al., 2004; Ortlieb et al., 2011). This value of *R* is included in the Marine13 radiocarbon calibration curve (Reimer et al., 2013).

However, the marine correction varies regionally, especially in high-latitude coastal zones (Hall et al., 2010; Ó Cofaigh et al., 2014). In coastal tropical regions, such as the western coast of Chile and Peru, upwelling of deep ^{14}C-depleted waters to the surface results in high regional reservoir effects. An additional regional reservoir correction (ΔR) is therefore required. The magnitude of this regional reservoir effect is related to ocean circulation changes, and has therefore changed through time (Ortlieb et al., 2011). In Chile, the modern *ΔR* value has been calculated as 190 ± 40 years (Stuiver and Braziunas, 1993), but was updated by Ortlieb et al. (2011) to 253 ± 207 years during the Twentieth Century. However, this *ΔR* value fluctuated over the Holocene. We used the Holocene *ΔR* values presented by Ortlieb et al. (2011) in our marine radiocarbon age calibration (Table 1). For older samples, in the absence of further data, we apply a *ΔR* value of 511 ± 278 years, but emphasise that this correction remains poorly understood.

Table 1. ΔR values along the Chile-Peru coastline, from Ortlieb et al., 2011.

Time range	***ΔR* value**	**Number of ages in database**
Prior to 10,400 cal. BP	511 ± 278 years	16 ages
10,400 to 6840 cal. BP	511 ± 278 years	8 ages
5180 to 1160 cal. BP	226 ± 98 years	2 ages
1000 cal. BP to present	355 ± 105 years	2 age
Early Twentieth Century	253 ± 207 years	

The PATICE shapefile comprises:

1. Unique ID (>1000)
2. Reference
3. Icefield
4. Outlet lobe
5. Site number/name
6. Sample ID
7. Sample Site
8. Latitude (decimal degrees)
9. Longitude (decimal degrees)
10. Altitude (m asl)
11. Description
12. ^{14}C age
13. Given ^{14}C age (integer)
14. ^{14}C uncertainty
15. Terrestrial or Marine age
16. Del13C (δ^{13}C)
17. Calibration curve applied
18. Material dated
19. Two sigma min age
20. Two sigma max age
21. Significant error (ka)
22. Calibrated age Mean
23. Delta R (ΔR)
24. Delta R Uncertainty
25. Delta R Reference
26. Recalibrated age (ka)
27. Age reliability
28. Reliability assessment

2.3 ^{10}Be and ^{26}Al cosmogenic nuclide exposure ages

Surface exposure dating using cosmogenic nuclide ages has been widely applied in Patagonia, primarily using boulders on moraines. We recalibrated all ^{10}Be and ^{26}Al ages using the CRONUS-Earth online exposure age calculator, version 3.0 (Balco et al., 2008). Sample thickness, quartz density, ^{10}Be and ^{26}Al standards, concentrations and shielding corrections were taken from the original publications. We include ages relevant to the LGM and Holocene, but also include selected key pre-LGM ages in our compilation, as older ages on more extensive moraines conclusively constrain the LGM ice extent.

2.3.1 Scaling scheme

We use the time-dependent scaling scheme (LSDn) (Lifton et al., 2014), following Borchers et al. (2016). The LSDn scaling scheme is a newer, more complex scaling scheme based on particle transport models (Borchers et al., 2016; Lifton et al., 2014). A comparison of the ages calculated using the different scaling schemes available results in differences within the uncertainties of the age, given that we present external uncertainties (Figure 2). Ages calculated using all scaling schemes are provided in Supplementary Data for comparison. In general, differences are less than 5% in age, given the relatively high latitude and low altitude of almost all the ages presented in this paper. Furthermore, in some areas, such as the Chilean Lake district, the chronologies (Figure 9) are based on terrestrial ^{14}C data. Therefore, the choice of scaling scheme is unlikely to affect the conclusions of the paper, especially given the focus on 5 ka time slices. That is, we assume differences in ice sheet area and ice sheet volume as shown in our 5 ka time slices are not likely to be affected. One exception to note is the precise timing during the ACR and Younger Dryas intervals; differences in scaling scheme must be noted when focused on respective studies. The precise timing of the Termination, as well, is susceptible to slight differences in production rate and scaling used; however, our time slices of 20 and 15 ka are on either side and well beyond such differences.

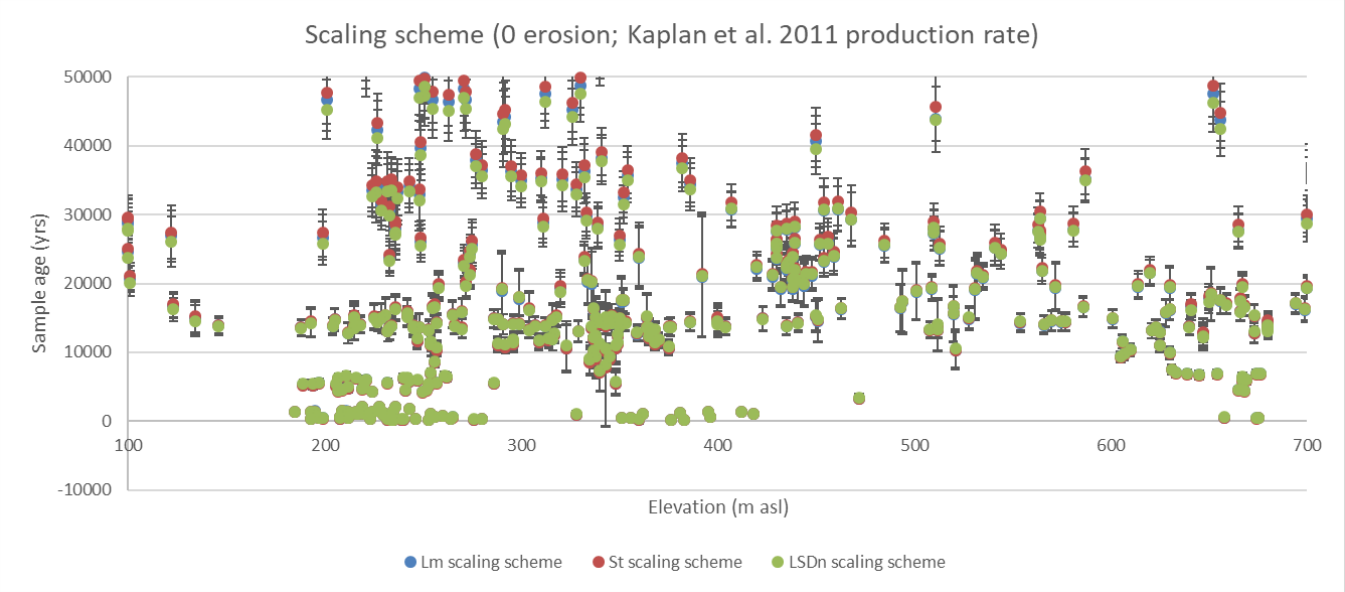

Figure 2. Differences in age calculation with choice of scaling scheme. The Kaplan et al. (2011) production rate and 0 erosion rate are used throughout.

2.3.2 Production rate

We used a locally calibrated production rate for Patagonia based on both the Puerto Bandera and Herminita calibration data, which are in the ICE-D dataset (Kaplan et al., 2011). This rate is similar to that in Kaplan et al. (2011,2016 [as well as Strelin et al., 2014, Sagredo et al., 2018, and Reynhout et al. (2019)]), which used a

higher resolution geomagnetic field history, and a midpoint of the ^{14}C limiting data (see Kaplan et al., 2011). The original rate calculated in Kaplan et al. (2011) is 3.70 ± 0.08 atoms/g/yr (for Lm scaling) at sea level and high latitude, with version 2.2 of the Cronus online calculator. A comparison with the ages derived using this local production rate and the Cronus default production rate in Borchers et al. (2016), results in age differences within the uncertainties of the age, given we use 'external uncertainties' (Figure 3). For reasons elaborated on above, choice of Borchers et al. or rate derived regionally in Patagonia, which also is indistinguishable from that of the other Southern Hemisphere production rate site in New Zealand (Putnam et al., 2010) (as well as other sites), does not affect our main conclusions given a 5 ka time slice reconstruction. However, use of the rate in Borchers et al. (2016) results in the calibration data at Lago Argentino, fitting 'less well' with the limiting ^{14}C data (Figure 4); hence, we suggest to use the regional or local production rate in southern South America, as we do here.

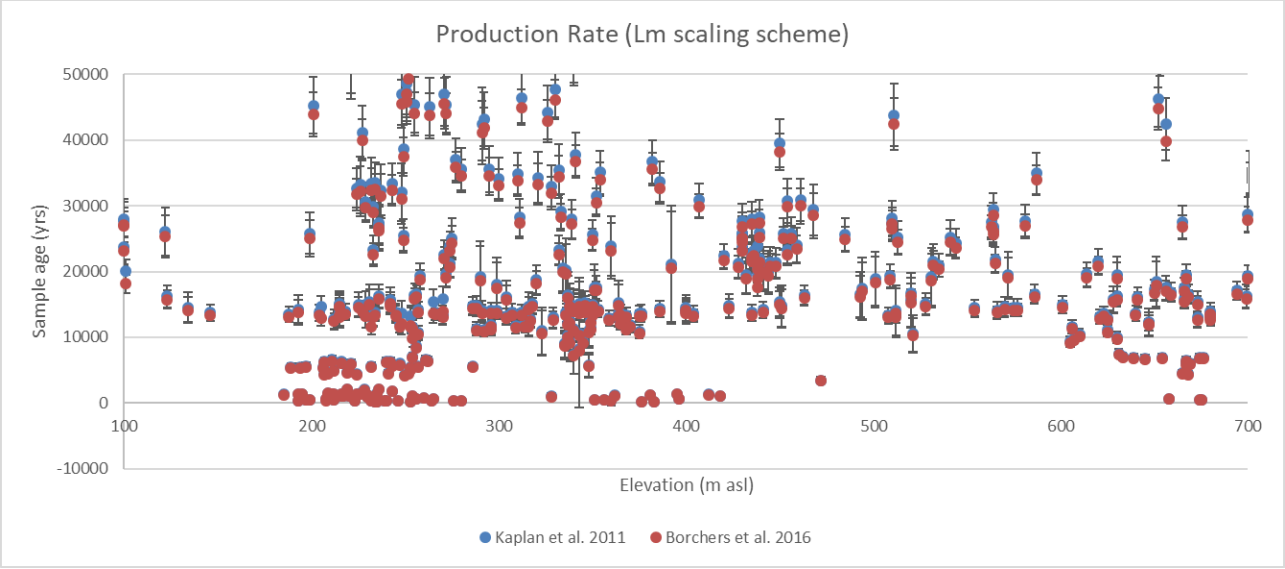

Figure 3. Differences in age calculation using different production rates. Sample Unique ID can be cross-referenced in the Supplementary Data.

Figure 4 below shows the summed probability plots and average age (± 1 standard deviation) for the ^{10}Be age distribution for the Herminita and Puerto Bandera moraines with the Borchers et al. (2016) production rate used in CRONUS calculators version 3, and three scaling factors. Also shown are the minimum-limiting ^{14}C age calibration for the Herminita moraines, and maximum and minimum-limiting ^{14}C age calibrations for the Puerto Bandera moraine sequence, 12,990±80 cal. yrs BP (13,047 ± 80 cal. yrs before CE2007 or 11,100 ± 60 ^{14}C yr) and 12,660 ± 70 cal. yrs BP (12,718 ± 70 ^{14}C before CE2007 or 10,750 ± 75 ^{14}C yrs BP), respectively (Strelin and Denton, 2005; Strelin et al., 2011). Also shown is the age of 12,220 ± 110 cal. yrs BP (12,777 ± 70 before CE2007 or 10,350 ± 45 ^{14}C yrs BP) from the Herminita Peninsula. Specifically, the top panel of Figure 4

shows the summed probability plots and average ages (±1 standard deviation) for the Herminita Peninsula samples (n=11), and bottom panel for Puerto Bandera samples (n=8).

Figure 4 shows that, for Herminita samples, most ages are too young compared with the minimum-limiting ^{14}C age, if the Borcher et al. (2016) rate is used, for all three scaling schemes. That is, they "fit relatively poor" with the ^{14}C constraint. For Puerto Bandera samples, LSD scaling affords ages coherent with the ^{14}C calibration ages. Taken together, however, when both the Herminita and Puerto Bandera ^{10}Be concentrations are considered, the Borchers et al. (2016) rate affords ages that fit less well (and often do not fit) with the ^{14}C boundaries. We thus argue the regional production rate (Kaplan et al., 2011), based on the Herminita and Puerto Bandera sites and ^{10}Be concentrations, is the best to use for southern South America.

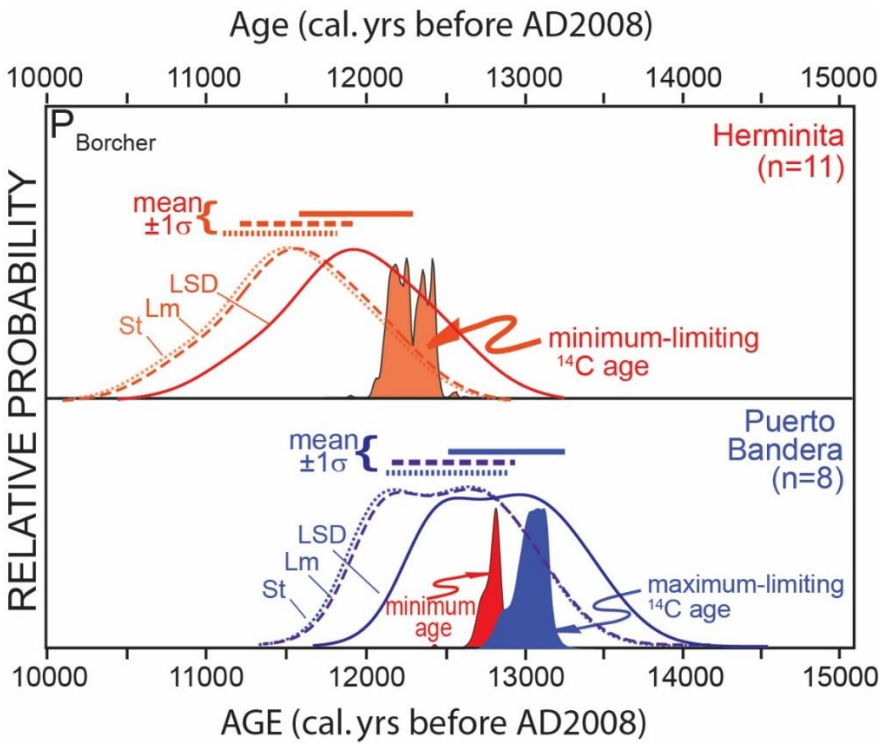

Figure 4. Summed probability plots and average age (±1 standard deviation) for ^{10}Be age distributions for the Herminita and Puerto Bandera moraines, with the Borchers et al. (2016) production rate, version 3, and three scaling factors. Also shown are the minimum and maximum-limiting ^{14}C age calibration ages (see text) for the Herminita and Puerto Bandera moraine sequence (Strelin and Denton, 2005; Strelin et al., 2011; 2014).

2.3.3 Erosion rates and other corrections

Rock surface erosion rates reduce surface nuclide concentrations over time, but are relatively poorly constrained in Patagonia. Kaplan et al. (2005) reported a maximum erosion rate of 1.4 mm kyr^{-1} for boulders in semi-arid Patagonia around Lago Buenos Aires. This value was adjusted to about 0.2 mm kyr^{-1} (range 0.0-4.6 mm kyr^{-1}) by Douglass (2007) based on paired ^{36}Cl/^{10}Be concentrations (Hein et al., 2017). We apply no

erosion correction to the integrated dataset because even the higher erosion rate leads to little difference in the calculated age within the timescale of the LGM to present day (Figure 5; Figure 6). Consequently, a change in erosion rate is unlikely to affect the conclusions of this paper.

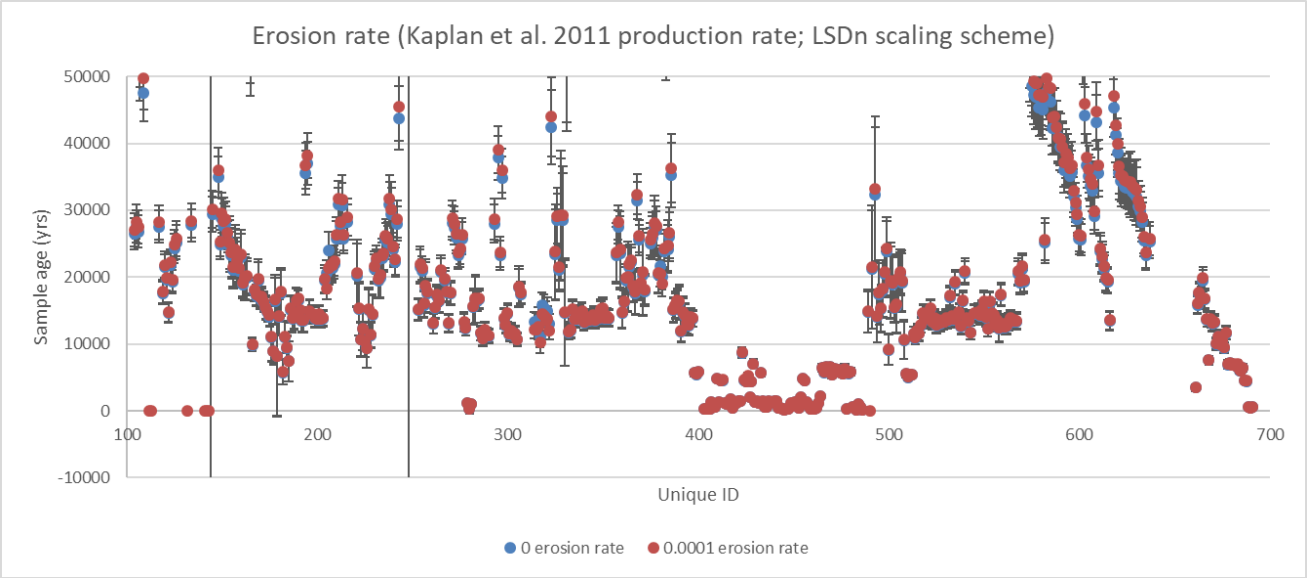

Figure 5. Comparison of calculated ages using different erosion rates. When an erosion rate of 1.4mm/kyr is applied, some older ages are saturated (unable to calculate age; plotting as 0 on the y axis). For 35 ka to present, the choice of erosion rate results in little difference to the calculated age. Sample Unique ID can be cross-referenced in the Supplementary Data.

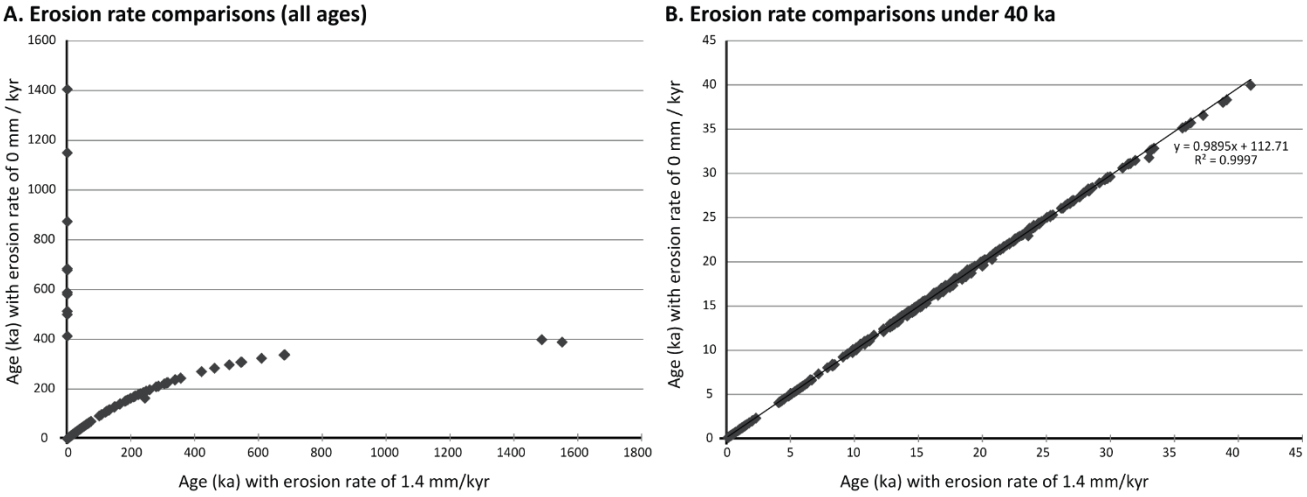

Figure 6. Comparison of ages with a 0 and 0.00014 erosion rate. With the higher erosion rate, some older ages are saturated and an age cannot be calculated.

We include no correction for periodic snow cover, which is likely to be negligible on the eastern (dry) side of the Andes where most of the cosmogenic nuclide data originate, because snow is normally blown free from

the tops of moraine boulders and aridity and wind intensity are generally considered to have increased during glacial maxima.

We also apply no correction for post-glacial uplift. As postglacial uplift or rebound exponentially decreases and hence rates quickly diminish after ice recession, the integrated exposure history of boulders in Patagonia is essentially at their present elevation on the timescales in this study. Furthermore, the highest isostatic uplift rates documented are on the order of 10s of meters (see text). By not including corrections for erosion, snow cover and uplift, the exposure ages reported here could be considered minimum ages. Where age distributions exist for a given moraine, statistics often show such effects, if they occurred, must be within uncertainties; we encourage analyses of such issues on a site-by-site basis depending on the nature of the age distribution (e.g., number of outliers, variance of dataset, and so on). We provide the entire dataset as excel spreadsheets in the Supplementary Data, formatted for straightforward recalculation.

2.3.4 Uncertainties

Reported uncertainties (1σ) are all external, which includes those uncertainties associated with production rate sites up to thousands of kilometres apart from each other and elevational scaling of thousands of meters of elevation. We note such errors are likely to be relatively conservative within Patagonia, which is close to the production rate site itself, both in terms of distance and elevation. Also, external uncertainties are not relevant when comparing the relative differences between time slices emphasized here, as they are systematic within a given area (we have no evidence to support statistically significant differences in the production rate over the last 30 ka at these latitudes; cf., Putnam et al., 2010). Last, we encourage researchers to propagate a production rate calibration uncertainty of 3% in mean moraine ages when they are calculated (e.g., Kaplan et al., 2016; Sagredo et al., 2018, Reynhout et al., 2019), to compare to other records dated with other approaches (Kaplan et al., 2011).

2.3.5 Moraine mean ages

Ages (where $n \geq 2$) from a single landform are used to calculate mean ages for that landform. This mean age (μ) is provided with the standard deviation (SD) of the samples. The mean age is based on high quality (green) ages only, using external uncertainties. Outliers without overlapping uncertainties at 2σ are excluded. Mean ages are used to simplify the data, and give an overall age for a landform such as a moraine, and they show the coherence of the distribution.

We do not use uncertainty weighted means for the following reasons. As most of the uncertainty on the individual ages comes from the uncertainties in the production rate and scaling scheme, the uncertainties of the ages within the same group of samples are usually quite homogeneous. Also, the scatter of the ages within the same group is typically higher than the individual age uncertainties, suggesting that the natural "noise" in the ^{10}Be ages due to the geological characterisation of the samples (i.e. position on the moraine, weathering, flaking, exhumation and denudation) is higher than the uncertainties considered in the age calculations (laboratory systematic errors, AMS precision, production rate and scaling uncertainties). Older moraines may be especially susceptible to these issues, where erosion may be more statistically important and where uncertainties in age calculations are higher. Therefore, we considered that the calculated mean ages and standard deviations should represent landform ages better than uncertainty weighted means. In addition, different samples may be more or less difficult to process in the laboratory; for instance, having more or less non-quartz minerals. This leads to samples having different precision on their measurements, but this is not reflective of sample quality (i.e. position on moraine, weathering, flaking, exhumation or denudation). This would then disproportionately weight the mean in a non-accurate way.

To avoid these issues, but to allow us to summarise and reduce the data, we simply provide the mean landform age and the standard deviation, which gives an indication of the spread of ages on the landform.

2.3.6 PATICE Shapefile

The PATICE shapefile comprises:

1. Unique ID (>100)
2. Reference
3. Icefield
4. Outlet lobe
5. Site number
6. Landform Name
7. Sample Name
8. Published age (integer)
9. Published uncertainty (integer)
10. Site description
11. Notes
12. Latitude (decimal degrees)
13. Longitude (decimal degrees)
14. Elevation (m asl)
15. Thickness (cm)
16. Density
17. Shielding

18. Erosion rate
19. ^{10}Be concentration
20. ^{10}Be uncertainty
21. ^{26}Al concentration
22. ^{26}Al uncertainty
23. AMS Reference (^{10}Be)
24. AMS reference (^{26}Al)
25. Elevation/pressure flag
26. Age calculator used
27. Production rate applied
28. Recalculated age
29. Recalculated uncertainty
30. Recalculated age (ka)
31. Age reliability
32. Reliability assessment
33. Landform mean age
34. Landform standard deviation age
35. Mean age label

2.4 ^{3}He and ^{36}Cl cosmogenic nuclide exposure ages

^{3}He and ^{36}Cl data were extracted from publications (Ackert et al., 2008; Douglass et al., 2005; Kaplan et al., 2004) and existing databases. However, extracting sufficient data from the published works to allow recalculation was not possible. We therefore present the original ages in the database. The ^{3}He ages are considered approximate maximum ages, because they do not consider the non-cosmogenic ^{3}He component. However, given the number of ages in question (24), recalculating the ages would not change the conclusions of the paper.

The PATICE shapefile includes:

1. Unique ID (>7000/8000)
2. Reference
3. Icefield
4. Site Number
5. Sample Name
6. Notes
7. Site description
8. Published age (integer)
9. Published uncertainty
10. Age (ka)

11. Latitude (decimal degrees)
12. Longitude (decimal degrees)
13. Elevation (m asl)
14. Thickness (cm)
15. Density
16. Shielding
17. Erosion rate
18. Elevation/pressure flag
19. Mineral
20. Nuclide
21. Date sample collected (year)
22. Noble gas standard
23. Nuclide concentration
24. Nuclide uncertainty
25. Age reliability

2.5 Cosmogenic nuclide depth profiles

Depth profiles use a number of samples (e.g. >5) through a sedimentary unit to provide a single surface exposure age based on cosmogenic nuclide concentration at different depths (Darvill, 2013). Samples are taken through a deep (e.g. >1.5 m) exposure in the sedimentary unit, either as amalgams or selected lithologies (e.g. targeting quartz-rich clasts or sand). Sampled units normally consist of sands to gravels or cobbles, although selecting fractions greater than sand-size may affect profile modelling (Hidy et al., 2010). The method assumes that the unit was deposited in a single geologic event such that subsequent nuclide accumulation through the sediments attenuates with depth (Anderson et al., 1996; Repka et al., 1997). Hence, to use the technique to establish surface exposure age, the principle geomorphic assumptions are: relatively rapid post-deposition stabilisation of the sedimentary unit; low nuclide inheritance; minimal post-deposition shielding; and little/no post-deposition sediment mixing (Hein et al., 2009). A modelled nuclide attenuation profile through several depth samples will yield a most probable age for surface exposure as well as average inheritance (nuclide concentrations deeper than the penetration of cosmic ray reactions) and surface erosion (projecting measured nuclide concentrations to the modelled surface according to the expected attenuation curve) in the unit (Hein et al., 2009; Hidy et al., 2010; Marrero et al., 2016). Exposure ages from depth profiles can be strengthened using single exposure ages from cobbles on the unit surface, to provide a check on the modelled exposure age and surface inflation/deflation (Cogez et al., 2018; Darvill et al., 2015; Hein et al., 2017; Hein et al., 2011; Hein et al., 2009). It is also possible to reconstruct more

complicated depositional histories using multiple cosmogenic nuclides (Balco and Rovey, 2008; Granger and Muzikar, 2001; Häuselmann et al., 2007; Hein et al., 2009).

The depth profile method offers a powerful approach to dating sedimentary units that can be useful in glacial setting where sampling of boulders or cobbles may be complicated by post-depositional erosion and/or exhumation (Darvill et al., 2015; Hein et al., 2017). This is particularly so on glacier or other sediments deposited prior to the last glacial cycle (Hein et al., 2010; 2017). For example, in Patagonia, depth profiles through outwash plains robustly mapped to associated moraine limits have been shown to be effective in exposure dating the former ice sheet history over a large spatial and temporal range (Cogez et al., 2018; Darvill et al., 2015; Hein et al., 2017; Hein et al., 2011; Hein et al., 2009).

The PATICE shapefile comprises:

1. Unique ID (> 2000)
2. Reference
3. Latitude
4. Longitude
5. Modelled age (ka)
6. Uncertainty
7. Geomorphological context

2.6 Optically stimulated luminescence ages

Luminescence dating can directly determine when a mineral grain was last deposited and buried. The technique relies upon the ability of quartz or K-feldspar grains to store energy within the crystal structure and release it when stimulated using light (optically stimulated luminescence; OSL) or heat (thermoluminescence; TL). The OSL signal of grains is reset (or bleached) when exposed to sunlight prior to burial and then accumulated again when the grains are exposed to constant natural radiation in the surrounding environment from the radioactive decay of U, Th, K and Rb, in addition to cosmic rays, that is termed the “dose-rate”. In glacial settings, OSL applied to glacial outwash sediments that can be directly linked to a moraine can constrain the position of the ice margin when it was at that moraine (Smedley et al., 2016).

Grains deposited in glacial settings typically have less opportunity for sunlight bleaching prior to burial than to aeolian sediments which are typically well bleached. Glaciofluvial sediments are therefore targeted to maximise the opportunity for bleaching, but the OSL signals of individual grains are typically incompletely

bleached prior to burial. For such sediments, single-grain OSL analysis (Bøtter-Jensen et al., 2003) and statistical age models (see Galbraith and Roberts, 2012) are often required to determine accurate ages.

An additional challenge for OSL dating of K-feldspar in comparison to quartz is that feldspars are prone to the effects of anomalous fading (Wintle, 1973) which manifests as age underestimations if not addressed (Huntley and Lamothe, 2001). OSL ages determined from feldspar must either be accurately corrected for fading (e.g., Huntley and Lamothe, 2001) or determined using more stable signals such as the post-IR IRSL signal (pIRIR) typically measured at 225°C or 290°C, which circumvent the issues of anomalous fading (Thomsen et al., 2008; Thomsen et al., 2011). Previous studies have successfully used the OSL signal of single grains of quartz (e.g., Glasser et al., 2006) and the pIRIR signal of single grains of K-feldspar (e.g., Smedley et al., 2016) to determine accurate ages for glaciofluvial sediments from Patagonia.

The PATICE shapefile comprises:

1. Unique ID (>700)
2. Reference
3. Landform name
4. Sample name
5. Latitude
6. Longitude
7. Elevation
8. Published age (years)
9. Published uncertainty
10. Age (ka)
11. Technique
12. Notes
13. Further comments
14. Age reliability
15. Reliability assessment

2.7 Tephrochronology

Several studies use tephrochronology of layers in lake sediment cores to provide an improved chronology. Where these are done in conjunction with repeated radiocarbon ages and subsequent tephra horizons, they provide an excellent independent marker horizon of a known age across several cores. In the absence of dateable organics at the base of sediment cores, tephra horizons can provide a constraint on the timing of

deglaciation, correlated across multiple cores and localities (e.g., Kilian et al., 2013; Kilian et al., 2003; Kilian et al., 2007; Stern, 2008). Tephra ages are chronologically constrained using ^{14}C dates from terrestrial sites, and are thus independent of marine reservoir corrections (Kilian et al., 2013). Six key volcanoes (Lautero, Viedma, Aguilera, Reclus, Mt. Burney and Cook Island) form the Andean Austal Volcanic Zone, which is the southernmost volcanically active segment in the Andes (Stern, 2008). Hudson volcano is important further north (Bendle et al., 2017). These volcanoes result from slow subduction of the Antarctic Plate (refer to Geological Setting). These volcanoes deposited regionally widespread Holocene tephra layers in Tierra del Fuego, which can be geochemically distinguished. The key tephras from this region are summarised in Table 2.

Although different papers assign different ages to each tephra horizon, in this study we use a consistent age for each horizon throughout the paper. These ages are given in Table 2, and are selected on the robustness of their independent ^{14}C age control. The ages used by the original authors are listed in the geodatabase's Tephra shapefile (Table 2).

Table 2. Details of key Holocene tephra layers distributed in southernmost South America.

Source	Tephra	Latitude	Average ^{14}C yrs BP	Average cal. yrs BP	Reference
Reclus	R_1	51°S	12,685 ± 260	14780 ± 560	Sagredo et al. (2011)
Mt Burney	MB_1	52°S	8440 ± 750	9400 ± 1100	Stern (2008)
Mt Burney	MB_2	52°S	4015 ± 720	4265 ± 895	Stern (2008)
Hudson	Ho	45°S	18820	17370 ± 70	Stern et al. (2015); Weller et al. (2015)
Hudson	H_1	45°S	6850 ± 160	7710 ± 280	Stern (2008)
Hudson	H_2	45°S		4000 ± 50	Stern et al. (2016); Naranjo and Stern (1998)
Hudson	H_3	45°S	-	1991 AD	Stern et al. (2016)
Aguilera	A_1	50°S	3000 ± 100	3200 ± 270	Stern (2008)
Mentolat	MEN_1	44°S	6782 ± 23	7490 ± 130	Stern et al. (2016)

The PATICE shapefile comprises:

1. Unique ID (>3000)
2. Reference
3. Location
4. Latitude (decimal degrees)
5. Longitude (decimal degrees)

6. Published age
7. Tephra source
8. Tephra layer
9. Description
10. Tephra range
11. Updated tephra age from Stern (2008)
12. Age (ka)
13. Age reliability

2.8 Historical documents

Chile has many historical documents and maps dating from Spanish colonial rule in the 16th Century that can assist in the identification of glacier extent over the last few centuries (Araneda et al., 2007). The first explorers to reach Glaciar San Rafael, for example, were Spanish explorers in 1675 AD. Later, scientific reports from expeditions (e.g., de Agostini, 1956; de Gasperi, 1922; Lawrence and Lawrence, 1959; Steffen, 1947) and accounts from early explorers (e.g., Darwin, 1839) also provide data on glacier positions that can be incorporated into later reconstructions (Harrison et al., 2007; Izagirre et al., 2018; Garibotti and Villalba, 2009). Maps compiled by República de Chile based on field surveys carried out in 1894-1899 provide information on glacier extent of the South Patagonian Icefield (Casassa et al., 1997). Trimetrogon aerial photographs taken by the United States Air Force in 1944/1945 provide further data on ice extent (Harrison et al., 2007). In this way, accurate reconstructions on a glacier-by-glacier basis can be compiled, dating from the Little Ice Age (LIA) through to the mid-20th Century.

The PATICE shapefile comprises:

1. Unique ID (>5000)
2. Reference
3. Document
4. Description
5. Age (years AD)
6. Latitude
7. Longitude
8. Altitude (m asl)
9. Age reliability

2.9 Dendrochronology

Trees colonising recently deglaciated land surfaces, especially on markers of ice advance such as moraines, provides a means of dating surfaces too young to date reliably by other means (Coulthard and Smith, 2013; Koch, 2009; Smith and Laroque, 1996). This has been termed 'dendroglaciology' (Masiokas et al., 2009a). This technique has been widely applied to date "Little Ice Age" moraines around the North Patagonian Icefield and South Patagonian Icefield (e.g., Boninsegna et al., 2009; Koch and Kilian, 2005; Masiokas et al., 2009b; Winchester and Harrison, 2000; Winchester et al., 2001; Winchester et al., 2014). In our study region, most tree-ring chronologies use the South American beech (*Nothofagus* sp.), the conifer *Pilgerodendron uviferum* or *Fitzroya cupressoides*.

We limit our database to those tree-ring chronologies that can establish a deglacial age for glacial landforms, such as moraines or trimlines. This method has a dating precision of around 10 years, and the age of the oldest tree provides a minimum estimate for the surface age (Coulthard and Smith, 2013). Limitations of the technique include that the ecesis time (time between surface exposure and tree germination) is challenging to estimate, and it makes the assumption that the oldest tree has been sampled. Our database includes information such as ecesis time, growth rate, tree age, a calculated date for tree germination, comments on geomorphological and geographical situation, source reference, and a Unique ID for each data entry.

The PATICE Dendrochronology shapefile includes:

1. Unique ID (>4000)
2. Reference
3. Latitude
4. Longitude
5. Altitude
6. Description
7. Location
8. Age (years AD)
9. Growth rate
10. Ecesis time (years)
11. Age reliability

2.10 Lichenometry

Lichenometry using the species *Rhizocarpon* subgenus *Rhizocarpon* has also been used to date constructional glacial landforms from the last 100 years or so (Harrison et al., 2007; Garibotti and Villalba,

2009; 2017). Our database includes information on the growth curve, sampling method, calculated moraine date, and any other relevant information. The growth rate of *Rhizocarpon* decreases over time, and the strong east-west precipitation gradient in Patagonia introduces statistically significant differences in the growth curves (Garibotti and Villalba, 2009).

The PATICE lichenometry shapefile comprises:

1. Unique ID (>4500)
2. Reference
3. Latitude
4. Longitude
5. Description
6. Species
7. Comments
8. Age (Year AD)
9. Location
10. Age (ka)

2.11 Varve records

Annually-laminated (varved) sediment sequences deposited in former proglacial lakes provide a means of dating ice-margin fluctuations and local geomorphological events (e.g. Bendle et al., 2017; Caldenius, 1932; Larsen et al., 2012; Ridge et al., 2012). In proglacial lakes, varves form in response to seasonal variations in sediment influx that lead to deposition of a coarse-grained (silt/sand) melt season layer, capped by a fine-grained (clay) non-melt season layer. Where deposited in continuous sequences, counts of the number of annual layers enable an incremental chronology to be developed. Before glacier fluctuations can be dated, this 'floating' varve chronology must be anchored in absolute time using an independent dating technique (e.g. tephrochronology, radiocarbon). Once time-anchored, a varve record can be used to infer glacier changes (often using a combination of varve thickness data and the morphostratigraphic relationship between varved sediment sequences and ice-marginal landforms, such as moraines) and date their timing. As an example, a sequence of varves deposited between two recessional moraines enables age estimates to be derived for each of these former glacier extents. Using this approach, the duration of glacier retreat cycles and rates of recession can be quantified (Bendle et al., 2017a).

In Patagonia, glaciolacustrine varve records were first studied by Caldenius (1932). However, in this early work, the absolute timing of glacial changes could not be ascertained as no means of independent dating

was readily available. Recently, however, a varve chronology of *ca.* 1000 years duration was developed at Lago GCBA. This record has been independently dated through tephrochronology, owing to the *in situ* presence of the Ho tephra (Table 2) in the varve sequence (Bendle et al., 2017). These ages complement ^{10}Be dating of moraine boulders in the same valley (Douglass et al., 2006; Kaplan et al., 2004; Thorndycraft et al., 2019).

The PATICE shapefile comprises:

1. Unique ID (>6000)
2. Reference
3. Description
4. Location
5. Landform
6. Start age (years)
7. End age (years)
8. Latitude (decimal degrees)
9. Longitude (decimal degrees)

3 References

Ackert, R.P., Becker, R.A., Singer, B.S., Kurz, M.D., Caffee, M.W., Mickelson, D.M., 2008. Patagonian Glacier Response During the Late Glacial–Holocene Transition. Science 321, 392-395.

Anderson, R.S., Repka, J.L., Dick, G.S., 1996. Explicit treatment of inheritance in dating depositional surfaces using in situ 10Be and 26Al. Geology 24, 47-51.

Araneda, A., Torrejon, F., Aguayo, M., Torres, L., Cruces, F., Cisternas, M., Urrutia, R., 2007. Historical records of San Rafael glacier advances (North Patagonian Icefield): another clue to 'Little Ice Age' timing in southern Chile? Holocene 17, 987-998.

Balco, G., Rovey, C.W., 2008. An isochron method for cosmogenic-nuclide dating of buried soils and sediments. American Journal of Science 308, 1083-1114.

Balco, G., Stone, J.O., Lifton, N.A., Dunai, T.J., 2008. A complete and easily accessible means of calculating surface exposure ages or erosion rates from ^{10}Be and ^{26}Al measurements. Quaternary Geochronology 3, 174-195.

Bendle, J.M., Palmer, A.P., Thorndycraft, V.R., Matthews, I.P., 2017. High-resolution chronology for deglaciation of the Patagonian Ice Sheet at Lago Buenos Aires (46.5°S) revealed through varve chronology and Bayesian age modelling. Quaternary Science Reviews 177, 314-339.

Bird, P., 2003. An updated digital model of plate boundaries. Geochemistry, Geophysics, Geosystems 4.

Boninsegna, J.A., Argollo, J., Aravena, J.C., Barichivich, J., Christie, D., Ferrero, M.E., Lara, A., Le Quesne, C., Luckman, B.H., Masiokas, M., Morales, M., Oliveira, J.M., Roig, F., Srur, A., Villalba, R., 2009.

Dendroclimatological reconstructions in South America: A review. Palaeogeography Palaeoclimatology Palaeoecology 281, 210-228.

Borchers, B., Marrero, S., Balco, G., Caffee, M., Goehring, B., Lifton, N., Nishiizumi, K., Phillips, F., Schaefer, J., Stone, J., 2016. Geological calibration of spallation production rates in the CRONUS-Earth project. Quaternary Geochronology 31, 188-198.

Bøtter-Jensen, L., Andersen, C., Duller, G., Murray, A., 2003. Developments in radiation, stimulation and observation facilities in luminescence measurements. Radiation Measurements 37, 535-541.

Bronk Ramsey, C., 2009. Bayesian analysis of radiocarbon dates. Radiocarbon 51, 337-360.

Caldenius, C.C., 1932. Las glaciaciones cuaternarias en la Patagonia y Tierra del Fuego. Geografiska Annaler 14, 1-164.

Casassa, G., Brecher, H., Rivera, A., Aniya, M., 1997. A century-long recession record of Glaciar O'Higgins, Chilean Patagonia. Annals of Glaciology 24, 106-110.

Cogez, A., Herman, F., Pelt, É., Reuschlé, T., Morvan, G., Darvill, C.M., Norton, K.P., Christl, M., Märki, L., Chabaux, F., 2018. U-Th and 10Be constraints on sediment recycling in proglacial settings, Lago Buenos Aires, Patagonia. Earth Surface Dynamics 6, 121-140.

Coulthard, B.L., Smith, D.J., 2013. Dendroglaciology in: Elias, S.A. (Ed.), Encyclopedia of Quaternary Science (Second Edition). Elsevier, Amsterdam, pp. 104-111.

Darvill, C.M., 2013. Cosmogenic Nuclide Analysis, in: Clarke, L., Nield, J. (Eds.), Geomorphological Techniques. British Society for Geomorphology, London.

Darvill, C.M., Bentley, M.J., Stokes, C.R., Hein, A.S., Rodés, Á., 2015. Extensive MIS 3 glaciation in southernmost Patagonia revealed by cosmogenic nuclide dating of outwash sediments. Earth and Planetary Science Letters 429, 157-169.

Darwin, C.R., 1839. Journal of research (volume 3). Henry Colburn, Narrative of the Surveying Voyages of H.M.S. Adventure and Beagle. Everyman reprint 1983, The Voyage of the Beagle.

de Agostini, A.M., 1956. Treinta años en Tierra del Fuego. Elefante Blanco, Buenos Aires.

de Gasperi, G.B., 1922. Scritti vari di geografia e geologia; pubblicazione postuma.

Douglass, D.C., Singer, B.S., Kaplan, M.R., Ackert, R.P., Mickelson, D.M., Caffee, M.W., 2005. Evidence of early Holocene glacial advances in southern South America from cosmogenic surface-exposure dating. Geology 33, 237-240.

Douglass, D., Singer, B., Kaplan, M., Mickelson, D., Caffee, M., 2006. Cosmogenic nuclide surface exposure dating of boulders on last-glacial and late-glacial moraines, Lago Buenos Aires, Argentina: interpretive strategies and paleoclimate implications. Quaternary Geochronology 1, 43-58.

Douglass, D.C., 2007. Constraining boulder erosion rates and ages of mid-Pleistocene moraines, Lago Buenos Aires, Argentina, Geological Society of America Abstracts with Programs, p. 65.

Garibotti, I.A., Villalba, R., 2009. Lichenometric dating using Rhizocarpon subgenus Rhizocarpon in the Patagonian Andes, Argentina. Quaternary Research 71, 271–283.

Garibotti, I.A., Villalba, R., 2017. Colonization of mid- and late-Holocene moraines by lichens and trees in the Magellanic sub-Antarctic province. Polar Biology 1–15.

Galbraith, R., Roberts, R.G., 2012. Statistical aspects of equivalent dose and error calculation and display in OSL dating: an overview and some recommendations. Quaternary Geochronology 11, 1-27.

Glasser, N.F., Harrison, S., Ivy-Ochs, S., Duller, G.A.T., Kubik, P.W., 2006. Evidence from the Rio Bayo valley on the extent of the North Patagonian Icefield during the Late Pleistocene - Holocene transition. Quaternary Research 65, 70-77.

Glasser, N.F., Jansson, K.N., Goodfellow, B.W., de Angelis, H., Rodnight, H., Rood, D.H., 2011. Cosmogenic nuclide exposure ages for moraines in the Lago San Martin Valley, Argentina. Quaternary Research 75, 636-646.

Granger, D.E., Muzikar, P.F., 2001. Dating sediment burial with in situ-produced cosmogenic nuclides: theory, techniques, and limitations. Earth and Planetary Science Letters 188, 269-281.

Hall, B.L., Henderson, G.M., Baroni, C., Kellogg, T.B., 2010. Constant Holocene Southern-Ocean ^{14}C reservoir ages and ice-shelf flow rates. Earth and Planetary Science Letters 296, 115-123.

Harrison, S., Winchester, V., Glasser, N., 2007. The timing and nature of recession of outlet glaciers of Hielo Patagonico Norte, Chile, from their Neoglacial IV (Little Ice Age) maximum positions. Global and Planetary Change 59, 67-78.

Häuselmann, P., Fiebig, M., Kubik, P., Adrian, H., 2007. A first attempt to date the original “Deckenschotter” of Penck and Brückner with cosmogenic nuclides. Quaternary International 164, 33-42.

Hatté, C., Jull, A.J.T., 2013. RADIOCARBON DATING | ^{14}C of Plant Macrofossils, in: Elias, S.A., Mock, C.J.B.T.-E. of Q.S. (Second E. (Eds.), . Elsevier, Amsterdam, pp. 361–367. https://doi.org/https://doi.org/10.1016/B978-0-444-53643-3.00049-2

Hein, A.S., Cogez, A., Darvill, C.M., Mendelova, M., Kaplan, M.R., Herman, F., Dunai, T.J., Norton, K., Xu, S., Christl, M., 2017. Regional mid-Pleistocene glaciation in central Patagonia. Quaternary Science Reviews 164, 77-94.

Hein, A.S., Dunai, T.J., Hulton, N.R.J., Xu, S., 2011. Exposure dating outwash gravels to determine the age of the greatest Patagonian glaciations. Geology 39, 103-106.

Hein, A.S., Hulton, N.R.J., Dunai, T.J., Schnabel, C., Kaplan, M.R., Naylor, M., Xu, S., 2009. Middle Pleistocene glaciation in Patagonia dated by cosmogenic-nuclide measurements on outwash gravels. Earth and Planetary Science Letters 286, 184-197.

Hogg, A.G., Hua, Q., Blackwell, P.G., Niu, M., Buck, C.E., Guilderson, T.P., Heaton, T.J., Palmer, J.G., Reimer, P.J., Reimer, R.W., Turney, C.S.M., Zimmerman, S.R.H., 2013. SHCal13 Southern Hemisphere Calibration, 0–50,000 Years cal BP. Radiocarbon 55, 1889-1903.

Hughen, K.A., Baillie, M.G.L., Bard, E., Beck, J.W., Bertrand, C.J.H., Blackwell, P.G., Buck, C.E., Burr, G.S., Cutler, K.B., Damon, P.E., Edwards, R.L., Fairbanks, R.G., Friedrich, M., Guilderson, T.P., Kromer, B., McCormac, G., Manning, S., Ramsey, C.B., Reimer, P.J., Reimer, R.W., Remmele, S., Southon, J.R., Stuiver, M., Talamo, S., Taylor, F.W., van der Plicht, J., Weyhenmeyer, C.E., 2004. Marine04 marine radiocarbon age calibration, 0-26 cal kyr BP. Radiocarbon 46, 1059-1086.

Huntley, D.J., Lamothe, M., 2001. Ubiquity of anomalous fading in K-feldspars and the measurement and correction for it in optical dating. Canadian Journal of Earth Sciences 38, 1093-1106.

Izagirre, E., Darvill, C.M., Rada, C., Aravena, J.C., 2018. Glacial geomorphology of the Marinelli and Pigafetta glaciers, Cordillera Darwin Icefield, southernmost Chile. Journal of Maps 14, 269-281.

Kaplan, M.R., Ackert, R.P., Singer, B.S., Douglass, D.C., Kurz, M.D., 2004. Cosmogenic nuclide chronology of millennial-scale glacial advances during O-isotope stage 2 in Patagonia. GSA Bulletin 116, 308-321.

Kaplan, M.R., Douglass, D.C., Singer, B.S., Ackert, R.P., Caffee, M.W., 2005. Cosmogenic nuclide chronology of pre-last glacial maximum moraines at Lago Buenos Aires, 46°S, Argentina. Quaternary Research 63, 301-315.

Kaplan, M.R., Strelin, J.A., Schaefer, J.M., Denton, G.H., Finkel, R.C., Schwartz, R., Putnam, A.E., Vandergoes, M.J., Goehring, B.M., Travis, S.G., 2011. In-situ cosmogenic ^{10}Be production rate at Lago Argentino, Patagonia: Implications for late-glacial climate chronology. Earth and Planetary Science Letters 309, 21-32.

Kilian, R., Baeza, O., Breuer, S., Ríos, F., Arz, H., Lamy, F., Wirtz, J., Baque, D., Korf, P., Kremer, K., 2013. Late Glacial and Holocene palaeogeographical and palaeoecological evolution of the Seno Skyring and Otway fjord systems in the Magellan Region. Anales del Instituto de la Patagonia 41, 5-26.

Kilian, R., Hohner, M., Biester, H., Wallrabe-Adams, H.J., Stern, C.R., 2003. Holocene peat and lake sediment tephra record from the southernmost Chilean Andes (53-55 S). Revista geologica de Chile 30, 23-37.

Kilian, R., Schneider, C., Koch, J., Fesq-Martin, M., Biester, H., Casassa, G., Arévalo, M., Wendt, G., Baeza, O., Behrmann, J., 2007. Palaeoecological constraints on late Glacial and Holocene ice retreat in the Southern Andes (53°S). Global and Planetary Change 59, 49-66.

Koch, J., 2009. Improving age estimates for late Holocene glacial landforms using dendrochronology–Some examples from Garibaldi Provincial Park, British Columbia. Quaternary Geochronology 4, 130-139.

Koch, J., Kilian, R., 2005. 'Little Ice Age' glacier fluctuations, Gran Campo Nevado, southernmost Chile. Holocene 15, 20-28.

Larsen, D.J., Miller, G.H., Geirsdóttir, Á., Ólafsdóttir, S., 2012. Non-linear Holocene climate evolution in the North Atlantic: a high-resolution, multi-proxy record of glacier activity and environmental change from Hvítárvatn, central Iceland. Quaternary Science Reviews 39, 14-25.

Lawrence, D.B., Lawrence, E.G., 1959. Recent glacier variations in southern South America. American Geographical Society New York.

Lifton, N., Sato, T., Dunai, T.J., 2014. Scaling in situ cosmogenic nuclide production rates using analytical approximations to atmospheric cosmic-ray fluxes. Earth and Planetary Science Letters 386, 149-160.

Marrero, S.M., Phillips, F.M., Caffee, M.W., Gosse, J.C., 2016. CRONUS-Earth cosmogenic Cl-36 calibration. Quaternary Geochronology 31, 199-219.

Masiokas, M., Luckman, B., Villalba, R., Delgado, S., Skvarca, P., Ripalta, A., 2009a. Little Ice Age fluctuations of small glaciers in the Monte Fitz Roy and Lago del Desierto areas, south Patagonian Andes, Argentina. Palaeogeography, Palaeoclimatology, Palaeoecology 281, 351-362.

Masiokas, M.H., Rivera, A., Espizua, L.E., Villalba, R., Delgado, S., Aravena, J.C., 2009b. Glacier fluctuations in extratropical South America during the past 1000 years. Palaeogeography, Palaeoclimatology, Palaeoecology 281, 242-268.

Naranjo, J.A., Stern, C.R., 1998. Holocene explosive activity of Hudson Volcano, southern Andes. Bulletin of Volcanology 59, 291-306.

Ó Cofaigh, C., Davies, B.J., Livingstone, S.J., Smith, J.A., Johnson, J.S., Hocking, E.P., Hodgson, D.A., Anderson, J.B., Bentley, M.J., Canals, M., Domack, E., Dowdeswell, J.A., Evans, J., Glasser, N.F., Hillenbrand, C.-D., Larter, R.D., Roberts, S.J., Simms, A.R., 2014. Reconstruction of ice-sheet changes in the Antarctic Peninsula since the Last Glacial Maximum. Quaternary Science Reviews 100, 87-110.

Ortlieb, L., Vargas, G., Saliège, J.-F., 2011. Marine radiocarbon reservoir effect along the northern Chile–southern Peru coast (14–24°S) throughout the Holocene. Quaternary Research 75, 91-103.

Phillips, F.M., Argento, D.C., Balco, G., Caffee, M.W., Clem, J., Dunai, T.J., Finkel, R., Goehring, B., Gosse, J.C., Hudson, A.M., Jull, A.J.T., Kelly, M.A., Kurz, M., Lal, D., Lifton, N., Marrero, S.M., Nishiizumi, K., Reedy, R.C., Schaefer, J., Stone, J.O.H., Swanson, T., Zreda, M.G., 2016. The CRONUS-Earth Project: A synthesis. Quaternary Geochronology 31, 119-154.

Reimer, P.J., Bard, E., Bayliss, A., Beck, J.W., Blackwell, P.G., Ramsey, C.B., Buck, C.E., Cheng, H., Edwards, R.L., Friedrich, M., 2013. IntCal13 and Marine13 radiocarbon age calibration curves 0–50,000 years cal BP. Radiocarbon 55, 1869-1887.

Repka, J.L., Anderson, R.S., Finkel, R.C., 1997. Cosmogenic dating of fluvial terraces, Fremont River, Utah. Earth and Planetary Science Letters 152, 59-73.

Reynhout, S., Sagredo, E.A., Kaplan, M.R., Aravena, J.C., Martini, M.A., Moreno, P.I., Rojas, M., Schwartz, R., Schaefer, J.M., 2019. Holocene glacier fluctuations in Patagonia are modulated by summer insolation intensity and paced by Southern Annular Mode-like variability. Quaternary Science Reviews in press.

Ridge, J.C., Balco, G., Bayless, R.L., Beck, C.C., Carter, L.B., Dean, J.L., Voytek, E.B., Wei, J.H., 2012. The new North American Varve Chronology: A precise record of southeastern Laurentide Ice Sheet deglaciation and climate, 18.2-12.5 kyr BP, and correlations with Greenland ice core records. American Journal of Science 312, 685-722.

Sagredo, E.A., Moreno, P.I., Villa-Martínez, R., Kaplan, M.R., Kubik, P.W., Stern, C.R., 2011. Fluctuations of the Última Esperanza ice lobe (52°S), Chilean Patagonia, during the last glacial maximum and termination 1. Geomorphology 125, 92-108.

Singer, B.S., Ackert, R.P., Guillou, H., 2004a. $^{40}Ar/^{39}Ar$ and K-Ar chronology of Pleistocene glaciations in Patagonia. Geological Society of America Bulletin 116, 434-450.

Singer, B.S., Brown, L.L., Rabassa, J.O., Guillou, H., 2004b. $^{40}Ar/^{39}Ar$ chronology of late Pliocene and Early Pleistocene geomagnetic and glacial events in southern Argentina. Timescales of the paleomagnetic field, 175-190.

Smedley, R., Glasser, N., Duller, G., 2016. Luminescence dating of glacial advances at Lago Buenos Aires (~ 46° S), Patagonia. Quaternary Science Reviews 134, 59-73.

Smith, D., Laroque, C., 1996. Dendroglaciological dating of a Little Ice Age glacial advance at Moving Glacier, Vancouver Island, British Columbia. Géographie physique et Quaternaire 50, 47-55.

Steffen, H., 1947. Patagonia Occidental: Las Cordilleras Patagónicas y sus regiones circundantes. Ediciones de la Universidad de Chile, vol. II, Santiago, Chile.

Stern, C.R., 2008. Holocene tephrochronology record of large explosive eruptions in the southernmost Patagonian Andes. Bulletin of Volcanology 70, 435-454.

Stern, C.R., de Porras, M.E., Maldonado, A., 2015. Tephrochronology of the upper Río Cisnes valley (44 S), southern Chile. Andean Geology 42.

Stern, C.R., Moreno, P.I., Henríquez, W.I., Villa-Martínez, R., Sagredo, E., Aravena, J.C., de Pol-Holz, R., 2016. Holocene tephrochronology around Cochrane (~ 47 S), southern Chile. Andean Geology 43.

Strelin, J., Denton, G., 2005. Las morenas de Puerto Bandera, Lago Argentino, in: Congreso Geológico Argentino.

Strelin, J.A., Denton, G.H., Vandergoes, M.J., Ninnemann, U.S., Putnam, A.E., 2011. Radiocarbon chronology of the late-glacial Puerto Bandera moraines, southern Patagonian Icefield, Argentina. Quaternary Science Reviews 30, 2551–2569.

Stuiver, M., Braziunas, T.F., 1993. Modeling atmospheric 14 C influences and 14 C ages of marine samples to 10,000 BC. Radiocarbon 35, 137-189.

Thomsen, K.J., Murray, A., Jain, M., Bøtter-Jensen, L., 2008. Laboratory fading rates of various luminescence signals from feldspar-rich sediment extracts. Radiation measurements 43, 1474-1486.

Thomsen, K.J., Murray, A.S., Jain, M., 2011. Stability of IRSL signals from sedimentary K-feldspar samples. Geochronometria 38, 1-13.

Thorndycraft, V.R., Bendle, J.M., Benito, G., Davies, B.J., Sancho, C., Palmer, A.P., Fabel, D., Medialdea, A., Martin, J.R.V., 2019. Glacial lake evolution and Atlantic-Pacific drainage reversals during deglaciation of the Patagonian Ice Sheet. Quaternary Science Reviews 203, 102-127.

Weller, D., Miranda, C., Moreno, P., Villa-Martínez, R., Stern, C., 2015. Tephrochronology of the southernmost Andean southern volcanic zone, Chile. Bulletin of Volcanology 77, 107.

Winchester, V., Harrison, S., 2000. Dendrochronology and lichenometry: colonization, growth rates and dating of geomorphological events on the east side of the North Patagonian Icefield, Chile. Geomorphology 34, 181-194.

Winchester, V., Harrison, S., Warren, C.R., 2001. Recent retreat Glaciar Nef, Chilean Patagonia, dated by lichenometry and dendrochronology. Arctic Antarctic and Alpine Research 33, 266-273.

Winchester, V., Sessions, M., Cerda, J.V., Wündrich, O., Clemmens, S., Glasser, N.F., Nash, M., 2014. Post-1850 changes in Glacier Benito, North Patagonian Icefield, Chile. Geografiska Annaler: Series A, Physical Geography 96, 43-59.

Wintle, A.G., 1973. Anomalous fading of thermo-luminescence in mineral samples. Nature 245, 143-144.